Advances in Nanocharacterization Techniques : 4D-STEM and XEOL Studies on Perfect and Defective h-BN

Laura Susana

THESE DE DOCTORAT

NNT : 2024UPASP016

Advances in Nanocharacterization Techniques: 4D-STEM and XEOL Studies on Perfect and Defective h-BN

Avancées dans les techniques de nanocaractérisation : études STEM-4D et XEOL du nitrure de bore hexagonal parfait et en présence de défauts.

Thèse de doctorat de l'université Paris-Saclay

École doctorale n° 564 : Physique en Île-de-France (PIF)
Spécialité de doctorat : Physique
Graduate School : Physique. Référent : Faculté des sciences d'Orsay

Thèse préparée dans l' unité de recherche **Laboratoire de Physique des Solides** (Université Paris-Saclay, CNRS), sous la direction de **Alberto ZOBELLI**, Maitre de conférences.

Thèse soutenue à Paris-Saclay, le 08 Mars 2024, par

Laura SUSANA

Composition du Jury

Membres du jury avec voix délibérative

Julien BARJON Professeur, GEMaC, Université Versailles Saint-Quentin-en-Yvelines	Président
Abhay SHUKLA Professeur, IMPMC, Sorbonne Université	Rapporteur & Examinateur
Hanako OKUNO Chargée de recherche (HDR), IRIG-MEM, CEA-Grenoble	Rapporteure & Examinatrice
Andrei ROGALEV Chargé de recherche, ESRF	Examinateur

université PARIS-SACLAY | ÉCOLE DOCTORALE Physique en Île-de-France (PIF)

Title : Advances in Nanocharacterization Techniques: 4D-STEM and XEOL Studies on Perfect and Defective h-BN

Keywords: 4D-STEM, charge density, XEOL, luminescence, hexagonal boron nitride

Abstract: Probing physical properties such as charge density and optical response, on a nanometric scale is an experimental challenge which motivates a continuous search for innovative instrumental techniques and methodologies. This thesis aligns within this context, presenting advances in characterization techniques utilizing transmission electron microscopy and X-ray synchrotron sources. Benchmarks of the technical and methodological developments performed have been obtained on hexagonal boron nitride (h-BN), a wide bandgap material characterized by a significant charge transfer, a complex defective landscape and original optical properties.

The first part of this work focuses on improvements in four-dimensional scanning transmission electron microscopy (4D-STEM) which has recently emerged as a powerful tool for simultaneously obtaining precise structural determinations and capturing details of local electric fields and charge densities. Accurately extracting quantitative data at the atomic scale poses challenges, primarily due to probe propagation and size-related effects which, when neglected, may even lead to misinterpretations of qualitative effects. This work establishes the accuracy of the technique for the measurement of electric fields and charge densities in thin materials via a comprehensive study on pristine and defective h-BN flakes. Through a combination of experiments and numerical simulations, it is demonstrated that while precise charge quantification at individual atomic sites is hindered by probe effects, 4D-STEM can directly measure charge transfer phenomena at an h-BN monolayer edge with sensitivity down to a few tenths of electron and a spatial resolution on the order of a few angstroms.

The second part of this thesis discusses the implementation of a novel X-Ray Optical Excited Luminescence (XEOL) setup at the Resonant Inelastic X-ray Scattering (RIXS) branch of the soft X-Ray SEXTANTS beamline of the Synchrotron SOLEIL. The combination of RIXS and XEOL opens new possibilities for correlated studies of excitation and recombination phenomena in the visible-far UV energy range. The synchronization of the XEOL spectrometer acquisition camera with the beamline X-Ray monochromator permits to acquire full luminescent spectra while scanning the incident radiation energy across the core absorption edge of a given element. From the 2D maps of excitation energy versus luminescence thus obtained, it is possible to associate specific near edge absorption fine structures to well defined luminescence features. Benchmarks have been obtained on perfect and doped cubic and hexagonal boron nitride with results acquired in the far UV comparable with state-of-art optical techniques. The analysis of near edge fine structures of h-BN has permitted to associate low energy emissions to the presence of B-O bonds. Finally the application of XEOL to the study of an h-BN/WS_2 monolayer vertical heterostructure luminescence has provided insights on the excitation transfer mechanism between the layers.

université PARIS-SACLAY | ÉCOLE DOCTORALE Physique en Île-de-France (PIF)

Titre : Avancées dans les techniques de nanocaractérisation : études STEM-4D et XEOL du nitrure de bore hexagonal parfait et en présence de défauts

Mots clés : 4D-STEM, densité de charge, XEOL, nitrure de bore hexagonal

Résumé : L'étude des propriétés physiques telles que la densité de charge et la réponse optique à l'échelle nanométrique est un défi expérimental qui motive une recherche continue de techniques instrumentales et de méthodologies innovantes. Cette thèse s'inscrit dans ce contexte, en présentant des avancées dans les techniques de caractérisation utilisant la microscopie électronique à transmission et les sources synchrotron de rayons X. Les références des développements techniques et méthodologiques réalisés ont été obtenues sur le nitrure de bore hexagonal (h-BN), un matériau à large bande interdite caractérisé par un transfert de charge important, un paysage défectueux complexe et des propriétés optiques originales.

La première partie de ce travail se concentre sur les améliorations apportées à la microscopie électronique à transmission à balayage quadridimensionnelle (4D-STEM), qui s'est récemment imposée comme un outil puissant permettant d'obtenir simultanément des déterminations structurelles précises et de saisir les détails des champs électriques locaux et des densités de charge. L'extraction précise de données quantitatives à l'échelle atomique pose des défis, principalement en raison de la propagation de la sonde et des effets liés à la taille qui, lorsqu'ils sont négligés, peuvent même conduire à des interprétations erronées des effets qualitatifs. Ce travail établit la précision de la technique pour la mesure des champs électriques et des densités de charge dans les matériaux minces par le biais d'une étude complète sur des plaquettes de h-BN vierges et défectueux. Grâce à une combinaison d'expériences et de simulations numériques, il est démontré que si la quantification précise des charges sur des sites atomiques individuels est limitée par les effets de sonde, la technique 4D-STEM peut mesurer directement les phénomènes de transfert de charge au bord d'une monocouche de h-BN avec une sensibilité de quelques dixièmes d'électrons et une résolution spatiale de l'ordre de quelques angströms.

La deuxième partie de cette thèse traite de la mise en œuvre d'une nouvelle installation de luminescence optique excitée par les rayons X (XEOL) à la branche de diffusion inélastique résonnante des rayons X (RIXS) de la ligne de faisceau de rayons X mous SEXTANTS du synchrotron SOLEIL. La combinaison de RIXS et de XEOL ouvre de nouvelles possibilités pour les études corrélées des phénomènes d'excitation et de recombinaison dans la gamme d'énergie du visible et de l'UV lointain. La synchronisation de la caméra d'acquisition du spectromètre XEOL avec le monochromateur de rayons X de la ligne de faisceau permet d'acquérir des spectres de luminescence complets tout en balayant l'énergie du rayonnement incident à travers le bord d'absorption du noyau d'un élément donné. À partir des cartes 2D de l'énergie d'excitation en fonction de la luminescence ainsi obtenues, il est possible d'associer des structures fines spécifiques des seuils d'absorption à des caractéristiques de luminescence bien définies. Des références ont été obtenues sur du nitrure de bore cubique et hexagonal parfait et dopé, avec des résultats acquis dans l'UV lointain comparables aux techniques optiques de pointe. L'analyse des structures fines des seuils d'absorption du h-BN a permis d'associer les émissions de faible énergie à la présence de liaisons B-O. Enfin, l'application de XEOL à l'étude de la luminescence d'une hétérostructure verticale composée de monocouches h-BN/WS_2 a permis de mieux comprendre le mécanisme de transfert de l'excitation entre les couches.

Acknowledgments

In these lines I would like to acknowledge all those who have contributed to the work presented in this thesis. First of all, I wish to thank my supervisor Alberto Zobelli as without him this thesis wouldn't have been possible. It has been a pleasure to work with a person who's such deeply passionate about science and physics, and who pushes you always to go further in the research. Thank you for being always available for helping me and for all the interesting debates and chats, involving science, culture and in general life.

I would like to thank the people of the STEM group, at the LPS laboratory in Orsay, who actively participated for the success of this Ph.D. thesis. In particular I deeply thank Alexandre Gloter, as without him the whole microscopy part wouldn't have been possible, and for his constant help and scientific debates, it was a true pleasure working with you. Following, I have to thank Marcel Tencè and Jean-Denis Blazit for their necessary and constant help with the microscopes, Steffi Woo and Luiz Tizei for their help in the sample preparation and Odile Stephan for her kindness and help throughout the whole thesis.

Regarding the experience at SOLEIL, a special thanks goes to Alessandro Nicolaou, for believing in our project and giving us full trust when operating at the SEXTANTS beamline, and for his constant help in understanding synchrotron related phenomena. Furthermore, I deeply thank Victor Porée for his help and his infinite kindness and liveliness, that made the days at the synchrotron lighter and funnier.

A global thanks to the whole STEM group, with who I spent three magical years, laughing, eating and drinking, and watching smart movies (and working obviously). In particular, I want to personally thank Maeva, Aravind, Marc and Jassem for helping me and making me laugh a lot.

I want to thank my family for his support, even if from far, my italian and international friends and my two cats.

Lastly, the biggest thanks goes to my boyfriend, Mattia, who stayed by my side during the whole experience and most importantly put up with me, cooked for me and deeply helped me all these years. Grazie Tia!

Contents

Abbreviations

4D-STEM	Four dimensional Scanning Transmission Electron Microscopy
ADF	Angular Dark Field
AFM	Atomic Force Microscopy
BF	Bright Field
CBED	Convergent Beam Electron Diffraction
***c*-BN**	cubic Boron Nitride
CCD	Charge-Coupled Device
CL	Cathodoluminescence
CoM	Center of Mass
CTEM	Conventional Transmission Electron Microscopy
CTF	Contrast Transfer Function
CVD	Chemical Vapour Deposition
DPC	Differential Phase Contrast
DFT	Density Functional Theory
EELS	Electron Energy Loss Spectroscopy
EFM	Electrostatic Force Microscopy
ELNES	Energy Loss Near Edge Structure
FWHM	Full Width at Half Maximum
***h*-BN**	hexagonal Boron Nitride

HAADF	High Angle Annular Dark Field
HRTEM	High Resolution Transmission Electron Microscopy
IAM	Indipendent Atomic Model
IMFP	Inelastic Mean Free Path
KPFM	Kelvin Probe Force Microscopy
LAADF	Low Angle Annular Dark Field
MAADF	Medium Angle Annular Dark Field
NEXAFS	Near Edge X-ray Absorption Fine Structure
NRIXS	Non Resonant Inelastic X-ray Scattering
ODXAS	Optically Detected X-ray Absorption Spectroscopy
PL	Photoluminescence
PLY	Partial Luminescence Yield
POA	Phase Object Approximation
ELNES	Resonant Inelastic X-ray Scattering
SNR	Signal to Noise Ratio
STEM	Scanning Transmission Electron Microscopy
STM	Scanning Tunneling Microscopy
TEM	Transmission Electron Microscpy
TEY	Total Electron Yield
TFY	Total Fluerescence Yield
TMD	Transition Metal Dichalcogenide
WPA	Weak Phase Approximation
XANES	X-ray Absorption Near-Edge Spectroscopy
XEOL	X-ray Excited Optical Luminescence
ZLP	Zero Phonon Line

CHAPTER 1

Introduction

Over the past two decades, the field of nanoscience has garnered increasing attention due to the wide scientific disciplines that it covers, spanning physics, chemistry, materials science and biology. This interest is driven by the desire to understand the distinctive functionalities of nanoscale phenomena and use them for innovative technological advancements. In this context, properties such as structure, charge distribution, optical response, and their evolution across the nanosystem are key elements for understanding its capabilities.

A common approach is to observe some of these properties on the nanosystem and note a qualitative difference from their bulk counterpart. The measurement is often qualitative, as the nanometric heterogeneity of the properties is frequently beyond the reach of many bulk experimental techniques. It often provides only a first glimpse that a new functionality might arise from a local alteration of one of these properties. However, establishing cause-and-effect relationships or aiming for the optimization of the functionality often relies on more quantitative measurements, even such quantification poses an experimental challenge when performed "nanometer per nanometer". Furthermore, this local quantification enables an interesting direct comparison with what modern first-principle-based calculation techniques can provide (e.g., relaxed structure on thousands of atoms or a precise charge distribution). Both approaches thus synergistically enrich each other.

Yet, probing these properties experimentally necessitates a continuous quest for novel instrumental techniques and methodologies and the search for possibilities to combine or correlate several of those techniques. Transmission electron microscopy (TEM) and its associated spectroscopies are among the most established techniques for accessing relevant information at the nanometric scale and, with the advent of modern aberration correctors, at the atomic one. Another route for studying localized phenomena involves the use of resonant techniques,

where the localization is achieved through the selective energy of the primary excitation, following specific transitions of the material under investigation. X-ray spectroscopies performed at synchrotron radiation sources are well-adapted to this goal.

This manuscript aligns within this context, presenting advancements in characterization techniques utilizing transmission electron microscopy and X-ray synchrotron sources. The first part of this work focuses on improving four-dimensional scanning transmission electron microscopy (4D-STEM), establishing its accuracy for the the measurement of charge density at the atomic resolution. In the second part, I will present the integration of an X-ray excited optical luminescence (XEOL) system within a resonant inelastic X-ray scattering (RIXS) soft X-ray beamline at the synchrotron SOLEIL, with the aim of correlative studies between luminescence and structure.

Both studies will be performed on hexagonal boron nitride (*h*–BN), a wide bandgap material characterized by a significant charge transfer, a complex defective landscape and original optical properties which will later sketched in this chapter. These properties make *h*–BN a perfect test sample for the 4D-STEM and XEOL development but also serve as the basis for its integration into heterostructures and devices, such as for memristor [1] and as a dielectric [2], or as a possible quantum optic source [3].

New implementations in (S)TEM microscopy. Despite TEM foundation dates back to almost one century ago, it still remains a very dynamical field of research. A sub-category of TEM is scanning transmission electron microscopy (STEM), where a highly focused electron probe is scanned across a sample's area of interest. Thanks to the incorporation of multiple detectors capturing signals from electrons scattered at different angles, STEM offers the capability to generate a variety of imaging modes unveiling specific structural details. Low-angle scattered electrons contribute to STEM bright-field images, where, for thin objects, the contrast relates with the sample phase. The integration of high-angle scattered electrons produces STEM dark-field images, where the contrast correlates with the atomic number of the atoms. Recent advances in fast and highly sensitive detectors have significantly enhanced the capabilities of STEM microscopy. In particular, the implementation of pixellated direct detectors at the diffraction plane has enabled the collection of the complete convergent beam electron diffraction (CBED) pattern for every probe position, leading to the creation of a four-dimensional dataset (4D-STEM). This advancement has broadened the capabilities of electron microscopy, opening the way towards new observables.

In the last five years, 4D-STEM has emerged as a valuable tool for the investigation of charge density distribution across different classes of materials,

ranging from ferroelectric oxides to defective low-dimensional materials. Up to now, most of works have only provided a qualitative discussion of charge redistribution phenomena, but more quantitative analysis would be desirable. The influence of the electron probe-material interactions has been also only seldom discussed despite probe effects can significantly affect the measurements, with the risk of inaccuracies in the physical interpretation of the findings.

In this thesis, these limits have been overcome by a comprehensive study on the ultimate capabilities of 4D-STEM in providing quantitative information on electric field and charge density distribution in low-dimensional materials. Particular emphasis has been given on understanding the influence of electron probe related effects and to define an appropriate methodology to extract quantitative estimation of charge accumulation in defective systems.

This study has been conducted on self-suspended monolayer hexagonal boron nitride (*h*–BN), which combines ideal characteristics for charge redistribution studies via 4D-STEM. In particular, the advantage of *h*–BN for 4D-STEM studies relies in its polarity, which is attributed to the marked difference in electronegativity between boron and nitrogen and implies a significant charge transfer between the two atoms [4–8]. Moreover, the lightweight nature of *h*–BN, coupled with a favorable balance between core and valence electrons, positions it as an optimal candidate for exploring the capabilities of quantitative 4D-STEM in evaluating charge transfer phenomena.

Defects in *h*–BN have also been extensively studied by STEM microscopy, where the high polarity of *h*–BN is expected to produce significant charge redistribution at defective sites but these effects have not been yet investigated experimentally. 4D-STEM could in principle help in addressing these open questions, as it will be later discussed in this thesis.

Implementation of a XEOL setup for a RIXS beamline. STEM imaging is essentially based on information arising from elastic scattered electrons but inelastic processes can also be investigated with the same high spatial resolution down to the atomic level. Electron energy loss spectroscopy (EELS) is a well-established technique which in the last years has benefited from the availability of performant monochromated equipments which have permitted to extended its energy domain of applicability. It is now possible to investigate a broad energy range, from few tenths of meV up to a few keV, giving access to diverse excitations such as phonons, excitons, plasmons, and core excitations. Over the last fifteen years my host-group at the LPS has also developed a specific catholuminescence equipment for STEM microscopy. This setup combining EELS and nano-CL has opened the way to correlative studies of excitation de-excitation processes with a nanometric space resolution.

While STEM electron spectroscopies offer high spatial selectivity, synchrotron sources provide well-defined polarization of the exciting radiation and element selectivity when the energy is chosen in resonance with specific core edges. EELS spectroscopy has been traditionally paired with X-ray absorption near edge spectroscopy (XANES) for investigating fine structures at core absorption edges. Recent advances in low-energy EELS spectroscopy has easied studies in the IR-optical range, an energy domain accessible also via (resonant) inelastic X-ray spectroscopy, (R)IXS. RIXS focuses on neutral excitation phenomena with identical initial and final energy states as EELS, but its distinctive features lie in being a resonant technique. The two techniques appear therefore as highly complementary and correlative studies are particularly suitable.

As for the study of recombination phenomena in the optical domain, cathodoluminescence can be linked to X-Ray excited optical luminescence (XEOL) spectroscopy. XEOL is an X-ray photon in/optical photon out technique which involves the conversion of the X-ray energy absorbed by the materials to optical photons, involving multi-step energy transfer processes. This technique dates back from the early days of X-Rays and over the past decades XEOL setups have been installed in various synchrotron facilities and coupled with several X-ray techniques. However, its integration with synchrotron spectroscopies investigating the optical domain has not been fully explored yet. In this context it is highly suitable to combine RIXS and XEOL within a single beamline. This approach would be similar to the EELS-CL coupling in a STEM permitting correlated studies of excitation and recombination phenomena. These four spectroscopic techniques have access to the UV-C spectral domain, generally challenging to reach by optical techniques but critical for understanding wide bandgap materials.

A significant portion of my thesis has been dedicated to the implementation and commissioning of a novel UV-VIS XEOL setup at the RIXS-dedicated branch of the soft X-rays SEXTANTS beamline, situated at the synchrotron SOLEIL. A particular focus has been posed on exploring the correlation between the structure and luminescence through XEOL. Indeed, XEOL allows measuring the luminescence as a function of the incident beam energy, scanned across core absorption edges of the specimen's elements. From the integration of the XEOL intensity it can be reconstructed the so called Near-Edge XEOL, from which specific absorption fine structures can be associated with well defined luminescence features.

To benchmark the novel UV-VIS XEOL setup, *h*–BN results once more to be an ideal system due to its unique properties making it an emerging advanced optical material. The presence of bright UV luminescence and stable color centers in a far range from visible to UV makes hexagonal boron nitride (*h*–BN) an excellent choice for testing XEOL optical performance. The use of high-energy radiation as excitation source provides an alternative way for investigating the

intricate optical properties of *h*–BN, where optical measurements are challenging due to its wide band gap. Another interesting property of *h*–BN is the presence of strong cross sections for X-Ray adsorption at both the B and N K edges with fine structures presenting a significant polarization dependence associated to the high anisotropy of the system. These features are particularly sensitive to the chemical environment. X-Ray absorption is a significant component in defining the XEOL intensity and therefore the *h*–BN XEOL signal might reflect the richness of this information. All these aspects have been extensively studied within this thesis work.

Finally, *h*–BN is also extensively employed as the ideal substrate for a different class of 2D materials due to its wide band gap, high temperature and mechanical stability, which allow to preserve the pristine electronic and optical properties of the overlapping materials. In the last years, different van der Waals heterostructures have been produced by the encapsulation of transition metal dichalcogenides (TMDs) between thick *h*–BN flakes, showing enhanced and unique optical properties with respect to the non stacked counterpart. However, the physical mechanism behind the enhancement of the optical properties when the heterostructure is illuminated with an high energy radiation is not yet fully understood. An approach to investigate possible excitation transfer phenomena between the layers is to perform XEOL measurement across the boron K-edge and studying the behavior of the TMDs' emission.

Hexagonal boron nitride

As already mentioned, *h*–BN has been used as a prototype material in this thesis to test both the 4D-STEM capabilities and the novel installed XEOL setup at the SEXTANTS beamline. In this section I am going to summarize the main physical properties of this materials, which is at the center of many different research for both its unique electronic and optical properties.

Boron nitride is a synthetic material which was firstly produced in 1842 in its hexagonal form and in 1957 in its cubic form. Currently, BN is extensively employed in number of applications ranging from optics, cosmetics, lubricants, ceramics etc. The hexagonal phase of boron nitride (*h*–BN) has strong structural analogies with graphite, both crystals being constituted by piled up mono-atomic layers weakly interacting and formed by an hexagonal lattice where atomic orbitals at both atomic species are sp^2 hybridized. The B-N bond length is 1.46 Å and the in plane lattice parameter is 2.52 Å. The most common stacking for *h*–BN is the AA′, where all atoms are arranged in columns alternating boron and nitrogen atoms, with an inter-layer distance of 3.3 Å.

First high quality macroscopic mono-crystals of *h*–BN were obtained by T. Taniguchi in the early 2000's [9]. In the same period the discovery of graphene

and of its exceptional electronic properties motivated a large interest for all layered materials. The first *h*–BN monolayer was isolated in 2008 through exfoliation from a microscopic crystal [10]. Nowadays monolayer *h*–BN is commercially available in the form of a CVD grown material. Due to its simple and reliable structure, *h*–BN has been widely used to benchmark novel electron microscopy and spectroscopy techniques, in particular to test the ultimate performance of high resolution imaging modes. (S)TEM microscopy has also permitted to observe a large variety of point and extended defects. Indeed, atoms can be ejected by the electron beam by direct knock-on collision, leading to the formation of single and multi-vacancies, or more extended defects such as voids with sharp atomic edges. Finally individual atoms of different atomic species adsorbed at the pristine *h*–BN basal plane have also been often observed.

As mentioned before, despite being characterized by covalent sp^2 hybridized bonds, *h*–BN is expected to be a rather polar system. This is mainly due to the strong difference in electronegativity between the atoms, being 3.04 for nitrogen and 2.04 for boron. DFT calculation predicts an electron charge transfer of ca. 2.1 e^- from boron to nitrogen, which result in a high localization of the electron charge density at the nitrogen sites. This value has been confirmed by the electron charge density map obtained from X-ray diffraction of a bulk single crystal [5]. Its strong polarity and the *h*–BN availability in the monolayer form makes *h*–BN a good candidate for testing 4D-STEM capabilities in measuring charge transfer effects at the atomic level which can be significant at defective sites.

The last twenty years have seen an emerging interest on *h*–BN as an advanced optical material, since it acts as a strong optical source in the far ultraviolet (UV) and hosts bright and stable single photon emitters, generally associated to the presence of defects. In 2004, a major step towards the understanding of the optics of *h*–BN came from the first cathodoluminescence experiments on high quality monocrystals conducted by Watanabe and Taniguchi [9], which have shown a very strong signal in the far UV, at 5.75 eV. The high quantum yield observed was interpreted as indicative of a direct wide band gap, contrasting with theoretical calculations that characterized *h*–BN as an indirect band gap semiconductor. In 2006 first-principle many body perturbation theory calculations were able to reconcile theory and experiment demonstrating that *h*–BN is characterized by an indirect quasi particle band gap and strong excitonic effects [11–13]. More recently, Cassabois et al. demonstrated that the emission spectrum is profoundly structured by the phonon-assisted recombination of an indirect exciton and that the sole exciton-recombination provides only a faint luminescence [14, 15], further supported by theoretical calculations [16, 17]. Finally since 2016 several room temperature stable and bright single photon sources have been identified both in the visible [18, 19] and, by my host group in the LPS, in the far UV spectral range [3]. These discoveries have initiated a very dynamic research

activity on *h*–BN as a new material for quantum optics.

Outline of this thesis

This thesis is structured as follows. Chapter 2 will be dedicated to the presentation of the (S)TEM techniques employed. Firstly, an overview of the physical principles governing image formation in TEM will be given, followed by a presentation of STEM microscopy. As a primary interest of this thesis work regards the study of charge density and electric field distribution, the experimental techniques used thus far to this aim will be illustrated, together with their limitations. The last part of the chapter will be dedicated to 4D-STEM. After presenting the principles of the technique and how it permits to extract insight on electric fields and charge density, I will provide a short overview of significant examples extracted from the recent literature.

Chapter 3 is dedicated to the implementation of a 4D-STEM setup and the presentation of key results obtained on pristine and defective *h*–BN. Firstly a brief overview of previous literature on 4D-STEM measurements on 2D materials will be given, with a specific focus on *h*–BN and the limits encountered for the quantitative determination of charge density and electric fields. The 4D-STEM setup implementation for our Nion UltraSTEM 200 microscope will be later detailed together with a precise operating protocol. This methodology will be then applied to the study of pristine *h*–BN, combining 4D-STEM experiments, image simulations and DFT-derived calculations. Afterwords, results obtained for various defective systems will be given. An in depth quantitative analysis of both electric field and charge density will be presented for a nitrogen terminating zig-zag edge. Lastly, a qualitative analysis of point defects as boron vacancies and heavy adatoms will be presented, demonstrating the high sensibility of this technique with respect to conventional imaging techniques.

Chapter 4 focuses on the development of a XEOL setup at the RIXS beamline SEXTANTS, within the SOLEIL synchrotron facility. The chapter begins with a comparison between EELS and RIXS spectroscopies, presenting original results on the spectroscopic response of *h*–BN. Later, the design of the XEOL setup implemented at the SEXTANTS beamline will be detailed. Benchmarks on the system performance have been obtained on different BN allotropes. A post-processing methodology will be presented to correlate specific luminescence features with well characterized near absorption edge fine structure. The final section of the chapter covers the application of XEOL measurements in the study of excitation transfer phenomena within *h*–BN/TMDs vertical heterostructures.

In the concluding Chapter 5, the primary results and findings of this thesis will be summarized, together with an overview of potential uses and planned upgrades of the methods and setups developed in this thesis work.

CHAPTER 2

(S)TEM microscopy: from a short introduction to 4D-STEM theory

Transmission electron microscopy (TEM) has evolved into a sophisticated sub-nanometer-resolution imaging technique that has revolutionized our understanding of the nanoscale world. Its development has not only allowed to visualize structures at the atomic level, but has also opened to the exploration of a vast array of physical properties and phenomena. This versatility is a direct result of the rich and intricate interaction between electrons and matter. In particular, two main physical phenomena can be distinguished: elastic and inelastic scattering [20].

Elastic scattering arises from the interaction between incident electrons and the nuclei within the specimen under investigation. These electrons can disperse across a broad range of angles, spanning from zero deviation up to 200 milliradians ca. Small-angle deviations are associated with coherent electrons, while higher-angle deviations indicate incoherent scattering. The majority of incident electrons experience weak scattering, and the signal generated is extensively utilized in conventional TEM techniques to achieve high-resolution imaging of materials and to explore diffraction phenomena in crystalline samples. High-angle scattered electrons, which result from strong interactions with nuclei, are usually employed in scanning transmission electron microscopy (STEM) to generate high-resolution images, known as dark-field images, where the contrast is directly proportional to the atomic number of the elements present in the material.

Inelastic scattering, instead, occurs between particles with similar masses, like the fast electrons in the beam of a TEM and the atomic electrons surrounding the nuclei within a specimen. This phenomenon has paved the way for the development of various spectroscopic techniques, like electron energy loss spectroscopy (EELS).

With the development of fast and sensible detectors of the last decade, other microscopy methods have emerged, as four dimensional (4D-) STEM. This technique involves the collection of converged-beam electron diffraction (CBED) patterns for each probe position during the scanning process, resulting in the generation of a 4D dataset. The range of applications is really wide, spanning from the local mapping of crystal phases and orientations to the enhancement of image resolution. Another key application, which is the central focus of the electron microscopy part of my thesis, is the capability to map electric fields and charge densities at the atomic scale. Whereas these information can be extracted theoretically form first-principle calculations, there is currently a shortage of experimental techniques capable of achieving this at the atomic level and in a quantitative way.

While conventional (S)TEM techniques are well-established within my host team, the STEM group at LPS, a consistent part of my thesis has been dedicated to the development and exploration of 4D-STEM. This chapter provides a comprehensive overview of the aforementioned conventional and innovative electron microscopy methods.

Section 2.1 offers an in-depth examination of conventional and high-resolution TEM. During my thesis, this technique has been essential for preliminary sample investigations and verifying sample preparation quality. In Section 2.2, we delve into the fundamental principles of STEM techniques, encompassing the generation of diverse imaging contrasts, achieving high resolution, and EELS spectroscopy. This techniques enabled advanced structural studies at atomic resolution and facilitated the assessment of sample quality through EELS.

An overview of the different experimental techniques generally employed for the detection of electrostatic properties, such as electric field and charge density, will be exposed in Section 2.3, together with their limitations and so the quest for a new technique. Section 2.4 will expose the underlying physical principles of 4D-STEM, with a particular focus on CBED theory. This section will illustrate how the study of CBED patterns can yield valuable insights into the electrostatic properties of materials. These concepts are essential for a comprehensive understanding of the preliminary works done on thick materials, presented in Section 2.5, and more importantly the experimental results obtained and presented in this thesis in Chapter 3, regarding the study of pristine and defective *h*–BN.

2.1. Conventional transmission electron microscopy

The foundation of conventional TEM (CTEM) microscopy can be traced back to the pioneering contributions of Ernst Ruska and Max Knoll in 1932 [21, 22]. Several decades later, in 1986, this research earned Ernst Ruska a Nobel Prize,

Max Knoll being already deceased. This microscopy technique operates based on the fundamental principle of transmitting a beam of electrons through a suitably thin sample, followed by the use of various optical systems to focus and magnify the resulting image of the studied sample. A scheme of a TEM microscope is given in Fig. 2.1. The electron beam is generated by condensing and accelerating

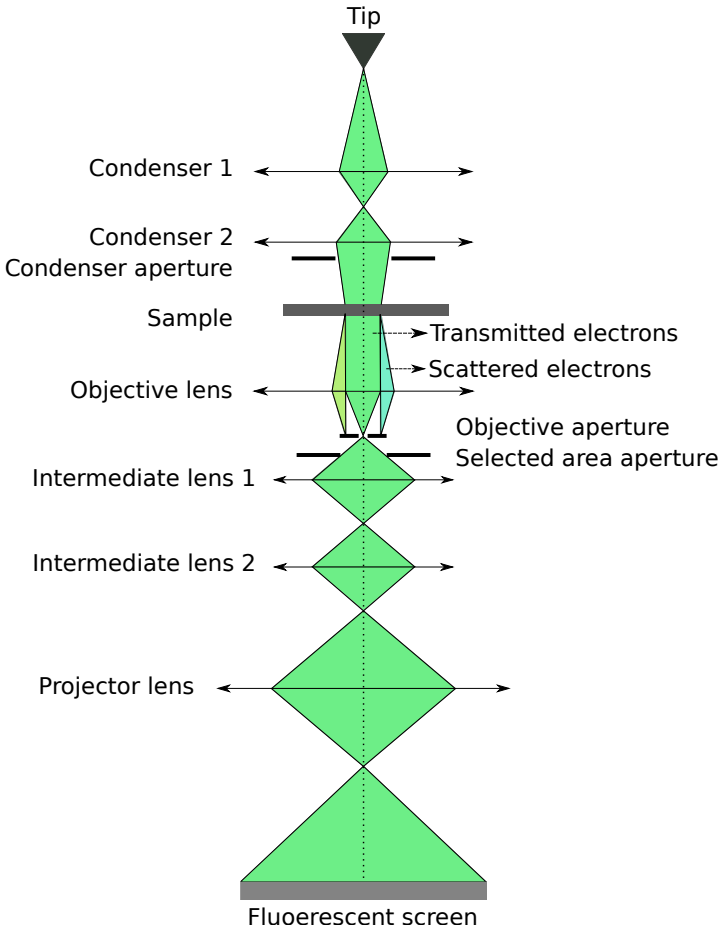

Figure 2.1: *Schematic representation of a transmission electron microscope.*

electrons that are extracted through thermionic or field emission processes from a sharp refractory metal tip, commonly referred to as electron gun. Typically, acceleration voltages within the range of 60-300 kV are employed.

A series of electromagnetic lenses and apertures positioned along the optical axis of the microscope enables the manipulation of the electron beam. Condenser lenses are responsible for collimating the beam, which subsequently interacts with the specimen and undergoes partial diffraction. The objective lens then focuses the transmitted electrons, resulting in the formation of an image of the sample on the image plane of the lens. Subsequently, the intermediate lenses further

magnify the image, which is ultimately projected onto a phosphorescent screen or a charge-coupled device (CCD) camera. Along the optical axis, different metallic apertures can be inserted at the objective focal plane (objective aperture) or the image plane (selected area aperture) to enhance the control and selectivity of the imaging process.

In conventional TEM, the objective aperture serves the purpose of selecting specific spots within the diffraction plane resulting from the illuminated specimen (Bragg diffraction). Different kind of images can then be produced, classified on the basis of their contrast. In the bright field imaging mode the objective aperture allows the integration of the signal deriving from the sole low angle diffracted electrons. Conversely, in the dark field mode the aperture selects only one diffracted spot, related to specific families of crystal planes, providing space selectivity in the imaging process. The selected area aperture, on the other hand, is employed to designate the specific area of the specimen from which the diffraction pattern is projected onto the fluorescent screen [21].

In high resolution transmission electron microscopy (HRTEM) the image contrast arises from the self-interference in the image plane of the electron wave with itself. This allows to image crystallographic or amorphous structures at the atomic scale and makes HRTEM one of the main tools for structural and morphological studies of solids. At the sample level, the electrons waves can be approximated as a coherent plane waves, which are diffracted by the interaction with the sample. The frequencies of these diffracted waves correspond to the spatial frequency distribution of the crystal structure within the sample.

Phase object approximation In a simplified form, for thin materials the electron wave function exiting the sample under study can be derived as the product of the incident wave function, Ψ_0, multiplied by the so-called transmission function $q(\vec{r})$, which depends on the position. This function is generally written as the sum of two contributions, considering both elastic and inelastic phenomena [23–25]. In a first approximation, since the scattering angles for electrons are relatively small (about 10^{-2} rad), in traversing relatively thin samples the electron wave does not suffer a sideways displacement of more than about 1 Å. Therefore, one can assume that an electron wave traversing a thin specimen, elastically suffers a phase change that depends on the distribution of potential along a straight-line path through the object. Thus, if the potential distribution in the object is presented by the function $V(x, y, z)$, a plane wave transmitted through the object in the z-direction suffers a phase change that is a function of the (x,y)-coordinates, proportional to the projection of the potential in the z-direction:

$$V(x, y) = \int V(x, y, z)dz \tag{2.1}$$

Similarly, absorption effects related to inelastic-scattering can be represented by a function $\mu(x, y)$, and act on the amplitude terms. Considering all these contributions, the transmission factor can then be written as:

$$q(x, y) = exp[-\mu(x, y) - i\sigma V(x, y)], \tag{2.2}$$

where the interaction constant σ is equal to $\pi/\lambda E$, and defines the strength of the interaction between the electron waves and matter. Usually the contribution of absorption to the image is small for thin specimen, and equation 2.2 can be re-written as:

$$q(x, y) = exp[-i\sigma V(x, y)]. \tag{2.3}$$

This equation is the main results of the phase object approximation (POA). Indeed, it is an approximation in that it ignores the sideways scattering of the waves and absorption phenomena, which can have significant effects, in practice, for thickness greater than a few tens of angstroms. For the class of materials where the POA doesn't apply, the transmission function may be complicate to derive. The POA is useful because it emphasizes the nonlinear nature of electron scattering, in fact changes in the projected potential do not give proportionate changes in the transmission function.

Weak phase approximation The discussion of phase contrast imaging for thin specimens becomes simpler if it is possible to make the further assumption that the phase changes of the electron wave are small. This is generally the case when $\sigma V(x, y)$ is much less than one, that is for very thin materials possibly composed of light atoms. In this case, the expression for the transmission function can be modified using a first order expansion of the exponential, resulting in:

$$q(x, y) = 1 - i\sigma V(x, y) \tag{2.4}$$

The constant 1 then represents the directly transmitted wave unaffected by the object, and gives rise to the sharp central peak of the beam in the diffraction pattern, at the back focal plane of the objective level. The $i\sigma V(x, y)$ term represents the scattering function, which gives rise to the distribution of scattered amplitude in the back focal plane. This approximation and derivation of $q(x, y)$ is called Weak Phase Approximation (WPA). The wave function exiting by the sample, $\Psi_{exit}(x, y)$, is then equal to:

$$\Psi_{exit}(x, y) = \Psi_0(x, y)[1 - i\sigma V(x, y)] \tag{2.5}$$

To form the image, the exit wave function has then to interact with the objective lens, whose effect is a blurring. In the image plane, this can be expressed by a convolution between the exit wave and the lens transfer function, $h(x, y)$:

$$\Psi_I(x, y) = \Psi_{exit}(x, y) * h(x, y) = \Psi_0(x, y)[1 - i\sigma V(x, y)] * h(x, y), \tag{2.6}$$

Being a transfer function, $h(x, y)$ is a complex function, and can be generally written as $h(x, y) = c(x, y) + is(x, y)$. Then Eq 2.6, normalized by the incident amplitude $\Psi_0(x, y)$, becomes:

$$\Psi_I(x, y) = 1 + \sigma V(x, y) * s(x, y) - i\sigma V(x, y) * c(x, y). \tag{2.7}$$

The image intensity is found by multiplying $\Psi_I(x, y)$ by its complex conjugate; ignoring terms of second order in $\sigma V(x, y)$, we obtain

$$I(x, y) = |\Psi_I(x, y)|^2 = 1 + 2\sigma V(x, y) * s(x, y), \tag{2.8}$$

which produce a signal that is proportional to the projected potential of the sample. This is the core of WPA, making TEM technique a tool to get insights on the electrostatic potential and charge density distribution for thin materials [8]. However, the transfer function of the lens contributes as well to a phase change, and may complicate the contrast produced during the imaging formation. In particular, h is composed of different contributions, and to study them in detail it is better to re-write all the quantities in the reciprocal space, corresponding to the diffraction plane in a TEM. Then Eq. 2.6 becomes:

$$\widetilde{\Psi}_I(k_x, k_y) = \widetilde{\Psi}_{exit}(k_x, k_y) \cdot \widetilde{h}(k_x, k_y), \tag{2.9}$$

where $\widetilde{h}(k_x, k_y)$ is called the contrast transfer function (CTF). In general the CTF includes the effect of the objective aperture (A), coherence of the lens (E) and all the aberrations produced by the lens itself (B). Considering all these contributions, we can re-write $\widetilde{h}(k_x, k_y)$ as:

$$\widetilde{h}(k) = A(k) \cdot E(k) \cdot B(k). \tag{2.10}$$

For a microscope characterized by a lens having no aberrations, the transfer function only includes the aperture, whose effect can be represented by multiplying the wave function in the back focal plane by the aperture function $A(k_x, k_y)$, which is 1 for $k_x^2 + k_y^2 < k_0$ and zero elsewhere. k_0 is the maximum scattering vector and is related to the maximum scattering angle passing through the aperture α. Thus, the objective aperture acts as a filter on the sample frequencies that can be imaged by the microscope. In this ideal situation the image or spatial resolution, which is defined as the minimum distance at which two distinct features can be discerned, can be expressed as:

$$r_d = 0.61\frac{\lambda}{nsin\alpha}, \tag{2.11}$$

where λ denotes the electron wavelength and it's related to the acceleration voltage employed, while $nsin\alpha$ represents the numerical aperture. This expression is

defined as the Rayleigh criterion, and it is a direct consequence of the diffraction limit. However, lens produce aberrations which are usually classified as: defocus, spherical aberration, astigmatism, and chromatic aberration. All of these contributions enter in the $B(k)$ term, which can be rewritten as:

$$B(k) = K(k)exp[i\chi(k)], \tag{2.12}$$

where $\chi(k)$ is the total phase error, and it is imparted by astigmatism, spherical aberration and defocus, while $K(k)$ acts on the amplitude of the scattered electron waves and is due to incoherence effects.

Astigmatism refers to differences in focal lengths of a lens in various planes containing the optic axis and results from a lack of cylindrical symmetry of the magnetic field of the lens. This fault is quite common and can be corrected by the presence of stigmators that supply correcting fields.

Defocus and spherical aberration are usually treated together as providing the most significant, cylindricallly symmetrical perturbations of the phase changed produced by a lens [23]. In particular, spherical aberration arises from the inability of the lenses to focus all rays passing through different parts of the lens aperture to a common focal point. This is due to the fact that electrons passing through the periphery of the lens are refracted more than those passing along the axis, leading to a degradation of the image sharpness and resolution (Fig. 2.2). These aberrations have a proportionality dependence on the semi-convergence (α) angle of the kind α^3, meaning that its effect dramatically increases as α increases. This dependence is in contrast with the diffraction limit one, meaning that a compromise in choosing the α value has to be made. The aperture is also used to reduce the number of peripheral electrons contributing to a degradation in the imaging process. Each of these aberrations have a specific contribution to

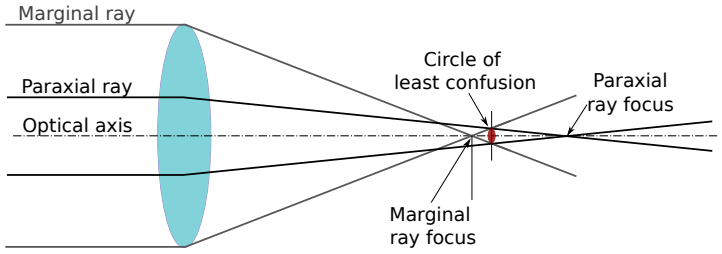

Figure 2.2: *Schematic representation of spherical aberrations.*

the phase error $\chi(k)$, which can be written as:

$$\chi(\vec{k}) = \chi_{\Delta f}(k) + \chi_S(k) = \pi\Delta f\lambda k^2 + \frac{1}{2}\pi C_s\lambda^3 k^4, \tag{2.13}$$

with Δf the defocus amount and C_s the spherical-aberration constant.

As already mentioned, the resolution is also limited by the spatial coherence of the source and by chromatic effects. In particular, the effect of chromatic aberrations is seen when electrons traveling at different velocities experience a different Lorentz force as they cross the lens, and are focused at different distances along the optic axis. This translates in a degradation of the resolution of the image, but can be reduced substantially by using a FEG electron source with a small energy spread. However, even with a non-spreading electron source, it is important to note that the beam energy distribution always broadens due to inelastic interactions between incident electrons and the specimen through. Hence small chromatic distortions are unavoidable in TEM images. This kind of aberration induce a blurring of the focal point defined as:

$$\Delta f = \frac{\Delta E}{E} C_c, \tag{2.14}$$

where C_c is the chromatic aberration coefficient, ΔE is the spread in energy produced by the tip, and E is the energy at which the microscope operates.

Due to all these contributions to the phase shift and amplitude modification imparted to the electron wave during the whole process, interpreting the resulting image's contrast can be challenging. Even slight variations in residual aberrations or defocus values can produce different contrasts. Therefore, interpretation is usually accomplished through a comparison with well-implemented image simulations.

Typical angles in a TEM are limited to about 10 mrad to reduce spherical aberration effects; working with a typical acceleration voltage of 100 kV, i.e. a wavelength of about 3.7 pm, gives a resolution of ca. 2.2 Å. The development of aberration correctors has opened the possibilities to use larger semi-convergence angle without introducing strong aberrations effects, and achieve a sub-Ångström final resolution, as we will see in the next section.

JEOL JEM-2010 High resolution imaged have been acquired on the JEOL JEM 2010 transmission electron microscope. It is a HRTEM with an operating accelerating voltage at 80, 100, 120 and 200 kV, ensuring a point resolution of 0.19 nm. A double tilt holder is available with 35/24 degrees of tilt, enabling micro-structural analysis for a variety of crystalline materials. It provides bright or dark field morphology images, and the corresponding crystal structures by electron diffraction. The pole piece has a spherical aberration of C_s=0.5 mm and a chromatic aberration of C_c=1.1 mm. The electron source used is a heated LaB_6 tip. Vacuum systems operates in the range of 10^{-7} Torr.

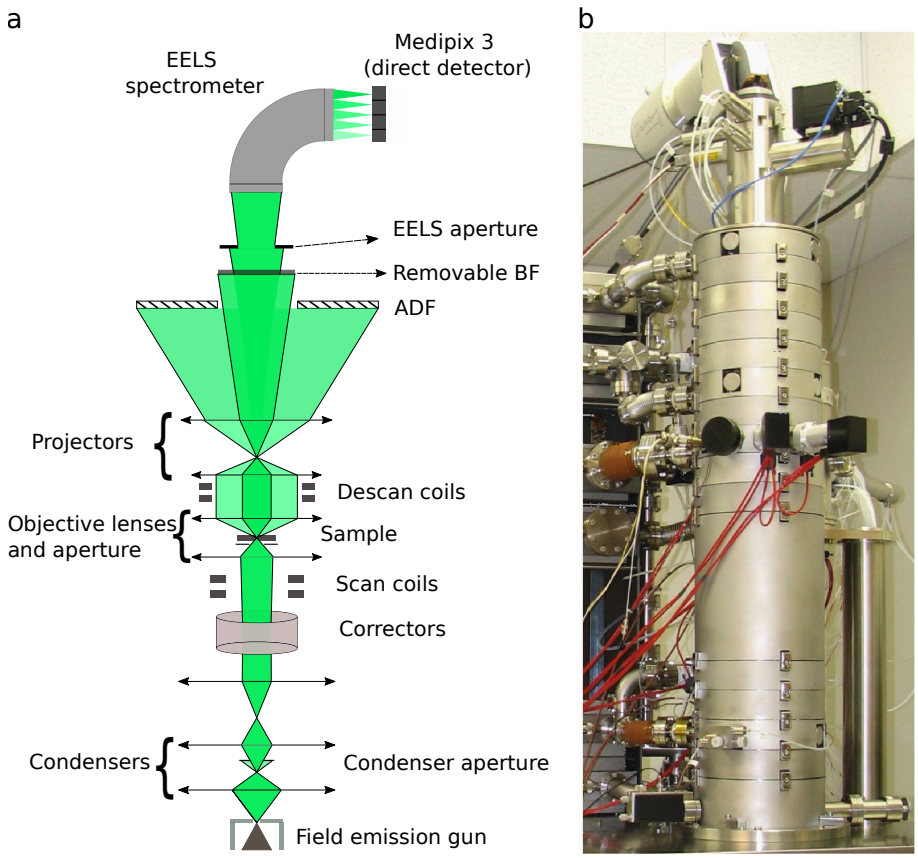

Figure 2.3: *(a) Schematic representation of a scanning transmission electron microscope. (b) Photograph of an UltraSTEM200 extracted from Ref. 26.*

2.2. Scanning transmission electron microscopy

Like conventional TEM, STEM employs electrons that traverse through a suitably thin specimen to create images. A schematic representation of a STEM microscope is provided in Fig. 2.3. In a STEM the electrons are generally emitted by a cold field emission gun (cFEG), which produces a very bright electron beam with a narrow energy spread of approximately 0.3-0.5 eV. This energy distribution can be further reduced to only a few meV via an additional monochromator before the sample stage; this requirement is more related to the EELS spectroscopy study.

The distinguishing feature of STEM lies in its capability to precisely focus the electron beam onto a specific spot, achieved through a sophisticated arrangement of electromagnetic lenses, represented as the condensers in Fig. 2.3. This focused spot is systematically scanned across the sample using a raster illumination

system, ensuring that each point on the sample is illuminated by the beam in parallel to the optical axis. The scanning process is facilitated by the coils located before the objective lens, guaranteeing a precise and controlled scan of the electron beam [27]. Similarly to the image resolution explained in the previous section, the size of the spot in a STEM, commonly referred to as the probe size, is influenced by several factors, including acceleration voltage, convergence semi-angle, and microscope aberrations. In an ideal case, where no aberrations are introduced by the electromagnetic lenses to the electron wavelengths, the spatial resolution is the same as stated in equation 2.11. This implies that to achieve higher resolution, it is essential to employ higher semi-convergence angles and higher accelerating voltages. The choice of the acceleration voltages is however linked to the sample's characteristics, and in the case of *h*–BN is limited to 60 kV due to its sensitivity to the electron beam [28].

By using a setting of magnetic multi-poles, such as the coupling in series of quadrupoles and octupoles [27], correction and compensation of the spherical aberration is possible. Thanks to recent development in aberration corrected STEM (Cs-STEM), such as those used in these investigations, high spatial resolution can be achieved by correcting and compensating for aberrations up to 5th order [26].

The source size itself also plays a significant role in determining the spatial resolution and exhibits an angular dependence of $1/\alpha$ as indicated by the expression:

$$d_s = \left(\frac{4I}{B\pi^2\alpha^2} \right)^{\frac{1}{2}} \tag{2.15}$$

where I and B represent the probe's current and the brightness of the electronic source, respectively. In general, smaller source sizes result in more coherent electron beams and finer probe sizes, leading to improved spatial resolution. Finally, spatial resolution is given by:

$$d = \sqrt{d_a^2 + d_s^2} \tag{2.16}$$

where d_a is the probe size taking into account the diffraction limit and aberrations. Presently, convergence semi-angles ranging from 10 to 40 mrad can be used, resulting in sub-Angstrom probe sizes. As just stated, for higher resolution images a larger semi-angle convergence is employed, whereas a smaller convergence is chosen for diffraction mode, enabling a more parallel beam and facilitating diffraction experiments. This strategic selection of the convergence semi-angle allows for versatile operation and tailored imaging based on specific experimental requirements. In some cases, STEM instruments may also be equipped with a parabolic mirror positioned just before the sample. This mirror

serves to collect luminescence emitted by the sample, a phenomenon known as cathodoluminescence (CL). A set of detectors is employed to capture electrons that experience elastic or inelastic scattering at different angles.

Bright Field and Dark Field imaging modes in a STEM

Typically, in STEM, a scintillator/photomultiplier combination serves as the detector. As electrons reach the scintillator, they are converted into photons, which are then transformed into an electrical signal by the photomultiplier, allowing for recording. During the beam scanning process, each individual detector collects the signal and accumulates the transmitted electrons within its designated area, yielding a parameter referred to as "counts" for each pixel. Images with different contrast can be generated by integrating the signals produced by electrons scattered at different angles. Fig. 2.4.a illustrates the different detectors, and Fig. 2.4.b-d the images produced, characterized by their integration angles, on a multilayer *h*–BN flake where moiré patterns are formed.

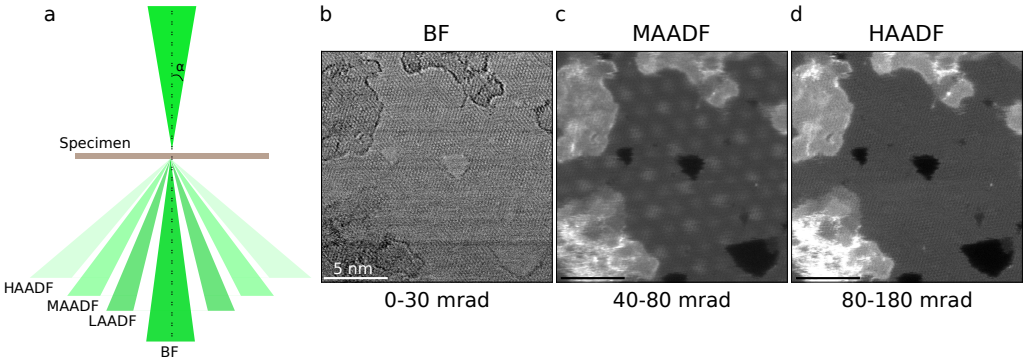

Figure 2.4: *(a) Different imaging modes in a STEM, characterized as a function of the integrated angles. (b) BF image, (c) MAADF image and (d) HAADF image of a few-layer h–BN flake characterized by a moiré pattern.*

In the bright field mode, the image is generated by collecting electrons scattered at low angles near the microscope axis. Similar to conventional TEM, the signals combine coherently, leading to interference and the formation of the bright-field image. This imaging mode is particularly useful for providing valuable information about the sample's structural features.

Some of the incident electrons are deflected by the strong potential well surrounding the atomic nuclei, resulting in scattering angles higher than 30 mrad [29]. This phenomena is known as Rutherford scattering. To collect these scattered electrons, annular detectors are employed, centered at the optic axis of the microscope, producing what are known as annular dark field (ADF) images. Depending on the collecting angle, we can distinguish between low angle (LA-),

medium angle (MA-), or high angle (HA-) ADF images [27]. The intensity obtained in HAADF images depends on the composition, thickness and density of the sample, following the formula:

$$I_{el} = I_0 \rho_t \sigma_{el} \tag{2.17}$$

where I_0 is the incident beam intensity, ρ_t is the projected atom density in the analyzed volume and σ_{el} the elastic cross section. This latter has a dependence on the atomic number given by Z^n, with $n \sim 1.2 - 2$. Thus, thicker or denser zones of the sample appear as brighter regions on a darker background, from which dark field term derives. Furthermore, due to its dependence on the atomic number (Z), the High-Angle Annular Dark Field (HAADF) mode allows distinguishing different atoms based on their Z number. For this reason HAADF is often referred to as "Z-contrast" imaging [30]. Consequently, in HAADF mode, heavier atoms appear brighter compared to lighter ones. This characteristic renders HAADF images more straightforward to interpret than BF images. However, when dealing with extremely thin materials and light atoms, such as *h*–BN monolayers, obtaining high-quality images can be challenging, especially when attempting to simultaneously image both nitrogen and boron. It is interesting to note that the image generated by the MAADF detector (Fig. 2.4.c), present diffraction phenomena. Indeed, the bright periodic spots are related to different stacking order, and it is a direct effect of the different long angle diffraction pattern of the related stacking.

Electron energy loss spectroscopy

The incorporation of various detectors in a STEM allows for the simultaneous acquisition of diverse spectroscopic information along with images. In most cases, STEM microscopes are equipped with electron spectrometers, enabling the recording of electron energy loss spectra (EELS). EELS is a powerful technique that involves measuring the energy lost by an electron when it undergoes inelastic scattering while interacting with the sample. In a simplified explanation, a monochromatic electron beam locally illuminates the sample, leading to an excitation with an energy ΔE, which results in an equivalent loss of kinetic energy in the incoming electron. By precisely measuring this energy loss using an electron spectrometer, valuable insights into the energy characteristics of the excitation can be obtained. EELS spectroscopy allows for the investigation of a wide energy range, spanning from the visible to the soft X-rays.

The overall spectrum can be partitioned into distinct regions, as shown in Fig 2.5. The lowest energy portion, centered around 0 eV, corresponds to the zero-loss peak (ZLP), where the electrons are collected without experiencing

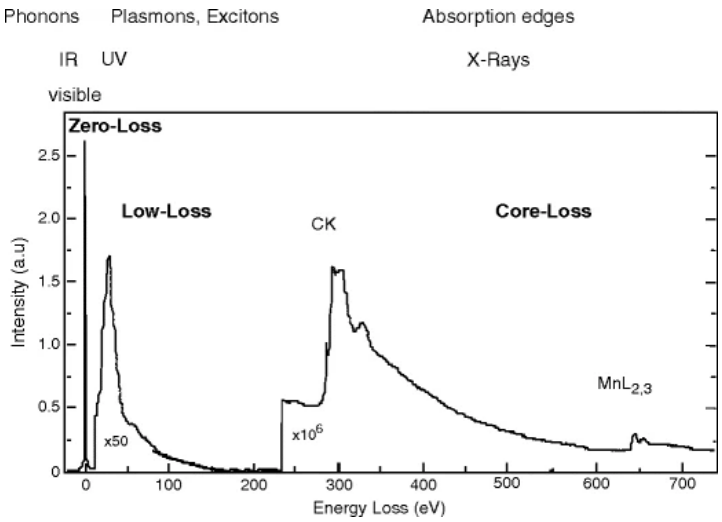

Figure 2.5: *Typical EELS spectrum. The ZLP dominates the spectrum at the zero energy loss position. At higher values of the energy loss, in the low-loss region, energy levels are typical of valence excitation. At higher energies, in the core-loss region, resonances from core level excitation appear with a much less intensity. Extracted from Ref. 31.*

any energy loss. Typically, the full width half maximum (FWHM) of the ZLP is of 0.3 eV, but it can be reduced down to ca 10 meV by the presence of a monochromator. The energy range spanning from 0 eV to 40 eV is referred to as the low-loss region. Within this range, various excitations occur involving valence and conduction states, which can have diverse physical origins. These include phenomena such as surface and bulk plasmons, intra-band transitions, and excitons in semiconducting materials.

At higher energies, we encounter the core-loss region, where the excitation involves core electrons unique to each chemical species transitioning to the conduction band. Within this energy range a specific sub-category of EELS analysis is applied, known as Energy-Loss Near Edge Structure (ELNES). This technique is primarily employed for compositional analysis, providing precise elemental information. As it pertains to core signals, ELNES analysis is highly localized, and depending on the microscope's resolution, it can achieve atomic one [31–34].

The spectrometer used for EELS experiments is a magnetic prism, which permits to separate the inelastically scattered transmitted electrons along different trajectories depending on their energy, and therefore the losses encountered in the material. This separation takes place along a direction called the dispersion direction [20]. The electrons separated in the spectrometer are then focused according to the energy dispersion, and are transferred to the EELS detector, to finally generate a spectrum. Experimentally, to perform EELS measurements

the BF detector has to be removed to allow the low angle scattered electrons to reach the EELS spectrometer's entrance. Generally EELS detectors can be CCDs, complementary metal-oxide semiconductor (CMOS) spectral sensors or, more recently, direct single electron detectors.

Typically, in a STEM is possible to generate either a point spectrum or a spectral image (SPIM). In the latter mode, a complete spectroscopic signature is collected for each probe position while acquiring the HAADF signal. This results in a data-cube, where for each pixel of the HAADF image, there is a complete EELS spectrum.

NION ULTRASTEM 200 The spherical aberration corrected STEM electron microscope used during this thesis is the NION ULTRASTEM 200. It is a high resolution STEM equipped with a tungsten cold field emission gun. The vacuum in the gun is typically in the low 10^{-11} Torr range and in the vicinity of the sample the vacuum is around 10^{-9} torr. The microscope is equipped with an oil-free pumping system. The beam convergence half-angle can be set up to 33 mrad while the acceleration voltage can be chosen between 60 kV, 100 kV and 200 kV. The used pole piece has a spherical aberration of Cs=0.5 mm, zeroed thanks to the aberration corrector, and a chromatic aberration of Cc=0.95 mm.

In all the experiments described in this thesis the acceleration voltage used was 60 kV to reduce beam damage degradation effects, while the semi-convergence angle used was 33 mrad to increase the final resolution. With this set-up the theoretical probe size should be around 1 Å. For the acquisition of EELS spectra the direct detector MerlinEM - Medipix3 has been recently installed on the Gatan ENFINA spectrometer mounted on the microscope [35, 36]. This detector has been designed by Quantum Detectors, and is composed of 4 Medipix3 chips, each of which is an hybrid pixel detector (256×256 px), capable of direct electron detection. In order to be used for EELS measurement, the 4 pixelated detectors are aligned in a 4×1 configuration, resulting in a 1024×256 px detector. Common detectors, as CCD and CMOS, need to convert the electrons into visible light as an intermediate step, thus losing information and increasing noise in the data collection. Conversely, direct electron detectors convert incoming electrons, with directly into electron/hole pairs in the silicon wafer, providing higher sensitivity and dynamical ranges, with an adaptability from 30 to 300 keV. Another important feature of the MerlinEM - Medipix3 detector is the possibility to chose only one of the four chip, allowing to faster dwell time and reduce the data size.

2.3. Charge density and electric field imaging

The redistribution of the electronic charge density resulting from the arrangement of free atoms into a solid is of primary significance. Indeed, it is

through the distribution of binding electrons and their energy levels that physical properties of materials such as chemical bonding, electronic transport, and mechanical properties, are defined [37]. The Hohenberg-Kohn theorem establishes that all ground-state electronic properties can be derived from the electronic charge density distribution [38, 39]. This theorem serves as the foundational principle for the DFT approach to first-principles electronic structure calculations, but its importance can be seen in a more general context with also strong experimental implications [8]. Thus, visualizing the real-space electronic charge density distribution in materials is of critical importance. However, unlike conventional structural and chemical characterization, the direct visualization of the charge density in heterogeneous materials with high spatial resolution remains a significant experimental challenge.

X-ray and electron diffraction

Indirect measurements of charge densities or electrostatic potential have been performed with high accuracy by means of X-ray or electron diffraction in several works [40–46]. In the case of X-rays and parallel electron beam, the experimental diffraction pattern is used to retrieve the structure factor, F, that is lately compared with the one calculated assuming an independent atomic model (IAM), where bonding and local chemical environment of each atom are not taken into account. Since experimental diffraction patterns do in principle include these factors, the difference between the IAM calculated structure factor and the one derived from experiments can be attributed to the bonding characteristic of the materials. Once the structure factor is determined, it is possible to derive the charge density since, for perfect periodic crystals, the structure factor is the Fourier transform of the electron charge density in a unit cell:

$$F(\Delta k) = \sum_{1}^{N} \int \rho_i(r) e^{-2\pi i \Delta k \cdot r} dr \tag{2.18}$$

where r is the electron position and Δk is the wave vector change of the scattered X-ray. A schematic representation of the scattering process is depicted in Fig. 2.6.a.

The derivation of the electron charge density map through X-ray diffraction for h–BN has been reported by Yamamura et al. in 1997 [5]. In Fig. 2.6.b,c core and valence electron maps are shown respectively, revealing a higher localization at the nitrogen sites, indicating a charge transfer from boron to nitrogen. Fig. 2.6.d is the profile of the electron charge density taken along the B-N bond (red lines in Fig. 2.6.b,c), where the atoms positions correspond to the two maxima of the profile and the saddle point is determined at 0.49 Å from the B atom, showing

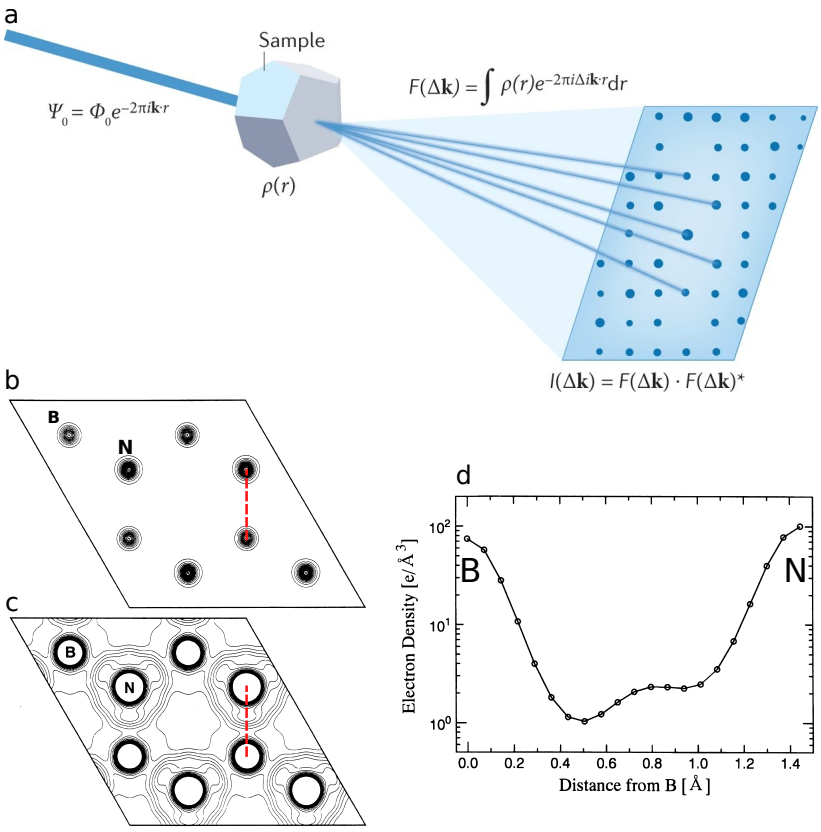

Figure 2.6: *(a) A schematic of the scattering process and the formation of a diffraction pattern applicable to the scattering of both X-rays and electrons. (b) Core and (c) valence electron charge density derived from X-ray diffraction measurements on h–BN.(d) Line profile taken along the red line in (b) and (c) . Adapted from Refs. 5, 37*

once more the higher number of electrons around the nitrogen atom. In their work, a quantitative determination of the electron charge transfer between the the two atoms has also been calculated by integrating the total electron charge density. The resulting integration gave +2.7 electrons for the boron and -1.9 electrons for the nitrogen, which has been interpreted as the transfer of 2 electron from boron to nitrogen, to form N^{2-} anions, while the remaining electrons stay in the interatomic region. This work holds importance as one of the first experimental work reporting the derivation of electron charge density for *h*–BN.

Deriving charge density from TEM diffraction experiments is more complex compared to X-ray for several reasons. Firstly, the structure factor obtained through electron diffraction involves atomic scattering factors influenced by the Coulomb interaction with both the surrounding electron density and the positive nuclear charges[37]. Additionally, as the electrons traverse the sample, multiple scattering phenomena may occur, necessitating the consideration of dynamic

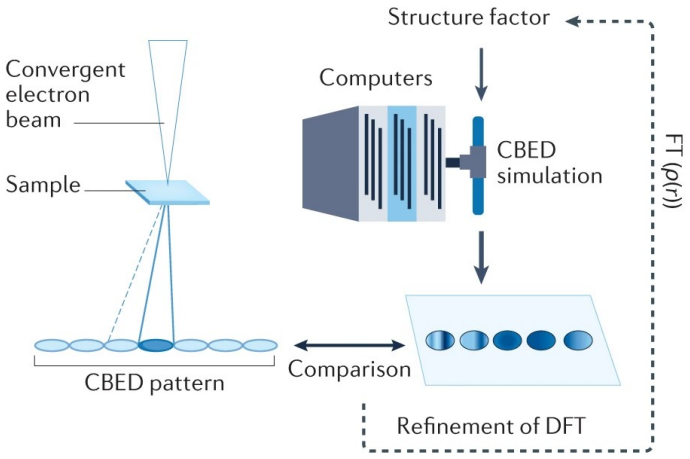

Figure 2.7: *Schematic of the workflow for quantitative convergent beam electron diffraction. Adapted from Ref. 37*

theory. This complexity makes it challenging to invert the expression for the structure factor and recover the charge density distribution.

In case of electron diffraction experiment with a convergent beam, the diffraction pattern is no more constituted by spots but of discs, as shown in Fig 2.7, and what is called a convergent beam electron diffraction (CBED) pattern is generated. The intensity within the diffraction discs in the CBED pattern originates from electrons with a range of incident angles, thereby containing a wealth of information regarding the electron–sample interaction. In this approach, the typical procedure involves simulating the diffraction discs by solving the Schrödinger equation using the Bloch wave method. This procedure includes all possible incident electrons directions and their interaction with the potential, generated by the charge distribution within the sample. Subsequently, fitting the potential, and consequently the resulting CBED patterns, to the experimental data provides a precise determination of both the structure factor and charge density.

Compared to structure factor measurements via X-ray diffraction, CBED takes into account the dynamic scattering process, enabling multiple scattering interactions within thick crystal samples. Moreover, it does not encounter the same extinction effects generally seen in X-ray diffraction, which often diminish the accuracy of structure factors calculated from low-order diffraction spots. On the other hand, X-ray diffraction excels at precisely capturing the weak intensity emanating from high-order reflections, which are frequently absent or characterized by noise in CBED images. Thus, in general, a more precise quantification can be achieved by combining the two techniques.

Nevertheless, both X-ray and electrons diffraction techniques require large, crystalline and rather homogeneous samples to be performed with high preci-

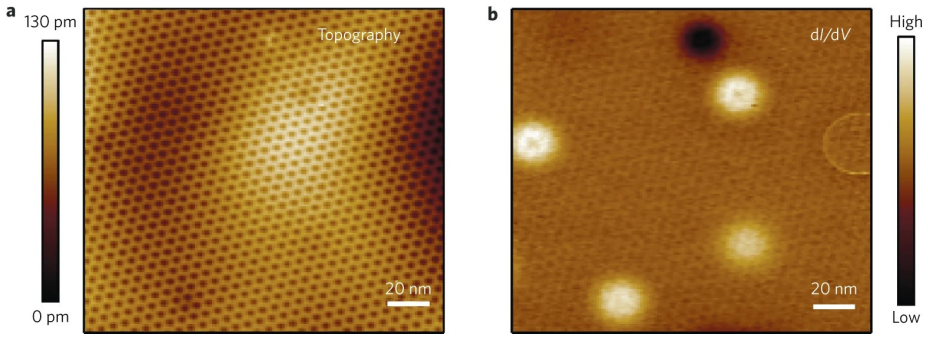

Figure 2.8: *(a) STM topographic image of a clean graphene/BN area. (b) dI/dV map acquired simultaneously with a exhibits various new features: bright dots, a dark dot and a ring. Extracted from Ref. 50*

sion and resolution. This results in a strong limitation, since many properties nowadays are tailored by the presence of defects or from specific properties at the interfaces between two different materials. More importantly, the techniques discussed thus far rely on indirect measurements, necessitating prior knowledge and assumptions regarding the expected structure factors and potentials for the purpose of fitting.

Surface-sensible scanning probe methods

Another set of experimental techniques employed for mapping charge densities and electric fields includes surface-sensitive scanning techniques, such as scanning tunneling microscopy (STM) and the electrical extension of atomic force microscopy (AFM). In these methods, various functionalized probes are scanned across the sample, providing local information about the sample's electron density or potential. These techniques have found application in the study of numerous 2D materials.

Scanning tunneling microscopy STM allows the visualization of chemical bonds and provides information on interfaces or point defects [47–49]. However, this technique has its limitations. It represents the density of states near the Fermi level and does not offer a comprehensive view of the total charge density. Additionally, it is not applicable to wide band gap materials as it requires a conductive substrate for execution. Nevertheless, even for semiconductor materials, achieving high-resolution information, particularly at the atomic level, remains a challenge, and the technique is inherently restricted to surface analysis.

In this regard, a work performed on thick *h*–BN to study the behavior of different point defects has been reported in 2015 by Wong at al. [50]. As just

outlined, being *h*–BN a rather insulting material, with a band gap around 6 eV, STM studies would typically be impossible due to the lack of a conducting drain path for electrical current. Wong and collaborators overcame this problem by using a graphene/boron nitride heterostructure, which exploits the atomically thin nature of graphene to allow the visualization of defect phenomena in the underlying bulk boron nitride. Figure 2.8.a displays the topography map of the graphene-*h*–BN heterostructure, where the periodicity observed is due to the a moirè structure formed between graphene and *h*–BN. Notably, the dI/dV map in Fig 2.8.b highlights bright and dark spots. The authors associated these spots with various point defects in the underlying bulk *h*–BN, exhibiting different charge states and, consequently, distinct electronic behavior. Through STM spectroscopy on the same spots, they determined that bright spots correspond to positively charged defects, while black spots indicate negatively charged ones. However a direct correlation between the point defect structure and its electronic behavior cannot be achieved in *h*–BN though this measurements.

Electrical atomic force microscopies A class of electrical extension of the AFM, as Kelvin probe force microscopy (KPFM) and electrostatic force microscopy (EFM), have been extensively used for the visualization of local electric charges by detecting variations in the surface potential of the materials under study. In recent studies, various investigations have employed these techniques to explore the electric properties of moiré structures in *h*–BN. These structures result from twisting two crystals (or monolayers) at a small angle θ, creating a variable stacking order dependent on spatial positioning [51–53]. The emergence of polarized superlattices, linked to specific stacking orders, has showcased diverse electronic applications, manifesting in a ferroelectric behavior.

The study of Woods et al [51], whose main results are summarize in Fig. 2.9, has been the first one showing this behavior. Fig. 2.9.a shows different stacking configuration for *h*–BN, where parallel stands for crystal alignments at 0° and anti-parallel for 180°. Fig. 2.9.b shows the different triangular domain generated by the predominant AB and BA regions. Measurements of the electronic properties in this work have been made employing a dc-EFM (schematic representation reported in Fig. 2.9.c). In these measurements the phase of the materials is retrieved as a the deflection in angles of the local tip at a given applied bias. Fig. 2.9.d shows the results of such measurements performed on two thick *h*–BN crystals twisted by a small θ angle (<1°). The creation of two opposite domains is clearly showed in Fig. 2.9.f, where each triangle is either an AB or BA stacking order. The explanation of this behavior is due to the creation of opposite dipoles in presence of those specific stacking orders, generated by aligned pairs of BN or NB dipoles aligned along the *h*–BN *c*-axis. This creates a confined ferroelectric

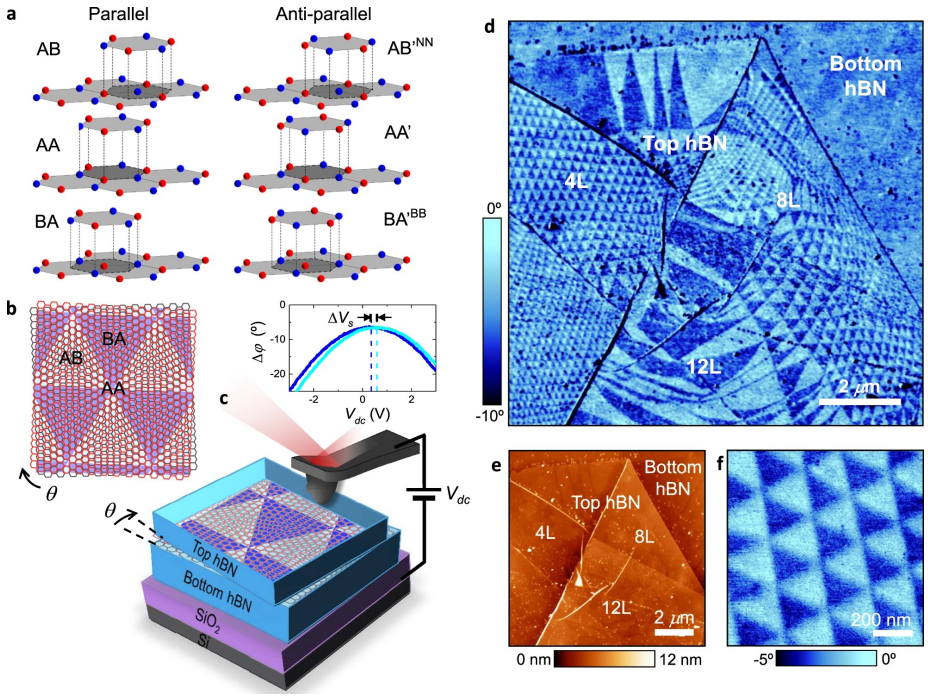

Figure 2.9: *(a) Illustration of six high-symmetry stacking configurations for the h–BN-h–BN interface. Nitrogen atoms are in red, boron in blue. (b) Schematic of adjacent h–BN atomic layers misaligned by a small angle, θ. (c) Schematic of the experimental setup used. (d) Representative dc-EFM image (phase) of twisted h–BN showing large areas with triangular potential modulation. (e) AFM topography image. (f) Zoom-in of a region in (d) with regular domains. Adapted from Ref. 51*

bilayer.

TEM techniques

As detailed in Chapter 1, a primary objective of this thesis is to explore the feasibility of mapping the electric potential and charge density at the atomic scale within an electron microscope. Since the fundamental mechanism governing TEM image formation is the Coulomb interaction between the relativistic electrons of the beam and charges within the system, transmission electron microscopy techniques can provide, in principle, direct access to charge density in real space at the atomic scale.

In Section 2.1, it has been shown that in presence of very thin materials (within the weak phase approximation) and suitable microscope setup and alignment, the phase shift that gives rise to the image contrast is directly proportional to the potential of the specimen under investigation. This characteristic has been

harnessed for preliminary investigations on charge redistribution phenomena for low-dimensional materials through HRTEM.

High resolution transmission electron microscopy Several studies employed HRTEM to investigate the impact of charge redistribution on electron image contrast. This was achieved through image simulations using various potentials, accounting for bonding effects or neglecting them [54, 55], but not tested experimentally. Indeed, the difficulty arises from the relatively small charge redistribution resulting from chemical bonding when compared to the total charge density, rendering precise measurements challenging.

An early exception is given by the work of Meyer and co-workers of 2011, where a comprehensive study of bonding effects on the HRTEM imaging formation has been conducted for nitrogen-substitution point defects in graphene and pristine *h*–BN monolayer [8]. As already mentioned, HRTEM image simulations can be run using different potentials. The most widely used approach, similarly to what has been explained for diffraction measurements, is to employ an independent atomic model (IAM), wherein the potential of a solid is calculated as a superposition of atomic potentials previously computed for isolated atoms of each element [56]. This choice is justified as a reasonable first approximation, given that the adjustments to the potentials resulting from bonding electrons are relatively small in the image formation. More precise simulations employ DFT-derived potentials [57], where the effect of charge redistribution resulting from chemical bonds is considered, and yield a distinct contrasts in the HRTEM images when compared with IAM derived ones. Applied to *h*–BN monolayer, this procedure has revealed that HRTEM imaging is sensitive to the electron charge redistribution between boron and nitrogen associated with the strong ionicity of the bond [4–7]

Fig. 2.10.a-d, show the contrast produced by IAM and DFT potentials for the case of a *h*–BN monolayer. In Fig. 2.10.e the profiles taken out of the two images simulations are reported, where boron and nitrogen correspond to the minima of the curve. The effect of the bond between boron and nitrogen produces a less pronounced contrast between the two atoms, which is due to the electronic charge redistribution that results more localized on the nitrogen site, screening the nuclear contribution. Fig. 2.10.f,g illustrate the experimental images taken for both *h*–BN mono- and bi-layer, and in Fig. 2.10 the experimental profiles. Images obtained employing a DFT-derived potential reproduce the experimental profile more closely than IAM, providing evidence of the charge transfer between boron and nitrogen. These findings demonstrate the importance of considering the influence of chemical bonding in HRTEM simulations, and prove the high sensitivity of such technique. Although this procedure yields

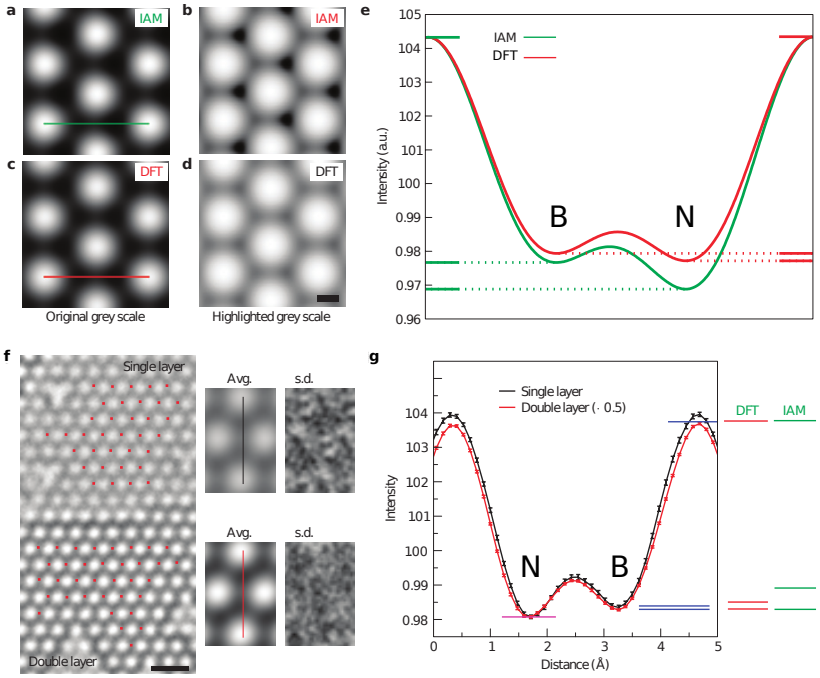

Figure 2.10: *(a),(b) IAM TEM image simulation for single layer h–BN. (c),(d), TEM simulation using potentials from the all-electron DFT calculations. The scale bar in (d) is 1 Å. (e) Intensity profile plots for the two simulations. (f) Experimental image of single- and bi-layer h–BN (scale bar is 5 Å). (g) Intensity profiles from the single- and double-layer average. The contrast of the double layer was numerically reduced by a factor of 2 for comparison. Extracted and adapted from Ref. 8.*

promising qualitative results, the quantitative aspect remains incomplete, and there is no direct measurement or image of the charge itself, which has been instead presented by X-ray diffraction before.

Electron holography Another TEM technique that has been used to image and evaluate charge distribution and electrostatic potential is electron holography. It consists in the measure of the change in the phase of the electron wave function after it has interacted with the sample. Originally proposed in 1948 [58, 59], holography enables phase reconstruction by modifying the electron exit wave, so that the wave incident on the detector will carry phase information that is either imaged directly or reconstructed iteratively. This can be done either through interference of the exit wave with a reference wave of known phase (off-axis holography, Fig. 2.11.a) or by collecting multiple images with a known phase shift between them (in-line holography) [60]. Electron holography is nowadays a well-established technique for studying electronic properties of materials, and has been used for example to visualize the potential energy profile across p-n

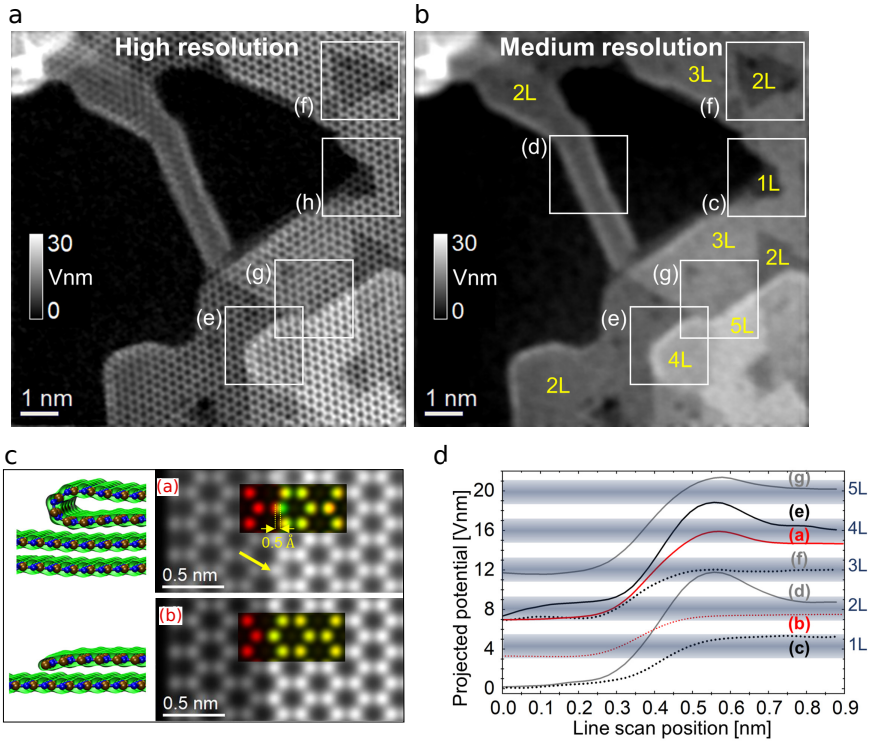

Figure 2.11: *(a) Atomic-scale (high resolution) and (b) nanometer-scale (medium resolution) projected potential of multilayer h–BN reconstructed by off-axis electron holography. (c) On the left, Ab initio relaxed structure from DFT calculations for folded bi-layer and monolayer steps, while on the right the projections of the DFT potentials along the out-of-plane direction. (d) Line profiles pertaining to region (a,b) in figure (c), and regions (d-g) in figure (b). Adapted from Ref. 63, 64.*

junctions [61, 62]. Before the development of 4D-STEM, holography was the only method capable of mapping the embedded fields in semiconductor devices at the manometer resolution.

Thanks to different advances in TEM, such as the availability of Cs-correctors, high-brightness sources and direct electron detectors this technique has more recently been applied to the study of a different class of low-dimensional materials, where in general it is more difficult due to the low phase shift induced, reaching the Angstrom resolution [65–68]. Nevertheless, this technique needs post-acquisition corrections and requires a prior knowledge of the sample and of the instrumentation characteristics, that are usually used to reconstruct and correct the phase. Furthermore, performing images at high resolution and high phase sensitivity is demanding, since the latter has an error which is inversely proportional to the spatial resolution [69, 70]. Moreover, because of high beam

sensitivity of low-dimensional materials, a combination of low electron beam current density and long exposure time is required, and generally a series of hologram are acquired to increase the signal to noise ratio. This lead to the necessity of post-acquisition corrections for the microscope and specimen instabilities over the acquisition time [71].

For *h*–BN, in 2023, off-axis holography has been used to investigate edge reconstruction by examining the potential shape [64, 72]. Fig. 2.11.a,b show the phase images captured on a few layer flake, where different edges can be identified (indicated by the white squares). In particular, in this work it has been pointed out that primarily two kind of edges can be distinguished: folded bi-layers (Fig. 2.11.d) and monolayer steps (Fig. 2.11.e). Fig. 2.11.f shows that, depending on the edge kind, a different potential is produced, generating in the second case a picked enhancement at the edge position, not present in the case of step edges, due to the folded layer. This result is a great step forward for electron holography, since it combine high spatial resolution and high phase sensitivity. Moreover, from Fig. 2.11.b,c the phase seems to be linearly increasing up to five layers, which is already a good result itself. Nevertheless, until now this method has been applied to map the phase of materials, but it is not clear if the effect of charge redistribution at the atomic scale can be detected through this method.

2.4. 4D-STEM imaging principles

Recent advancements in fast and highly sensitive detectors have significantly enhanced the capabilities of STEM microscopes. These developments have opened the way for the emergence of new imaging techniques and expanded the microscope's potential beyond the functionalities described in the previous sections. Particularly, by employing fast pixellated detectors with high dynamics at the diffraction plane of a STEM microscope, comprehensive four-dimensional (4D-) datasets can be acquired. In this process, for every spatial position of the electron probe, a two-dimensional (2D) image of the CBED pattern is recorded. This advanced imaging technique enables the simultaneous capture of both spatial and diffraction information, providing a wealth of valuable data for the analysis and characterization of materials [73–75].

4D-STEM for structure determination

One of the remarkable advantages of 4D-STEM diffraction imaging is its capacity to employ arbitrary virtual detectors, effectively transforming a pixellated detector into a "universal" one [75]. This versatility is achieved by applying masks of various shapes and integrating different angles in the diffraction space, resulting in bright-field (BF) or annular dark-field (ADF) images, all within a

single 4D-STEM dataset. As a result, this overcomes one of the limitations of conventional STEM imaging, where a limited number of bright and dark field detectors must be physically positioned at fixed angles relative to the optical axis, preventing real-time adjustments during measurements. In Fig. 2.12 an example of virtual detectors reproducing BF and DF images is represented, from an experiment of Hachtel et al. on $DyScO_3$ [76].

In microscopy, the diffraction pattern analysis has played an important role in the study of structural properties and features of the specimen, as showed in Section 2.3. In a STEM it is possible to work in the diffraction mode while degradating the space resolution, by reducing the semi-convergence angle. Typically angle of 5 mrad are used for this kind of study. Since in 4D-STEM the whole diffraction pattern is acquired at each probe position, it offers opportunities for an in-depth analyses of sample structures at the nanometric or even atomic scale. Fig. 2.13.a shows how different phases or orientation generally produces different CBED patterns. In this optic, this technique has been employed for the mapping of different crystal phases in the specimen as well as the mapping of their orientation in the space [77–79]. Structural details such as strain can be extracted as well from the study of diffraction patterns, as shown in Fig. 2.13.c [80–82].

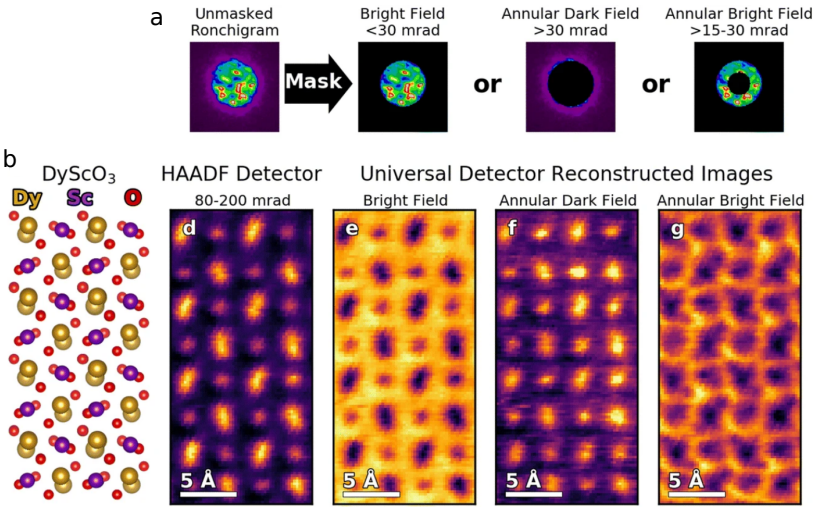

Figure 2.12: *(a) Procedure to generate different virtual detectors, with the respective mask shapes. (b) Images produced by the virtual detectors shown in (a). Adapted from Ref. 76*

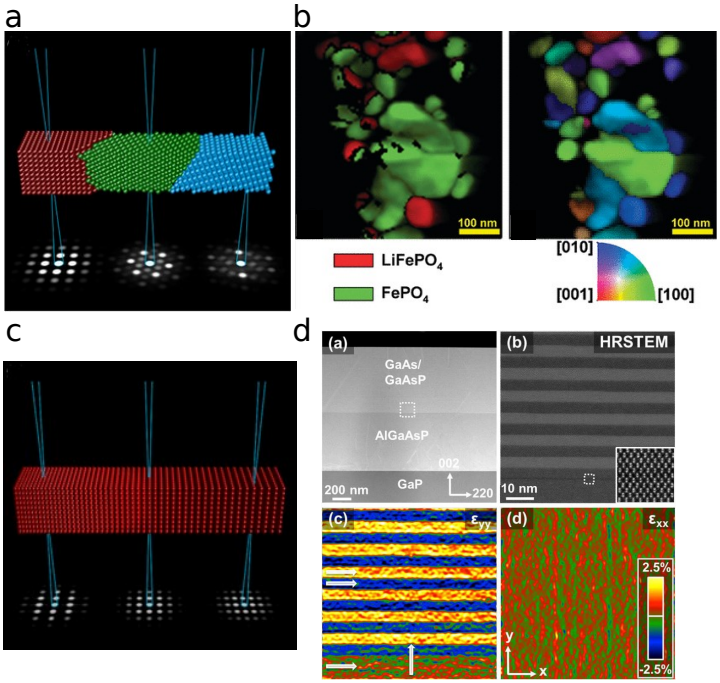

Figure 2.13: *(a) 4D-STEM measurements for the mapping of different crystalline phases and orientation. (b) Example of this application for a multiphase $LiFePO_4/FePO_4$ crystal. (c) 4D-STEM measurements for the mapping of strains. (d) Example of the technique applied to a GaAs/GaAsP multilayer structure. Adapted from Refs. 75, 78, 80*

Ptychography

By recording the full STEM probe diffraction pattern, we are measuring the degree of scattering for many different spatial frequencies of the sample's projected potential. Combining many such overlapping measurements, through the use of different computational methods, it possible to reconstruct both the complex electron probe and sample phase with high accuracy. This procedure is called electron ptychography. Since the electron probe shape can be retrieved, in principle it is possible to perform a deconvolution of it to the experimental measurements, and thus correct the aberrations. This procedure can be used to increase the final image resolution.

To date, the highest resolution achieved by 4D-STEM ptychography experiments have been performed by Jiang et al. [83]. In this study a bi-layer MoS_2, showed in Fig. 2.14.a, has been imaged with an estimated resolution of 0.39 Å using an electron voltage of 80 kV, significantly beyond the conventional imaging resolution of 0.98 Å for these microscope parameters. This technique is of particular interest for 2D materials, since most of them are beam sensible, making it is difficult to have such high resolution because of the impossibility to use

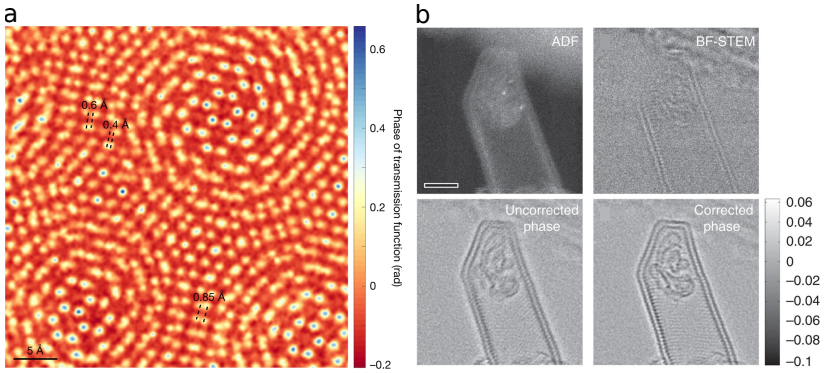

Figure 2.14: *(a) Ptychography image reconstruction of a MoS_2 bilayer showing a resolution of 0.4 Å. (b) Ptychographic post-collection corrected phase reconstruction of carbon nanotubes.Extracted from Refs. 83, 84*

high acceleration voltages, and being the SNR value reduced for the necessity of using low electron doses. Generally to improve the resolution in ptychography is required an oversampling, in a way to produce more interference between the different diffraction disks. Another important parameter is the maximum collection angle, which must be larger of the semi-angle aperture, in a way to better reconstruct the probe shape.

Although originally developed as a means of achieving super resolution, this technique has recently been employed to provide high signal-to-noise phase images [73, 84–86] This particular characteristic has been recently used to gain information about charge re-distribution in low dimensional materials [87, 88]. Similar to the study discussed in Section 2.3, which explored the use of HRTEM [8], these investigations are generally carried out by comparing the post-collection aberration corrected experimental measurements with multi-slice probe propagation simulations performed employing either a IAM potential or a first-principle DFT derived one. However, these studies remains qualitative studies from the experimental point of view, and the evaluation of charge redistribution is only evaluated in the theoretical framework.

Differential phase contrast imaging

Shortly after the practical demonstration of field emission STEM instruments capable of forming a small probe, researchers began exploring imaging modes capable of retrieving the phase information present in the convergent beam diffraction patterns formed by a coherent, focused electron beam. This technique takes the name of differential phase contrast (DPC) imaging technique.

DPC is based on a general statement that when the size of a converged elec-

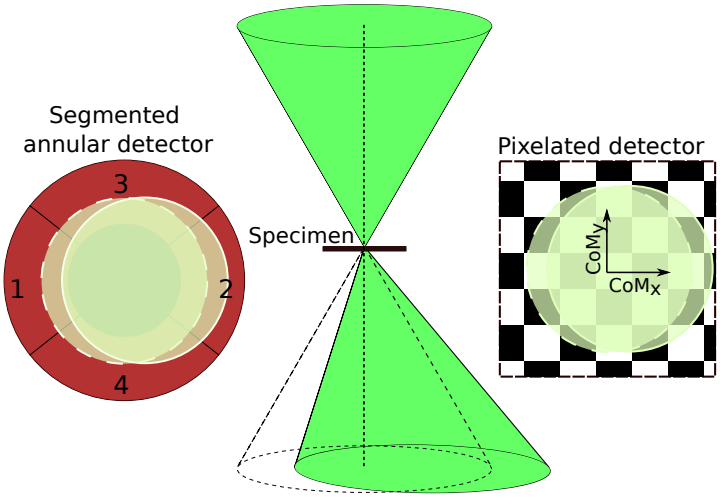

Figure 2.15: *Different detectors for DPC imaging, employing an annular segmented detector or a pixelated one.*

tron probe closely matches the length scale of the variations in a sample's electric field (gradient of the electrostatic potential), the electron probe experiences partial or complete deflection [89]. This change in momentum of the STEM probe can be measured in the diffraction space through the use of various detector configurations, as shown in Fig. 2.15. One such method involves employing segmented detectors without rotational symmetry, as originally introduced by Dekkers [90]. Segmented detectors diverge from traditional circular or annular geometries, since they are partitioned into a series of adjacent segments, further divided into quadrants [91]. In this configuration, the gradient of a weak phase object is measured as the difference between the intensity of the two opposite quadrants [92]. This innovative design with a limited number of segments enables fast, efficient acquisitions, and real-time atomic DPC imaging [93]. In recent years, researchers have increasingly employed STEM-DPC to measure the intrinsic electric and magnetic fields of nanoscale phenomena, such as p-n junctions [94], quantum wells [95], magnetic domains [96, 97], ferroelectric polarizations, skyrmions, and even extended to map the fields surrounding individual atoms [98].

The use of fixed segmented detectors for DPC measurements, however, has been shown to reduce the information transfer efficiency of various spatial frequencies [73, 99, 100]. To address this issue, one effective approach is to conduct a full 4D-STEM scan utilizing a pixellated detector and measure the momentum change of the electron probe using a center of mass (CoM) measurement across all pixels. Waddell and Chapman showed that the gradient of a potential is exactly recovered within the weak phase approximation by calculating the center of mass

(CoM) of the diffraction pattern [101].

While both the split detector and the center of mass approach serve as measures of DPC, historical naming conventions within the electron microscopy community commonly refer to split (quadrant) detector measurements as a DPC imaging. Meanwhile, the first momentum measurements using pixellated detectors, derived from 4D-STEM, are typically called CoM imaging. It is however recognized that 4D-STEM derived measurements are generally more complete, since both conventional DPC and CoM approach can be performed though an accurate analysis of the CBED pattern.

Both DPC and CoM images are formed by summing over the diffraction pattern using an anti-symmetric weighting function over the detector. DPC uses a weighting function of 1 and -1 over the two halves of the detector. CoM uses the coordinate in momentum space $\vec{k}$ as the weighting function. Any asymmetry in the diffraction pattern would then lead to a difference signal. Classically, this asymmetry is due to a displacement of the BF disk. However, despite the presence of a field, there are numerous instances where the boundaries of the central disk do not move [100, 102, 103]. Instead, there is a redistribution of intensity within the BF disk itself. By using a quantum mechanical approach and treating the sample as a phase object, it is possible to explain both behaviors as a result of differing length scales between probe and scattering potential [104].

Converged electron beam diffraction pattern theory

In order to calculate a diffraction pattern, we start by writing the probe wave functions in the moment and real space, without taking into account any spatial or temporal coherence related problem. Recalling what has been said in Section 2.1, the incident electron wavelength in the back focal plane of the lens, $\Psi_0(\vec{k})$, depends on a factor describing the objective aperture $A(\vec{k})$ and one taking into account aberrations, $\exp(i\chi(\vec{k}))$, imparted by the lens itself. The wave function in the image plane results to be its Fourier transform, and can be written as:

$$\Psi_0(\vec{r}) = \mathcal{F}\{\Psi_0(\vec{k})\}(\vec{r}) = \frac{1}{2\pi}\int A(\vec{k})\exp\left(i\chi(\vec{k})\right)\exp(i\vec{k}\cdot\vec{r})\exp(-i\vec{k}\cdot\vec{r})d\vec{k} \tag{2.19}$$

For convenience, we will assume an aberration-free probe throughout this section. This simplifies the interpretation but does not limit the generality. The objective aperture term, $A(\vec{k})$, is defined as:

$$A(\vec{k}) = \begin{cases} 1 & k \geq k_0 \\ 0 & k \leq k_0 \end{cases} \tag{2.20}$$

where k_0 is the maximum angle of the aperture, and is related to the semi-angle aperture α of the beam through $k_0 = \alpha/\lambda$, with λ the wavelength of the

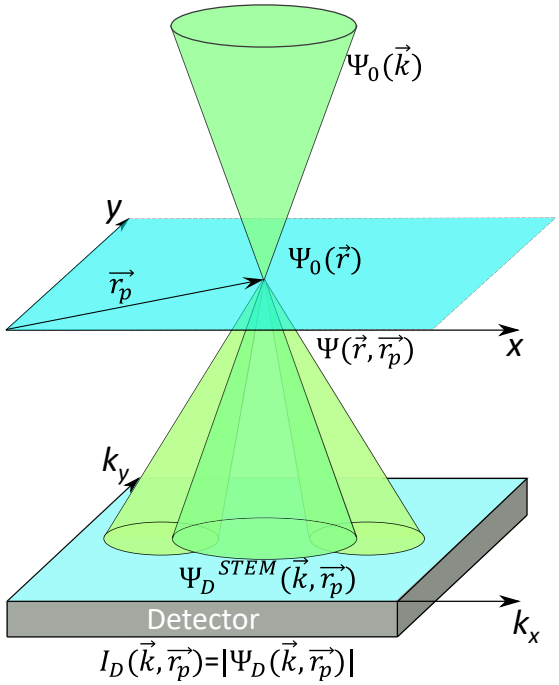

Figure 2.16: *Schematic overview of diffraction pattern formation in a STEM.*

incident electron wave. We will refer to this disk in the $\vec{k}$ space as the bright field disk. After the probe formation, it is then rastered all over the sample, and during this scanning process electron interacts with the specimen. Recalling the POA approximation, during this interaction the initial electron wave acquires an additional phase, φ, defined as the product between the interaction factor σ and the specimen integrated potential $V(\vec{r})$. Then, the electron exit wave for each probe position $\vec{r_p}$ can be written as:

$$\Psi(\vec{r},\vec{r_p}) = \Psi_0(\vec{r}-\vec{r_p})\exp(i\varphi(\vec{r})) = \Psi_0(\vec{r}-\vec{r_p})\exp(i\sigma V(\vec{r})), \tag{2.21}$$

In the far field detector plane, positioned at the diffraction plane or BFP, the wave function $\Psi_D^{STEM}(\vec{k},\vec{r_p})$ is the Fourier transform of the wave emerging from the sample just derived:

$$\Psi_D^{STEM}(\vec{k},\vec{r_p}) = \mathcal{F}\{\Psi(\vec{r},\vec{r_p})\} = \mathcal{F}\{\Psi_0(\vec{r}-\vec{r_p})\}(\vec{k}) * \mathcal{F}\{\exp(i\sigma V(\vec{r}))\} \tag{2.22}$$

where the operator $*$ denotes convolution, and derive from the multiplication of two functions in the Fourier space.

The CBED pattern intensity, I_D, collected by the detector is defined as:

$$I_D(\vec{k},\vec{r_p}) = |\Psi_D^{STEM}(\vec{k},\vec{r_p})|^2. \tag{2.23}$$

This process is outlined in Fig 2.16. Note that in case no sample is present, Eq. 2.23 becomes $A^2(\vec{k})$, which, as stated before, is the bright field disk. Once defined the CBED pattern formation processes, we can divide two extreme cases can be discussed: when the potential is long range and with constant slope, and the more general case where the potential $V(\vec{r})$ may vary not linearly as a function of the probe position. It is worth specifying that during this dissertation specimens are treated as sufficiently thin and non-magnetic, meaning that the potential $V(\vec{r})$ only depends on the electric field, and so on the charge density distribution.

Probe size $\ll$ Feature size When the probe size is much smaller than the feature size, the sample potential can be modeled as a linear ramp $V(\vec{r}) = -E_0 \cdot \vec{r}$, and Eq. 2.21 becomes:

$$\Psi(\vec{r}, \vec{r_p}) = \Psi_0(\vec{r} - \vec{r_p}) \exp(i\sigma E_0 \vec{r}). \tag{2.24}$$

Finally, the diffraction intensity, as derived from Eq. 2.23 and Eq. 2.22, becomes:

$$I_D(\vec{k}, \vec{r_p}) = |\Psi_0(-\vec{k} - \sigma E_0 \hat{\vec{r}})|^2. \tag{2.25}$$

This means that the resulting diffraction pattern is just the BF disk of the unscattered beam uniformly shifted. This shift results to be proportional to the strength of the field, and thereby also to the phase shift, due to the phase object approximation.

Probe size $\gg$ Feature size In the other limiting case, where the feature size is much smaller than the probe, the sample potential can be modeled as a delta function:

$$V(\vec{r}) = V_0 \delta(\vec{r}) \tag{2.26}$$

For analytic simplicity, from here we will assume that is possible to use the WPA, so that the exit probe wave function at every scanning position can be written as:

$$\Psi(\vec{r}, \vec{r_p}) = \Psi_0(\vec{r} - \vec{r_p})[1 + i\sigma V_0 \delta(\vec{r})]. \tag{2.27}$$

The diffraction pattern expression, derived applying Eq. 2.23, is:

$$I_D(\vec{k}, \vec{r_p}) = |A(\vec{k})| - 4\pi A(\vec{k}) \sigma V_0 \Psi_0(\vec{k}, \vec{r_p}) \sin(\vec{k} \cdot \vec{r_p}) + \left| 2\pi\sigma V_0 \Psi_0(\vec{k}, \vec{r_p}) \right|^2 \tag{2.28}$$

The first term, as already discussed, represents the BF disk, while the second one gives structure to the BF disk. The third term, being a second order term in σ, is much weaker in intensity than the previous ones. Furthermore, for delta function

like potentials this last term is uniform in $\vec{k}$, providing an offset to the diffraction pattern intensity, without contributing to the CoM shift signal.

Eq. 2.28 is then dominated by the second term, $-\sigma V_0 \sin(\vec{k} \cdot \vec{r_p})$, that is a first-order term in σ. Its effect is a modulation of the contrast in the diffraction pattern. So, instead of a rigid shift of the BF disk, as in the previous case, the $\vec{k}$-dependence causes the asymmetry to occur in the intensity of the BF disk itself and it is probe position dependent. It is interesting to notice that the modulation produced is proportional to V_0; this means that the contrast of the DPC base images will be proportional to the atomic number Z, generating a different contrast when compared to the ADF one, that is proportional to Z^2. Moreover, it is important to note that the presence of a single $A(\vec{k})$ in the second term ensures that no intensity redistribution outside the central BF disk is allowed, so shifts of the disk boundary, as seen in the classical case, cannot occur in this extreme case.

Consequently, whether the CoM/DPC signal is caused by a rigid shift of the bright disk or its intensity redistribution inside the disk, depends on specimen under study features and the probe size employed. Moreover, Eq. 2.25 and Eq. 2.28 reveal that short-range and long-range field information is encoded differently. Low spatial frequency information, linked to long-range potentials, is present in the uniform displacement of the BF disk, while high spatial frequency information concerning short-range potentials is evident in the redistribution of intensity within the disk itself.

Thus, to differentiate the two contribution, that in most of the case are present simultaneously, different approach can be used. One possibility relies in the use of different integration areas, where integrating the changes in the signal generated by low-angle scattered electrons will give purely information about the short-range field, while integrating the outer angles may filter the sole long-range signals.

CoM imaging in real space and connection with the electric field - Analysis of the CBED CoM In a more general case, when $V(\vec{r})$ varies arbitrarily in the sample, and so does the electric field, $\vec{E}(\vec{r}) = -\nabla V(\vec{r})$, the analysis becomes more complicated. As just outlined, in this general case, there is a redistribution of the intensities inside the BF disk, and the shift imparted by the material's potential on the incident electrons is linked to the shift of center of mass (CoM) of the CBED pattern along the two direction, $\vec{k}_x$ and $\vec{k}_y$.

In the first momentum image, also called CoM image, each pixel has value equal to the centroid of the diffraction pattern. However, the CoM signal has a physical meaning in its own right, being the expectation value of the quantum mechanical probability current flow of the electron beam through the sample

[102, 105]. So the CoM signal at each probe position can be written as:

$$\mathrm{CoM}(\vec{r_p}) = \int \vec{k} I_D(\vec{k}, \vec{r_p}) d\vec{k} = \int \Psi_D^{*STEM}(\vec{k}, \vec{r_p}) \vec{k} \Psi_D^{STEM}(\vec{k}, \vec{r_p}) d\vec{k} = \frac{\lambda \langle \vec{p}_\perp \rangle}{h} \tag{2.29}$$

where h is the Planck constant, λ the electron wavelength and $\langle \vec{p}_\perp \rangle$ the expectation value of the momentum transfer orthogonal to the electron initial propagation direction. Following the Ehrenfest theorem the moment transfer of an electron caused by a perpendicular electric field $\vec{E}_\perp(z)$ at a position z can be written as:

$$d\langle \vec{p}_\perp \rangle = -e \langle \vec{E}_\perp(z) \rangle dt. \tag{2.30}$$

For thin materials, deviation from the initial propagation direction are small and therefore it is licit to assume the paraxial approximation for which $dt = \frac{dz}{v}$, with v being the electron velocity along the microscope axis which depends on the acceleration voltage applied. Integrating along the optical axis z, Eq. 2.30 becomes:

$$\langle \vec{p}_\perp \rangle = \int -e \langle \vec{E}_\perp(z) \rangle \frac{dz}{v}$$

From Eq. 2.29 it can then be obtained:

$$\vec{E}_\perp^m = \int \langle E_\perp \rangle dz = -\frac{v}{e} \langle p_\perp \rangle = -\frac{hv}{\lambda e} \cdot (\mathrm{CoM}_{\vec{r}}) \tag{2.31}$$

The vector quantity $\vec{E}_\perp^m$, expressed in units of Volt, is therefore simply linked to the measured $\mathrm{CoM}_{\vec{r}}$ and it gives information on the local transversal electric field which origin of the probe deflection. It is important to point out that the finite probe size induces a non-negligible spatial broadening. Therefore, the evaluated $\vec{E}_\perp^m$ does not correspond to the effective field integrated along the propagation path, $\vec{E}_\perp^T$, but to this quantity convoluted by a function, I_{Probe}, which takes into account the probe size and its spatial and temporal incoherence [93, 102, 105, 106]:

$$\vec{E}_\perp^m = \vec{E}_\perp^T * I_{\mathrm{Probe}} \tag{2.32}$$

From the Maxwell's equations, it is then possible to derive the projected charge density as the divergence of the measured electric field:

$$\rho_m = \varepsilon_0 \nabla \cdot \vec{E}_\perp^m \tag{2.33}$$

This evaluation of the charge density will still be affected by the probe size broadening effects mentioned above. Fig. 2.17.a provides a simplified representation of typical 4D-STEM experimental setup, where simultaneously to the

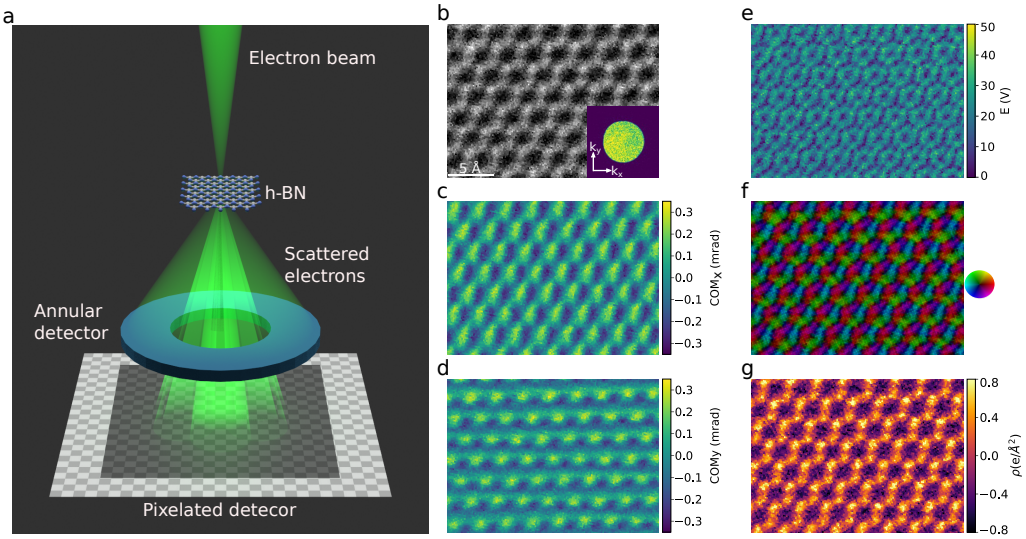

Figure 2.17: *Scheme of the 4D-STEM acquisition mode on an hBN monolayer.*

HAADF image acquisition (Fig. 2.17.b), the complete CBED pattern is collected for each probe position (Fig. 2.17.b insert) . By evaluating the shift along x (CoM_x) and y (CoM_y) direction of the center of mass for each CBED pattern, it is possible to derive Fig 2.17.c,d, which represents the shift imparted on the incident electrons by the local electric field. The module can then be derived as $CoM = \sqrt{CoM_x^2 + CoM_y^2}$, and it is presented in Fig. 2.17.e, while the orientation is shown in Fig. 2.17.f, encoded by the color schema. Finally, the charge density can be derived using Eq. 2.33, and it is shown in Fig. 2.17.g.

2.5. Atomic scale and long-range electric field mapping by 4D-STEM

The last ten years have seen both conventional DPC and 4D-STEM as emerging techniques to study the electric field and charge density characteristics for a wide class of materials. As mentioned in the previous section, generally two different case can be considered: long-range electric fields, where variations of the electric field happen on distances greatly larger than the probe size, and short-range, where the potential changes occur at the atomic scale. Both cases have been studied and gave excellent results. Hereby an overview of this application for thick materials is given, whereas the case of low dimensional materials and *h*–BN will be treated at the beginning of the next chapter.

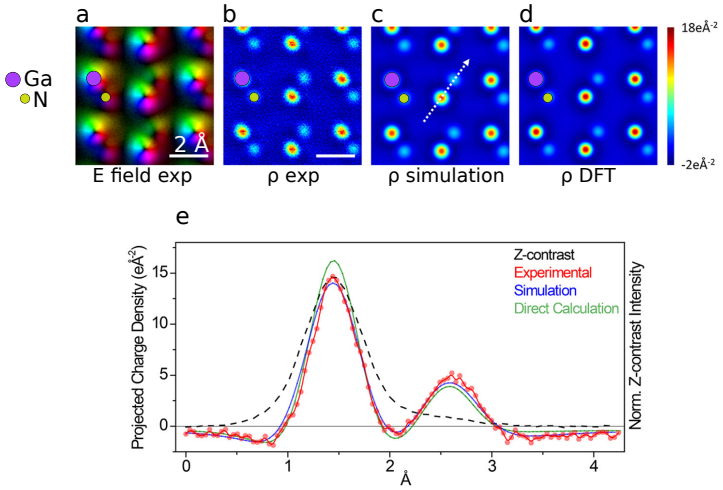

Figure 2.18: *(a) Experimental Image of the projected electric field for GaN. The color and brightness, respectively, denote the direction and magnitude of the field. (b) Projected total charge density map calculated from (a). (c) Projected total charge density map obtained from the scattering simulation. (d) Projected total charge density calculated directly from the isolated-atom form factors, convolved with the probe intensity. (e) Line profiles taken along the white arrow in (c) showing the normalized Z-contrast signal profile (dashed black line) and the experimental (red dots), simulated (blue) and calculated (light green) projected total charge density profiles. Adapted from Ref. 107*

Atomic scale electric fields

Initial studies on the electric field and charge density of individual atoms have been performed in 2014 by K. Müller et al. [102] on GaN employing an acceleration voltage of 300 kV. In this work, Müller and co-workers firstly explain in detail the quantum approach linking the CoM shift to the projected electric field causing a shift of the electron probe. The authors also explained that the sole use of conventional DPC employing segmented detectors may not be accurate, leading to a wrong quantification of the total shift. Indeed the diffraction disk does not undergo a rigid shift but rather an intensity redistribution occurs.

On the same material, few years later Santolino et al. [107] focused the attention on the charge density distribution, showing negative-charge pockets surrounding both Ga and N atomic columns (Fig. 2.18.a-d). To demonstrate the influence of the nuclei and electrons separately, image simulations were performed in which the scattering potential of the positive and negative charges could be separately included/excluded during the calculation. Only the simulation including both the positive nuclear charge and the electron cloud reproduced the same charge density profile observed in the experiment, demonstrating that DPC/4D-STEM is sensitive to both the nuclear charge and the surrounding

electron cloud [37].

Few years later Shibata et al. [91], following a previous work of 2015 [103], showed the fine sensitivity of such measurements to ionic bonding for a $SrTiO_3$ crystal. This has been achieved by comparing experimental measurements to simulations performed employing different potentials, with and without the consideration of bonding effects. These works have also shown that mapping the electric field at the atomic scale permits structural determination with a higher sensitivity with respect to HAADF. While oxygen atoms can not be observed by HAADF due to their high atomic number difference with Sr and Ti atoms, they can be easily distinguished by CoM images.

Long-range electric field

Although initial studies focused on the individual atom sensitivity, the case of slow-changing electric field has been investigated as well, providing important information for device applications. In 2015 it was first demonstrated that DPC can detect the built-in electric field at a GaAs p–n junction[94]. This is a rather challenging study, since the changes in the local field and charge caused by the dopants are relatively weak compared with that of atomic nuclei. To overpass this problem, a 0.13 convergence semi-angle has been employed, corresponding to a 12 nm spatial resolution, in a way to suppress the contribution of individual atomic columns and averaging the field over a large area. The obtained electric field was in agreement with the expectation, and it is shown in Fig. 2.19.

Despite the use of a rather low convergence angle results in non-overlapping disks, care is still required in the interpretation of the DPC signal since diffraction effect can still prevail [108]. Similar cares have been point-out lately in the case of a COM approach for measuring the electric field across an AlN/GaN interface [109, 110]. While the polarization induced internal electric field was properly measured, even for lamellae as thick as 110 nm, the electric field associated to the interfaces between the two materials was more difficult to quantify. Indeed, the differences of the mean-inner potential gives rise to a strong COM at the interface between AlN and GaN, but it is also shown that dynamical scattering can redistributed the intensity in such a way that the COM sign can even be reversed. In 2022, de Silva and co-workers published a work showing that reasonable electric field maps in a p-n junction can be provided even with a low electron dose using nanobeam STEM mode [111]. Following this study they also showed the potentiality of 4D-STEM to evaluate the $p-n$ junction interface quality, by performing CoM measurements applying an *in situ* bias, in a way to follow the dependence of the electric field with external voltages [112]. Compared to common techniques used for this purpose, as secondary ion mass spectroscopy, electron holography and capacitance-voltage, 4D-STEM has the

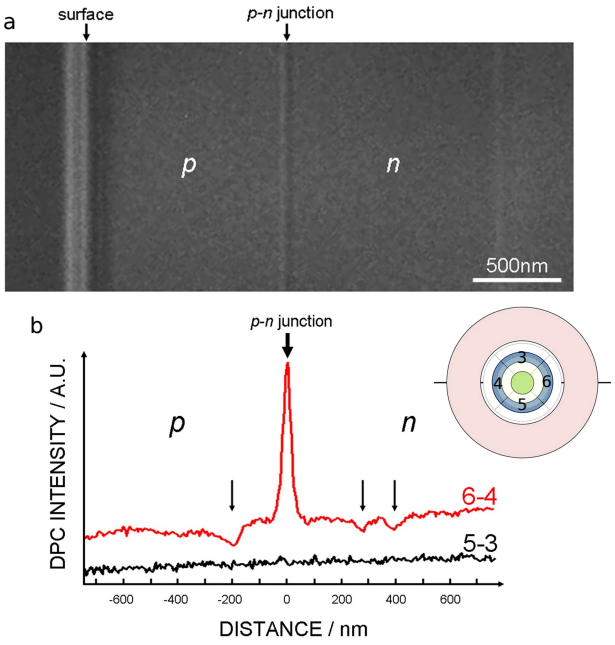

Figure 2.19: *(a)TEM image of the GaAs p-n junction. (b) Projected intensity profile of the DPC (5–3) and (6–4) images in the direction perpendicular to the p-n junction. Adapted from Ref. 94*

advantages of not being destructive, sensible to the pure electrical activity, it has a sub-nanometer resolution and can be performed while an electrical contact is applied to the materials under study.

Still in regards of large-scale electric field studies different works focused attention on the properties of oxides interfaces, which may present polarization effects .Yang et al. [113] reported the electrostatic characteristic of a grain boundary in a $SrTiO_3$ bi-crystal. They used two sets of collection semi-angles, 20 mrad for atomical resolved electric field investigations, and 6 mrad for the large-scale electric field measurements next to the grain boundary. The electric field distribution observed by the 4D-STEM was then in agreement with the one expected, extending over ca. 10 nm.

More recently, two members of our group, Qingxuan Jia and Alexandre Gloter, realized a study on the reconstruction of the potential at the interface between a metallic oxide $SrRuO_3$ thin film (SRO) and the insulating $DyScO_3$ substrate (DSO) [114]. In this study, significant focus has been directed towards comprehending the methods for distinguishing between long and short-distance electric field contributions in 4D-STEM. In general, different sections of the diffraction pattern can be defined: the bright field disk (BF 0-30 mrad), the outer part, corresponding to the MAADF detector (MA 40-100 mrad) and finally the

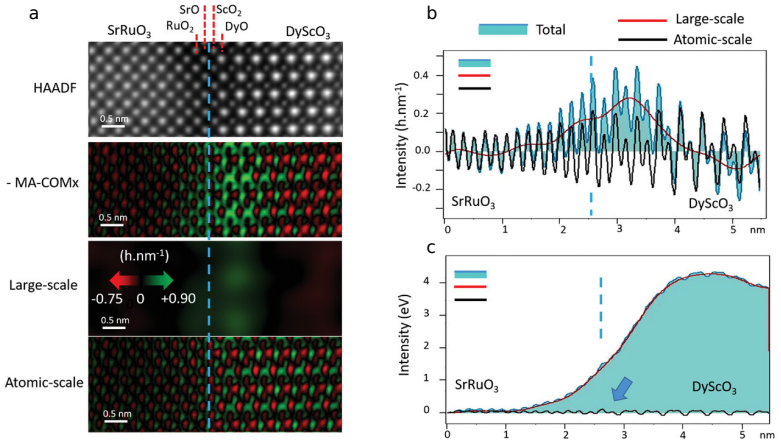

Figure 2.20: *(a) HAADF-STEM images, COM component across the interface (MA-COM$_x$) and its decomposition between a large-scale and an atomic-scale component. (b) Profiles of the total MA-COM$_x$ and its two components. (c) Profiles of the potentials estimated by integrating the MA-COM$_x$ and a thickness normalization. Adapted from Ref. 114.*

whole pattern (WP 0-100 mrad). From the work of Qingxuan Jia, it results that the MA-CoM images are more stable to thickness effects, namely scattering. Indeed, since it integrates thermal diffused scattering electrons, this signal is less sensible to strong diffraction process. Furthermore, this signal results to be more sensible and proportional to the presence of homogeneous large scale electric fields.

This behavior is shown in Fig. 2.20.a, where the 4D-STEM measurements performed on a SRO/DSO interface are reported. In particular the MA-CoM map, as taken experimentally, presents both long-range and atomic scale features; however, when applying filters, it is possible to separate the two different contributions. This clearly appears in the upper profile presented in Fig. 2.20, where the total, large-scale and atomic-scale profile for the same region are plotted. By integrating the electric field it is possible to derive the potential, showed in the lower panel of Fig. 2.20. This work is important in the optic of defining rules to identify, form a unique measurement, different components of the electric field.

All the works presented so far have been performed on relatively thick materials and stable to irradiation, where the acceleration voltages employed can be as high as 300 kV, and the resulting probe size is lower than 1 Å. Importantly, when experimental conditions are limited by sample characteristics, the probe effects in the determination of the final electric field and charge density may be more complicated and particular attention has to be paid.

CHAPTER 3

Charge transfer detection in pristine and defective *h*–BN by 4D-STEM

Following substantial success in utilizing DPC and 4D-STEM for studying electric fields and charge densities in thick materials, there has been an increasing interest in investigating the properties of low-dimensional materials. In general, 2D materials often exhibit unique electronic characteristics owing to their distinct atomic arrangement, and the presence of defects can frequently impart distinctive properties not found in pristine monolayers, thus giving rise to their own potential applications. However, this particular category of materials is typically sensitive to electron beam damage, which restricts the operation acceleration voltage of the microscope to lower values, typically ranging between 60 kV and 80 kV. This limitation results in a larger probe size and, consequently, a generally lower image resolution. A comprehensive state of the art review regarding the use of 4D-STEM for the study of 2D materials, with particular emphasis on *h*–BN, will be presented in Section 3.1, showing the limits that may arise form incoherence effects of the incident probe size.

With the aim of facilitating the study of such phenomena, we have integrated a 4D-STEM setup into the Nion ULTRASTEM200 microscope installed in our laboratory, which provides a very high space resolution and is equipped with an EELS spectrometer. Unlike most 4D-STEM setups, which typically incorporate segmented or pixelated detectors at the diffraction plane[73], our implementation is distinctive, since it makes use of the high performance direct detector commonly used for EELS measurements. Nevertheless, employing the EELS spectrometer in a non-dispersive mode it is still possible to perform 4D-STEM measurements, as will be illustrated in Section 3.2.

This setup has been employed to study both pristine and defective *h*–BN monolayer. Section 3.3 will delve into the details of the sample preparation

procedure necessary to prepare mono and few layers *h*–BN adapted to STEM observations, process that usually requires many and complicate steps.

In Section 3.4 the main results obtained for pristine *h*–BN monolayer are presented. Here a comprehensive analysis of electric fields and charge densities is carried on, with the aim of exploring 4D-STEM capabilities and getting more quantitative insight about charge redistribution in *h*–BN. To validate our experimental findings, we compare them with multi-slice 4D-STEM simulations based on the Coulomb potential derived from density functional theory (DFT), demonstrating the validity of experimental results.

After the study of non defective *h*–BN, Section 3.5 will examine the study of the electric field and charge density rearrangement in presence of a nitrogen terminating zig-zag edge. An enhancement of the electric filed is observed at the edge, with a direction perpendicular to the edge. This behavior has already been reported in previous studies, and such enhancement has been linked to the presence of a higher potential. However, with a thoughtful analysis and comparison with first-principle derived electric field, we show that the probe size plays a crucial role, and the interpretation of the experimental results is more complicated. Nevertheless, the evaluation of charge accumulation at the edge is still possible by defining appropriate integrating regions. This methodology has been applied for the first time in this thesis work.

In Section 3.6 a purely qualitative analysis of electric field and charge density modification in presence of point defects will be exposed. Two types of point defects are discussed: calcium and silicon adatoms, that are residues deriving from the sample preparation procedure, and boron vacancies, usually generated by the electron beam during the microscope session.

3.1. 2D materials

The first example of 4D-STEM electric field and charge density imaging on 2D materials was conducted in 2018 by Muller-Caspary et al. to identify the stacking sequence in MoS_2 [115]. Experimental 4D-STEM data were collected from a monolayer–bilayer interface from which the total charge density was extracted (Fig. 3.1.a). Experimental measurements were then compared with the charge density maps generated from first principles calculations, were two different stackings, AA and AA', were considered (Fig. 3.1.b). From the comparison of the line profiles, reported in Fig. 3.1.c, the authors were able to determine the experimental stacking order of the MoS_2 bilayer as the AA. Later in the same year, studies of the electric field at the monolayer–bilayer interface of graphene nanopores were conducted by Ishikawa and co-workers [116]. This work demonstrated that by examining the atomic-scale electric field image is possible to determine the symmetry and bonding configuration of adatoms

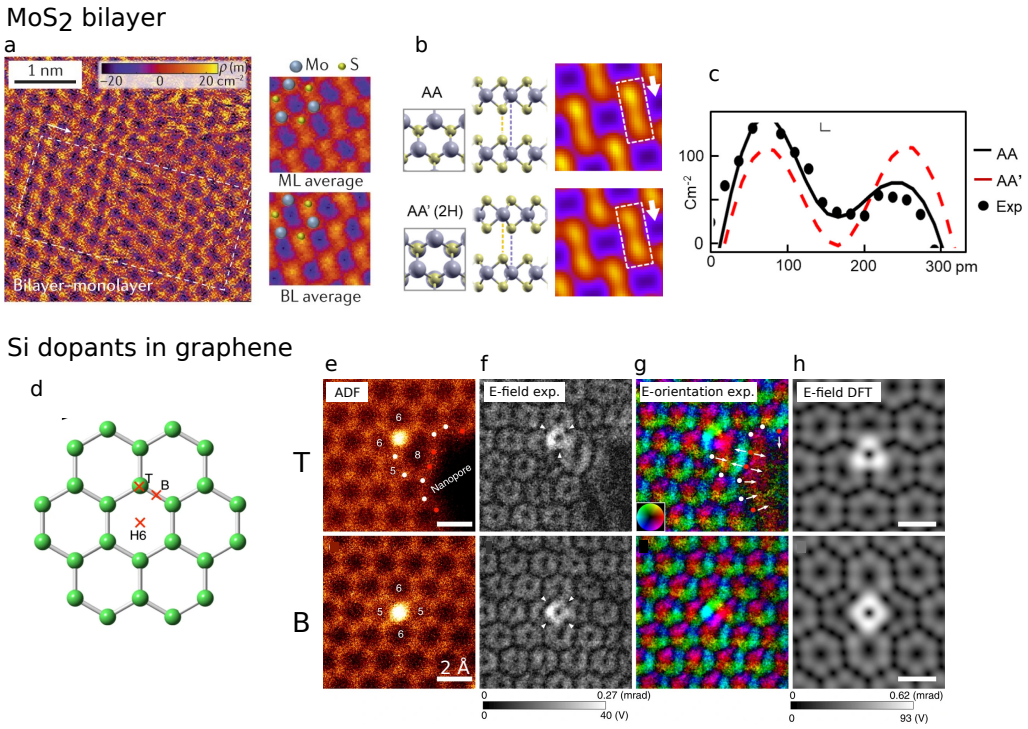

Figure 3.1: *(a) Charge density atomic map of a MoS_2 region showing a step from monolayer to a bilayer, with the relative averages over different unit cells. (b) Simulated charge density for AA an AA' stacking order MoS_2 bilayer. (c) Charge density profiles taken from experiments in (a) and simulations in (b), showing a better match with AA stacking. (d) Schematic view of graphene monolayer, showing the high symmetry positions. (e) ADF, (f) experimental electric field strength and (g) orientation, (h) calculated electric field strength maps from simulated STEM images for two different type of Si dopants configurations. Extracted from Refs. 115, 116*

and dopants, as shown in Fig. 3.1.d-h. Typically, extracting this information would necessitate a detailed examination of the HAADF images. These first studies demonstrated that electric field and charge density imaging in 4D-STEM is highly sensitive to the atomic structure and specific bonding arrangement of light elements in 2D materials, and they paved the way to further studies into the electronic structure of 2D materials.

In 2019, 4D-STEM has been used by Fang et al. to image for the first time the electric field and charge density generated by line defects in MoS_2 and WS_2, showing the formation of metallic conducting channel [117] (Fig. 3.2.a-c). A few months later, Wen et al. conducted a similar study, mapping the 1D states of MoS_2 edges. However, instead of focusing on electromagnetic behavior, they utilized electric field maps to glean insights into the intricate structures of the edges. Notably, the use of standard HAADF images makes it challenging to

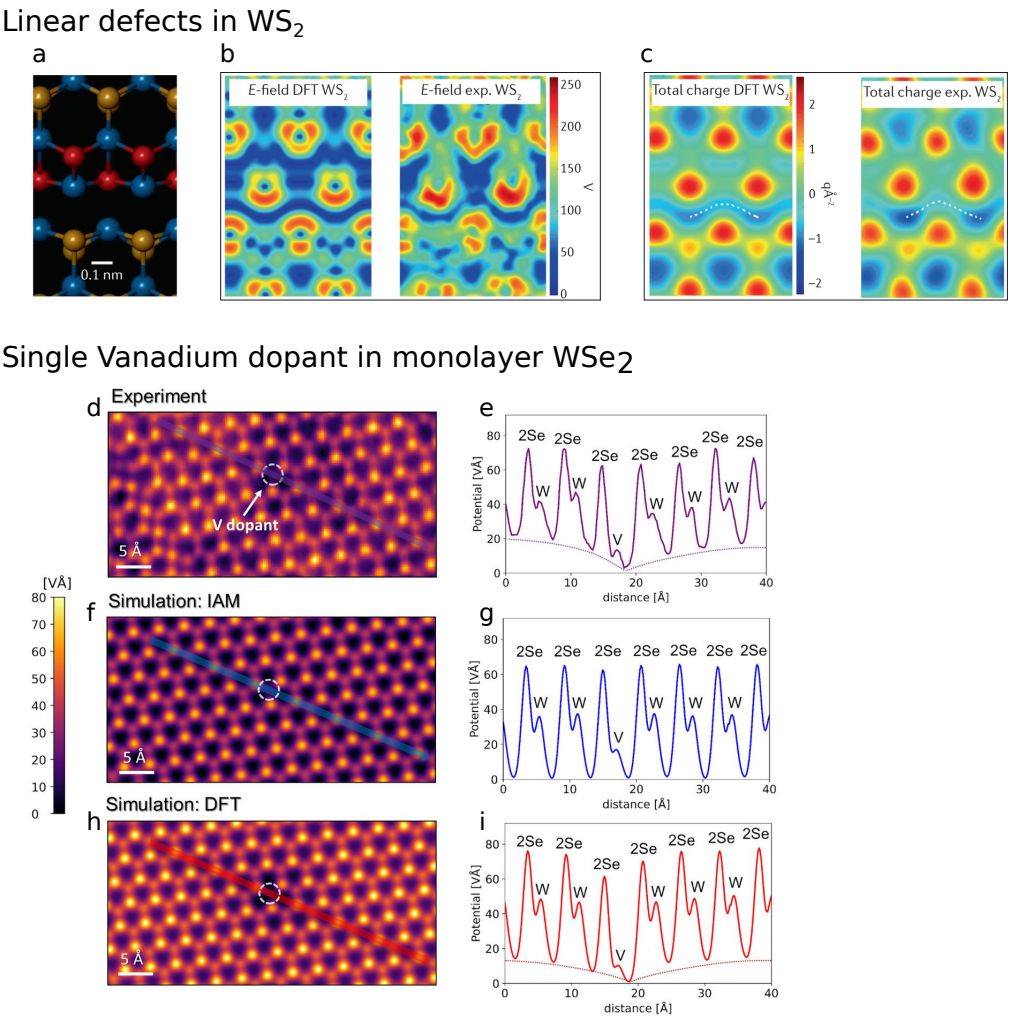

Figure 3.2: *(a) Atomic model of 1D line defects in MoS_2 and WS_2. Experimental and DFT derived electric field for (b) WS_2 and (c) MoS_2. (d) Representation of the projected atomic electric field calculated from experimental, 4D-STEM multislice image simulations and DFT calculations. The scale bar corresponds to 2 Å. (d) Normalized projected electric field integrated over the blue arrays in (d), where the pristine region images are used as the references for normalization. Extracted from Refs. 117, 119*

resolve individual sulfur atoms located at the edges, given their lower atomic number (Z=32) in comparison to the molybdenum (Z=42) or tungsten (Z=74) atoms. In contrast, CoM-derived images have proven to be sensitive to lower atomic number atoms [118].

Further studies on TMDs focused the attention on different point defects. The effect of mono- (V_{1S}) and di-sulfur (V_{2S}) vacancies has been studied for both MoS_2 and WS_2, showing in both cases a reduction of the total charge density,

in good agreement with 4D-STEM simulations and DFT derived calculations [119, 120].

More recently, a similar study has been conducted by Hofer et al. [88] using a different approach: charge redistribution related to sulfur vacancies in WS_2 has been detected via ptychography phase reconstruction. As detailed in Section 2.4, ptychography can lead to an aberration corrected phase reconstruction, permitting the study of charge redistribution phenomena, similarly to what is done in HRTEM since long time [8]. In particular, the work of Hofer and co-workers showed that both charge redistribution due to bonds and the charge transfer generated by defects can be detected by comparing the phase contrast extracted experimentally with images simulations. Bond effects have been studied employing first-principle DFT, where charge transfer is taken into account, or IAM derived potentials, where all the atoms remain in a neutral state. Interestingly this study has shown how residual aberrations may lead to a wrong phase contrast if not corrected, leading to a greater agreement with IAM derived potential. However, charge quantification has not been retrieved directly from the experiments, but obtained from a Bader charges analysis on the DFT derived simulations, which permit to reproduce the experimental result.

Another class of point defects which modify the charge density distribution, and the electrostatic potential associated, is the presence of dopants. A recent work by Dosenovic et al. [121] studied this effect on a vanadium doped WSe_2 monolayer. In this work experimental 4D-STEM derived projected potential has been compared with those reconstructed using an IAM or a DFT model. While considering an independent atom model results in a neutral dopant, introducing bonding effects by employing DFT potentials, a net negative charge is assigned to vanadium, resulting in a deep in the projected potential, which is in agreement with the experimental results (Fig. 3.2.d-i). This work demonstrates the high sensitivity of 4D-STEM derived charge density maps to bonding rearrangement.

In all the works on 2D materials presented up to this point, only the total charge density has been discussed. However, only the electron charge density is involved in chemical bonding. Furthermore, only valence electrons contribute to charge redistribution, meaning that modification on the total charge density happens on a tiny percentage. For these reasons, ideally it would be better to isolate the sole electronic component. In this context, a recent study done by Martins et al. [122] succeeded in imaging the sole electron charge density at the atomic scale on MoS_2 starting from 4D-STEM measurements. Following precedent similar procedures employed for thick materials [107], the nuclear contribution can be represented by delta function normalized by their atomic number located at the atomic positions, which can be easily determined by the HAADF image. The as constructed nuclear charge density is then convoluted by the probe function. This contribution has then to be subtracted from the total charge density derived from

the COM maps to extract the electronic charge density. However, the so derived total electron charge density is actually governed by core electrons convoluted by the probe size. In particular, Martins and co-workers show that, in the case of MoS_2, a valuable insight on valence electrons may be achieved employing a probe size of the order of 0.35 Å, corresponding, for a microscope operating at 80 kV, to a convergence angle of 60 mrad and no chromatic aberrations. However, such probe sizes are beyond the limits of current technology. While the choice of a compound with relatively heavy atoms, as in the Martis et al. work, facilitates 4D-stem imaging, it may represent a strong limitation in the investigation of charge transfer effects due to the small fraction of the total electronic charge involved in the process.

h–BN

Comprised of lightweight atoms, *h*–BN represents the ideal candidate to explore 4D-STEM ultimate capabilities for quantification studies of electric field and charge density. More importantly, *h*–BN is characterized by a number of valence and core electrons that are comparable, making it possible to distinguish the two contributions, and exhibits a significant charge transfer between boron and nitrogen [5–7, 15, 123]. This strong charge transfer leads also to a pronounced charge redistribution in the vicinity of defective sites, further reinforcing the significance of *h*–BN for an in-depth study of the 4D-STEM potential. Conversely, conducting experiments on *h*–BN is more challenging than on TMDs due to a higher sensitivity to electron irradiation and CBED shifts in 4D-STEM less pronounced.

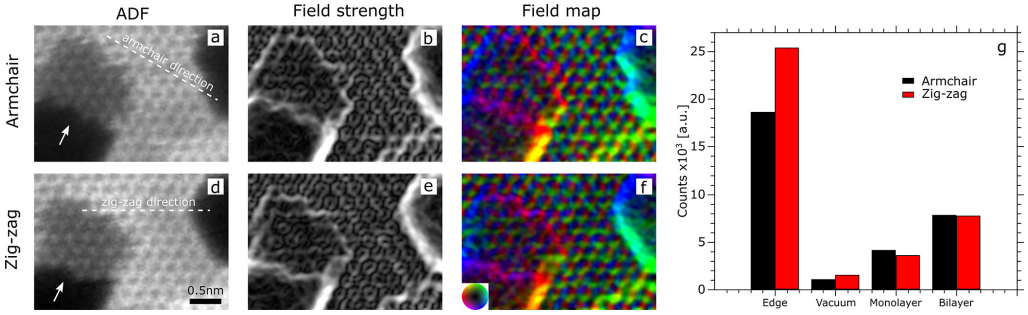

Figure 3.3: *(a-c) Dark filed, electric field strength and orientation respectively for an h–BN armchair edge, (d-f) dark field , electric field strength and orientation respectively for an h–BN zig-zag edge. (g) Histograms of the electric field strength for different zones of the armchair and zig-zag h–BN edges. Extracted from[124]*

To the best of our knowledge, as of the time of this thesis, there are only two works pertaining to the utilization of DPC and 4D-STEM techniques for

the examination of *h*–BN. In the first work, Cretu et al. recorded the CoM atomic-scale maps for a few-layers *h*–BN flake, using a four quadrants detector [124]. This work has proven qualitative analysis on the electric field and charge density, showing good agreement with DPC imaging simulations. The article also reported the study of the electric field changes at defective sites, showing a strong enhancement of the COM shift signal in correspondence with point defects, such as boron vacancy, and edges. Fig. 3.3 shows measurements performed on two different edge configurations, zig-zag and arm-chair. This image clearly shows a strong enhancement of the CoM signal at the edge, independently from their configuration. In the histogram reported in Fig. 3.3.g it appears that this enhancement is more intense for the zig-zag edges with respect to the armchair ones. In the supplementary information of the article they also discuss that the electric field enhancement produced by a zig-zag edge is of ca 60% compared to the bulk situation. The presence of such a high electric field has been related to the formation of dipoles at the surface, generated by the different charge states of the N terminating atom compared to the bulk. However, in the absence of a detailed discussion of Coulomb interactions and effects of probe size and incoherence, these results provide a rather qualitative picture that can only be loosely linked to the effective charge density and electric fields of the system under investigation.

In the same year, Madsen and co-workers [87] reported ptychography phase reconstruction, with aberration correction post acquisition, for an *h*–BN monolayer. Similarly to what has been done in HRTEM [8] and for WS_2 [88], in this study the experimental images have been compared to image simulations, generated employing different potentials. Fig. 3.4.a,b show the phase reconstruction maps obtained from experiments and the one where the aberration correction (AC) has been applied. From the intensity histograms produced for the two types of atoms, reported in Fig. 3.4.f,g, it is clear that the aberration plays an important role in determining the phase contrast, leading to a possible inversion, making necessary the post-acquisition correction. In Fig. 3.4.c,d are reported the images simulations performed using an IAM potential model and a DFT derived one, respectively. Focusing on the intensity histograms obtained in the two cases, (Fig. 3.4.h,i), accounting for bonding reduces the contrast between boron and nitrogen atoms with respect to the one produced by employing a IAM potential. More importantly, the contrast derived form the experimental measurements is in a better match with the latter case, showing once more the high sensitivity of this technique to bonding charge redistribution. This result is in fully agreement with the study of Meyer et al. [8]. However, even in this study, a quantitative evaluation of charge redistribution is not directly accessible from the experimental results.

In this regard, the 4D-STEM setup implemented in this thesis has been used to investigate electrostatic properties related to charge redistribution and transfer

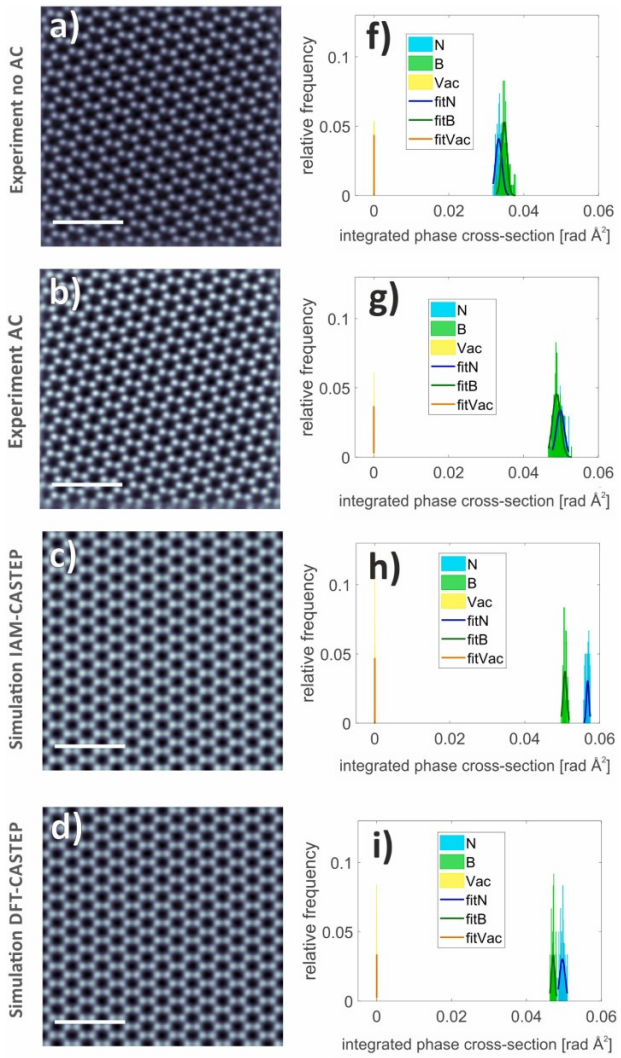

Figure 3.4: *Ptychographic phase images of h–BN from 4D-STEM experimental data (a) without and (b) with post-collection aberration correction, compared to simulated data using (c) the IAM and (d) DFT. (f) to (i) corresponding histograms of the integrated phase cross-sections of N and B with respect to vacuum (Vac). The scale bar in (a) to (d) is 1 nm. Extracted from[87]*

in pristine and defective *h*–BN.

3.2. Implementation of 4D-STEM at the Ultra-STEM

The spherical aberration corrected STEM electron microscope used for the implementation of the 4D-STEM setup is the NION ULTRASTEM 200, already presented in Section 2.3. The direct detector MerlinEM - Medipix3 has been

recently installed on the Gatan ENFINA EELS spectrometer mounted on the microscope [35, 36], already detailed at the end of Section 2.2.

Because the pixellated direct electron detector is positioned at the exit of the EELS spectrometer, rather than directly at the diffraction plane as in standard microscopes used for 4D-STEM experiments, the setup for this microscope differs. Nevertheless, even in this configuration, with a careful adjustment of the EELS spectrometer 4D-STEM measurements can still be performed.

For EELS measurements the electron beam needs to be focused along one direction by the octupoles and quadrupoles system and the spectrometer works in a dispersive mode. For 4D-STEM, the beam at the entrance of the spectrometer is not focused and the spectrometer is tuned in a non dispersive mode to obtain a direct image of the beam. On the spectrometer detector is then acquired the full CBED pattern. With the help of Alexandre Gloter, it has been possible to tune and align the EELS spectrometer to implement such 4D-STEM set-up. Using this spectrometer configuration, the CBED pattern result to be spread in one of the four chips. During the measurements it is then possible to select only the chip containing the CBED pattern, which enables a faster readout time and lower data sizes.

Implementation of a live analysis of 4D-STEM dataset Soon after the implementation of the 4D-STEM implementation, with the help of Marcel Tencé (CNRS engineer), a live 4D-STEM dataset analysis mode has been developed in the software usually employed during the microscope session, Gatan DigitalMicrograph. Within this live mode it is possible to have a live acquisition of the HAADF image together with BF and MAADF virtual detectors, CoM and DPC signal along X and Y direction, and any geometric detector defined by other masks. All of this is possible thanks to home made compiled plug-in. A pre-acquisition of the CBED pattern permits to define the different masks that will be used to create the virtual detectors. The plug-in also allows to modify the mask of the detectors during the acquisition, but the number of detectors cannot be changed during the acquisition. All the desired quantities are directly saved as an image stack, where each frame corresponds to a different quantity. The full 4D-STEM dataset is not recorded, and therefore it is not possible to perform any further data analysis, as an evaluation the center of mass in a different way, the study the diffraction pattern itself, or to perform ptychography. For this reason this live mode is essentially used to tune the acquisition parameters for the complete measurement, i.e. dwell time, step size and collection mode. The live analysis represents also an efficient solution for data compression: 4D-STEM datasets are composed of the HAADF image size multiplied by the CBED image size, resulting in an average of 5 GB per data, while with the online mode the

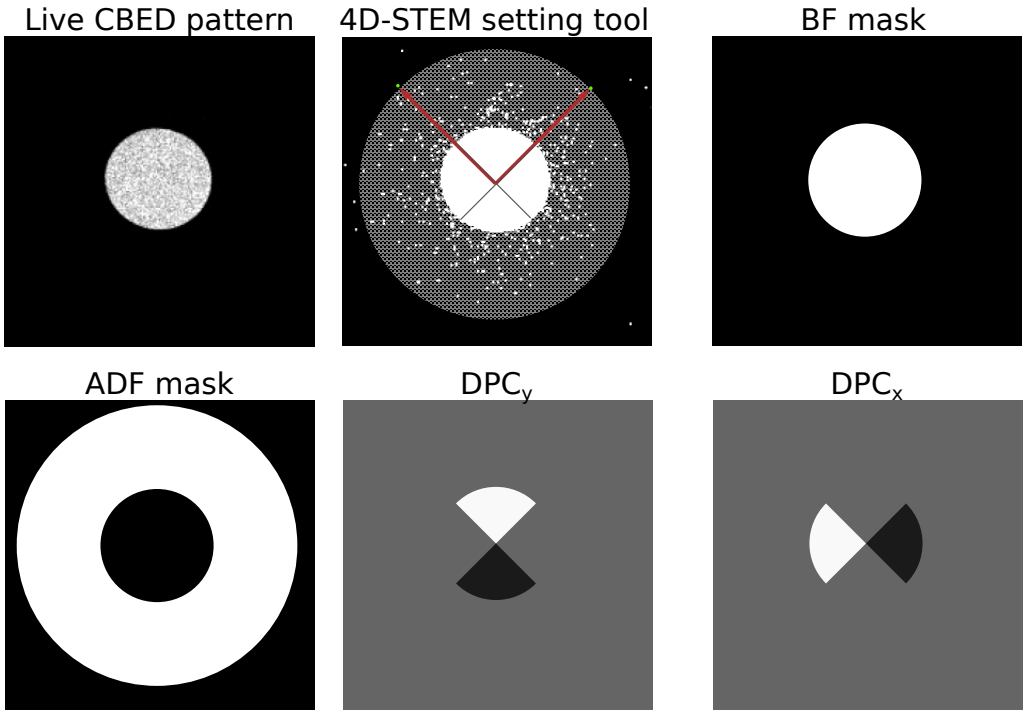

Figure 3.5: *Scheme of the 4D-STEM live acquisition mode, with the different selection of detectors.*

size is reduced to the HAADF image size multiplied by the number of desired quantities, resulting in a few MB of data.

4D-STEM Acquisition details

Different 4D-STEM configurations have been set on the microscope, characterized by a different magnification of the beam at the entrance of the EELS spectrometer, resulting in different values of mrad/pixel. The availability of several configurations is useful since different study may have the need for a different resolution in the determination of the CoM shift, or conversely need a higher maximum collection angle.

The measurements showcased and examined in this thesis were conducted using two different 4D-STEM configurations: the more magnified one, with a pixel size of 0.5 mrad for quantitative analysis, and the 1 mrad/pixel one for more general studies. For quantitative analysis the aim is to achieve precise measurements with the utmost accuracy of the observed parameters, translating in the need for higher shift resolution. Conversely, the other 1 mrad/pix configuration allows for a larger maximum collection angle, that is a crucial requirement for applications like virtual detectors, ptychography or study of long-range fields.

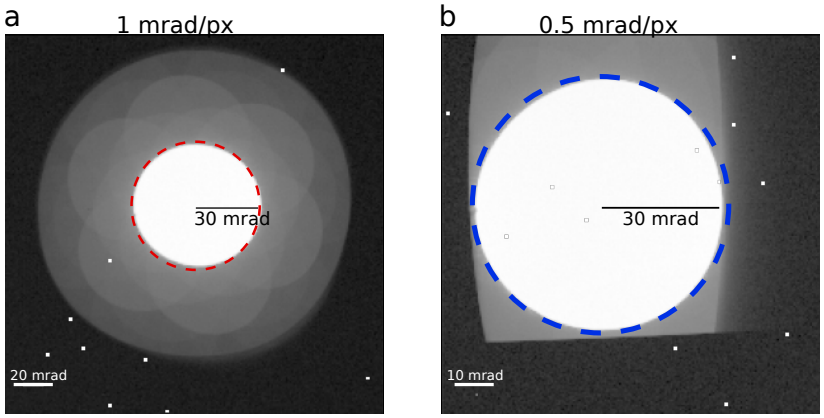

Figure 3.6: *Different setups implemented for 4D-STEM measurements: (a) setup with a pixel size of 1 mrad and a maximum collection angle of ca 80 mrad and (b) a more magnified one, with a pixel size of 0.5 mrad and a maximum integration angle of 30 mrad due to the spectrometer geometrical constrain.*

Furthermore the 1 mrad/pixel setup allows faster acquisition time, making it a better choice when dealing with electron-sensible structures.

All the 4D-STEM measurements were conducted with a depth of 6 bits and varying dwell times based on the specific setup employed. Generally, dwell times of 0.6-0.8 ms/pixel were used for the less magnified setup, while 0.3-0.6 ms were used for the other configuration. It is important to note that when operating at 6 bits, dwell times lower than 0.3 ms cannot be used due to the reading speed limit of the MerlinEM-Medipix3 detector. Depending on the analyzed structure and the region of interest, the spatial steps ranges from 0.1 Å to a maximum of 0.25 Å, ensuring atom sensitivity at all times.

Acquisition of the zero level for each set-up used The electron beam may exhibit asymmetry or, more commonly, there might be distortions in the intensity distribution before it interacts with the sample. This aspect holds significant importance when assessing the center of mass shift. Specifically, in cases where the beam remains undistorted and maintains a perfect circular shape, the shift should be calculated relative to the center of the circular area itself.

In cases where distortions are evident, it becomes essential to determine the center of mass of the beam intensity and subsequently calculate the shift from that reference point. Thus, to address this concern, vacuum measurements are conducted for each setup and measurement session. In this context, with no sample interaction taking place, the average center of mass from these vacuum measurements is established as the reference Center of Mass (CoM) for that specific setup. This step is essential not only for accurately assessing the values

of electric field or charge density but also for establishing a reliable zero level.

Virtual detectors

Among the various applications of 4D-STEM measurements is the intriguing potential of generating virtual detectors, which facilitates the comparison of distinct signals. This can be achieved through the utilization of different masks to selectively integrate signals originating from specific angles, according to the desired signal type and contrast. In pursuit of such applications, particularly in replicating ADF images, it is imperative that the maximum collection angle surpasses that of the BF disk, which corresponds to a semi-angle aperture of 33 milliradians in our experimental setup. Consequently, for the purpose of implementing virtual detectors, we employed the 1 mrad/pixel configuration, offering a maximum integration angle of approximately 70 to 80 milliradians. The CBED pattern, as acquired during 4D-STEM measurements, is depicted in Fig. 3.7.a, where a logarithmic scale is employed to accentuate the contrast and show the signal out of the semi-angle aperture size, that is the BF disk. Fig. 3.7.b,c,d show the mask of integration to simulate a bright field, annular bright field or annular dark field detectors respectively. Fig. 3.7.e is the live HAADF, acquired during the experiment, that is obtained by integrating angles spanning from 80 to ca 180 milliradians. Fig. 3.7.f,g,h are the image derived form the integration of the relative masks.

Examining the BF image, no discernible signal is observed. This arises from the minimal phase shift experienced by the incident electron wave in the presence of a monolayer. This small phase shift is overshadowed by the intensity of elastically transmitted electrons, rendering signal acquisition challenging. This image essentially captures the intensity of the electron probe throughout the measurement. When employing an annular detector, designated as ABF, to somewhat "attenuate" the signal originating from the purely transmitted electrons, a slight signal becomes visible, as depicted in Fig 3.7. Finally, we can generate the ADF image, which, depending on the integration angles, combines the characteristics of both the LAADF and MAADF detectors. This results in an atomic-resolved image, exhibiting superior contrast compared to the experimental one. Applying the contrast definition of $C = (I_{max} - I_{min})/(I_{max} + I_{min})$, we obtain a value of 0.2 for Fig 3.7.e and 0.52 for Fig. 3.7.h.

3.3. Sample preparation

To achieve a comprehensive quantitative analysis of electric field and charge density, it is imperative to work with extremely thin samples, ideally focusing on monolayers, ensuring the applicability of the weak phase approximation.

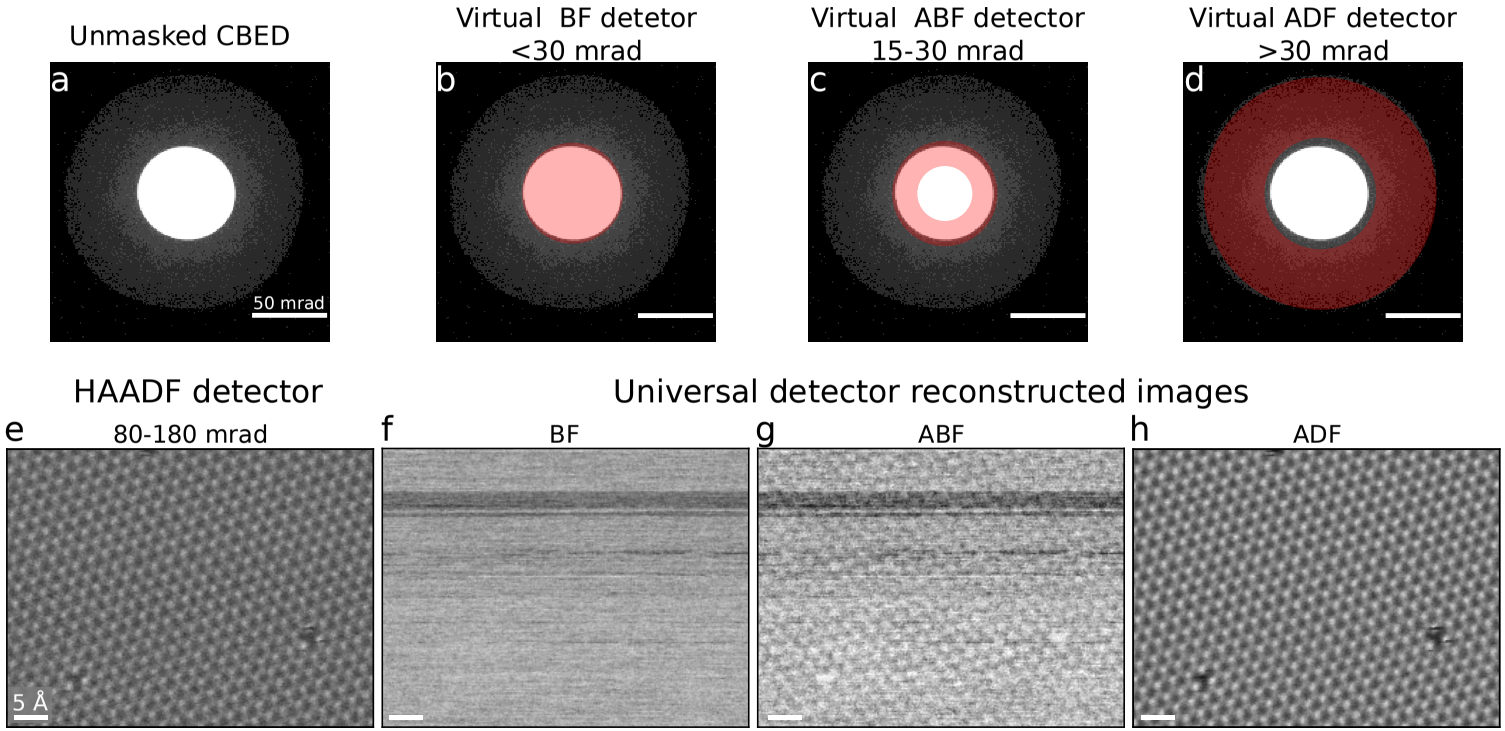

Figure 3.7: *(a) CBED pattern as acquired during the 4D-STEM measurement on an h–BN monolayer, using the 1 mrad/pix setup. (b-d) Masks applied to the CBED pattern to reproduce the BF, ABF and ADF virtual detectors. (e) HAADF image simultaneously acquired to the CBED patterns. (f-h) Reconstructed STEM images from 4D-STEM dataset for the BF, ABF and ADF virtual detectors respectively.*

However, obtaining suitable samples for (S)TEM investigations involves more than just obtaining monolayer materials. In order to be studied in a (S)TEM, the specimen has to be transferred onto a specific TEM grid, which allows its insertion into the microscope, and which are specifically designed to study transmission electron phenomena. There exist different transfer procedures as well as different TEM grids, depending on the samples dimension and physical properties. A common adopted method is the chemical exfoliation. It is a well known technique to produce few layer flakes in a relatively cheap and scalable way. This procedure involves the dispersion of the desired materials, as could be *h*–BN flakes, in a suitable organic solvent, as ethanol or isopropanol, followed by a sonication which may last from few second to hours depending on the initial state of the flake and the desired final size [125, 126]. Successively the upper part of the solution, that is often the more dispersed one, is collected and few drops are deposited on the TEM grid. However, when it comes to *h*–BN, this approach becomes notably challenging for separating individual monolayers. This is potentially due to factors like the most common AA' stacking, slightly ionic bonds, and a distinct flatness that results in stronger adhesion between *h*–BN layers and other surfaces compared to other 2D materials [127].

Due to these considerations, prior investigations focusing on *h*–BN monolayers through STEM techniques have often opted for another preparation method [128–131]. This involves directly starting from the synthesized monolayer, typically produced through the chemical vapor deposition (CVD) technique, and then employing a polymer-assisted procedure to facilitate its transfer onto a TEM grid [123, 132]. *h*–BN monolayer is commercially available as CVD grown films on copper foils. The starting material employed for all subsequent experiments was acquired from Graphene Supermarket, and the procedure for polymer-assisted transfer is depicted in Fig. 3.8.

A small drop of Cellulose Acetate Butyrate (CAB) is cast on the h-BN/Cu/*h*–BN foils. The copper substrate is later dissolved using ammonium per-sulfate (APS) and let to react overnight. The monolayer+CAB is then rinsed in deionized (DI) water to remove APS residues. The film is picked up with the Au Quantum foil TEM grid (TED-PELLA) with holes of 100 μm and later heated at 150 °C to promote the adhesion of the CAB layer with the carbon foil. In order to remove the CAB layer, the grid is then put in three different organic baths, respectively Ethyl acetate, Acetone and Isopropanol for 30 minutes each. Finally, the grid is heated in a furnace oven, with a 200 °C annealing process with an Argon flow of 150 cc/min at a pressure of 300 mbar followed by a further annealing at 550 °C under vacuum conditions (10^{-5} mbar) to remove any residual carbon contamination.

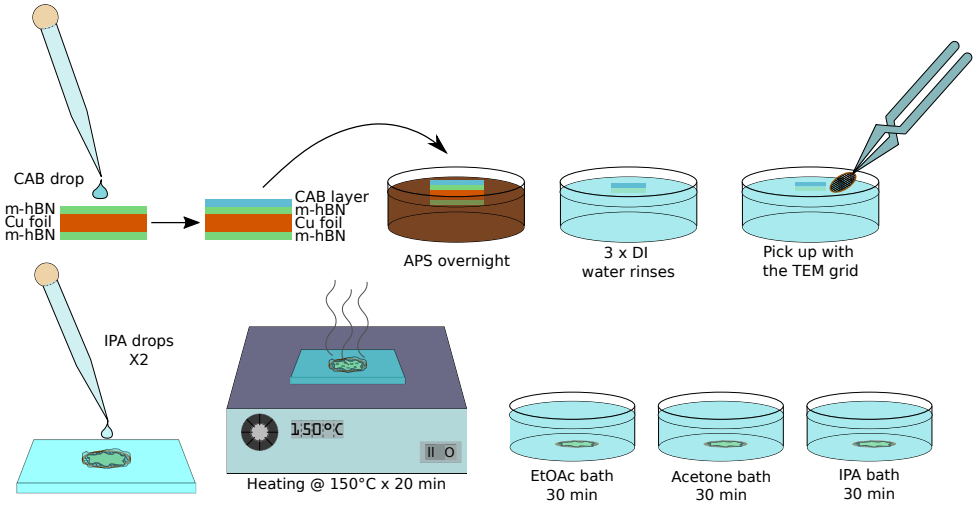

Figure 3.8: *Scheme of the polymer assisted transfer process of CVD grown hBN monolayer to TEM grid.*

Check of the sample quality by TEM, HAADF and EELS

The transfer procedure just illustrated is not without challenges, and there are instances where its efficiency is compromised or the sample's condition is not optimal. In some cases, due to the fishing pick-up method employed, the surface tension can cause the *h*–BN layer to fracture or inadequately fill the holes of the quanti-foil grid. An example of this phenomenon is illustrated in Fig. 3.9.a, where the hole in lower-right part is empty. Additionally, even after undergoing the two annealing procedures, the *h*–BN layer frequently retains contamination, commonly in the form of polymer residues. The more heavily contaminated areas are evident even at low magnification, as indicated by the green circle in Fig. 3.9.a, zoomed in Fig. 3.9.b. Conversely, areas with less contamination appear nearly transparent (red circle in Fig. 3.9.b), where however in most of the case a complete coverage of the hole is not reached, as shown in Fig. 3.9.c

Nonetheless, even in the areas where contamination are apparently lower, zones with both clean regions and residues are consistently present. This feature is illustrated in Fig. 3.9.d, where darker zones correspond to clean *h*–BN, while the bright white spots are contamination coming from the sample preparation procedure. EELS are then usually performed to localize the pure zones, where the core-loss EELS spectrum presents the sole boron and nitrogen K-edges (Fig. 3.9.e). On the other side, in contaminated areas, the EELS spectrum, reported in Fig. 3.9.f, presents supplementary peaks, relative to the C K-edge, confirming that the majority of contamination comes from residual components of the CAB polymer.

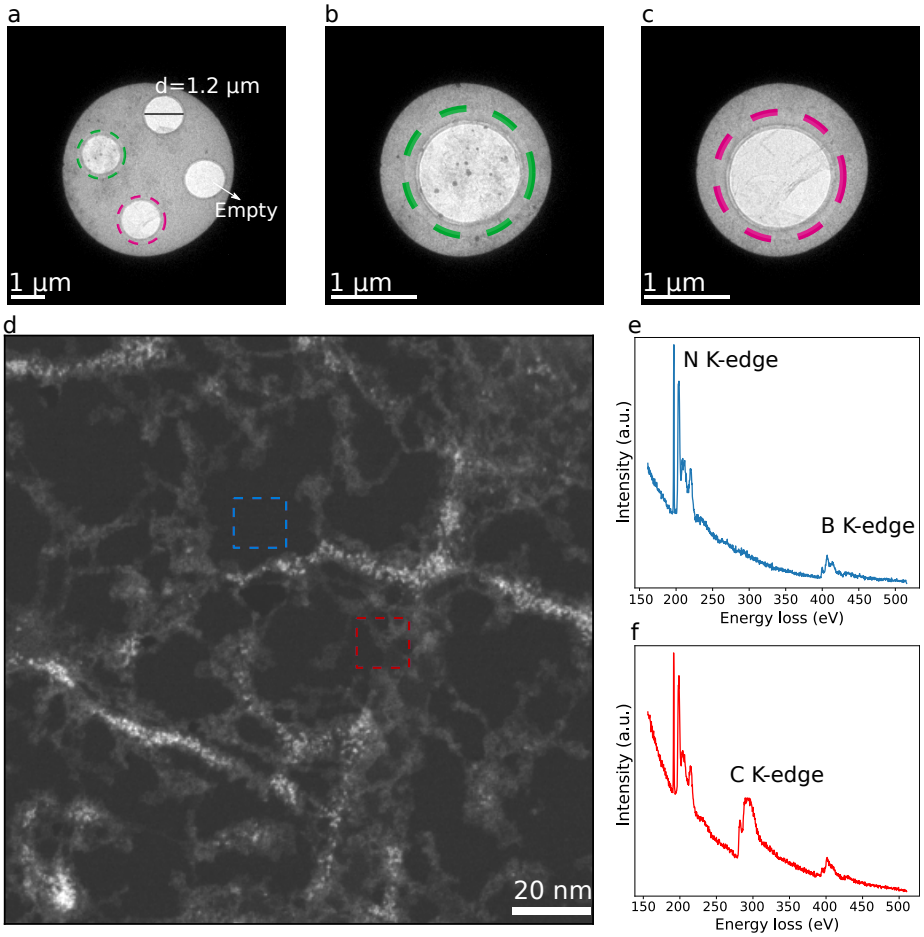

Figure 3.9: *(a) TEM images of a grid portion showing the partial fill of the holes. (b) Some holes are heavily contaminated and it is visible, while cleaner parts appear almost transparent (c). (d) HAADF image of h–BN monolayer showing the presence of clean area, characterized by pure h–BN and other with presence of carbon contamination, shown in the EELS spectra (f) and (g).*

The quality check procedure serves a dual purpose: it aids in identifying clean areas and provides an estimation of their size. As shown in Figure 3.9.d, these clean areas are approximately 20 nm in size, showing that the transfer process has inherent limitations. These limitations are not only due to the presence of empty or fractured regions within the TEM grid's holes but also pertain to the cleanliness of the 'intact' zones, where only small portions are suitable for experimental use. An additional step to enhance the cleanliness of the monolayer and achieve larger uncontaminated regions is performed within the microscope and it involves a technique known as "electron shower." In this process, the incident high-energy electrons of a STEM are employed to sputter

carbon contaminants from the surface. However, it is important to exercise caution when applying this technique to *h*–BN, considering its sensitivity to radiation effects [28, 133, 134].

3.4. Pristine *h*–BN monolayer

As already emphasized in the previous chapter, electric field and charge density derived from CoM maps can be in principle extracted in a quantitative way, at the atomic scale, for very thin materials, e.g. monolayer. For this reason we mainly focused our attention on the *h*–BN few- to mono-layer system, prepared and transferred onto a TEM grid following the procedure just explained in the previous section. In a first step, we have performed a comprehensive study on perfect *h*–BN monolayer to identify the ultimate 4D-STEM capabilities.

Quantitative analysis of electric field and charge density at the atomic scale
Fig. 3.10.a presents a HAADF image of an *h*–BN monolayer acquired together with CBED patterns at each probe position; the dashed line indicates the region from which the intensity profile represented in Fig. 3.10.c has been extracted. The CoM derived electric field amplitude is given in the upper panel of Fig. 3.10.d expressed in both Volt and mrad, with a conversion constant of 113.7 V/mrad for a microscope operating at 60 kV. The bottom panel of 3.10.d is the direction of the electric field, coded in the color schema. From the image it appears that the electric field points outwards from the atoms towards the center of the hexagons.

In Fig.3.10.g is represented the total charge density as derived from the divergence of the measured electric field. Positive values are observed in proximity of the atoms positions while negative charges occur close to the hexagon centers. This picture can be understood by considering that the recorded charge density is a result of both nuclear and total electron charges and that in proximity of the atoms only core electrons partially screen the positive nuclear charges.

While it is theoretically possible to extract the pristine charge density function by de-convolving the recorded displacement map, this process would require an exceptionally precise understanding of the probe's shape. In a different approach this information can be retrieved by comparing the experimental measurements with first principle simulations performed onto realistic atomic models. As described in Section 3.1, qualitative agreements between experiments and density functional theory simulation have been reported in a few works of 2D materials [117–119, 122, 124, 135]. However, this juxtaposition should be made with particular care. In particular, when performing DFT simulation, it is fundamental to explicitly consider the core electrons density since the electron beam impact parameter can be much lower of the cut-off radius. This can be done either

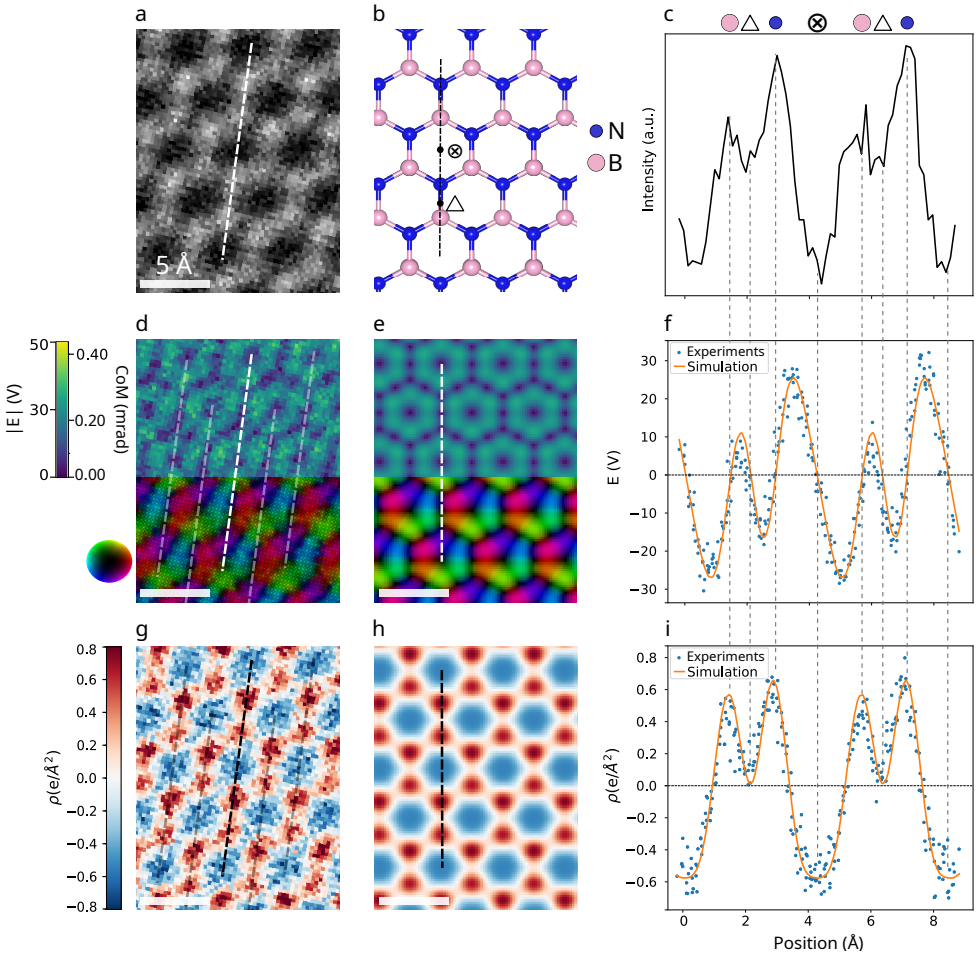

Figure 3.10: *(a) HAADF of an h–BN monolayer and (b) corresponding atomic model. (c) profile of the HAADF image along the white line in (a). (d) Electric field modulus (upper panel) and orientation (lower panel) obtained from the 4D-STEM dataset acquired synchronously with the HAADF image. (e) Electric field map obtained from multi-slice simulations using the DFT derived potential. (f) Profile of the simulated electric field (orange line) and experimental measurements obtained from equivalent directions passing through the hexagons diagonals (points). Different experimental profiles have been overlapped in the figure after realigning them minimizing of the cross correlation function. (g,h) Experimental and probe-propagation simulation of the total charge density obtained from the electric fields and (i) the relative line profiles.*

by performing all electron calculations or by reconstructing the core density using the PAW approach. The latter technique is usually employed, since the computation is less demanding. However for a more accurate representation, an all-electron calculation is preferred. Furthermore, the nuclear charge contributes to the electron beam deviation as clearly visible from the positive charge density discussed above. Finally experimental parameters like the finite size of the probe need to be taken into account for a quantitative comparison.

Multi-slice 4D-STEM simulations For a better understanding of the recorded field and charge density maps, before directly compare the experimental results and the pure theoretical calculations, 4D-STEM simulations have been performed using a multi-slice algorithm, as implemented in the open-source code abTEM code [136]. abTEM is a python package used for the simulation of (S)TEM images or diffraction patterns using a multislice algorithm, which consists in dividing the specimen electrostatic potential into thin slices along the beam propagation direction (which by abTEM convention is the z axis). Scattering is then calculated by alternating so-called phase object transmission through each slice with propagation of the wave to the next. TEM simulation method, as detailed in Section 2.3, use by default an IAM potential. abTEM, instead, has been designed explicitly for ab initio potentials, and give the possibility of merging DFT and other atomistic modeling methods with electron scattering simulations, providing a much easier way of performing TEM simulations with an ab initio description of bonding.

In this thesis, abTEM has been used to simulate the CBED patterns generated by an *h*–BN monolayer, where the potential used for the multislice algorithm is the Coulomb potential obtained from an all electron full-potential DFT calculation, for the reasons just explained. Importantly, abTEM gives also the possibility of setting different parameters to reproduce the experimental condition, as convergence angle, acceleration voltage, defocus and spherical aberrations of the electron probe. Once the CBED patterns are generated, the CoM shift along the x and y direction has been evaluated in the same way as done for the experimental measurements.

Fig. 3.10.e,h show the electric field obtained from the simulated CoM and the respective charge density map derived from the Poisson relation. Blue points in Fig. 3.10.f,i correspond to the profile of the electric field and charge density obtained from equivalent directions passing through the hexagons diagonals. Different profiles have been overlapped in the figure after realigning them minimizing the cross correlation function. These experimental values match excellently with the simulated profiles represented by the orange lines. From a comparison with the HAADF image, one can see that the electric field vanishes

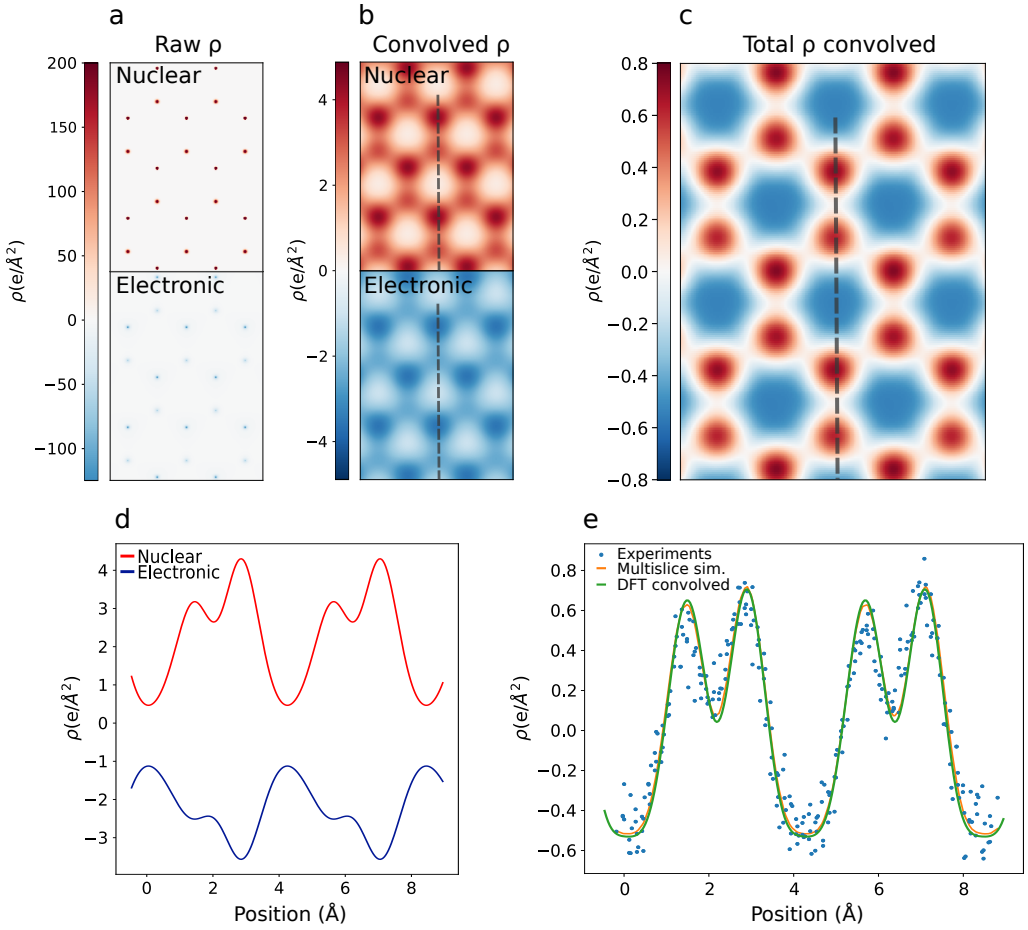

Figure 3.11: *(a) Nuclear and electronic charge density maps derived form DFT simulations .(b) Nuclear and electronic charge densities convolved with the electron-probe function. (c) Theoretical total charge density derived from the sum of nuclear and electronic component in (b). (d) Theoretical nuclear and electron charge density profiles. (e) Experimental total charge density profile (points) overlapped with theoretical values obtained from multi-slice simulations and DFT convoluted data.*

at the atom and hexagons centers (marked with X in the image), which are high symmetry positions, and at a point within the B-N bonds closer to the B atom than the N atom position (marked with a triangle).

Despite these results represent a significant improvement in respect to conventional TEM imaging, a more quantitative analysis of 4D-STEM derived charge density maps could permit to gather insights on charge re-distribution phenomena. As described in Section 2.3, charge transfer from the polarity of the B-N bond has been inferred using various phase imaging techniques like HRTEM or electron ptychography [8, 87]. Indeed, these studies have shown that a bet-

ter agreement between experimental data and multi-slice image simulations of a *h*–BN monolayer are achieved when employing potentials derived from DFT simulations instead of the independent atomic models (IAM), on which no ionicity is included. Although promising qualitative results have been obtained, there are significant limitations with regard to quantitative measurements of the charge.

On the other side, 4D-STEM offers quantitative insights into the total charge density, but the obtained result is affected by the finite size of the electron probe. Moreover, the charge redistribution primarily involves valence electrons, which represent only a portion of the total charge density. To accurately determine the pertinent total electron charge density, it is essential to correctly estimate the nuclear contribution, which must be subtracted from the measured total charge density map.

From the theory side, the electronic charge density can be derived directly from all electron DFT calculations, while nuclear charges can be constructed as delta functions centered at the atoms positions and normalized to their atomic number (Fig. 3.11.a). Finite probe size effects can be further included convolving the charge density by the electron probe function. These convoluted electronic and nuclear charge density maps are reported in Fig. 3.11.b together with their respective line profiles in Fig 3.11.d. The total charge density map presented in Fig. 3.11.c has been obtained as a sum of these two contributions.

Fig. 3.11.e shows the profile obtained along the dashed line of Fig. 3.11.c overlapped with the experimental data (points) and the multi-slice simulation. The best agreement with the experiments is obtained for the multi-slice simulation but the convoluted charge density presents only minor differences and therefore

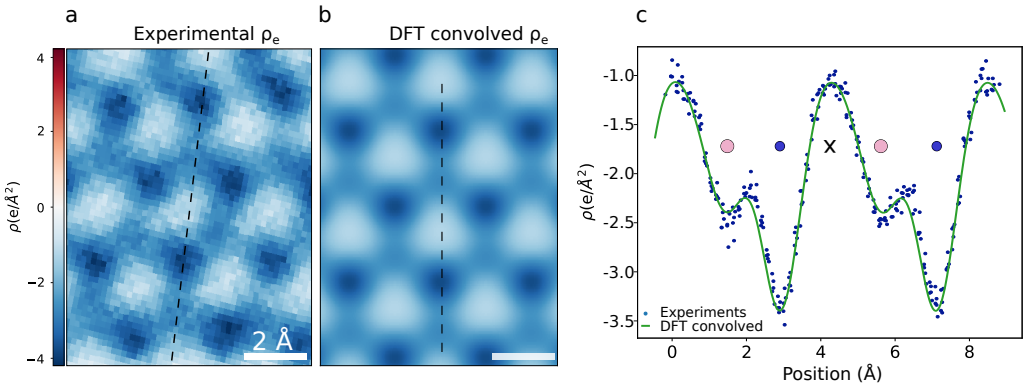

Figure 3.12: *(a) Experimental electron charge density map obtained after substracting the nuclear component from the measured total charge density. (b) Electronic charge density directly derived form DFT calculation convolved with the electron-probe function .(c) Experimental and DFT convoluted electron density profile.*

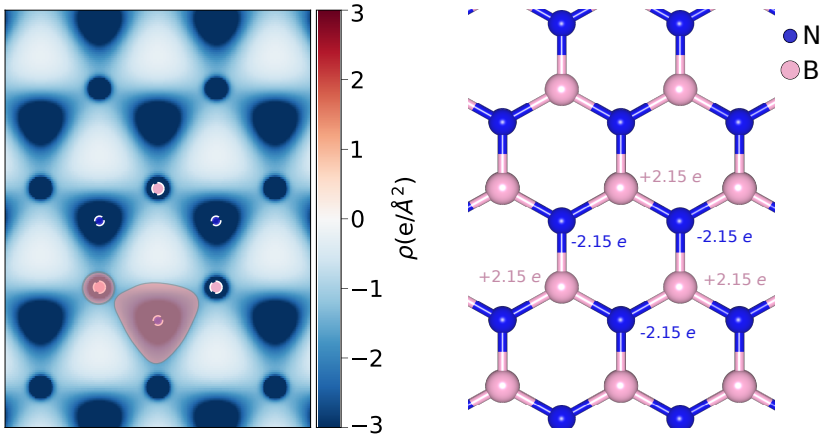

Figure 3.13: *Bader charges analysis applied to h–BN monolayer. (a) 2D representation of integration area for the nitrogen and boron atoms, (b) integrated electron charge transfer with respect to the nominal electron numbers.*

.

it can still be considered as a fair representation of the physical situation. This step ensures the adequacy of the constructed nuclear contribution.

Once this is verified, it is legitimate to subtract a similar nuclear charge density contribution from the experimental 4D-STEM total charge density map (Fig. 3.10.g). Possible drift effects can be taken into account using the atom position derived from the HAADF image. The retrieved experimental electron charge density is reported in Fig. 3.12.a, while in Fig. 3.12.b is reported the electronic charge density as derived from DFT calculations and convoluted by the probe function. The profile presented in Fig. 3.12.c shows once more an excellent quantitative agreement between theoretical and experimental results.

Charge density integration In order to estimate the charge transfer between nitrogen and boron atoms it is necessary to integrate the electron charge density map within an appropriate volume. Within the theoretical framework, one of the frequently employed techniques for charge integration is the well-established Bader charge analysis [137]. This method involves the three-dimensional integration of the charge density distribution, where the integration basins are determined by the local minima within the charge density distribution. This approach is highly accurate, providing a clear and localized partitioning of charges.

Fig. 3.13.a is a two-dimensional representation of the Bader charge integration method, where the red areas represent the integration basins for the nitrogen and boron atoms, showing the strong difference between the two areas. In the case of *h*–BN, the integration volume for nitrogen is found to be 2.3 times larger

than that for boron, reflecting the localization of bond electrons in proximity to nitrogen. The application of this integration method applied to the DFT electron charge density provides a charge transfer of about 2.15 e^- from boron to nitrogen (0.7 e^- per bond), in perfect agreement with previous similar studies [5–7, 123]. It is important to note that this method is primarily applicable to theoretical calculations as it is based on a partition of the volumetric data in three dimensions. Moreover, integration basins are delimited by zero gradient surfaces of the charge distribution, making it challenging to apply the technique to experimental data with a low signal-to-noise ratio.

Another viable approach is the Voronoi tessellation, which can be straightforward applied to experimental images which are confined to two dimensions. Moreover, since this method relies solely on a pure geometrical construction, a reduced SNR does not impose any limitations, making it a robust and reliable technique for analyzing the charge distribution in the system. In the case of the *h*–BN hexagonal lattice the integration areas for both nitrogen and boron are equilateral triangles of the same surface (Fig. 3.15.a). It is worth noticing that this partition will lead to a slight over-estimation of the electron charge at the boron site and a related under-estimation at the nitrogen site. Nevertheless the simplicity of this method permits an easy understanding of the effect of the probe size on the apparent charge at boron and nitrogen sites.

When considering probe sizes effects, it is convenient to employ a simplified probe function model where the probe dimension is defined by a single parameter. A suitable choice is to use Gaussian functions, as they exhibit only marginal differences at the tails in respect to a more complex probe model. In Fig. 3.14 are presented charge density maps of monolayer *h*–BN and respective profiles obtained by convoluting the DFT charge density using different probe function models. In Fig. 3.14.a a coherent probe solely defined by a convergence angle of 33 mrad, corresponding to the experimental value, has been employed. The resulting spatial resolution significantly exceeds the actual experimental resolution, underscoring the importance of considering additional parameters such as source demagnetization, incoherent effects, or thermal motion blurring. These effects were incorporated by applying to the probe function an additional 35 pm Gaussian blur, which permits an optimal alignment with the observed atom decay in the charge density map and HAADF images. In Fig. 3.14.c has been employed a more simple Gaussian probe model with a Full Width at Half Maximum (FWHM) of 1.15 Å. In respect to previous case, the convoluted charge density presents only minor differences at the local minima and therefore it can still be considered as a fair representation of the physical situation.

Fig. 3.15.b-d represent DFT electron charge density maps convoluted with Gaussian functions of different sizes, which are used to simulate electron probe size effects. In Fig. 3.15.e are then reported the integrated apparent electron

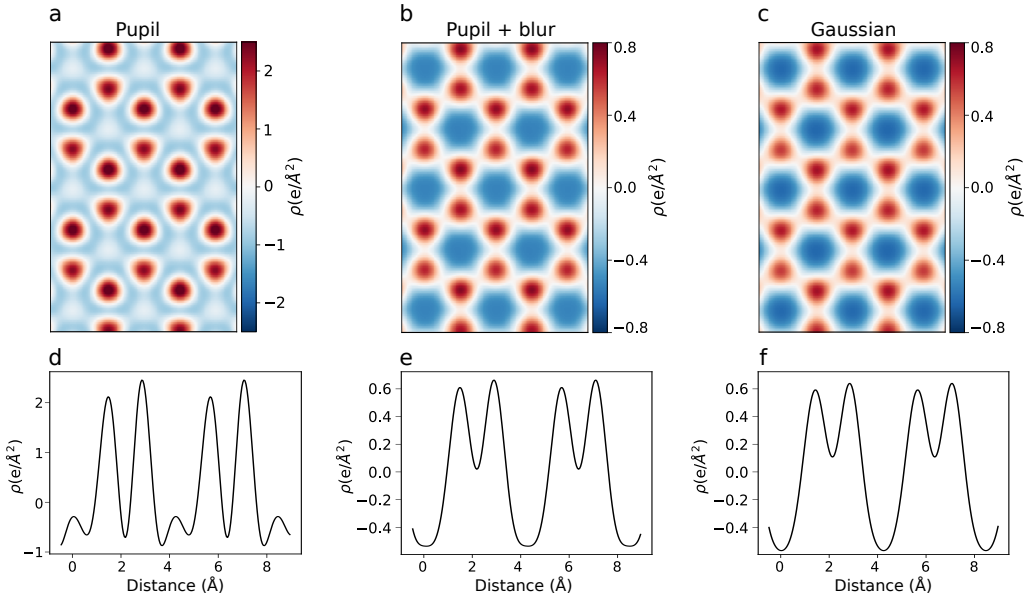

Figure 3.14: *Charge density maps convoluted by convoluting the DFT charge density using a probe function model (a) solely defined by a 33 mrad pupil, (b) the same function on which an additional Gaussian blurring has been added, (c) a simple Gaussian function.*

charges as a function of the probe size. In the ideal case of tiny probes the integrated electron charges at the nitrogen and boron site are approximately 7.45 e^- and 4.55 e^- respectively. These values indicate a charge transfer from boron to nitrogen of approximately 0.45 e^- (a significantly smaller estimation compared to the 2.15 e^- obtained from the Bader analysis on the volumetric DFT, due to the difference in the integration area), resulting in a bond ionicity of approximately 0.9 e^-. Both values progressively converge towards an average value of 6.0 e^- when the probe size is increased. For probe sizes above 1.1 Å, no bond ionicity can be detected. This can be attributed to the probe broadening effect, which is in this case only slightly smaller than the bond length. The same integration method has been applied to the nuclear charge density (Fig. 3.15.f-i). In this case charges are more localized and broadening effects become relevant for larger electron probes, approximately above 0.7 Å. When the total charge is considered (Fig. 3.15.j-m), the system exhibits an intrinsic charge imbalance of 0.9 e^- between boron and nitrogen sites. As the probe size increases, this values progressively decreases and for probe sizes exceeding 1 Å, the total charge results the same for the two sites. This can be attributed to the probe broadening effect, which is in this case only slightly smaller than the bond length.

The experimental conditions employed here correspond to a probe size, defined as the full-width-half-maximum of the probe function, of approximately

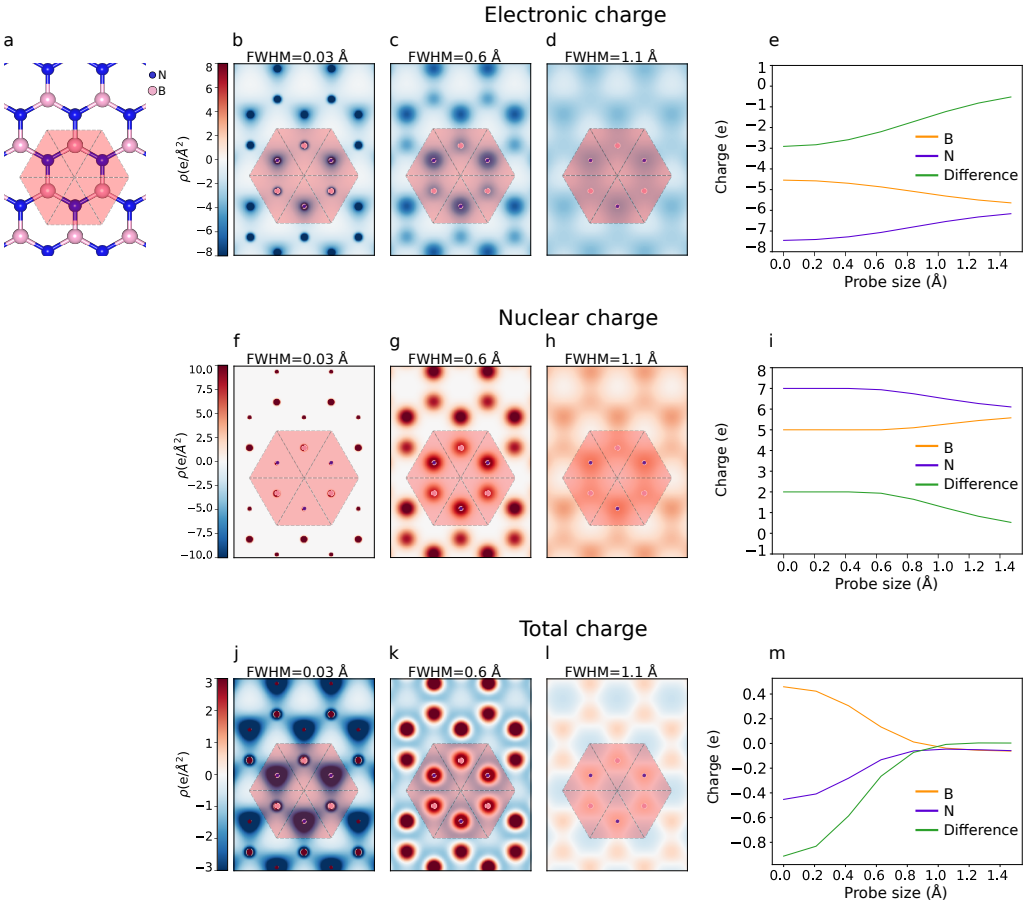

Figure 3.15: *(a) Voronoi partitioning of space for h–BN, (b-d) Voronoi integrations for electron charge density directly derived from DFT, and convoluted for probe sizes of 0.6 and 1.1 Å. (d) Integrated electron charges as a function of the probe size. (f-h) Voronoi integration for nuclear charge density as directly derived from DFT and convoluted for a probe size of 0.6 and 1.1 Å. (i) Integrated nuclear charges as a function of the probe size. (j-l) Voronoi integration for total charge density derived form the sum of the respective nuclear and electron contributions. (m) Integrated total charge density as a function of the probe size.*

1.15 Å, and charge transfer cannot be directly derived from the experimental measurements using the Voronoi method. However, the excellent agreement between the experimental and theoretical electron charge density distribution, once broadening effects are taken into account (Fig. 3.11.g and Fig. 3.11.b,d), shows that the experimental measurements can provide a solid validation of the theoretical estimations. While 4D-STEM measurements alone can not precisely quantify charge transfer effects at the probe size scale, this information can be retrieve via a thoughtful combination of experiments and first principle simulations.

3.5. *h*–BN zig-zag edge

h–BN is recognized as an electron beam-sensitive material, and point and extended defects can easily appear under standard illumination condition [28]. Previous studies have investigated the minimal energy threshold required to induce a knock-on effect, typically resulting in the ejection of one of the boron atoms from the material. This energy threshold resulted to be higher than 60 keV, coinciding with the operating energy of the microscope used for the measurements presented in this thesis. However, in a more recent study it has been shown that atom removal occurs even at such low acceleration voltages as a result of electron beam induced chemical etching in limited vacuum conditions [134]. It is not uncommon for the initial ejection of boron atoms to trigger a chain of reactions, leading to the expansion of generated holes and the formation of larger triangular shapes [133, 138, 139]. Extensive studies using various transmission electron microscopy techniques have consistently revealed that edges so formed predominantly exhibit a nitrogen-terminated zig-zag configuration [138, 140].

As outlined in Section 3.1, in their work of Cretu et al. observed a stronger deflections in DPC images at *h*–BN edge compared to the bulk, which has been estimated of ca 60%. This behavior has been associated to an enhancement of the electric field due to surface effects, which are assumed to be very strong in *h*–BN because of its ionicity. Similar results have been obtained for other 2D materials, like graphene, WS_2 and MoS_2 [116, 117, 135], where however the surface effects are not expected to be that strong. With the aim of understanding what is witnessed in the experimental measurements related to the electric field ad edge and to study charge transfer phenomena, we performed 4D-STEM measurements on nitrogen terminating zig-zag edges.

Electric field baseline

Fig. 3.16.a is the HAADF view of an *h*–BN monolayer void, where a zig-zag edge can be easily recognized. Fig. 3.16.b represents the associated 4D-STEM derived electric field amplitude where the high frequency noise has been filtered

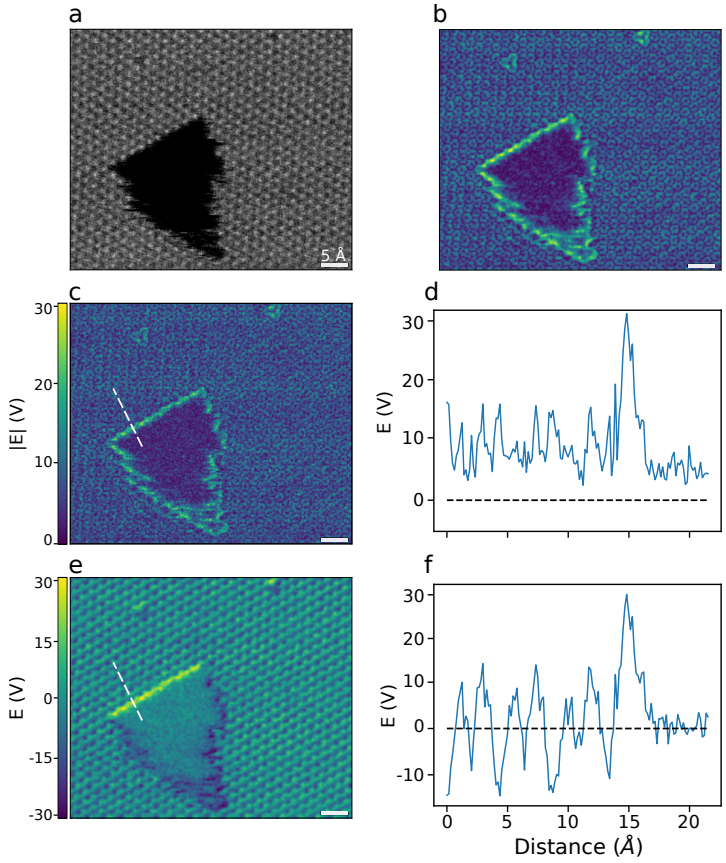

Figure 3.16: *(a) HAADF image of a void on an h-BN monolayer. (b) CoM derived module of the electric field where high frequency noise has been filtered out and (c) corresponding raw data. The white line orthogonal to the zigzag edge represent the path from which has been extracted the profile represented in (d). (e) Map of the electric field component orthogonal to the edge and (f) associated line profile.*

out, while Fig.3.16.c is the original unfiltered map, where the white line indicate the path from which the amplitude profile in Fig. 3.16.d has been extracted. The average value in the vacuum region, in Fig. 3.16.d, is about 5 V and thereby indicating an edge step of approximately 25 V. Most of previous works related to the study of electric field at the edges presented similar results, only showing and commenting the profile of the COM shift's modulus [84, 116, 124, 135]. However, the vacuum region average modulus corresponds to the noise amplitude and therefore it can not provide a correct estimation of baseline and may lead to inaccurate estimations. In Fig. 3.16.c is reported instead the CoM component orthogonal to the edge and in Fig. 3.16.d the corresponding profile. Here the baseline can be correctly estimated at 0 V and the step at the edge results about 30 V. As a consequence, performing the profile of the CoM's components along

the desired direction allows as well to determine the atoms position in a better way with respect to the modulus, since they correspond to the distance values where the field vanishes, as shown for the pristine *h*–BN monolayer in Fig. 3.10.

Electric field enhancement as a function of the probe size

In Fig. 3.17.a is presented the HAADF image of the N-terminated *h*–BN zigzag edge reported in Fig. 3.16.a, and in 3.17.b the 4D-STEM derived magnitude of the electric field; for greater clarity high frequency noise has been filtered out in the image but all processing was carried out on the raw data. In agreement with the previous works [116, 124, 135], the profile of the apparent electric field across the edge (Fig. 3.17.c) is strongly enhanced at the edge step. However, to correctly interpret this experimental observation, a comprehensive study regarding the effect of the electron probe size is necessary. To perform such study, the projected electric field has been evaluated starting from a DFT derived potential, and has been convolved with Gaussain functions of different FWHM, to simulate the effect of the incident electron probe size.

For small probe sizes (e.g. 3 pm in Fig.3.19.d), the electric field maxima at the edge are barely distinguishable from the bulk values. High electric fields are generated in proximity to the atom centers, driven by the elevated nuclear and core electron charge densities, while valence electrons, whose density may change at edges, contribute only minimally to the field far from the atoms. As the probe size increases(Fig.3.19.f-i), the difference between edge and bulk maxima becomes more pronounced, and the DFT simulation approaches closer to the experimental measurements. Indeed, the broadening effect essentially leads in an averaging of the electric field, which points in different directions across the illuminated area. This brings to a reduction in the resultant amplitude, but the effect is significantly less pronounced at the edge due to a reduction in symmetry. The apparent enhancement of the electric field at the edge discussed in the previous literature, can therefore be explained through the simple geometric arguments presented here.

Charges at the edge

While the probe finite size hinders a direct measurement of the surface field, charge accumulation can be precisely estimated when considering appropriate integration regions. In the previous section it has been shown that the ionicity of the B-N bond can not be correctly evaluated by 4D-STEM derived measurements due to the probe size, which is only slightly smaller than the bond length. However, surface charge effects can be discussed in terms of charge accumulation per formula unit at zigzag lines parallel to the edge instead of charges at the individual

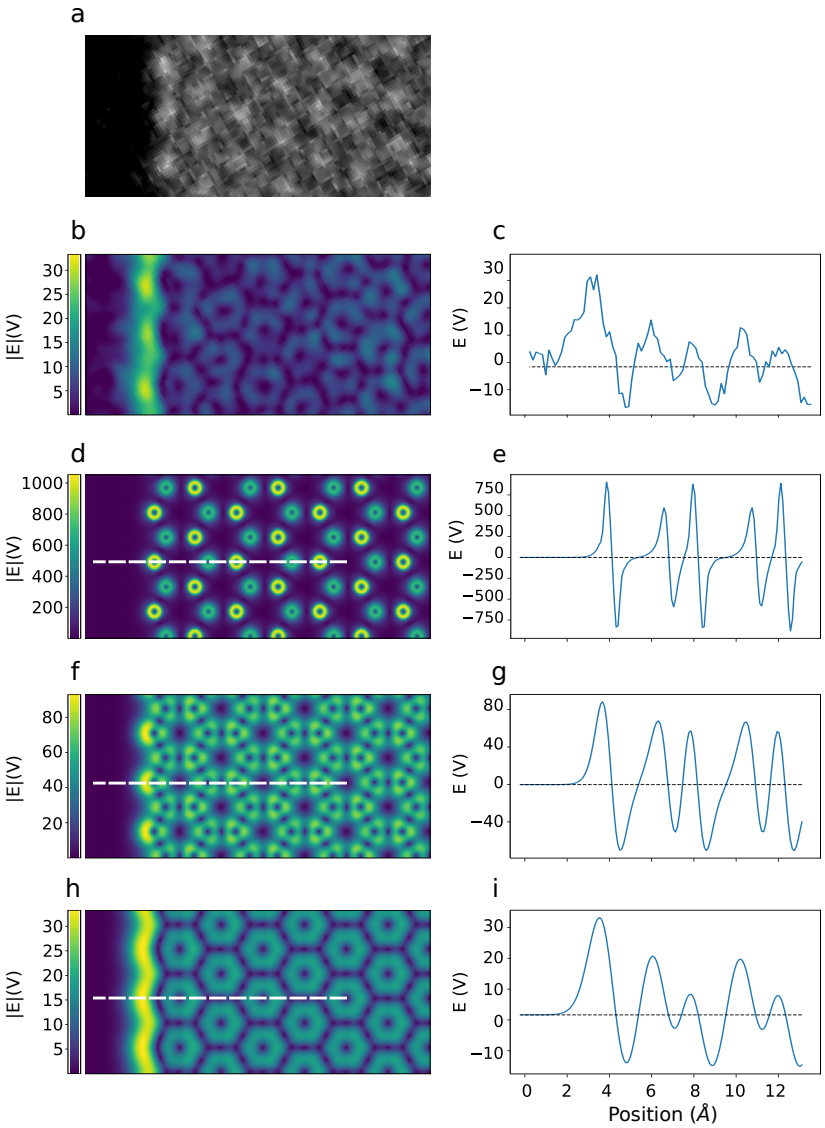

Figure 3.17: *(a) HAADF image of an N terminated BN edge and (b) corresponding electric field intensity map obtained from a synchronous 4D-stem acquisition. (c) Electric field profile. (d) DFT derived electric field obtained using a 0.03 Å Gaussian broadening, (e) DFT electric field profile. (f,g) and (h,i) DFT electric field intensities and profiles obtained using a broadening of 0.6 Å and 1.3 Å respectively.*

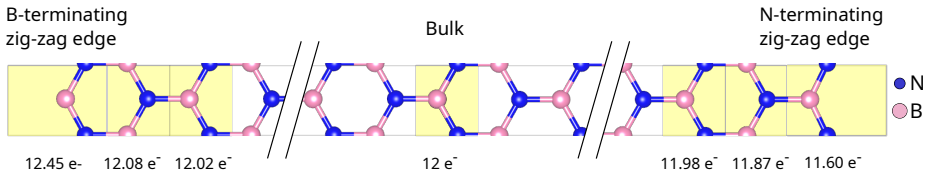

Figure 3.18: *DFT electron charge density of an h-BN nanoribbon integrated at different zig-zag lines parallel to the ribbon axis.*

atom level. Pertinent integration regions correspond therefore to stripes parallel to the surface having a width of 2.2 Å which is the distance between the center of the hexagons projected onto the direction orthogonal to the edge.

In Fig. 3.18 it is reported the integrated DFT electron charge obtained for different zig-zag stripes parallel to the edges of a 52 Å *h*–BN ribbon model. At the B terminated edge there is a charge accumulation of 0.55 e^- distributed over the first three zig-zag atomic lines. This charge is compensated by an equivalent hole accumulation at the nitrogen edge similarly distributed over three zigzag atomic lines. Using a truncation of the Coulomb interaction orthogonal to the edge helps prevent spurious interactions between charges at the edges in the vacuum region.

Fig. 3.19.a is the same HAADF image showed in Fig. 3.17.a, showing an N terminating *h*–BN zig-zag edge. Fig. 3.19.b is the experimental charge density derived from 4D-STEM measurements, and the integrated charge profile across the light yellow area is reported in Fig. 3.19.c. The charge values integrated for each window are reported on the top. In Fig. 3.19.d,e we report the DFT derived total charge density map and the corresponding integrated charge profile for an N-terminated zigzag edge obtained for a small broadening of 0.03 Å. The total charge at the first zig-zag line is 0.40 h^+ per formula unit which decreases to 0.13 h^+ per formula unit at the second line (where h^+ stands for a positive charge with the same magnitude as an electron's charge); all remaining lines have a total charge of 0. This indicates a charge neutrality in the bulk region and an electron depletion at the N-terminated edge. In our BN ribbon model this positive charge is compensated by equivalent negative charges located at the opposite B-terminated zigzag edge (see Fig. 3.18). These values, as expected, are invariant up to extended probe sizes (Fig. 3.19.f-i), reaching the experimental value of about 1.35 Å used for this acquisition.

When applying the same integration method to the experimental data we obtain an integrated charge of 0.37 h^+ per formula unit at the first zigzag row, 0.10 h^+ at the second row and no charge for all subsequent zigzag rows. The excellent agreement between the experimental measurements and theoretical estimates demonstrates the effective direct quantification by 4D-STEM of charge transfer effects. Additionally, with the support of DFT, the measured charge

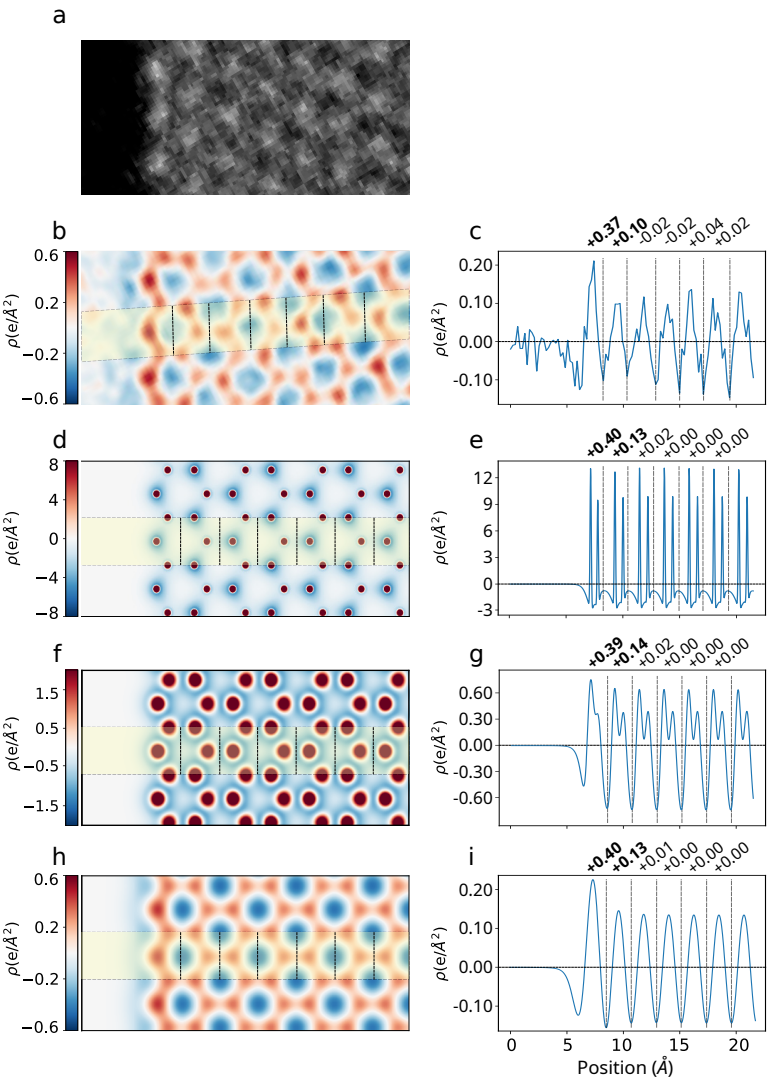

Figure 3.19: *(a) HAADF image of an N terminated BN edge. (b) 4D-STEM derived charge density map. (c) Charge density profile and integrated total charges (upper values) obtained from the shaded region in b. (d) DFT total charge density and (e) corresponding profile. (f,g) and (h,i) DFT charge densities obtained using a broadening of 0.6 Å and 1.3 Å respectively.*

difference can be attributed to the redistribution of valence electrons at the edge.

In Fig. 3.20, the electron, nuclear, and total charges are presented for the first zig-zag atomic line of an N-terminated h-BN ribbon, obtained as a function of the probe size. Unlikely the case of atomic charges discussed in the previous section, here the integrated values remain invariant up to large probe sizes of the same magnitude as the integration width (2.2 Å). The integrated nuclear charge

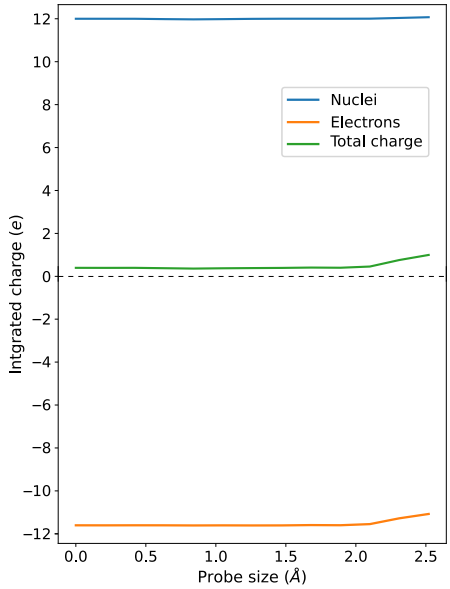

Figure 3.20: *Electron, nuclear and total charges obtained for the first zig-zag atomic line of an N-terminated h-BN ribbon as a function of the probe size.*

density is constantly 12 h^+ per formula unit independently from the distance from the edge and probe size confirming that the measured charge changes are purely electronic and do not arise from an incorrect evaluation of total nuclear charges.

Since the probe size used for this experimental measurements is estimated to be ca. 1.35 Å, the validity of this integration model should be granted.

Effect of second-order three-fold astigmatism

Until this moment, the effect of symmetric aberration, as the second-order three-fold astigmatism aberration, commonly referred to as $C_{2,3}$, has not been investigated in terms of quantification. Nevertheless, it has been reported that the effect of this aberration induces change in the charge density map [121]. Specifically, for WS_2 the intensity ratio between the tungsten atoms and the two solfurs column changes as a function of the $C_{2,3}$ value and its orientation with respect to the atomic structure, known as azimuthal angle. For these reasons we performed a similar study, with the focus on the N-terminated *h*–BN monolayer edge, where the effect of this aberration can be understood for both bulk and edge state. In Fig. 3.21.a is shown a probe function obtained considering a convergence angle of 33 mrad and an additional Gaussian broadening of 35 pm; in Fig. 3.21.b is given the corresponding convoluted total charge density map. The contrast in the probe image has been enhanced to highlight the first oscillation ring. In Fig. 3.21.c-h are presented probe functions and corresponding charge density

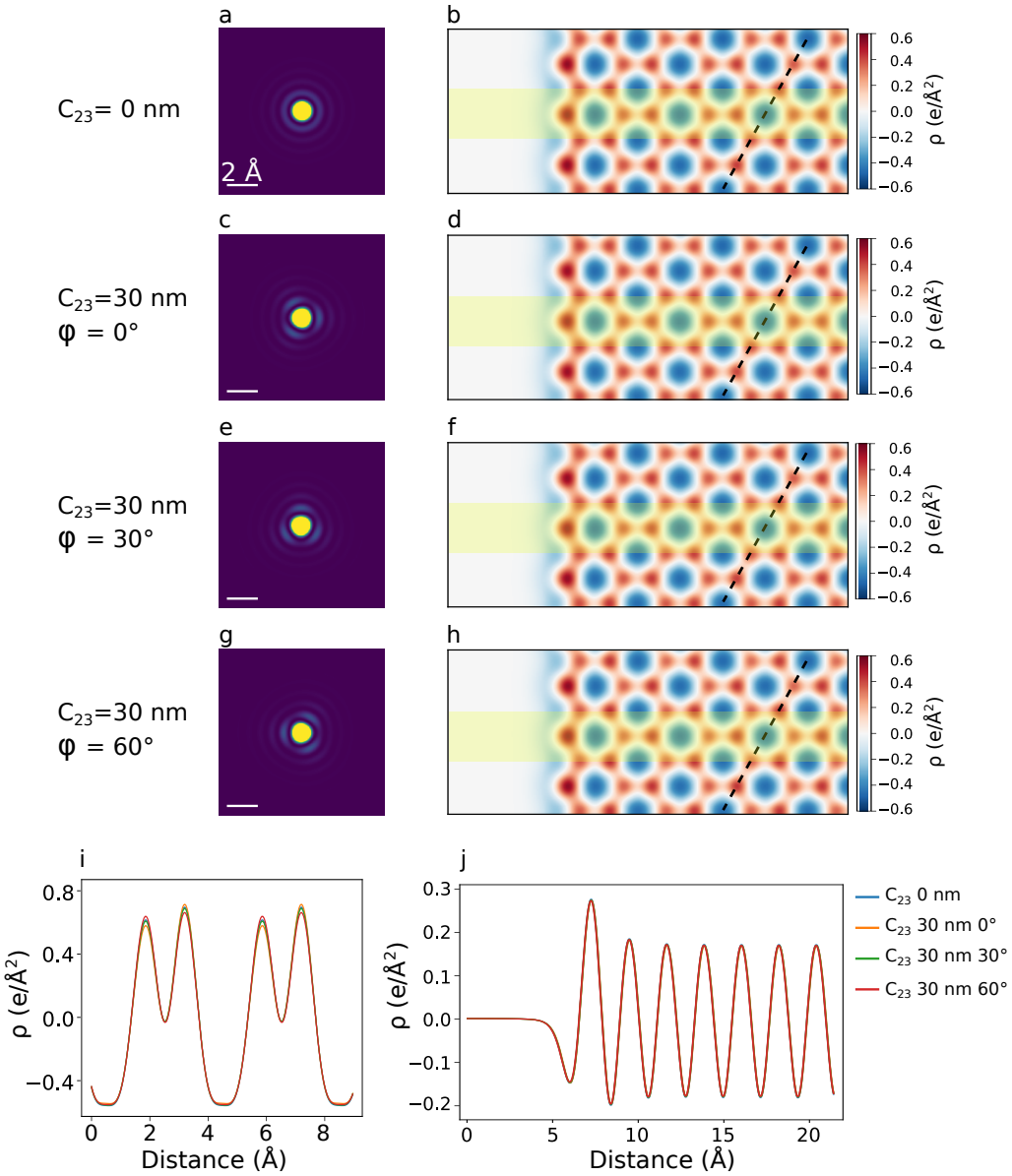

Figure 3.21: *(a) Probe function with no C_{23} and (b) corresponding probe convoluted total charge density map. (c-h) Probe functions and corresponding charge density maps obtained for C_{23}=30 nm and different azimuthal angles ϕ. (i) Charge density profiles obtained along the dashed lines indicated in the charge density maps. (j) Integrated charge density profiles obtained for the shadowed regions indicated in the charge density maps.*

maps obtained adding to the probe a second-order three-fold astigmatism (C_{23}) of 30 nm. This value has been decided because it corresponds to the minimum required precision for the aberration corrector of the microscope. The azimuthal angle ϕ is used to twist the probe shape in respect to the B-N bonds. The charge density profile presented in Fig. 3.21.i has been extracted from the dashed lines in the maps. A slight dependence of the charge density contrast between boron and nitrogen sites can be observed as a function of the aberration orientation. Figure 3.21.h shows the integrated charge density profile obtained for the shaded regions indicated in the charge density maps, also employed in the charge density analysis of the edge. Here there are no discernible differences between the aberration-free probe and the aberrant probes with different azimuthal angles.

Towards a quantitative analysis of charge transfer in 2D defective systems
The potential of 4D-STEM in measuring charge transfer phenomena at a very fine scale has been extensively discussed in the literature, but these speculations have not been supported by direct quantitative evidence. Previous studies have demonstrated strong modulations of the CoM at defective sites, but probe size effects have been largely neglected in linking measured CBED displacements to evaluated electric fields. Our results demonstrate that 4D-STEM is capable of directly measuring charge transfer phenomena with a sensitivity as low as a fraction of an electron and a spatial resolution on the order of lattice distances. This performance was achieved through a meticulous analysis of probe size effects, connecting experimental observations with first-principle simulations. The critical integration distance beyond which probe size effects result in an inaccurate evaluation of the charges is approximately twice the size of the electron beam probe. This limitation prevents the direct measurement of charges at the individual atomic scale using current STEM technologies. However, other phenomena occurring at a slightly larger scale, such as charge accumulation at defective sites, can in principle be accessible. For this purpose, 2D materials serve as an ideal testing ground, as the complex propagation of the electron probe within the material can be significantly simplified. Nevertheless, studying charge transfers in transition metal compounds might be challenging due to the high number of core electrons that dominate the signal detected by 4D-STEM. Instead, we can reasonably assume that charge quantification by 4D-STEM will find its primary domain of application in the study of charge redistribution in light-element systems such as boron-nitride-based nanostructures.

Further quantitative study may involve 4D-STEM measurements for the analysis of other line and point defects, as other edges, adatoms and vacancies. However, as done for the study of charge accumulation in zig-zag edge, for these analyses preliminary theoretical studies are necessary to define the appropriate

integration regions. Nevertheless, even in absence of theoretical expectations, qualitative analysis can still be performed as will be outlined in the next section.

3.6. 4D-STEM at point defects in *h*–BN

As just outlined in the previous sections, point defects in *h*–BN may alter the charge density distribution, which may translate in a local change of reactivity, or optical characteristics. It becomes then essential to have a straightforward means of pinpointing their location and nature. While STEM has indeed achieved sub-atomic scale resolution, it still faces limitations in certain structural determinations. As explained in Section 2.2, HAADF images contrast is circa proportional to Z^2, meaning that for elements where the atomic number ratio is high a stronger contrast is expected. The most common *h*–BN stacking order is the AA′, where there is the superposition of N and B atoms from one layer to the other, which minimize the contrast in the HAADF image for multilayered *h*–BN flakes. This complicates the localization and determination of different point defect which may be present in the sample, as adatoms and monovacancies. While for instance a vacancy can still be imaged in two or three layered flakes, it might be hard to discriminate its chemical nature. Exploring the CoM maps has already proved to give more structural information when compared to conventional STEM imaging techniques, as discussed in the case of 2D materials in Section 3.1. Other than reflecting the symmetry of a point defect, which is useful for the determination of the adatom or vacancy structure, the apparent signal enhancement in CoM images, due to spurious effects coming from the probe-material interaction, can be used for their easier localization in a system where the standard HAADF image contrast may not be sufficient.

In this section, I will present 4D-STEM measurements for structural determination, focusing on distinct point defects: silicon and calcium ad-atoms and boron monovacancies.

Adatoms: structural information beyond conventional TEM techniques

Fig. 3.22.a shows an HAADF image of a large *h*–BN region, where other than amorphous carbon, depicted by the gray cloud, there is the presence of heavier atoms, as showed by brightest spots in the image. For the determination of the chemical nature of the adatoms, an EELS hyperspectral imaging has been performed on the sample's region indicated by the red square in Fig. 3.22.a. Obtaining accurate measurements of the ELNES fine structures can be challenging, primarily due to adatoms displacements when exposed to the electron beam. This behavior is attributed to the fact that, unlike dopants or lattice-implanted

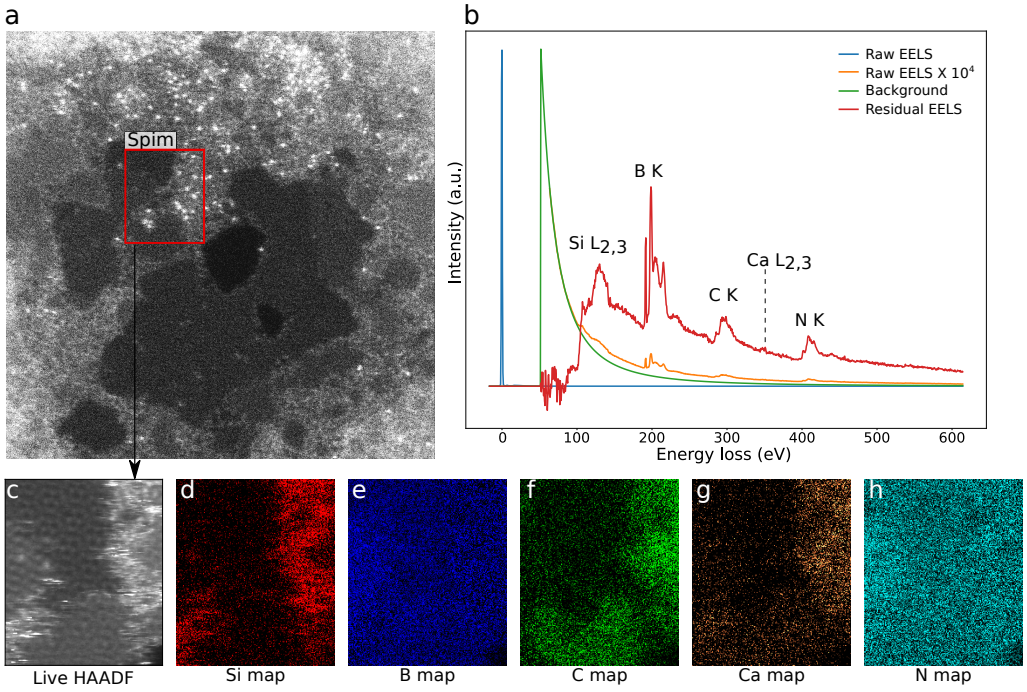

Figure 3.22: *(a) HAADF image of a multilayered contaminated h–BN flake. (b) Sum of the EELS spectra derived from the hyperspectral image performed in the red area in (a), showing the presence of different core absorption edges. (c) HAADF image simultaneously acquired with the EELS spectra. (d-h) Filtered images integrating the silicon, boron, carbon, calcium and nitrogen absorption edge peak respectively.*

species, adatoms are only weakly bonded and therefore they are highly mobile at the *h*–BN basal plane. The spectrum shown in Fig. 3.22.b represents the sum of all the EELS spectra within the hyperspectral image. Distinct absorption edges are observed, corresponding to silicon, boron, carbon, nitrogen, and calcium atomic species. Fig. 3.22.c is the HAADF image simultaneously acquired with the EELS spectra, while Fig. 3.22.d-h are the chemical maps of the respective atomic species, obtained by integrating the corresponding core absorption edges in the hyperspectral image. Fig. 3.22.e,h reveal an homogeneous presence of both boron and nitrogen throughout the area. Carbon (Fig. 3.22.f) is instead primarily concentrated within the region corresponding to the gray area observed in the HAADF image (Fig. 3.22.c), while silicon (Fig. 3.22.d) and calcium (Fig. 3.22.g) exhibit prominent localization where the brightest spots appear in the dark field image. This observation could potentially be attributed to residual contamination coming from the glassware used in the transfer procedure discussed in Section 3.3.

Other than identifying the chemical species of the adatoms, it is important to

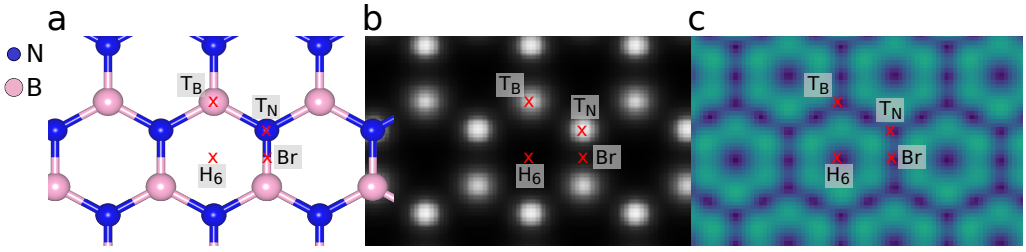

Figure 3.23: *(a) Schematic representation of the adatoms position for h–BN: on top of the boron or nitrogen atoms (T_b, T_N), in a bridge position between the two atoms (Br) or at the center of the hexagons, usually referred to as hollow position (H_6). (b) h–BN potential, showing that the adatoms position are at the local minima or maxima of the atomic potential, (c) corresponding to the zero values of the electric field.*

determine their precise structural configuration, i.e. the *h*–BN site where they are placed. In general, there are limited stable positions for the adsorption sites, which are determined by the local minima of the total potential of the system, which correspond to the positions where the electric field vanishes, typically at high symmetry points. Fig. 3.23.a presents the atomic model of an *h*–BN monolayer, while in Fig. 3.23.b,c are reported the total projected potential and the derived projected electric field. Four potential different adsorption sites can be distinguished: on top of the atomic sites (T_N and T_B), in a position between boron and nitrogen, which is commonly denoted as bridge position (Br) and at the center of the hexagons (H_6). While determining the precise position of adatoms can be challenging using conventional STEM imaging modes for the aforementioned issues, exploring the electric field generated by adatoms could potentially offer a more straightforward means of identifying their sites, as the symmetry of the electric field reflects that of the structure. This approach has been demonstrated successful in a prior study on graphene [116].

The electric field generated by an adatom adsorbed at the T_N, T_B or hollow sites should maintain a three axes symmetry, relative to the point symmetry group they pertain C_{3v}, while those associated to an adatom adsorbed at the Br site should present the C_s symmetry. Examining the electric field's shape and orientation would then allow for an easier identification of the adatom.

Figure 3.24.a displays the HAADF image acquired on the same *h*–BN few layered flake showed in Fig. 3.22.a, revealing the presence of multiple adatoms as indicated by the bright spots. Figures 3.24.b and 3.24.c illustrate the electric field modulus and orientation, respectively. The two types of adatoms are indicated by the pink and red arrows in Fig. 3.24.a-c. These zones are then magnified in Fig. 3.24.e,f. The electric field shape of the adatom reported in Fig. 3.24.e presents a similarly C_{3v} symmetry, meaning that, in principle, it is an on top adatom. To determine if it is on top of the nitrogen or the boron atom, the charge density map

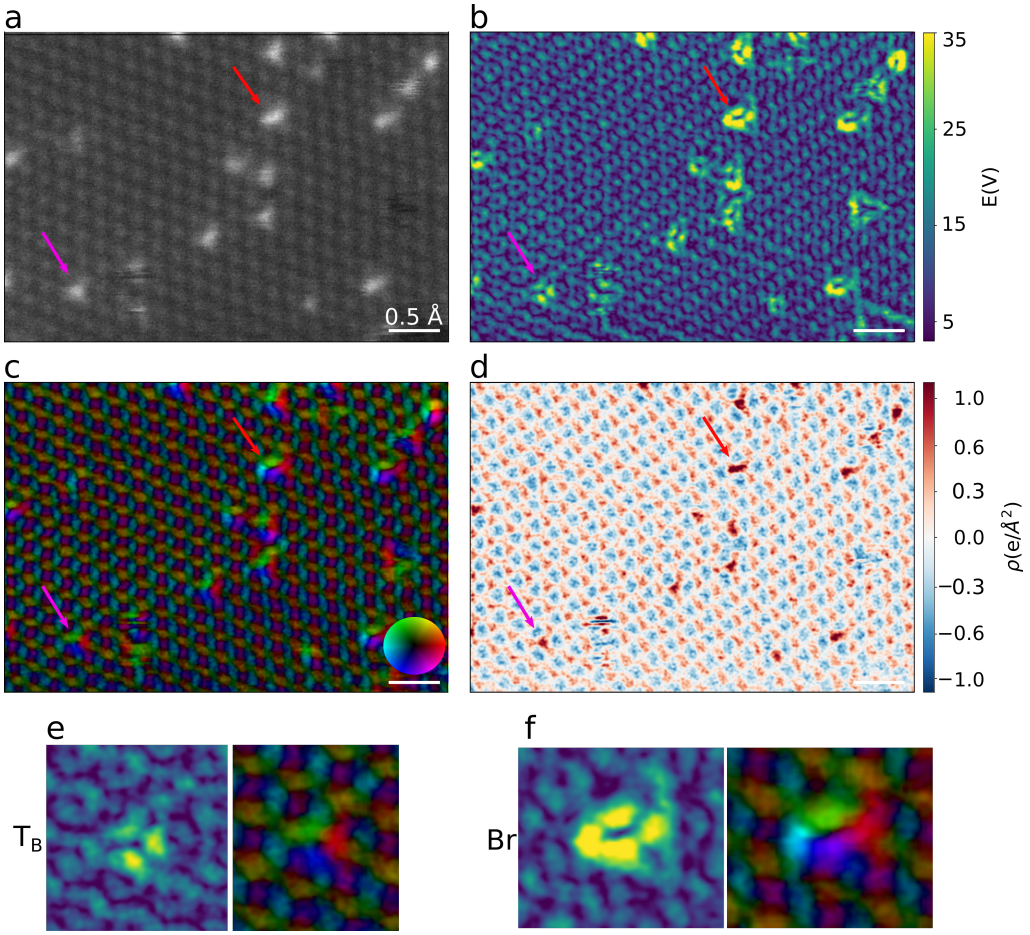

Figure 3.24: *(a) HAADF image of a multilayered h–BN showing the presence of heavy adatoms. (b,c) 4D-STEM derived electric field modulus and orientation respectively and (c) the derived charge density. Zoomed electric field modulus and orientation for (e) an adatom on top of a boron atom and (f) in a bridge position.*

image is then useful, demonstrating in this case that is an T_B site. It is important to mention that for *h*–BN flakes characterized by an even number of layer in a AA′ stacking configuration, where atoms of boron and nitrogen are alternately overlapped, the HAADF and charge density contrast is expected to be the same for the all the atomic columns. In this situation, the determination as T_B or T_N would probably not be possible.

The electric field's shape in Fig. 3.24.f, presents instead a rather C_s symmetry, demonstrating that it is an adatom in the bridge position. This deduction is supported by the corresponding charge density map shown in Figure 3.24.d, which present in general an improved contrast and resolution when compared to the HAADF image of Fig. 3.24.a.

Nevertheless, it is important to keep in mind that in both cases the reference symmetry is rather assumed, as no theoretical calculations have been conducted to support the experimental findings, and there are no prior works reported on *h*–BN in this particular context. Another aspect worth noting is that, in some instances, the symmetry is not completely intact. This imperfection may arise from scan distortions and the inherent noise present in all measurements. However, an alternative explanation could derive from a slightly displaced localization of the adatoms with respect to the expected high symmetry points, which might alter the shape of the electric field. In this context, exploring the electric field could provide additional insights into the structures of the adatoms. While confirming this modification of the electric field due to adatom displacement would require further DFT simulations, it does offer intriguing possibilities for future research endeavors regarding the anticipated symmetry.

Directing our focus to the intrinsic electrostatic properties, it is noteworthy that both the electric field and charge density exhibit heightened intensity precisely at the adatoms positions. This outcome aligns with intuition, given the heavier nature of these atoms compared to boron and nitrogen, thereby yielding an augmented charge density. In regard to the electric field orientation, a consistent outward orientation is observed for all the adatoms. This signifies that the electric field extends outward from the atoms, in alignment with expectations.

In conclusion, from experimental observations it appears that the two adatoms sites, T_B and Br, are the preferred choices for adatoms in *h*–BN. This determination has been largely influenced by the symmetry of the electric field produced by the adatoms, which is a more direct and simple way with respect to the study of the HAADF image, especially when the latter is of poor quality. Next steps regarding this study include DFT calculations to support these experimental findings.

Vacancies: an improved contrast and direct localization

Identifying structural defects such as mono vacancies could prove challenging beyond the monolayer case due to a general reduced contrast between the atomic columns and the center of the hexagons. Given the heightened sensitivity of 4D-STEM analysis to even subtle structural alterations and the increase of CoM intensity in presence of defects, this approach proves intriguing for the precise localization and identification of vacancies. In particular, boron monovacancies present as well a C_{3v} symmetry, which is expected to be found also in the electric field's modulus shape.

Fig. 3.25.a displays the HAADF image of a multilayer *h*–BN, revealing that with an increase of the number of layers, the contrast diminishes in comparison to the mono- or bi-layer scenarios. Conversely, the electric field image (Fig. 3.25.b) maintains a good contrast, and in the presence of vacancies, the electric

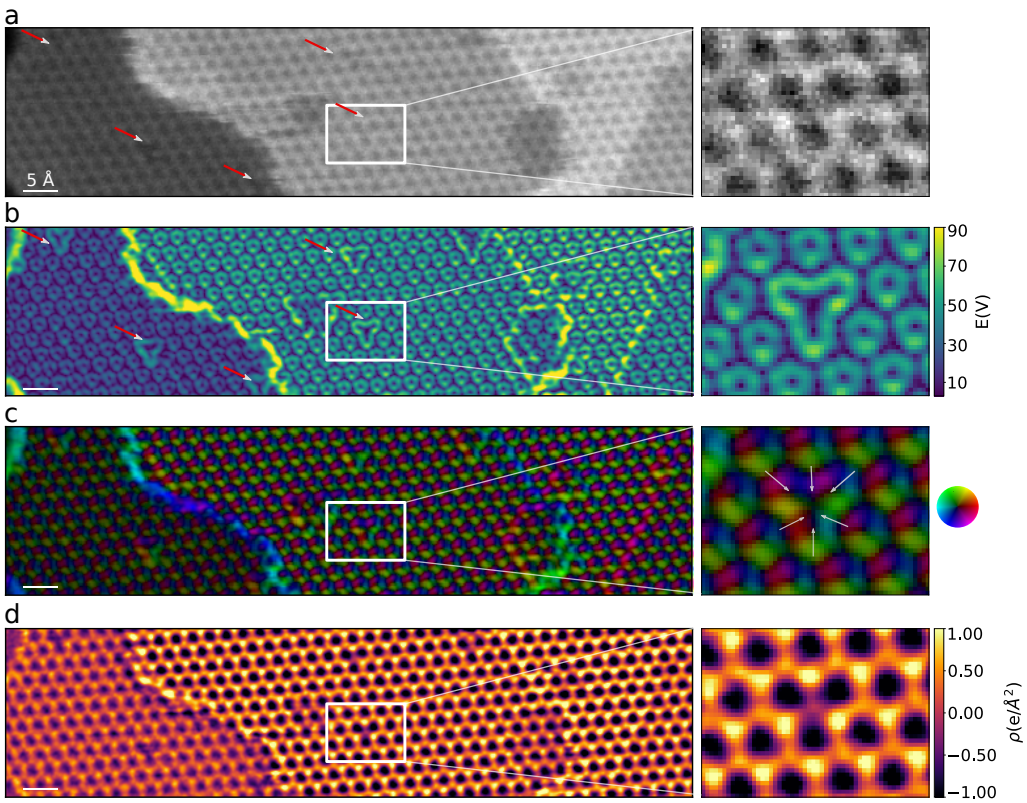

Figure 3.25: *(a) HAADF image of a multilayered h–BN flake. (b,c) 4D-STEM derived electric field modulus and orientation respectively, showing an enhanced contrast for the localization of boron monovacancies. (d) 4D-STEM derived charge density map.*

field intensity becomes more pronounced and adopts a distinctive triangular shape related to the C_{3v} point symmetry. Examining the orientation, reported in Fig. 3.25.c, reveals an inward pointing. Regarding the electric field intensity, there has been no investigation into whether it indeed signifies such higher reactivity at that site. However, similarly to the edge scenario, we believe that the enhancement is largely due to the probe size related effects. Nevertheless, as already outlined, while this spurious effect prevents from the quantitative analysis of the electric field in presence of a vacancy, it highlights its localization even in flakes made of more than three layers, overcoming the limits of HAADF images.

The charge density map in Fig. 3.25.d shows a reduction of positive charge in correspondence to the vacancy position, which is expected as due to the loss af a boron atom. However, quantitative information has not been achieved yet for this class of defects. This is mainly due to the difficulty in selecting an appropriate integration area. Despite being a point defect it is believed that the charge redistribution spreads on a larger area, which as shown for the pristine case is

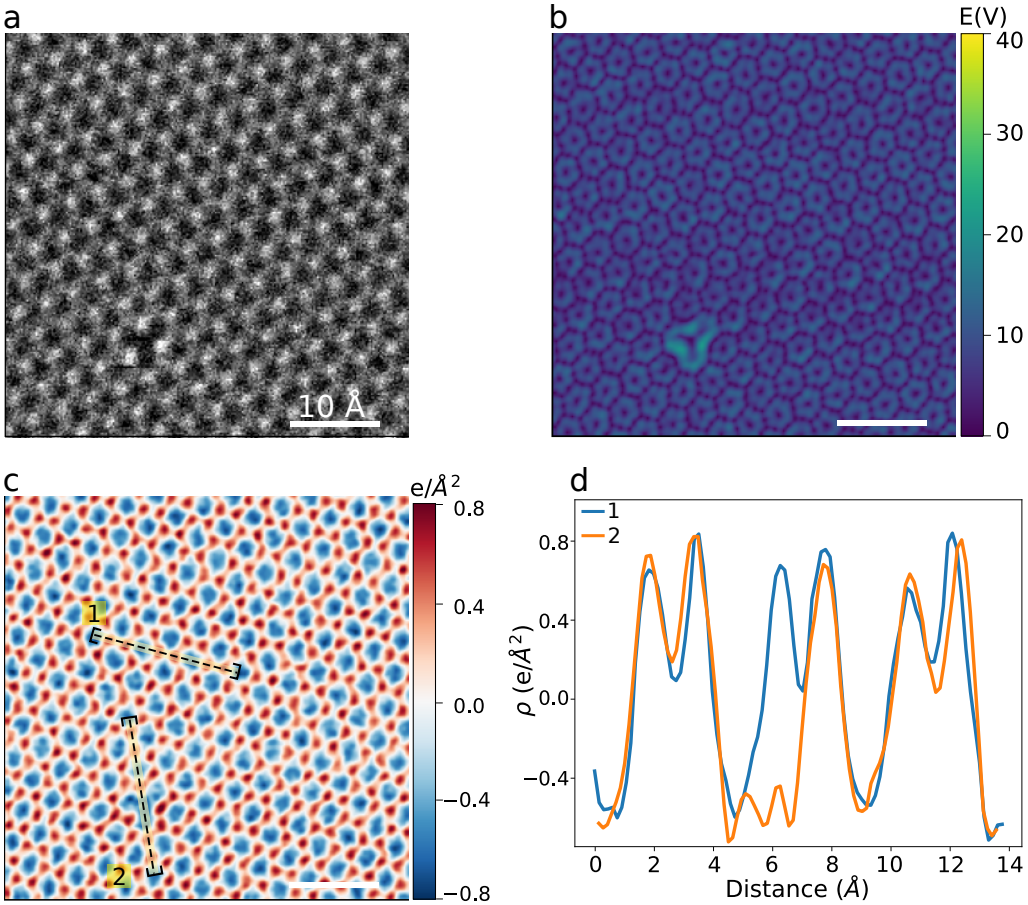

Figure 3.26: *(a) HAADF image of an h–BN monolayer with the presence of a boron monovacany. (b,c) 4D-STEM derived electric field modulus and charge density map acquired for the same area. (d) Line profiles taken across the regions 1 and 2 indicated in the charge density map.*

strongly dependent on the probe size. An effective strategy would be to consider very extended integration regions around the defect site, formed by several unit cells. However, the charge variation at the defect site might be difficult to evaluate because of the same magnitude of the integral precision. Indeed, incertainities in the definition of the integration area and possible scan distortions lead to non negligible numerical fluctuations. Nevertheless, qualitative analysis on charge redistribution can still be performed in presence of vacancies in monolayers.

Fig. 3.26.a shows the HAADF image of a boron monovacancy in a monolayer. Fig. 3.26.b is the 4D-STEM derived electric field modulus, while Fig. 3.26.b is the total charge density map. Fig. 3.26.d shows the charge density profiles taken on the bulk monolayer alongside those taken at the boron monovacancy. In this case, it is observed the absence of positive charge due to the removal of the

boron nucleus, and the presence of negative charge. An analysis of the extension of the charge redistribution around the defective site can not be performed due to the difficultly to separate the short range contribution, directly coming from the atomic lattice, and the "long-range" linked to the vacancy.

A possible procedure to isolate the sole defect contribution is to apply numerical filters on the charge density maps. A similar post processing procedure was performed by Meyer and co-workers on HRTEM images of nitrogen dopants in graphene [8].

For this study, we applied two distinct filters: a Fourier filter and a low-pass filter. The Fourier filter involves the application of disks on the Fourier transform of the original image (Fig. 3.27.a). These disks are specifically placed to mask the peaks corresponding to the lattice periodicity, as illustrated in Fig. 3.27.b. The low-pass filter utilized is the Chebyshev filter, depicted in Fig. 3.27.c and whose profile is shown in Fig. 3.27.d. This filter is designed to optimize the cutoff rate between the frequency response's passband and stopband, at the expense of ripple in the passband and increased ringing in the step response. In our study, the cutoff frequency was set slightly larger than the lattice periodicity, indicated by the green vertical line in Fig. 3.27.d.

Fig. 3.27.e shows a zoom of the charge density presented in Fig. 3.26.c, focusing on the boron monovacancy zone. Fig. 3.27.f is the charge density map after the application of the Fourier filter, while Fig. 3.27.g is the result of the Chebyshev filter. Fig. 3.27.h,i are the same filtered images overlapped with the HAADF image. In both cases an accumulation of negative charge is present in correspondence of the missing boron atom, while a positive charge can be seen solely on the nitrogen sites surrounding the vacancy. This behavior is in qualitative agreement with the edge case discussed before. Nevertheless, a quantitative analysis on charge redistribution from the filtered images might be inaccurate since amplitudes of low frequency components are not conserved. A future accurate quantitative analysis could give insights whether the boron monovacancy is negatively charged, as reported in several works, or it just corresponds to a neutral vacancy, where the negative charge accumulation is purely due to a broadening of the electron charge density of nitrogen atoms, and it is nullified by the more positive charge at the nuclei sites.

In conclusion, 4D-STEM has proven to be an efficient technique for the detection of charge density and electric fields in *h*–BN monolayer. This technique can also be used for structural determination beyond conventional imaging techniques employed in STEM microscopy. The improved contrast, which mainly depends on spurious effects deriving from the probe-size effects in presence of defects, ease their localization and identification. Furthermore, the space distribution of the charge density associated to defects can be extracted by filtering out the lattice periodicity. Nevertheless, for a more comprehensive understanding

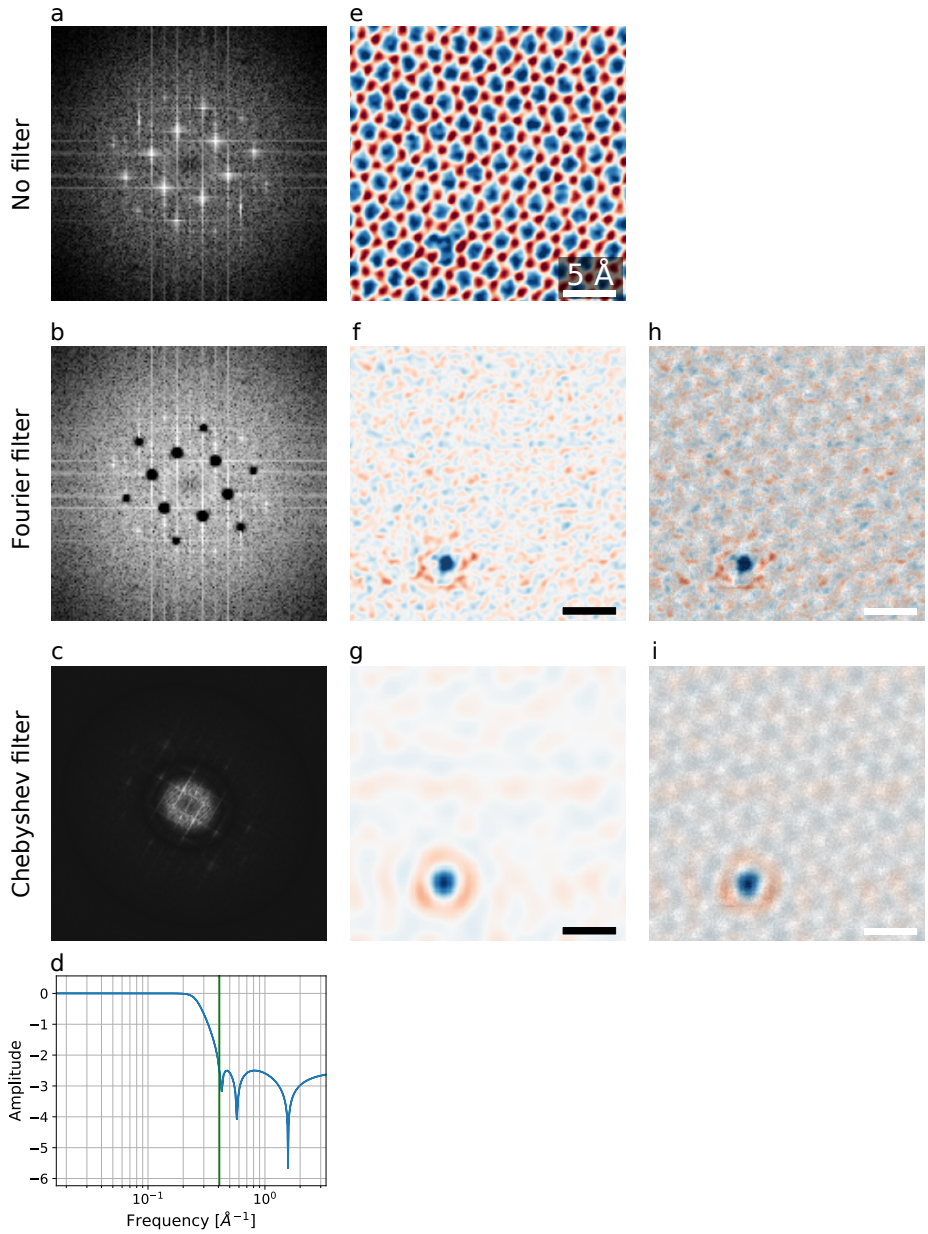

Figure 3.27: *(a) Unfiltered Fourier transform of the 4D-STEM charge density map reported in (e). (b) Fourier filter to remove the periodic components of the h–BN lattice applied and indicated by black circles. (c) Chebyshev filter applied to the Fourier image and (d) the relative profile, where h–BN lattice spacing is indicated by the vertical green line. (e) 4D-STEM charge density map of a boron monovacanvy with no filter applied. Filtered charge density maps resulting from the application of (f) the Fourier filter and (g) the Chebyshev filter. (h) Fourier filtered and (i) Chebyshev filtered charge density maps overlapped with the HAADF image.*

and to advance beyond qualitative analysis, further investigations are needed to determine the most suitable filtering as well as theoretical calculations to provide preliminary insight into the expected values.

CHAPTER 4

Development of a XEOL setup for a RIXS beamline

One of the remarkable advantage of STEM microscopy coupled with EELS spectroscopy is the possibility of studying excitation processes over a broad range of energies and with high spatial selectivity. Synchrotron sources, on the other hand, are photon sources that can provide element and orbital selectivity when a well-defined energy and polarization of the incident light is chosen. Among synchrotron spectroscopies, resonant inelastic X-ray scattering (RIXS) presents analogies with EELS, as it studies neutral excitation phenomena with the same initial and final energetic states, but with the peculiarity of being a resonant process. This provides an opportunity to obtain complementary information compared to EELS. Moreover, given the greater complexity of RIXS with respect to EELS, the comparative analysis between these methods can help clarify open questions associated with RIXS spectra interpretation.

Recombination phenomena can also be studied within a STEM microscope, thanks to the integration of a cathodoluminescence (CL) system. The coupling of EELS and CL permits to correlate excitation and recombination processes, similarly to what is done in optics, but with the advantage of having sub-wavelength spatial resolution and an access to high energy excitations. CL measurements in a STEM also allows the correlation between structure and luminescence, which is particularly desirable since it can permit to discern the structural origin of different luminescence features in a complex emission spectrum.

Using X-rays as excitation source, recombination phenomena can be studied by measuring the emission spectrum in the so-called X-ray Excited Optical Luminescence (XEOL) spectroscopy. Once more the capability of exciting in resonance with specific absorption edges and choosing the beam polarization provide the opportunity to disentangle the different contributions present in the photolu-

minescence spectra. The SEXTANTS beamline of the synchrotron SOLEIL is a unique place where our group in collaboration with the beamline staff implemented a XEOL setup coupled to the RIXS experiment. A significant part of my thesis work has been dedicated to the commissioning of such XEOL setup. The main objective was to put in relation EELS and nano-CL with the RIXS-XEOL pair. It is important to remark that while the first techniques are space selective, the latter are element and orbital selective.

Section 4.1 will give an introduction to RIXS experiments and how they can be put in relation with EELS. Both techniques are here applied to investigate the spectroscopic response of *h*–BN. In Section 4.2, the principles of both CL and XEOL will be discussed while the implementation of the new XEOL setup designed for the RIXS beamline SEXTANTS will be presented in Section 4.3. After detailing the optical setup and capabilities of the beamline, XEOL benchmarks obtained for different BN allotropes will be presented. Finally, Section 4.4 will be dedicated to the application of XEOL to the study of a complex process: the excitation transfer between *h*–BN and WS_2 in a vertical 2D heterostructure.

4.1. Coupling EELS and X-ray Inelastic Spectroscopy

EELS spectroscopy is nowadays a well-established spectroscopic technique, which measures neutral excitations in materials across a wide range of energies, allowing for the study of many different physical processes such as the generation of phonons, excitons, plasmons or core excitations, that would usually require the use of different optical techniques. Furthermore, the use of focused probes make EELS a highly spatially resolved technique. Another prominent capability of EELS, when compared to optical spectroscopies, is the possibility of measuring the momentum dependence of excitations in solids. Indeed, while optical spectroscopies often have an excellent energy resolution, they are limited to probe the long-wavelength limit $q \rightarrow 0$. Conversely, EELS can measure the momentum dependence of different excitations in solids, typically in the low momentum range ($q < 1$ Å^{-1}) [141]. Nonetheless, in respect to optical techniques, the polarization of the incident radiation can not be easily defined in EELS. Furthermore, EELS typically operates at a minimum experimental temperature limited to liquid nitrogen (mainly due to mechanical instabilities of the sample holder at low temperatures), while lower temperatures may be desired when performing optical experiments.

Synchrotron radiation permits instead an easy definition of the polarization of the exciting radiation, resonant excitation processes and there are lower constrains at the sample stage to operate at the liquid helium temperature. Furthermore the incident radiation energy can be tuned in resonance with a specific element absorption edge. Core-loss EELS, or ELNES, has been often associated

with X-ray absorption spectroscopy (XAS) and near edge X-ray absorption fine structure (NEXAFS). The enhanced energy resolution accessible by new STEM monochromators and the extended access to the lower energy spectral range are drawing EELS closer to inelastic X-ray spectroscopies (IXS) and their resonant counterpart (RIXS). Non resonant inelastic X-ray scattering (NRIXS) and EELS are both non resonant techniques and arise from similar excitation processes. In particular, NRIXS spectra measure the dynamical structure factor, defined as[142, 143]:

$$S(\mathbf{q},\omega) = \sum_f \left| \langle f | \sum_j^N e^{i\mathbf{q}\cdot\mathbf{r_j}} | g \rangle \right|^2 \times \delta(E_g - E_f + \omega), \tag{4.1}$$

where $|g\rangle$ and $|f\rangle$ represent the ground state and the final state of energies E_g and E_f respectively, $\omega = \omega_1 - \omega_2$ is the energy loss and $\mathbf{q} = \mathbf{k}_1 - \mathbf{k}_2$ is the momentum transfer. The dynamical structure factor is proportional to the loss function[142]: $S(\mathbf{q},\omega) \propto -q^2 \mathrm{Im}\epsilon^{-1}(\mathbf{q},\omega)$, where

$$-\mathrm{Im}\epsilon^{-1}(\mathbf{q},\omega) = \frac{\mathrm{Im}\epsilon(\mathbf{q},\omega)}{[\mathrm{Re}\epsilon(\mathbf{q},\omega)]^2 + [\mathrm{Im}\epsilon(\mathbf{q},\omega)]^2}. \tag{4.2}$$

The loss function is also directly measured in EELS [144, 145]:

$$\mathrm{EELS}(\mathbf{q},\omega) \propto -\frac{1}{q^2}\mathrm{Im}\epsilon^{-1}(\mathbf{q},\omega). \tag{4.3}$$

The resonant character of RIXS brings a complemental approach to EELS. RIXS is a photon-in photon-out technique in which the system is resonantly excited at and across an absorption edge. The scattered photons are measured in order to probe the energy and momentum transfer involving intrinsic excitations which can be electronic, magnetic or vibrational [146, 147]. The process of resonant inelastic photon scattering can be understood as the coherent combination of an X-ray absorption, which induces the excitation of a core electron into an empty or virtual state, and the emission of a lower energy X-ray photon in correspondence to the disexcitation of the system that fills the core hole (see Fig. 4.1). Therefore, the final state can be an excited state and the energy difference between in and out photons reflect the energy transfer to this material's excitation. Compared to non resonant inelastic X-ray scattering (NRIXS), the resonant character of RIXS makes it element and orbital selective. Similarly to EELS, RIXS provides an easy access to the high-energy and momentum dependent excitations. These capabilities, together with the impressive improvements in energy resolution obtained in the recent years, have made RIXS an emerging technique among synchrotron spectroscopies [143, 148]. Due to the low cross section, RIXS, is generally a low-yield technique, and a substantial incident photon flux needs to

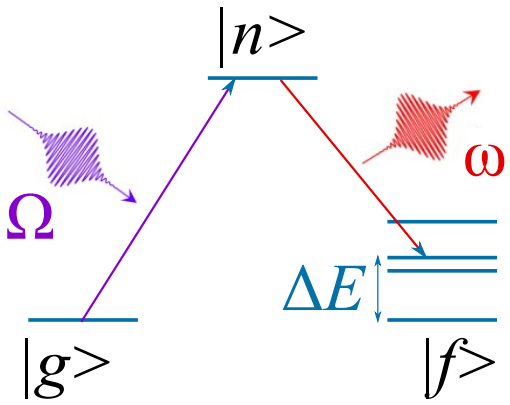

Figure 4.1: *Schematic representation of the RIXS process. Following the excitation of the materials with a X-ray of energy* Γ*, an electron pass from a gound state |g> to an intermediate excited state, |n>. The electron then relaxes to a lower excited state, |f> emitting an X-ray radiation of energy* γ*. The loss in energy between the incident and out photons,* Δ*E , is then measured.*

be employed (10^{11} photons/second at SEXTANTS). The richness of RIXS spectra comes at the price of the difficulty for their theoretical interpretation, which is largely due to the inherently complicated nature of the scattering process, of second order in the photon-matter interaction. RIXS spectra are described by the Kramers Heisenberg equation[142, 143, 148, 149], which expresses the second-order perturbative contribution of the electron-photon interaction $\mathbf{A}\cdot\mathbf{p}$, i.e., the product between the vector potential $\mathbf{A}$ of the electromagnetic field and the electron momentum $\mathbf{p}$. When the incident photon energy ω_1 is tuned to the vicinity of an absorption edge, it reads:

$$I(\omega_1\mathbf{k}_1\hat{\mathbf{e}}_1;\omega_2\mathbf{k}_2\hat{\mathbf{e}}_2) \propto \sum_f \left| \sum_n \sum_{jj'}^{N} \frac{\left\langle f \left| (\boldsymbol{\epsilon}_2^* \cdot \mathbf{p}_j) e^{-i\mathbf{k}_2\cdot\mathbf{r}_j} \right| n \right\rangle \left\langle n \left| (\boldsymbol{\epsilon}_1 \cdot \mathbf{p}_{j'}) e^{i\mathbf{k}_1\cdot\mathbf{r}_{j'}} \right| g \right\rangle}{E_g - E_n + \omega_1 - i\Gamma_n/2} \right|^2 \times \\ \times \delta(E_g - E_f + \omega), \quad (4.4)$$

where $|g\rangle$, $|f\rangle$ and $|n\rangle$ of energies E_g, E_f, and E_n (and lifetime $1/\Gamma_n$), denote, respectively, the ground state, the final state, and an intermediate state of the system of N interacting electrons (located at positions $\mathbf{r}_j$).

A strategy to improve the understanding of RIXS spectra is to establish a careful connection with EELS. Both techniques involves the same initial ground state and final excited state and investigate excitations at the same energies [150]. Therefore, in principle, it is possible to use either technique to interpret the other, but the spectral shapes can be very different, since oscillator strengths completely differ. It was to address this problem that a few years ago a collaboration has been started between our group and Alessandro Nicolaou at the SEXTANTS beamline of the synchrotron SOLEIL. Performing correlative EELS and RIXS experiments on well identified samples would to provide

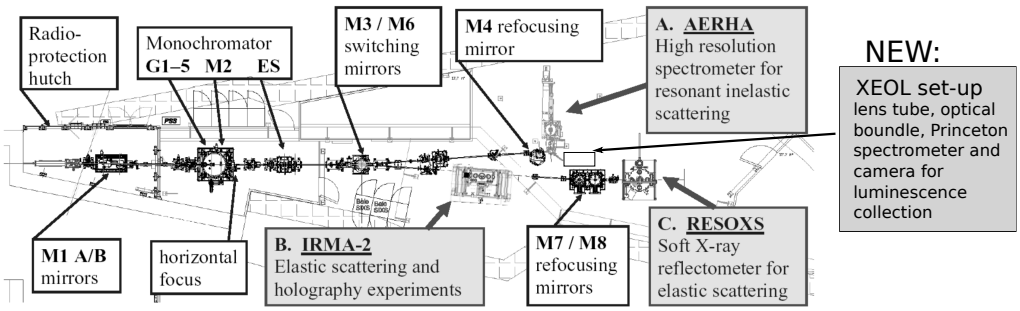

Figure 4.2: *SEXTANTS beamline layout. Main optical elements and the three working positions A, B and C are indicated. Adapted from Ref. 151*

a benchmark for the development of a theoretical framework for RIXS spectroscopies. Once more *h*–BN appears as an ideal test table for several reasons: it's a wide band gap material, which guarantees that its optical onset energy doesn't not overlap with the zero loss, for both RIXS and EELS, it is characterized by a strong exciton binding energy and excitonic features, and its anisotropic nature makes it interest to perform moment dependent measurements.

The SEXTANTS beamline at SOLEIL RIXS experiments were performed at the SEXTANTS beamline of the synchrotron SOLEIL [151, 152], which is dedicated to soft X-ray scattering techniques (Fig. 4.2). The beamline spans an energy range from 50 to 1700 eV and it features two Apple II undulators, providing full control of polarization throughout the broad energy range, and a monochromator equipped with five gratings which allows for highly energy resolved measurements [153]. The SEXTANTS beamline is divided in two branches: working position A hosts permanently the high resolution spectrometer AERHA (adjustable energy resolution high acceptance), which is used for inelastic scattering processes (RIXS) [154]. Working positions B and C, instead, are part of the second branch, and are dedicated to coherent resonant x-ray elastic scattering and holography respectively. During my thesis I have only worked on the inelastic branch.

For RIXS measurements, the 2 μm vertical spot-size of the incident X-ray beam arriving at A is a critical parameter for attaining nominal energy resolution. The sample, positioned on a sample holder, is aligned with respect to the X-ray beam using a four-axis manipulator. The sample can be cooled down to 18K thanks to an open flow liquid Helium cryostat, and it is located at the center of a quadrupolar electromagnet, allowing for operando experiments thanks to the MAGELEC sample environment. Finally the signal coming from the sample is vertically dispersed and focused on a low thermal noise liquid-nitrogen-cooled CCD detector thanks to the optics of the AERHA spectrometer.

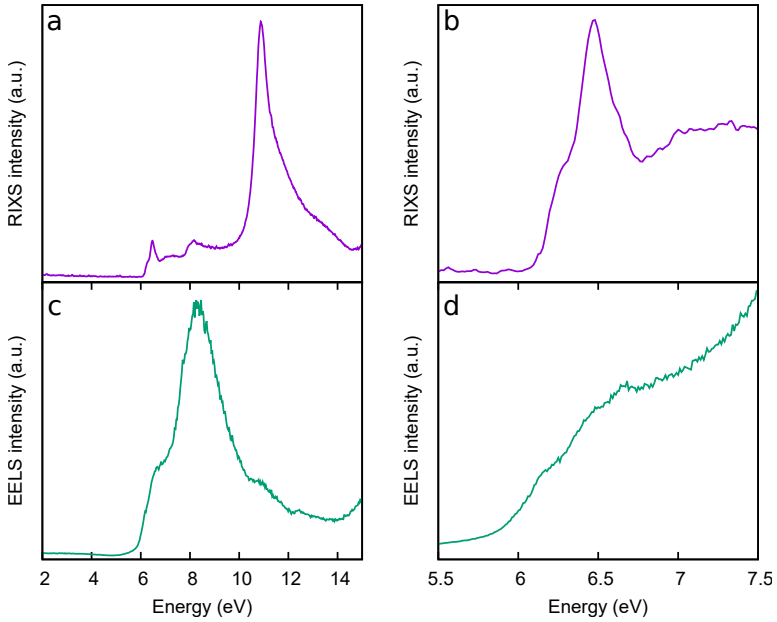

Figure 4.3: *RIXS and EELS spectra acquired over an high quality h–BN crystal. The RIXS spectra have been acquired at the the π^* of the B-K adsorption edge.*

Spectroscopic response of *h*–BN by Resonant Inelastic X-ray Scattering and EELS

For the RIXS experiments we employed high-quality colorless and transparent *h*–BN single crystals produced by a high-pressure and high-temperature method using a barium related solvent system as reported in Ref. [155]. Samples were cleaved in air by means of scotch tape under an optical microscope in order to assure a macroscopically flat surface, and they were introduced in the load lock only few minutes after cleaving. Crystals were mounted with the ΓK direction contained in the scattering plane. RIXS experiments have been performed using a scattering angle of 85°. The overall energy resolution estimated from the elastic peak FWHM was of 80 meV at the B K-edges.

The same type of high-quality *h*–BN single crystals used for RIXS were employed for EELS experiments. Microscopy samples were prepared by chemical exfoliation in ethanol of macroscopic *h*–BN crystals, later deposited onto a lacey carbon copper TEM grid to be analyzed. Monochromated EELS was performed on a modified Nion HERMES-S200 STEM microscope operated at 60 keV, with the sample cooled at ≈ 150 K. Experiments were performed monochromating the beam to a FWHM of 30 meV and using both a convergence and collecting semiangle of 5 mrad, corresponding to an integrated momentum transfer of about 0.6 $Å^{-1}$. Measurements presented have been recorded precisely orienting the *h*–BN crystal along the crystallographic *c* axis. Fig. 4.3.a shows the RIXS spectrum acquired on the *h*–BN crystal at the B K-edge in out of plane polarization for a momentum transfer of 0.01 $Å^{-1}$, while Fig. 4.3.b is the EELS

spectrum acquired in the same energy range as the one reported for RIXS. From a first comparison, the same spectral features can be identified in both EELS and RIXS. Both spectroscopies show a feature at 8 eV, which corresponds to the π plasmon of *h*–BN, and the excitons features around 6 eV. While the spectral features are the same, their intensities do differ. In particular, the high energy peaks present in the RIXS spectrum are strongly attenuated in EELS. Fig. 4.3.c,d provide a zoom near the *h*–BN absorption onset for RIXS and EELS respectively, where in both spectra additional features are clearly visible. The EELS spectrum reported in Fig. 4.3.d is comparable to previous EELS studies performed on *h*–BN [156, 157]. In particular, the highest energy peaks, around 6.65 eV and 6.4 eV, have been ascribed to transitions into unoccupied states associated to longitudinal and transversal dispersion. The lower energy peak at 6.1 eV has been already witnessed as well, and has been connected to absorption from valence band (VB) states into ionized impurity states below the band gap [157]. The RIXS spectrum in Fig. 4.3.d presents as well two main features, at 6.52 eV and 6.2 eV. While the comparison shows peaks at slightly different energies, there is still a good agreement within an range energy of 100 meV. This slight difference can be linked to the different momentum transfer investigated by the two techniques. Indeed, EELS spectra are recorded for q=0, but integrate almost the entire Brillouin zone, due to the relatively large semi-convergence angle used for the measurements. RIXS instead integrates over a small range of q, but for a momentum transfer which slightly differs from zero. When considering differences in intensity, it's important to note that RIXS and EELS have significantly different cross sections. This results in the modulation of all features in RIXS spectra in respect to EELS. These first comparative results show how EELS can help in the interpretation of the intrinsically more complex RIXS spectra. Indeed, while EELS spectra are nowadays well understood thanks to the comparison with ab-initio calculations, there is not an exact theory to describe RIXS phenomena. In this regard, the comparison with EELS allowed to determine that the RIXS onset can be attributed to the intrinsic *h*–BN exciton, while the feature at 8 eV is related to the π^* plasmon. These attributions wouldn't be possible without this comparison since so far there are no computational implementations capable of simulating RIXS phenomena.

4.2. Recombination phenomena: CL vs XEOL

While both EELS and RIXS investigate excitation processes, recombination processes can lead to luminescence in the visible-UV spectral range. As in optics this phenomena are generally studied by photoluminescence measurements, there exist different techniques that enable the exploration of luminescence using electrons and X-ray radiations as excitation sources: cathodoluminescence (CL) and X-ray excited optical luminescence (XEOL) spectroscopy respectively. While CL integrated in a STEM facilitates space-selective measurements, XEOL can offer element and orbital selectivity. In this section an overview of the state of the art for these two techniques will be given.

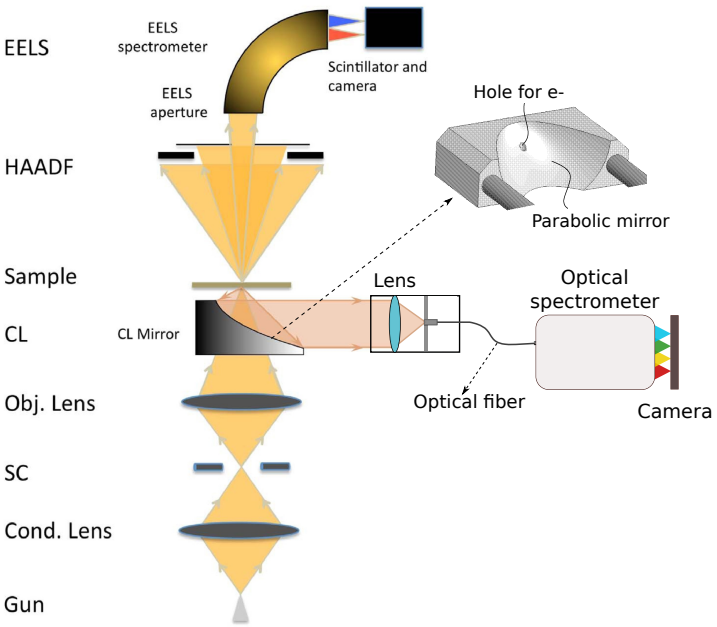

Figure 4.4: *Scheme of a STEM fitted with EELS and CL detectors. The parabolic mirror used to collect the luminescence produced by the sample is showed in the upper part, where the little hole is necessary to let the incident electrons hit the sample. The photon beam can then be directed to the entrance of a spectrometer via a collecting optics (here schematized by a lens converging to optical fibers). A spectrum can then be acquired on a CCD camera. Adapted from Ref. 158.*

Cathodoluminescence within a STEM

The energy transfer given by a high energy electron to a material can be radiated back into the far-field. Core level excitations give rise to X-ray florescence, which can be detected by energy-dispersive X-ray spectroscopy (EDXS) and it is used for elemental analysis of the sample. Lower energy excitations, in the infra-red/visible/ultra-violet (IR/Vis/UV) range, usually recombine in the same energy domain, giving rise to luminescence. This phenomenon is called cathodoluminescence (CL), and the generated signal can be collected through the use of different optical systems, which usually serves to guide the signal in a spectrometer and then read by a camera.

CL has been extensively used to characterize materials, providing similar information as photoluminescence, but with the advantages of an easy access to high energy excitations in respect to optical measurements. While usually integrated in scanning electron microscopes, a major technological development of our group has been the integration of a CL system within a STEM, giving the possibility to collect the light at a sub-wavelength scale, and so referred to as nano-CL [158]. This integration was achieved by positioning a movable parabolic mirror within the objective lens gap just before the sample, where

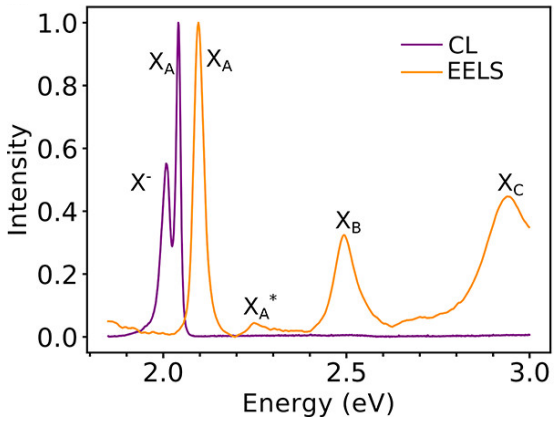

Figure 4.5: *EELS and CL spectra simultaneously acquired on a WS_2 flake.Extracted from Ref. 159.*

the mirror is specifically designed with a hole to allow the passage of electrons through it. Once the electrons interact with the sample and subsequent recombination processes occur, a luminescent signal arises. The focal point of the parabolic mirror is put in coincidence with the electron probe position in the sample. The emitted light is then driven parallel towards a lens which focus it to a fibers bundle, as illustrated in Fig. 4.4. Getting a single spectrum at a given position may not sufficient for an in-depth analysis of the optical properties of nanomaterials, therefore hyper-spectral images have to be acquired, similarly to what is done for EELS. The spatial resolution in CL is limited by whichever is the larger quantity between the probe size, the excitation pear radius and the diffusion length of the charge carriers.

EELS-CL coupling. The integration of EELS and CL techniques within a single STEM microscope has proven to be a valuable approach for studying excitation and recombination processes in various materials, much like what is conventionally achieved in optics through absorption and PL measurements. Fig. 4.5 shows the comparison between EELS and CL measurements performed on WS_2, a work conducted in the framework of the Ph.D. thesis of N. Bonnet [159–161]. While in EELS it is possible to isolate and study the contribute of all excitons up to high energies, indicated as X_A, X_B, X_C,CL studies the luminescence, and so the transitions that give rise to emission of light, which correspond to near band edge excitonic transitions. For WS_2, among all the excitons, only the neutral and charged X_A exciton can decay to photons, and thus emitting light. One interesting feature of the simultaneous excitation and recombination spectroscopy is the possibility to directly measure Stokes shifts, as usually done in optics.

Another application deriving from the coupling of these two techniques could be in principle the coupling between the elemental structure, which can be determined by HAADF and ELNES measurements, and the simultaneous acquisition of CL spectra.

X-ray Excited Optical Luminescence

In a synchrotron facility, recombination phenomena in the visible-UV range can be studied by X-ray excited optical luminescence spectroscopy, where the light emitted from materials upon X-ray excitation is collected. As for CL, one advantage of XEOL is the possibility of using excitation energies that can go far beyond the UV region, which is a typical limit when employing laser excitation techniques as in PL.

XEOL can also be used to monitor the luminescence response of a specimen as a function of the excitation energy [162]. This is usually achieved using a photo-multiplier to collect the whole luminescence emitted by the sample at each point of the energy scan. This advanced usage of XEOL is usually called Near-Edge XEOL or Optically Detected X-ray Absorption Spectroscopy (ODXAS) [163]. In the absorption edge extracted through Near-Edge XEOL the luminescence intensity is inversely proportional to the X-ray absorption cross section, i.e. a negative edge jump corresponds to an emission from within the bulk, while an augmentation in luminescence is due to a signal whose origin is from the surface of the specimen [163]. The limit of thickness for which the signal is considered coming from the surface or from the bulk depends however on different parameters, as the experimental geometry, by means of the incident grazing angle, and the material intrinsic properties as the absorption cross section of the X-ray photons, the diffusion length of the electronic excitation and the luminescence yield [163–165]. In XEOL excitations, the initial absorption of X-ray photons triggers a series of complex de-excitation processes culminating in the emission of optical photons. Each stage is distinguished by its specific efficiency, making it challenging to establish a unified and comprehensive theory [163]. Nevertheless a simplified description to understand the increase/reduction of signal at the absorption edges can still be given.

In general, X-rays are going to be absorbed in the studied sample inside a certain volume, determined by the penetration depth, which in case of soft X-ray is intrinsically lower. The energy transfer from X-rays absorbed by the specimen to the optical channel is carried out via the thermalization of energetic electrons, and the thermalization track can be understood on the basis of the universal curve of the inelastic mean free path (IMFP) or escape depth, of electrons. Their thermalization will then generate many secondary excitation which may finally lead to radiative recombination.

Typically, X-rays are going to be absorbed in the studied sample within a defined volume, determined by the penetration depth, notably reduced for soft X-rays and depending on the material itself. The energy transfer from the absorbed X-rays to the optical channel occurs through the thermalization of high-energy electrons. Understanding the thermalization trajectory relies on the universal curve of the inelastic mean free path (IMFP) or electron escape depth. This thermalization process gives rise to numerous secondary excitations, potentially culminating in radiative recombination.

Prior to reaching the absorption edge of a specific element, the material's absorption coefficient is anticipated to decrease, while the attenuation length increases, allowing X-rays to penetrate deeper into the bulk. Consequently, electron-hole pairs formed are dispersed throughout the penetration depth. At the absorption edge, the penetration depth abruptly diminishes, causing the majority of electron-hole pairs to form in the surface

layers. However, surface imperfections such as defects, dangling bonds, and charging effects may induce non-radiative recombination of the electron-hole pairs, resulting in a reduced luminescence. The photon flux being consistent in both scenarios, the quantity of primary excitations generated remains the same across the absorption edge. Yet, in the latter case, there is a notable loss of luminescence due to the proximity of the majority of electron-hole pairs to the surface. Consequently, the decrease in luminescence observed across the absorption edge is explicable. Thick samples, where all X-rays are generally absorbed, may exhibit this behavior. Conversely, in thin samples where the diffusion length of electron-hole pairs exceeds the penetration depth, the XEOL signal should consistently demonstrate an increase.

XEOL yield An extensive review on the current understanding of the XEOL process and efficiency can be found in Ref. [163]. The key factors that define the XEOL quantum yield can be linked to well identified energy transfer processes. Three main sequential steps can be listed:

- the X-ray absorption and the conversion of the primary excitation into thermalized secondary electronic excitations;
- the energy transfer via these secondary electronic excitations to the luminescent centers which are then promoted into excited states;
- the deexcitation of the luminescence centers with emission of optical photons.

The XEOL quantum yield can be then written as the product of three factors:

$$\eta_{XEOL} = N_{ee} S Q.$$

where N_{ee} is the number of secondary excitations generated and it is linked to the efficiency of the conversion process; S represents the efficiency of the transfer process; Q refers to the quantum efficiency of the luminescence centers. The number of secondary excitations generated at a distance z from the surface by the absorption of an X-ray at an energy E_X can be firstly expressed as:

$$N_{ee}(z) = N_0 \frac{E_X}{E_{ee}} \mu(E_X) \exp[-\mu(E_X) z], \tag{4.5}$$

where N_0 is the number of the incident X-rays photons, E_{ee} is the energy required to create a single secondary electronic excitation and μ is the absorption coefficient. By assuming that the energy transfer coefficient S and the quantum yield Q do not depend on the density of secondary excitations, the XEOL quantum yield for an incident beam energy E_X can be written as [166]:

$$\eta_{XEOL}(E_X) \approx SQ \frac{E_X}{E_{ee}} \{1 - \exp[-\mu(E_X) d]\}, \tag{4.6}$$

with d the sample thickness. In the case of thin samples, a simple expansion of Eq. 4.6 shows that the XEOL signal is proportional to the X-ray energy and to the absorption

coefficient of the sample, which gives an expected increase of the luminescence when the excitation energy is in resonance with an absorption edge. For thick samples, the exponential terms vanishes, and the XEOL yield results to be proportional to the sole excitation energy with a linear dependence. However, this behaviour is valid only for an incident energy far from an absorption edge and neglecting surface effects. In a more general case instead, the depth distribution of the secondary electron excitations is not only defined by the absorption of the primary excitation. In proximity of the surface energetic secondary electrons can escape without being fully thermalized. In the case of nanostructures, their size can be smaller than the thermalization mean free path. In solids, electrons and holes can also diffuse over long distances, of several lattice constants; excitations generated deep in the sample can then diffuse to a surface and recombine non-radiatively which means they lose their energy without emitting light. This process can occur instead of the formation of excitons or being trapped at defects or color centers within the material leading to a significant lowering of the XEOL intensity.

Taking into account these effects, the depth distribution of the secondary excitations become [163]:

$$N_{ee}(z) = \frac{\tau}{\mu^2 L^2 - 1}\left[\exp\left(-\frac{z}{L}\right) - \exp(-\mu z)\right]$$

where $L = (D\tau)^{1/2}$ is the diffusion length obtained for a diffusion rate D and a lifetime τ. From this, the total XEOL quantum yield at a given incident energy in a semi-infinite sample become:

$$\eta_{XEOL}(E_X) \approx SQ\frac{1}{1+\mu(E_X)L}.$$

This indicates that for a thick sample, the XEOL yield decreases as the absorption increases. When there is a sudden change in absorption coefficient at an absorption edge, the optical yield becomes inverted, resulting in a dip in the total luminescence yield.

Near-Edge XEOL vs NEXAFS Near-Edge XEOL measurements exhibit notable similarities with NEXAFS. Specifically, NEXAFS quantifies the X-ray absorption coefficient of a core electron as it transits into the unoccupied bound and quasi-bound states. This technique showcases element- and site-specific features, and it is generally used to distinguish the chemical bonding within the local environment of an atom in a material. Within the region of soft X-rays, NEXAFS is commonly acquired through the observation of both Total Electron Yield (TEY) and X-ray Total Fluorescence Yield (TFY). TEY quantifies the emission of photo-electrons, Auger electrons, and other secondary electrons originating from the sample when subjected to X-ray excitation, offering higher sensitivity to surface characteristics (few nanometers for *h*–BN). Conversely, TFY possesses a stronger affinity for bulk properties, since it collects the X-ray fluorescence [167]. Near-Edge XEOL on the other hand, offers the capability to simultaneously investigate both surface and bulk bonding. Deriving from the integration of visible-UV emitted light, it is in principle a volumetric response offering the possibility to decouple surface and bulk properties through their different energy dependencies.

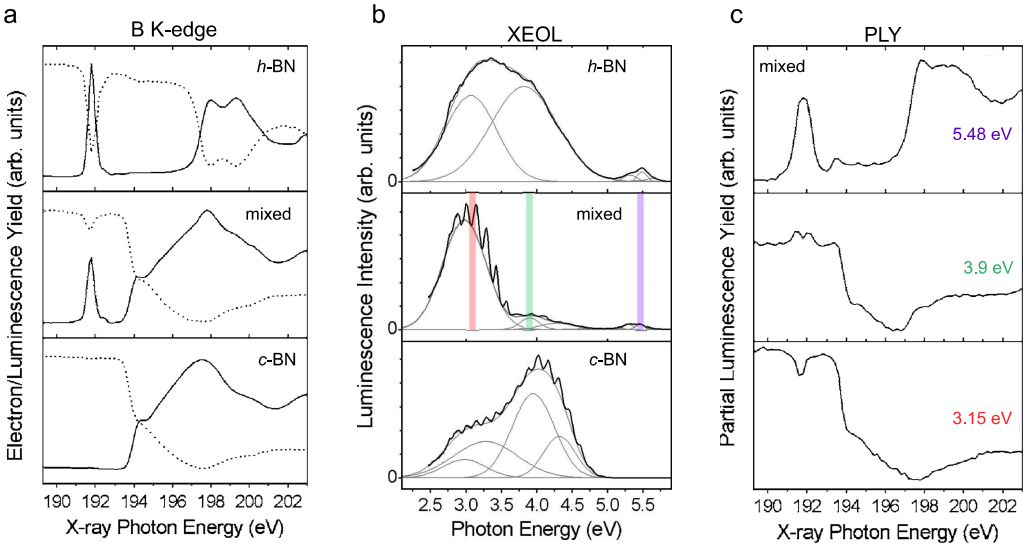

Figure 4.6: *(a) TEY (solid lines) and TLY (broken lines) spectra for three BN samples: pure h–BN, pure c–BN and a mixed one. (b) XEOL spectra acquired for the three different samples with an X-ray excitation energy of 300 eV. (c) Optically detected X-ray excitation spectra of the XEOL luminescence for the mixed crystal recorded at selected energies: 5.48 eV, 3.9 eV and 3.15 eV. Adapted from Ref. 169.*

Correlating structure and luminescence by XEOL

Samples with multiple phases and inhomogeneities can exhibit complex XEOL spectra, characterized by multiple luminescent features that may be linked to the presence of various allotropes and compounds. Typically, each of these phases has a distinctive near-edge absorption spectrum, enabling differentiation of their contributions to the overall luminescence spectrum. One method for conducting such measurements involves a specific Near-Edge XEOL measurement, known as partial luminescence yield (PLY). In contrast to the total luminescence yield, PLY measurements typically employ a filter placed in front of the photomultiplier, allowing the collection of luminescence within a specific optical window of the XEOL spectrum [168]. By integrating the signal from the selected wavelength window as a function of the incident X-ray energy, it becomes possible to correlate the corresponding near-edge structure responsible to the selected luminescence. Other than elemental analysis, thanks to the distinguishing capability of Near-Edge XEOL to differentiate surface signals from bulk it is also possible to gather in-depth information regarding the sample's chemistry and internal rearrangements.

This methodology has, for instance, been employed to examine the presence of *h*–BN at the surface of cubic boron nitride (*c*–BN) micro-crystals, as presented in Ref. 169, whose results have been summarized in Fig. 4.6. Fig. 4.6.a shows the NEXAFS TEY (continuous line) and Near-Edge XEOL TLY (dotted lines) measurements performed across the B K-edge on a pure *h*–BN crystal (top), a high quality *c*–BN crystal (bottom), and a lower quality one, composed by a mixture of cubic and hexagonal phases. The

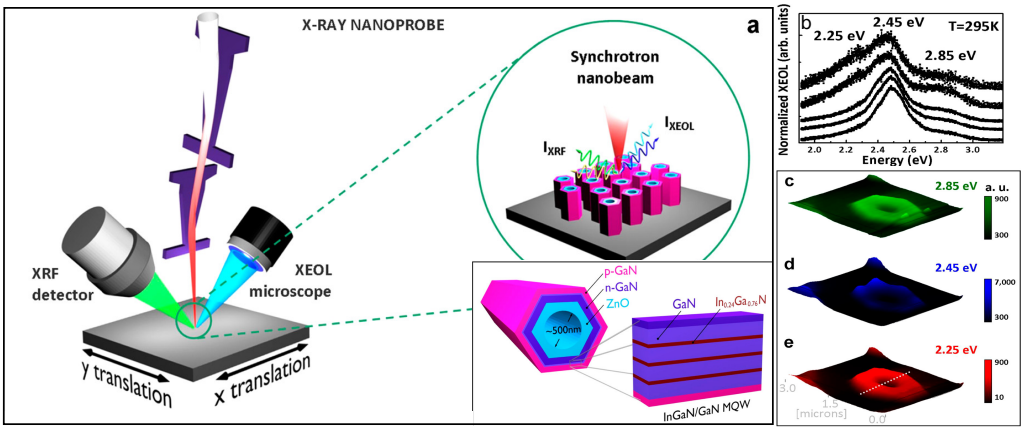

Figure 4.7: *(a) Schematic of experimental setup and the nanowire heterostructure. The X-ray nanobeam impinges on the sample, which emits luminescence and X-ray fluorescence photons.(b) XEOL spectra collected at different positions across the nanowire. (c-e) Luminescence mapping of the same nanowire, indicating spatial distribution for 2.25 (red), 2.45 (blue), and 2.85 eV (green) bands, respectively. Extracted from Ref. 170.*

different phases can be extracted from the absorption edges, as *h*–BN presents the typical features of sp^2 bounded BN, with a pronounced π^* peak at around 192 eV and the σ^* transition between 198 and 200 eV, while *c*–BN is characterized by one broad peak at around 198 eV. The mixed crystal present both features. The respective XEOL spectra are shown in Fig. 4.6.b, where it is clear that the different phases give rise to diverse XEOL features, with complex luminescence spectra arising from different components. Fig. 4.6.c shows the PLY fine structures obtained by filtering the full luminescence of the mixed phase crystal with different optical windows, indicated by the two colors in Fig. 4.6.b. The high energy peak (centered at 5.48 eV) is associated to the sole hexagonal phase, and present a positive sign, meaning that it is a signal mainly coming from the surface, while the lower energy one, at 3.15 eV, is related to the cubic phase and it arises from the bulk. Finally, the 3.9 eV peak is coming from both phases, and the absorption edge presents interesting features, where the fine structure peak associated to the hexagonal phase is positive while the one related to the cubic phase has a negative sign, confirming the position of the hexagonal phase on the surface of the mixed sample.

In modern implementations, the correlation between structure and optical properties can be achieved within individual nano-objects thanks to the use of highly focused X-ray beams [170–172]. One example is the implementation of a XEOL setup at the X-ray undulator beamline ID22, at the European Synchrotron Radiation Facility (ESRF). In this beamline, the use of a highly focused and intense hard X-ray beam, whose spot size is of 60×60 nm^2, allows for space selective acquisition of XEOL signals coupled with X-rat fluorescence (XRF) (Fig. 4.7.a). This setup has been employed for the study of quantum confinement within single core–multishell p-GaN/n-GaN/ZnO nanowires [170]. Fig. 4.7.b shows the XEOL spectra acquired at different position across the

nanowire, showing the presence of three main contribution: 2.25 eV, 2.45 eV and 2.85. The XEOL maps related to the main peaks is reported in Fig. 4.7.c-e, showing the different localization of the luminescence features.

4.3. Implementation of the XEOL setup and benchmarks

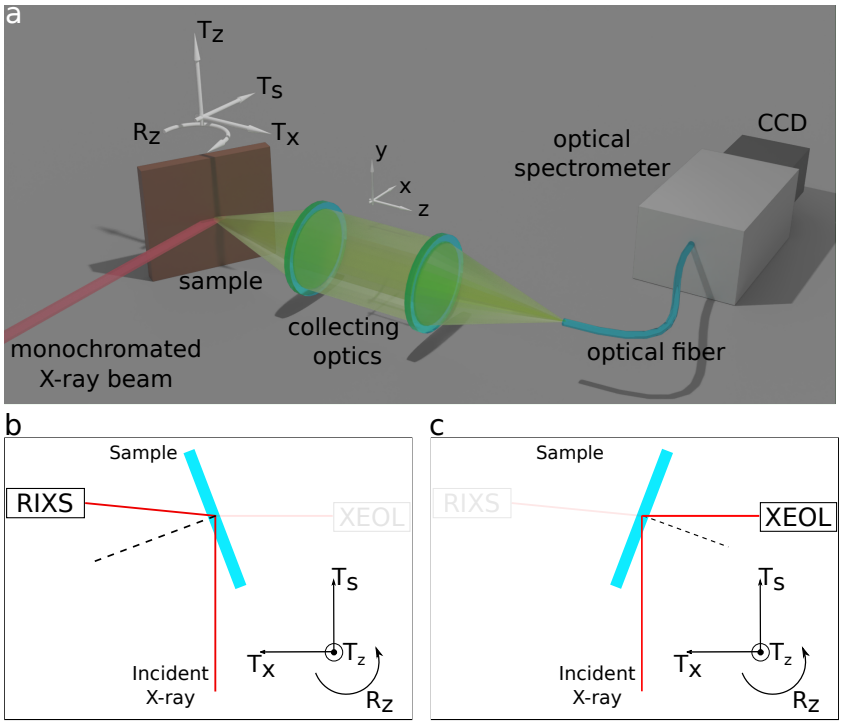

Figure 4.8: *(a)Schematic representation of the XEOL setup installed at SEXTANTS beamline of the synchrotron SOLEIL. (b,c) Sketch of the different sample positions for RIXS and XEOL.*

Inspired by the EELS-CL coupling in a STEM, in the last years the STEM group at LPS in collaboration with the beamline staff have developed a XEOL setup for the SEXTANTS beamline at SOLEIL. The design of the XEOL system integrated into the RIXS branch of the SEXTANTS beamline draws substantial inspiration from the LPS nano-CL setup. A sketch of the implemented setup is given in Fig. 4.8.a.

As for RIXS, the soft X-ray beam is precisely focused onto a confined area of the sample, measuring 2 μm $\times$ 100 μm circa. The sample is securely positioned on a holder equipped with three orthogonal translation axes (T_X, T_S and T_Z) along with an additional rotational axis (R_Z). As shown in the scheme reported in Figs. 4.8.b,c, the RIXS spectrometer is positioned in the opposite side with respect to the XEOL setup position.

The rotation axis permits to switch between the RIXS and XEOL modes and to define the beam incidence angle with respect to the sample normal.

The collection optical system is sketched in Fig. 4.9. A first tube mounts a transparent window to isolate the vacuum chamber and a collection lens (L1) is mounted at its end. A second removable tube, smaller in diameter, can be inserted in the first tube, and it disposes of a second lens (L2) and of a hole for the entrance of the optical fiber. The first lens is an aspheric UV fused silica lens, with a focal length of 50 mm, and coated for the UV range. The second one is a plano-convex lens, UV-VIS coated, with a nominal wavelength range of 250-700 nm and a focal length of 100 mm. The optical fiber entrance lies at the focal point of the L2 and it is composed by a bundle of 25 fibers, each with a diameter of 100 μm. The fibers are grouped at the collection side and vertically aligned on the spectrometer side. The choice of using a fibers bundle facilitates the alignment procedure, decoupling the collection alignment from the spectrometer light injection. The use of a bundle rather than a single fiber permits an easier light injection and limits the effect of chromatic aberration, since all the light is collected even if the L2 focal length changes. The system is compatible with standard fibers which can be adapted to the specific experiment. For all the experiments, a bundle of UV specific fibers has been employed [173].

The signal collected is driven to an aberration free Princeton Instrument IsoPlane® Advanced spectrometer, equipped with three distinct gratings. The first one, featuring a high dispersion rate of 150 grooves/mm blazed at 300 nm, was employed to capture spectra across a broad energy range, as the ones discussed in Fig. 4.11. The other two gratings have both a groove density of 1200 grooves/mm. One of them is UV-blazed holographic, with an optimal range spanning from 190 nm to 450 nm, while the other is VIS-blazed holographic, optimized for wavelengths higher than 450 nm. The reading of the spectra is performed on a high-resolution Princeton Instrument ProEM® 1600 EMCCD camera which, thanks to an UV coating, provides high sensitivity within the NIR-UV range up to $\sim$ 180 nm.

The top of Fig. 4.10 shows the 200 $\times$ 1600 pixellated camera reading the signal of

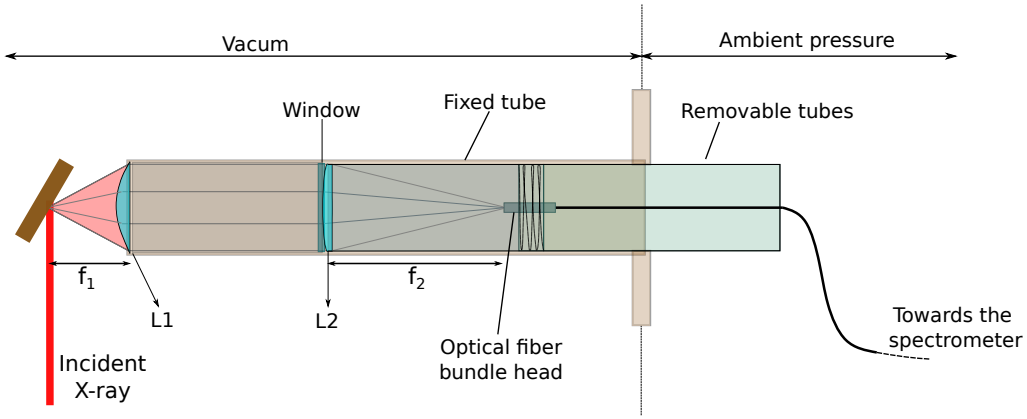

Figure 4.9: *Schematic representation of the collection optics of the XEOL setup.*

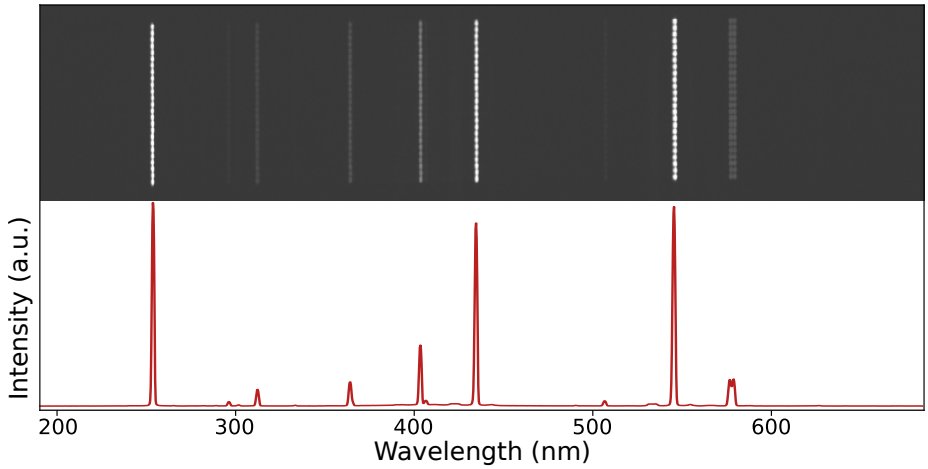

Figure 4.10: *Hg lamp emission acquired at the XEOL spectrometer (200 × 1600 pixels). Optical fibers are focused over the whole camera showing the absence of aberrations within the spectrometer.*

a mercury lamp used for the calibration. The vertical integration over the 200 pixels is reported in the red spectrum at the bottom. In this case the grating employed is the most dispersive one, as it is possible to collect signal in both UV and Visible range (200-700 nm ca). Having a better look at the white lines in the 2D image, it is possible to distinguish the different optical fibers that compose the bundle, meaning that they are well focused, allowing for a better spectral resolution. Importantly, the fibers are well focused all over the camera, showing the absence of aberrations.

The collection system is mounted over a three axes (x,y,z) micrometric translator, which allows to precisely position the optical axis with the beam spot at the sample. This is achieved by moving the collection system in the x-y plane. The translation parallel to the optical axis (z) permits to adjust the distance between the sample and the L1 lens to put at the precise focal length at a given wavelength. This becomes extremely important when operating in the far UV due to significant chromatic aberration of the lens in this wavelength domain. This depth-axis can be adjusted over 50 mm distance (Fig. 4.11.a). To calibrate the optical position as a function of wavelength, an *h*–BN crystal whose luminescence spans from ~200 nm to ~500 nm has been employed. Fig. 4.11.b shows the different luminescence spectra acquired as a function of the lens position. The value set as 0 corresponds to the mechanical limit of the lens manipulator, which is of about 4 cm far from the sample. For shorter distances, the far UV energy range (200-250 nm) shows the typical *h*–BN excitonic peak with the phonon replicas. This signal is completely lost when moving the lenses complex far from the sample, while enhancing the signal in the near visible range (300-400 nm) with the pronounced peaks related to defects. The 2D map of the measurements is reported in Fig. 4.11.c. Red crosses indicate the optimal lens position for each wavelength. A planned upgrade will be the substitution of the refractive collection optics with reflective optics, which will avoid

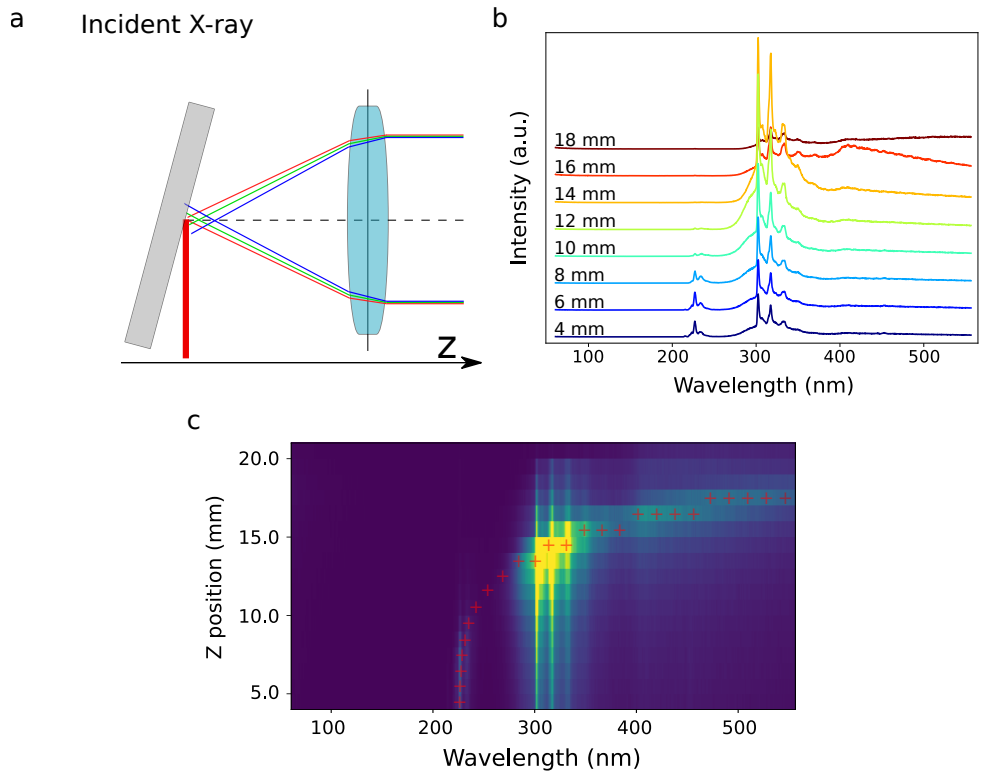

Figure 4.11: *(a) Schema of the collection lens positioning to account for chromatic aberrations. (b) h–BN spectra acquired for different lens positions showing the effect of chromatic aberrations on the collected luminescence. (c) XEOL signal acquired as a function of the z position of the lenses. Red crosses corresponds to the optimal position for each wavelength.*

chromatic aberration problems.

As for RIXS measurements, the XEOL setup is integrated and profit of the MAGELEC sample environment, allowing to perform experiments under electric and a vectorial magnetic field as high as 0.5 T in a temperature range from 400 K down to 18 K. However, when inserted, the presence of the quadrupolar electromagnet restricts movement along the z-direction and imposes a long work distance, complicating the acquisition of far UV signals. During the XEOL commitment the magnet was temporarily removed, facilitating an in-depth exploration of the UV range. A possible way to overcome this limitation and exploit the full UV range, is to mount the specimen on a dedicated sample holder which bring the sample out of the electromagnet plane.

XEOL performance. Figures 4.12.a and 4.12.b give an example of the energy resolution and far UV range detectable [1]. Both spectra have been acquired for an

[1] All the XEOL spectra shown in this thesis haven't been corrected by the instrumentation optical response (e.g. spectrometer response, camera gain etc.).

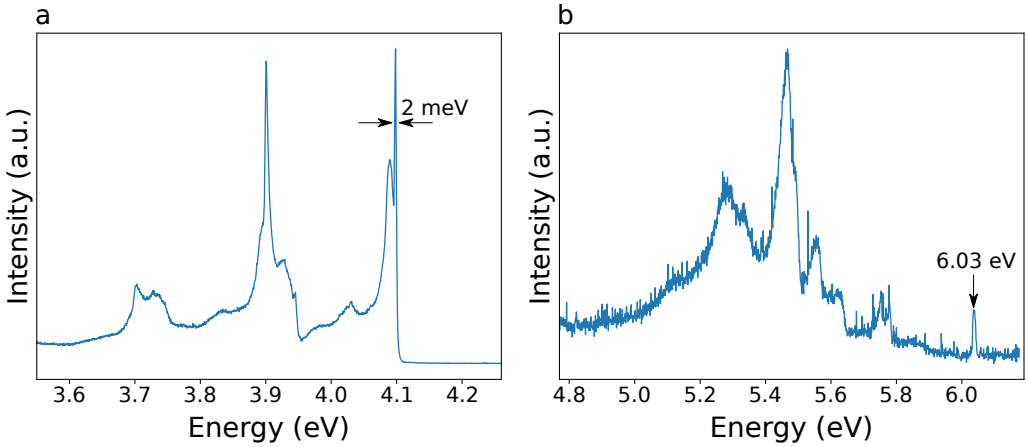

Figure 4.12: *(a) XEOL spectra acquired at 18K for an heavily carbon doped h–BN crystal and (b) a pure h–BN crystal respectively. The high energy emission at 4.09 eV correspond to a non AA′ stacking inclusion*

incident X-ray beam energy of 190 eV, just before the resonance with the onset of the B-K absorption edge. The spectrum in Fig. 4.12.b has been recorded over a heavily carbon doped high quality *h*–BN crystal [174] cooled at 18 K. The peaks shown in the spectrum correspond to the 4.09 eV emission group characteristic of defective *h*–BN, as already reported in previous works [3, 18, 175–179]. Thanks to the low temperature employed, the zero phonon line has a line-width of only 2 meV, much lower than those obtained via nano-CL and comparable with optical measurements. The phonon structure recorded is in perfect agreement with reported PL observations. Fig. 4.12.b shows the high energy emission acquired over a high quality *h*–BN monocrystal. Once more the XEOL spectrum is in perfect agreement with what previously obtained by UV-PL [180]. The highest energy peak at 6.03 eV has been previously observed only very recently, and it has been attributed to regions presenting a direct exciton as a consequence of the breaking of the AA′ stacking order [181]. These examples illustrate the high efficiency of our XEOL setup which can operate with a high energy resolution from the visible to the far UV.

The SEXTANTS beamline offers the full control of the light polarization. Fig. 4.13.a shows the TEY signal acquired on a pure *h*–BN crystal for horizontal (LH, blue curve) and vertical (LV, orange curve) linear polarization across the boron K absorption edge. The characteristic near edge fine structures inherent to the *h*–BN B K-edge can be observed: the 1s-π^* peak around 192 eV, characteristic of sp^2 hybridized materials, and the 1s-σ^* at approximately 197.5 eV. The same main features can be observed in the Near-Edge XEOL TLY curve synchronously acquired and reported in Fig. 4.13.b, where the negative sign indicate a bulk origin. Fig. 4.13.c shows the TLY signal acquired on the same *h*–BN crystal across the nitrogen K-edge for both horizontal and vertical linear polarization. Even in this case the peculiar fine structures of the *h*–BN N K-edge are discernible: the prominent peak around 400 eV is the 1s-π^* peak, while the one

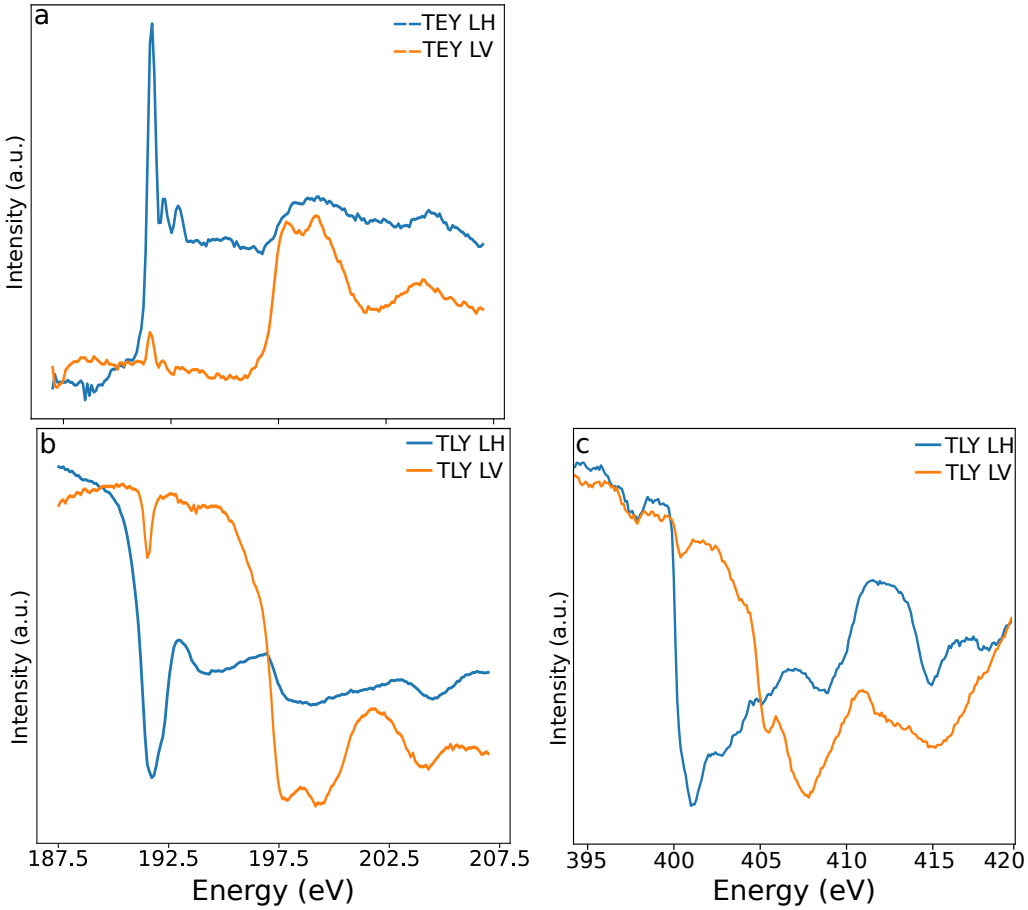

Figure 4.13: *(a) TEY and (b) TLY spectra acquired across the B K-edge of an h–BN single crystal as a function of linear polarization. (c) TLY spectra acquired on the same crystal across the N K-edge as a function of linear polarization. The spectra were measured at 20° grazing incident geometry at T=18K.*

around 406 eV is relative to the 1s-σ^* transition. Observing the distinct polarization for both edges, a prominent contrast emerges: horizontal polarization exhibits a substantial reduction in the σ peak, whereas vertical polarization shows an attenuation of the π peak. This behavior is a direct outcome of polarization dynamics. In vertical polarization the electric field is in the *h*–BN plane and it exclusively triggers in-plane transitions via σ orbitals. In the horizontal polarization, instead, the electric field is orthogonal to the *h*–BN layers, eliciting a response from π orbitals. In principle, in the two different polarization, the distinct peaks of π o σ orbitals should be completely extinguished. However, experimentally we still have small signals of both components because of a not perfect alignment between the incident X-ray beam and the sample surface.

Excitation vs Emission maps: benchmarks

As discussed in the previous Section, the usual operating condition for XEOL consists in the acquisition of the full luminescence spectra at a fixed incident beam energy, while for the Near-Edge XEOL measurements the luminescence yield is usually collected at the zero order of the spectrometer order to retrieve the TLY, and at a fixed wavelength or wavelength window for PLY studies. Few works showed the possibility of collecting the full photoluminescence spectrum while changing the X-ray energy [172, 182–184]. In order to perform such measurements we have synchronized the XEOL CCD camera with the beamline monochromator, enabling automatic recording of full luminescent spectra for each excitation energy (Excitation vs Emission maps). This capability is particularly valuable for our primary goal, which is to correlate structural information with luminescence.

The synchronization is granted by a series of home-made python scripts coupled to the SOLEIL control and acquisition structure, ensuring that when the X-ray incident energy is changed, the system sends a trigger to the camera to initiate data acquisition. Once the camera finishes reading the signal, which depends on the integration time, it sends another trigger to the system to change the energy, and this process continues iteratively. A shutter permits to not expose the camera out of the acquisition time. The communication and reading times are about a few ms and therefore the dead time is essentially dominated by the energy change time of the beamline monochromator. Thanks to this development, fast acquisitions, of the order of a few second per spectrum, are permitted by the high collection numerical aperture of the setup combined with a precise control of the alignment between the sample and source with respect to the XEOL optics. The camera and spectrometer controls are decoupled from the beamline control software. The development of a TANGO (the device controls toolkit used in SOLEIL for acquisitions) device is currently ongoing, and will permit a complete integration of the XEOL setup in the acquisition and control infrastructure of SOLEIL.

The luminescence-versus-X-ray-energy maps collected can be further processed to separate the distinct contributions of individual spectral characteristics. As a result, both XEOL and ODXAS signals, in both total and partial luminescence yield, can be derived from a single measurement. This approach eliminates the need for conducting separate measurements at different wavelengths to determine the Partial Luminescence Yield (PLY). Instead, this information can be extracted afterward, covering the entire range of acquired wavelengths. Furthermore, the use of adapted post-processing tools permits to decouple overlapping luminescence signals.

For all the following experimental measurements, where different BN structures have been studied, the main absorption edge investigated is the boron K-edge and the geometry used for XEOL experiments corresponds to an incident grazing angle of circa 20°. In these conditions, the penetration length is of few tenths of nm.

Europium doped *c*–BN. To test the performance of the implemented setup, the first E vs E maps have been obtained on an heavily Europium-doped *c*–BN (Eu^{3+}*c*–

BN) crystal, whose picture is presented in Fig. 4.14.a. *c*–BN is one of the hardest materials known and it ranks just below diamond in terms of hardness. It stands out as the most basic III-V compound with a substantial energy gap of 10.8 eV between its valence and conduction bands [185]. This significant band gap, combined with the unique ability to incorporate impurities with a reduced diffusion rate, presents an opportunity for the development of an efficient impurity related light-emitting materials. Furthermore, *c*–BN can have advantages over existing light-emitting materials due to its remarkable resilience, where the material remains unaffected even when subjected to severe environmental conditions such as elevated temperatures, chemically corrosive surroundings, and substantial radiation exposure.

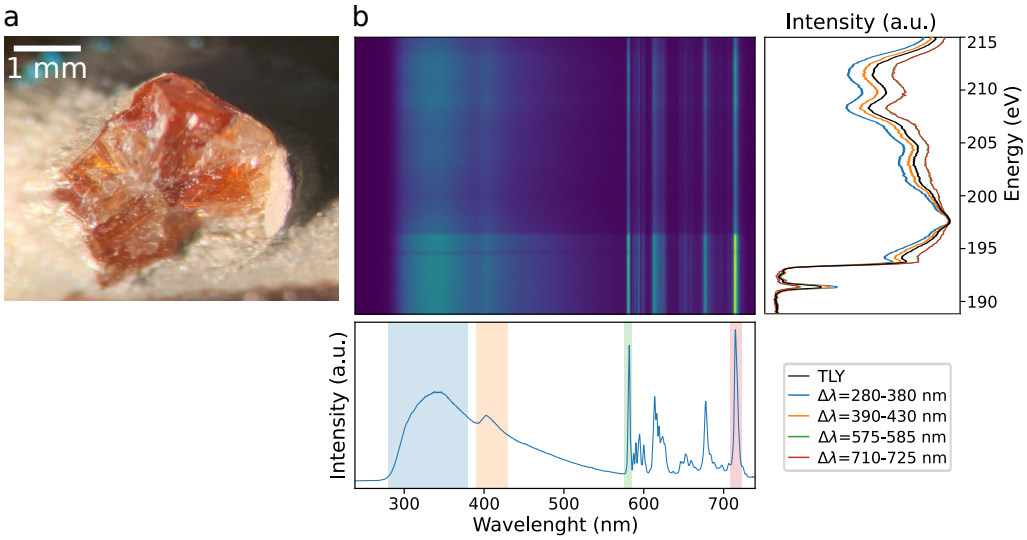

Figure 4.14: *(a) Eu^{3+}c–BN crystal used for the excitation-versus-emission map showed in (b), reporting the TLY and PLY, whose integration window are indicated by the colored columns in the XEOL spectrum in the lower panel.*

One approach to generate light emitting materials involves doping *c*–BN with various rare-earth (RE) elements. In the early 2000s, the doping of *c*–BN with RE ions was demonstrated using the ion-implantation technique [186, 187]. Later, in order to provide a large amount of samples with homogeneous properties, single crystals of *c*–BN doped with europium were obtained through an in-situ doping process during the synthesis of *c*–BN single crystals, performed via a high pressure and temperature process [188, 189], with the addition of RE fluorides as sources for the doping [190]. However, during the synthesis of *c*–BN, traces of *h*–BN may still be present, while the entirety of the Eu dopants is expected to be distributed within the cubic phase. This material is anticipated to exhibit a complex luminescence spectrum comprising contributions from *h*–BN, *c*–BN, and the fine Eu peaks. As a result, it serves as an excellent candidate for investigating the relationship between luminescence and crystal structures, as well as for testing the functionality of the XEOL setup.

Fig.4.14.b shows the Excitation vs. Emission map acquired across the B K-edge with the sample cooled at 18 K. In the lower part of the image the total luminescence spectrum has been extracted as the integration of all the XEOL spectra over the excitation energies. The main features reported in the previous works [190, 191] are here also observed, with the first two peaks referred to the pure cubic phase and the narrow peaks in the visible range, related to the Eu ions emission. These features correspond to transitions from the ^5D states to the ^7F ones. On the right side of Fig.4.14.b is reported the integrated luminescence, corresponding to the ODXAS signal. The total luminescence yield, represented by the black curve, is the sum over all the wavelength range, while the other curves represent the partial luminescence yield extracted from the indicated wavelength windows. All the curve present two main features, the sharp π^* peak at 192 eV, relative to the presence of the hexagonal residues, and the broad $sp^3 - \sigma^*$ bond typical of the cubic phase [169, 192–194]. All the spectra have been normalized with respect to the σ^* peak. Interestingly, when the luminescence peaks related to europium are integrated, the σ^* peak is strongly reduced and we can recover the distinctive boron absorption edge associated with the cubic phase. This indicates that the primary excitation responsible for the Eu luminescence occurs in the *c*–BN matrix, which effectively acts as the absorption medium for the europium ions.

I have performed these measurements and developed these data analyses in the ambit of the commissioning of the newly implemented XEOL setup at the Sextants beamline. This approach could be in principle used to show the relation between a specific luminescence peak and a particular dopant atom.

In the case of Eu doped *c*–BN this could be tested by performing an Excitation vs. Emission map across the Europium M absorption edge. A positive Near-Edge XEOL should be recorded for the Eu M edge, since exciting dispersed dopants wouldn't involve a volumetric response. First trials have been conducted, but results are not conclusive due to the low absorption cross section. Indeed, these experiments are challenging due to the weak active cross section of this edge.

Oxygen-related defects in *h*–BN A limitation of the conventional operational XEOL-ODXAS system is the inability to isolate contributions from overlapping luminescence signals within a selected integration window. This characteristic can pose challenges, particularly in the case of boron nitride, as illustrated in Fig. 4.6. These figures show that within a given wavelength window there is a superposition of several independent luminescence signals. Consequently, the integrated ODXAS signal may not solely reflect the component of interest, thereby limiting the direct correlation between luminescence and structure.

Within our implemented setup, however, it is possible to separate different luminescence features and extract the related ODXAS spectrum within a unique measurements by employing a post-processing fitting routine. To illustrate the method, in the Fig. 4.15.b it is presented the Excitation vs. Emission map obtained across the B-K absorption edge for the high quality *h*–BN monocrystal shown in Fig. 4.15.a, kept at 18 K. Fig. 4.15.b shows the XEOL spectra acquired for different excitation energies. For each

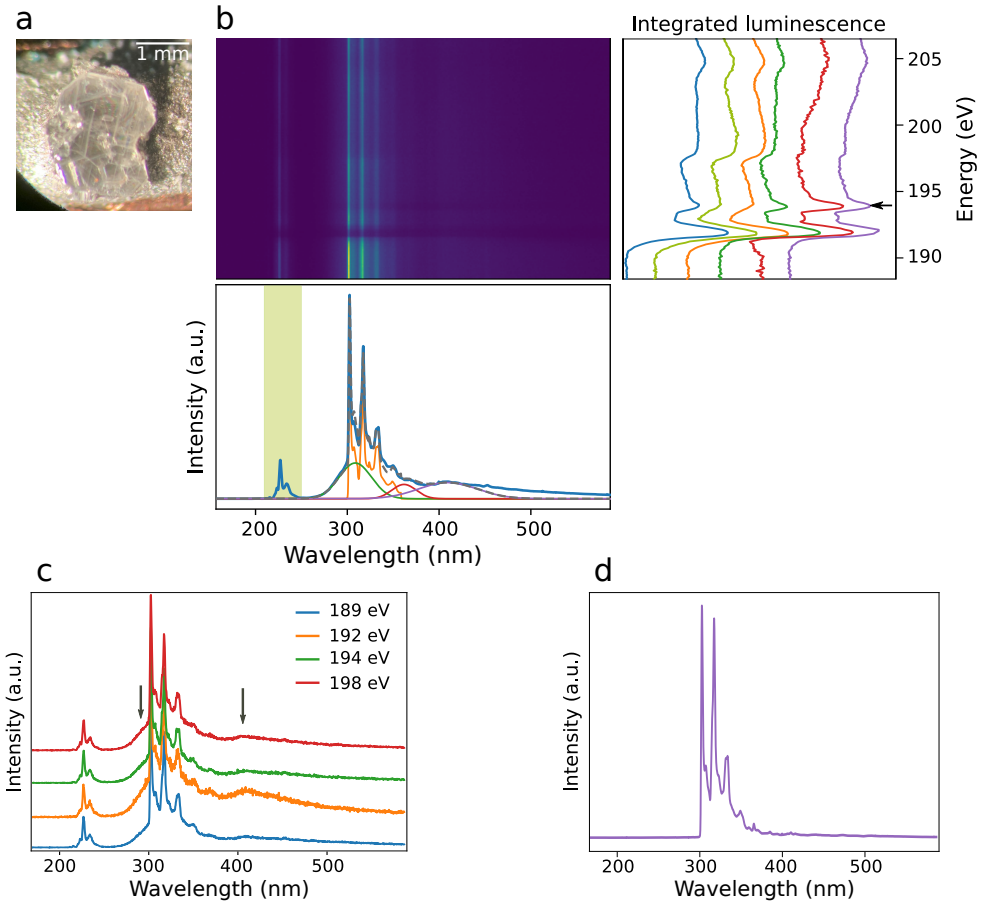

Figure 4.15: *(a) High quality h–BN monocrystal. (b) Excitation-versus-emission map acquired across the B K-edge of the h–BN monocrystal in (a). On the bottom panel the XEOL spectrum is reported with the fitting routine showing the different components whose PLY is reported on the right panel, together with the TLY in blue. (c) XEOL spectra collected at different excitation energy. (d) XEOL spectrum of an heavily carbon doped h–BN crystal used for the fitting in figure (b) lower panel.*

spectrum several components can be clearly distinguished in the luminescent spectrum: the high energy spectral features around 220 nm (main exciton with the relative phonon replica), the sharp group of peaks related to the 4.1 eV defect emission and its phonon replica and additional unstructured broad bands centered at about 308 nm, 360 nm and 410 nm. Interestingly, for different excitation energies the luminescence components act differently, suggesting a different structural origin.

The blue curve in the bottom graph of Fig. 4.15.b corresponds to the complete luminescence spectrum integrated over the X-ray beam energies while the blue curve in the right graph is the total luminescence yield. In correspondence with the B-K absorption edge there is a decrease in the luminescence intensity indicating a bulk origin

of the signal. While the excitonic signal can be easily integrated within a wavelength window, the other components overlap in a complicate way, and the window integration would not give the appropriate results related to the components.

An approach that can be used is to employ a fitting routine in the 250-450 nm range, using the four components highlighted on the bottom graph of Fig. 4.15.b. The three broad bands have been fitted using Gaussian functions, while to fit the sharp defect related emission peaks a spectrum obtained from a heavily carbon doped *h*–BN crystal, reported in Fig. 4.15.d, has been used as reference component. Once the different components are evaluated, only the amplitudes have been used as free parameter of the fit.

The curves in the side graphs of Fig. 4.15.b correspond to the weight of each component as a function of the incident beam energy. The yellow curve correspond to the integration of the exciton group peaks, while the orange curve corresponds to the 4.1 eV group. The near structures deriving from those two components, perfectly match with the near edge fine structure of *h*–BN, indicating that the 4.1 eV emission arises from regions of well crystallized pure *h*–BN. The absorption spectra corresponding to the other broad band emissions present instead an addition peak at 194 eV, which can be correlated with B-O bonds [167, 195, 196]. This indicate that unstructured features in the *h*–BN emission spectrum, and in particular emissions in the 400 nm range, arise from regions with a detectable content of oxygen. To further show this behavior, in Fig. 4.15.c different XEOL spectra are reported for the different excitation energies.

Whereas these results do not provide an unequivocal attribution of a specific emission line to a well identified *h*–BN chemical environment, they give a good proof of principle of the utility of acquiring excitation VS emission energies maps to decompose a complex emission spectrum in its chemical origin.

4.4. XEOL study of excitation transfer processes in *h*–BN-TMDs heterostructures

The results presented so far relate to the commissioning of the new XEOL experimental setup. In this section I will expose the application of the explained approach for the study of the excitation transfer in van der Waals heterostructures formed by *h*–BN and transition metal dichalcogenides.

In recent years, transition metal dichalcogenides (TMDs) have gained significant attention due to their unique electronic, optical, and mechanical properties, making them suitable for various applications. TMDs belong to the family of two-dimensional (2D) materials, where each layer consists of transition metal atoms covalently bonded to two dichalcogenides, while the layers interact through van der Waals forces. The 2D nature of TMDs renders them exceptionally intriguing for application in nanoscale devices and materials engineering. Notably, these layered materials exhibit a direct bandgap within the visible range when reduced to monolayers [197, 198]. Consequently, monolayer TMDs often display efficient luminescence in comparison to their multilayer counterparts, where the bandgap is indirect. Due to the weak internal dielectric screening, the optical response of the TMDs is determined by excitonic resonances [161].

Recently, transition metal dichalcogenides (TMDs) have been combined with other 2D materials to create diverse van der Waals heterostructures. Typically, this integration involves vertically stacking various 2D semiconductors, giving rise to types I and II heterojunctions with distinctive properties.

However, the optical properties of TMDs are significantly influenced by their local environment due to the high specific surface area of monolayers, making them exceptionally sensitive to external factors, including disorder and the surrounding dielectric environment [199–202]. Moreover, TMDs are susceptible to oxidation and light exposure, factors that can compromise their optical properties. Heterostructures provide a direct solution to ensure both the material's flatness at the scale of tens of picometers and its protection from external agents [159, 161, 202–204]. This protection can be achieved by incorporating a high-bandgap and resilient material, such as *h*–BN, characterized by an optical gap of ca 6 eV, which acts as a transparent protective medium.

When producing this heterojuctions the optical properties of the capped TMD can be modified and improved. As an example, a recent study by Zheng et al. showed that the CL signal of different TMDs can be enhanced and efficiently detected in a van der Waals heterostructure, in which the luminescent monolayer is sandwiched between two thick *h*–BN flakes [205]. Non-capped monolayers, instead, do not show any CL signal. In these heterostructure, excitonic emissions can indeed be a consequence of a direct excitation of the TMD or an excitation diffusion from the *h*–BN to the TMD monolayer. The band alignments between the TMDs and *h*–BN, which is schematically depicted in Fig. 4.16.a for the case of WSe_2, is such that the stack can be considered as a type I junction. As proposed in Ref. 205, excitation in the *h*–BN slab can therefore diffuse and recombine in the TMD monolayer leading to significant enhancement of the emission, comparatively to an isolated layer (4.16.b).

This explanation appear as highly reasonable since the absorption on the *h*–BN

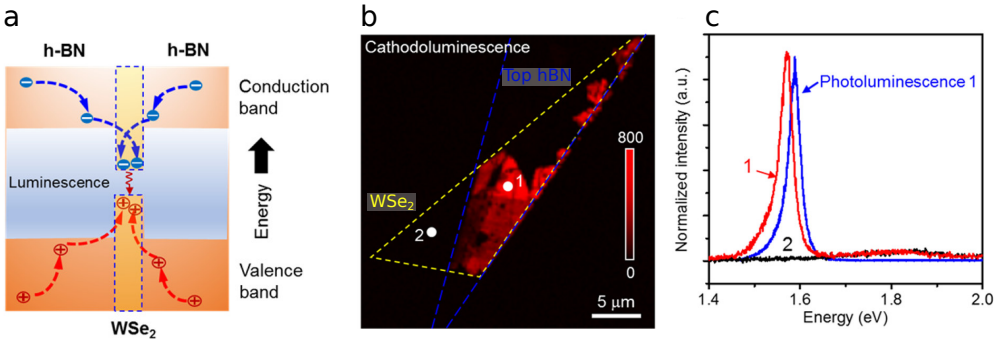

Figure 4.16: *(a) Process of the generation, diffusion, and recombination of electron–hole (e-h) pairs in an h–BN/MX_2/h–BN van der Waals heterostructure. (b) Monochromatic CL map of the heterostructure at WSe_2 emission energy, 1.66 eV. (c) CL spectra generated by electron beam impact on WSe_2 at position 1 and 2 in (b) are shown together with a PL spectrum acquired at position 1 in (b). Extracted from Ref. 205*

flakes is significantly higher than in the TMD due to their greater thickness. However, this mechanism can not be proved by the sole CL experiments since it is not possible to precisely locate the primary excitation responsible for the TMD luminescence. Other phenomena could in principle be responsible of the observed CL enhancement:

- capping effect, which serves to protect the delicate monolayer from adsorbing molecules which would quench the luminescence,
- radiative excitation of the TMD triggered by the luminescence of *h*–BN: UV photons arising from the *h*–BN luminescence would excite the TMD layer.
- secondary electrons produced during the excitation of the encapsulating *h*–BN which can further stimulate the TMD monolayer.

In depth insights on the photo-physics of the 2D heterostructures could be gathered by linking specific spectroscopic signatures with the knowledge of the layer on which holes are created. Whereas this objective cannot be achieved through standard optical methods, layer specific selectivity can be obtained by using X-ray element sensitivity, i.e. by tuning the incident beam at a core level resonance of the atomic species of one of the layers. This can be in principle achieved by exciting a TMD-*h*–BN stack across the boron or nitrogen absorption edge and collecting the luminescence of the TMD to study how and if it varies as a function of the excitation energy. If it is true that the *h*–BN substrate acts as the primary absorption medium for the TMD luminescence, an intensity dependence is expected for excitations at the B or N K-edges. In fact, this ensure the primary excitation fo the *h*–BN substrate, and a very weak direct excitation of the TMD monolayer. This hypothesis has been tested using our XEOL setup on a 2D stack of WS_2 over a thick *h*–BN flake.

Sample preparation and characterization

The WS_2 monolayer used for this experience was synthesized by CVD by the team of Cecilia Mattevi, from the Imperial College of London.

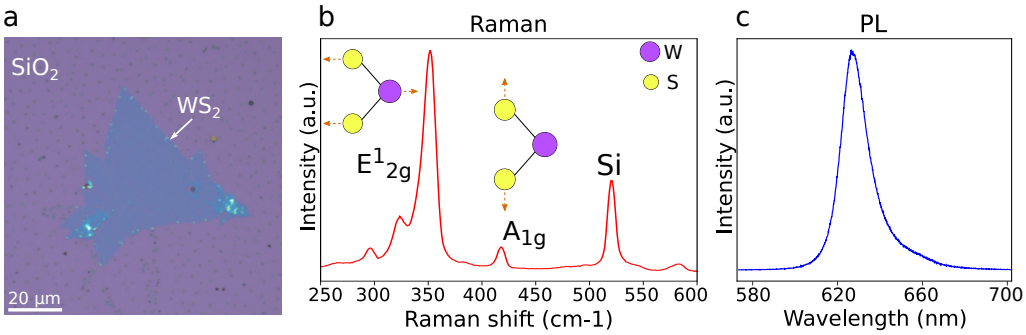

Figure 4.17: *(a) WS_2 monolayer on top of the Si/SiO_2 substrate. (b) Raman and (c) PL spectra acquired on the WS_2 monolayer presented in (a).*

Fig. 4.17.a shows the as-synthesized WS_2 on top of the SiO_2/Si substrate, where the triangular shape is typical of CVD grown TMDs materials. Both Raman and PL measurements have been performed using a 532 nm laser excitation (Fig. 4.17.b,c). The Raman spectrum shows the typical features of WS_2 monolayer vibration modes, characterized by the presence of two peaks relative to the E^1_{2g} in-plane optical mode and the A_{1g} out-of-plane mode [206–208]. The strong peak at 521 cm^{-1} is related to Silicon and is attributed to the substrate. The PL spectrum was acquired at room temperature, and presents a relatively broad peak at around 630 nm, typical of monolayer WS_2 in these experimental conditions.

h–BN/TMDs heterostructures are usually produced in from of sandwich, meaning that the WS_2 monolayer is placed between two thick *h*–BN flakes. As explained before, this is done to protect the fragile monolayer from oxidation and direct exposure to light radiations, and to keep the TMD layer flat and to enhance its luminescence [159, 205]. Usually the stacks are produced on top of a SiO_2/Si substrate, and have very small lateral dimension, of the order of tens of micrometers. First tests have demonstrated these heterostructures are not adapted for XEOL measurements. Due to the large spot size (100 μm $\times$ 2 μm) and the reduced sample dimension it is unavoidable to illuminate the SiO_2/Si substrate. Unlikely in PL, the SiO_2/Si substrate gives rise to a very strong XEOL signal, which masks the monolayer luminescence. This different behavior is due to the excitation energy employed for PL and XEOL: while in the first technique lasers with excitation wavelength in the visible range are used, in XEOL the excitation energy is enough high to excite the SiO_2. Moreover, polymer residues are generally present on the top of the heterostructure, which add unwanted components to the luminescence.

A modified sample preparation has then to be employed. A stack of a WS_2 monolayer over a thick *h*–BN crystal has been built over a thick polymeric substrate. This procedure is a simplification of the normal procedure used to transfer 2D-stacks onto TEM grids [209, 210]. Preparation steps are sketched in Fig. 4.18. A thick polydimethylsiloxane (PDMS) block is covered by a viscoelastic thin film of polycarbonate (PC) that enters in contact with the thick *h*–BN flake (a-c). The same procedure is then applied to pick-up the WS_2 monolayer (d-f), via Van der Waals forces between *h*–BN and the TMD layer. To build up normal TMDs sandwiches further steps are usually needed, which include the deposition of the WS_2/*h*–BN stack on another *h*–BN flake on SiO_2/Si substrate. In respect to more common sandwiched structures the sample so produced is more fragile since the heterostructures is positioned on top of a polymeric substrate, which other than being more flexible with respect to common SiO_2/Si substrates, is more difficult to handle. Furthermore, the WS_2 monolayer is not covered and more subjected to external stimuli as oxidation and direct light.

The deposition of the thin monolayer on the top of *h*–BN is more difficult to grant since the optical contrast produced by the stack is minimal and may be difficult to detect. A common route to demonstrate the transfer of the TMD monolayer is done by checking on a CVD growth substrate the area where the monolayer hypothetically transferred was placed. If the transfer process has been successful, no material should be seen anymore in that same area. Nevertheless, a more fine verification can be done by Raman

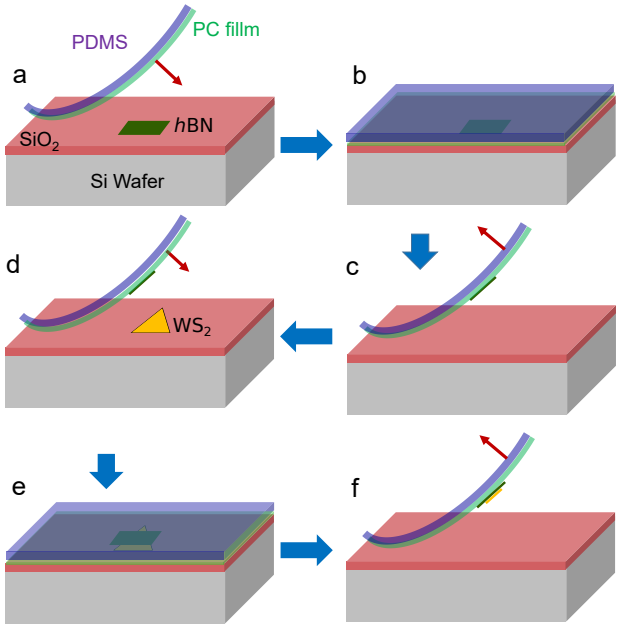

Figure 4.18: *Schematics of the dry transfer process to fabricate the hBN/WS_2 heterostructures. Adapted from Ref. 205.*

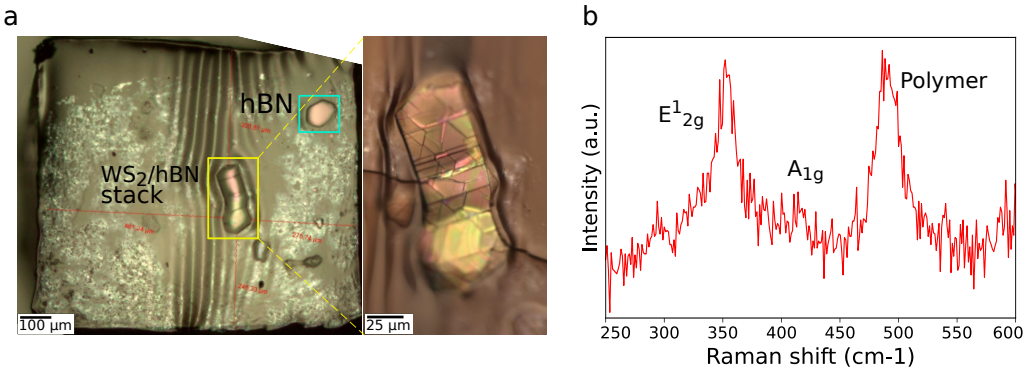

Figure 4.19: *(a) Optical image of the WS_2/h–BN stack on a thick polymer cube, where zooming the stack it is possible to notice different fractures of the h–BN flake. (b) Raman spectrum of the as-prepared stack, showing the Raman feature of WS_2 and of the polymeric substrate.*

spectroscopies, even if the TMD signal is expected to be very weak being the material on the top of a thick (5 mm) polymer cube and another thick (100 μm) *h*–BN crystal.

Fig. 4.19.a shows the sample prepared with the procedure described here. The large gray area is the ensemble of the thick PDMS and PC polymers. On top of the polymeric film two different *h*–BN flakes can be distinguished, where the biggest one, whose size is approximately 100 μm $\times$ 5 μm, has the WS_2 monolayer stacked on it. From the zoomed image it appears that the surface of the *h*–BN flake is not completely flat, but it

is characterized by different thicknesses, which appear as different colors in the optical image. This feature may produce a less homogeneous luminescence response of the WS_2 monolayer, due to the strong luminescence dependence of TMDs from the surrounding disorder. Fig. 4.19.b is the Raman spectrum acquired on the stack, and it presents once again the typical WS_2 Raman features already described in Fig. 4.17.b. This is a prove that the TMD monolayer has been transferred on the *h*–BN flake. The other strong peak, at around 500 cm^{-1}, is related to the polymeric block and it is in common for both PC and PDMS.

Experimental results

Due to the large incident beam size, samples generally studied at the SEXTANTS beamline are much larger than the WS_2/*h*–BN stack prepared for this experiment, and the exact sample positioning is usually done by measuring the sample current. However, due to the small size and the fact that the stack has been positioned on a thick insulating polymer cube, this standard procedure couldn't be used. Nevertheless, thanks to the sample's strong luminescence, the few tens of micrometers WS_2 monolayer flake over the *h*–BN crystal can be localized performing XEOL maps as a function of the sample's position. Once the sample has been mounted on the beamline holder, it has been placed at the beam position firstly by illuminating it with the visible synchrotron light, using the zero order of the X-ray monochromator, and then by precisely displacing the sample to optimize the XEOL signal of *h*–BN. For this procedure, the sample-XEOL distance was set at Z=15 mm to optimize the collection of both UV and visible signals, corresponding to the *h*–BN and WS_2 luminescence range.

Fig. 4.20.a shows the XEOL signal acquired as a function of the T_Z position (height) of the sample for an excitation energy of 192 eV and a cooling temperature of 18 K, with an integration time of 30 s per spectrum. A broad emission centered at $\sim$ 480 nm is obtained over the whole scan region and it can be interpreted as arising from the polymeric substrate. From the XEOL map it is then possible to precisely localize the *h*–BN flake by looking at the luminescence of the defects related 4.1 eV peaks group (corresponding to a wavelength of 300 nm). This signal spans about 150 μm which corresponds to the value found from the optical microscope image. Fig. 4.20.b displays the XEOL spectra taken at different T_Z values, showing that two extra peaks in the visible range appear in correspondence with the *h*–BN position. Moreover, due to the XEOL-sample position, which has been set to collect both UV and visible signal, an intense broader peak, probably relative to the *h*–BN luminescence tail, strongly overlap with the supplementary peaks.

For a finer detection and localization of these two peaks, a second map has been performed as a function of T_Z after moving the XEOL position at Z=19.5 mm, to maximizing the XEOL signal collection in the 550-700 nm wavelength range (Fig. 4.21.a). The two peaks, highlighted by the two arrows, appears now as strongly localized. The XEOL spectrum corresponding to T_Z=38.66 mm is shown in Fig. 4.21.b, on which the two peaks are better resolved. A Gaussian fitting has been performed for a fine

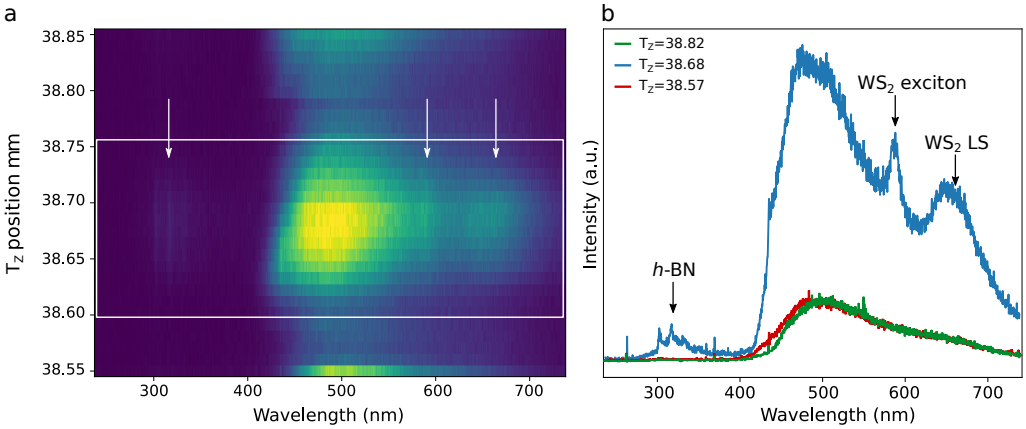

Figure 4.20: *(a) XEOL map acquired for different T_Z positions at a XEOL distance Z=15 mm. (b) XEOL spectra extracted form the relative T_Z values in the XEOL map, showing the presence of extra peaks in the Visible range in correspondence of the h–BN position.*

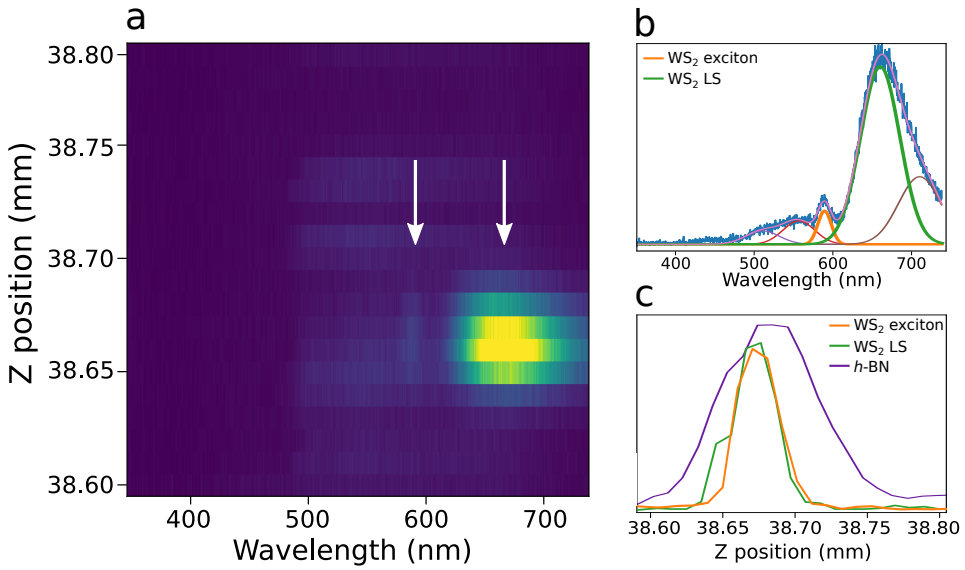

Figure 4.21: *(a) XEOL map acquired for different T_Z positions. (b-d) XEOL spectra extracted form the relative color line in the XEOL map, showing the presence of extra peaks in correspondence of the h–BN position, determined by the UV peaks.*

determination of the peaks' energy and width. The higher energy peak is centered at λ=590 nm (2.1 eV) with a FWHM of 21 nm (75 meV), while the second peak is centered at 660 nm (1.89 eV) and has a FWHM of 72 nm (200 meV). The highest energy luminescence can be attributed to the X_A exciton of WS_2 while the second one has been previously reported to localized states (LS) [211–213].

These peaks are slightly shifted in energy with respect to the PL spectrum acquired

at room temperature shown in Fig. 4.17. The LS peak at low energy has been reported to appear only at cryogenic experiments, for temperatures lower than 80 K [214]. Moreover, the energies of the TMDs are sensible to temperatures, where usually a blue-shift of the exciton is witnessed for decreasing temperatures. In a previous work it has also been showed that transferred WS_2 may show a further blue shift of the X_A exciton together with a red shift of the LS peak [213]. Similar emission bands with the lower energies than those of exciton and trions states have often been observed in other TMDs monolayers of MoS_2, $MoSe_2$ and WSe_2 [215–218]. These effects have been linked to bandgap vibrations associated to tensile strain and bonding. In our case the WS_2 monolayer is mounted over a thin BN crystal lying over a very flexible polymer film. Possible deformations of the TMD are therefore highly likely.

The intensity ratio between the exciton and LS peak has been studied to depend on many factors, including the incident photon flux [212, 213]. Using a Gaussian fitting routine, the luminescence intensity of the X_A exciton and LS peaks has been extracted as a function of the T_Z position, and is reported in Fig. 4.21.c together with the *h*–BN one extracted from the integration of the 4.1 eV group peak in the previous XEOL map (Fig. 4.20.a). Both the X_A and LS peaks appears more localized with respect to *h*–BN and the extracted size is of ca 60 μm, corresponding to the original size of the synthesized flakes.

To study the dependence of the WS_2 luminescence as a function of the *h*–BN excitation, we performed a map over the boron K-edge for both horizontal and vertical polarization at 18 K. Fig. 4.22.a shows the XEOL map obtained while scanning the incident beam energy between 185 and 205 eV with horizontal polarization, with energy steps of 0.1 eV, and Fig. 4.22.b shows a single spectrum extracted from the map. The high-energy continuous emission, which corresponds to the tail of the *h*–BN defects luminescence, is here strongly attenuated by the lens chromatic aberrations.

The intensity of the main spectral components has been extracted as a function of the excitation energy using a multi-Gaussian fitting routine, similarly to what has been done for the oxygen related luminescence (Fig. 4.15). The partial luminescence yield derived from the *h*–BN emission (Fig. 4.22.c) shows the same features as pristine *h*–BN (Fig. 4.13.b), but with different relative intensities between π^* and σ^* peaks. While for the perfect *h*–BN crystal the contribution of the σ^* was significantly reduced at horizontal polarization, in this case it results to be comparable with the one of the π^*. This observation can be explained as a different incident angle less grazing to the normal surface. While the *h*–BN monocrystal was directly glued on the beamline sample holder, the *h*–BN/WS_2 heterostructure is placed on the less flat surface of a thick polymer. The edge jump of the signal is negative, as expected for XEOL deriving from primary excitations in the bulk. The partial luminescence yield of the WS_2 exciton and LS peaks present instead a positive edge jump, and therefore they derive from surface excitations. This result indicates that the WS_2 luminescence is linked to primary excitations at the *h*–BN surface, providing a strong evidence for an excitation transfer mechanism even if the effective process can not be easily discriminated. Indeed, for thin and strongly luminescent materials on top of a thick absorbing substrate, if the electronic

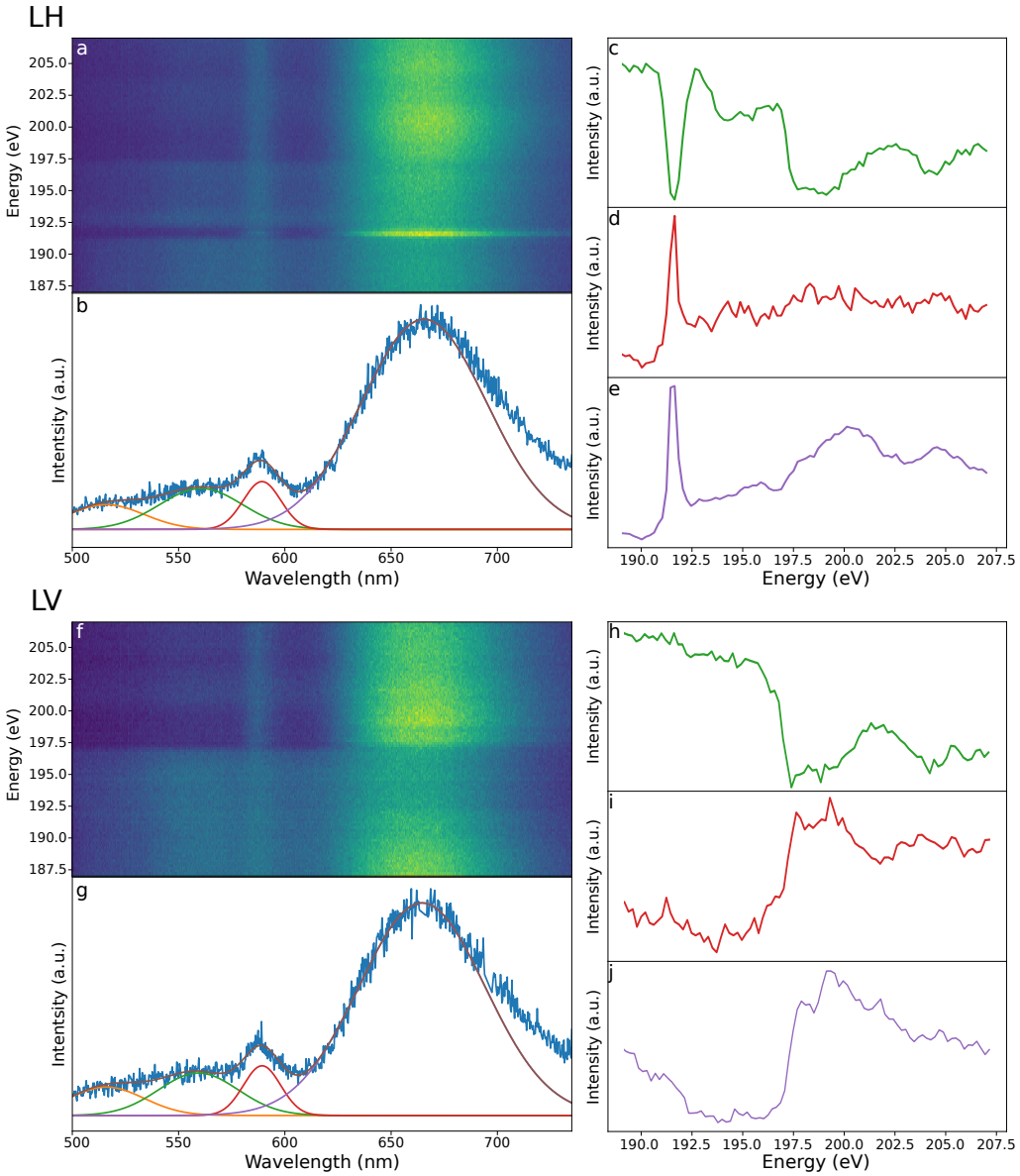

Figure 4.22: *(a) XEOL map of a stack of a WS_2 monolayer over an h–BN crystal across the B K-edge for an horizontal polarization. (b) XEOL spectrum obtained at the 192 eV beam energy. The orange and green Gaussians have been used to fit the h–BN luminescence while the red and violet curves corresponds to the WS_2 exciton and trion emissions. (c-e) Intensity as a function of the beam energy of the spectral component indicated in (b). (f-j) Same measurements across the B K-edge for a vertical polarization*

excitation can migrate to the surface of the substrate, no-matter the kind of excitation transfer between the two materials, the Near-Edge XEOL structure signal coming form the top-layer is expected to be positive when the incident X-ray energy is tuned at the absorption edge of a given element present in the substrate [163]. This is exactly the case of our heterostructure, since the penetration depth for *h*–BN under the experimental conditions employed, of ca. 30 nm, is believed to be less than the diffusion length of the excitation. Interestingly, the near edge adsorption fine structure extracted from the TMD emission peaks differs from that of bulk *h*–BN, as shown in Fig. 4.22.d,e. Both the WS_2 exciton and LS peak derived PLY spectra show a very strong π^* peak, in agreement with Fig. 4.22.c. However, the fine structure of the boron absorption edge differs at higher energies. At a first look, it resembles the σ^* structure observed on the *h*–BN monocrystal for an incident linear horizontal polarization (4.13.b, blue curve) suggesting a different orientation of the WS_2 flake in respect to the substrate. However orientation can not explain alone the differences observed: for a linear horizontal polarization , while the σ^* peak of an *h*–BN crystal (4.13.b) is centered at 198 eV, the structure observed for the WS_2 derived PLY curves is centered at 200 eV. This difference can be tentatively attributed to a re-hybridization between the boron out of plane orbitals of *h*–BN and the ones of the TMD monolayer. This effect can occur only for the upper *h*–BN layer directly in contact with the WS_2, which would also explain the positive sign of Near-Edge XEOL.

The Excitation vs. Emission map obtained for an incident vertical polarization is reported in Fig. 4.22.f, while Fig. 4.22.g shows a single spectrum extracted from the map, which resembles the one of Fig. 4.22.b. The PLY signal derived for the *h*–BN emission (Fig. 4.22.h) is characterized by the sole σ^* contribution, in agreement with an incident vertical polarization. The same structure can be found in both the PLY signal derived from the WS_2 exciton (Fig. 4.22.i) and LS peak (Fig. 4.22.j). This result suggests that if the re-hybridization is responsible for the different fine structures observed in Fig. 4.22.d,e, it is solely linked to the out of plane orbitals of boron.

XEOL measurements were employed to investigate excitation transfer between WS_2 and *h*–BN in their vertical heterostructure. An enhancement in the WS_2 XEOL signal was observed when the incident X-ray photons resonate with the boron K-edge, indicating excitations within the *h*–BN substrate in the heterostructure. The Near-Edge XEOL structure derived aligns with the B-K edge of *h*–BN, signifying that the excitation of the *h*–BN substrate triggers the TMD's excitation. Nevertheless, a distinct absorption fine structure is observed for an incident horizontal polarization, with a broad peak centered at 200 eV. To our knowledge this feature can not be associated to any known boron fine structure, suggesting a possible re-hybridization of the electronic states at the WS_2 monolayer with the ones at the upper *h*–BN layer. As for the newly implemented XEOL setup, this study, in conjunction with the benchmarks presented in the previous section, demonstrates its operation, limitations, and potential applications.

CHAPTER 5

Concluding remarks and perspectives

This thesis has been devoted to the development of novel instrumental and methodological characterization techniques tackling both electron microscopy and synchrotron based spectroscopies. In particular, at my host laboratory I have established a new 4D-STEM operating mode for the there installed aberration corrected microscopes and developed a new more general data analysis protocol. At the SOLEIL synchrotron, I have commissioned a novel XEOL setup integrated into the RIXS branch of the SEXTANTS beamline and established data acquisition and analysis strategies which permit to link specific near absorption edge fine structures to well defined luminescence signals. Benchmarks of these realizations have been performed over *h*–BN based samples and the performance obtained outcomes previous results.

Charge density redistribution in defective and heterogeneous crystals can be in principle effectively evaluated by modern numerical methods such as DFT, but these theoretical predictions still requires experimental validations. However, there is still a lack of experimental techniques which can provide this information at the relevant atomic scale with the required precision. The novel 4D-STEM technique, where a complete CBED pattern is collected for each position of a highly focused electron probe scanning the sample, may in principle address this problem. While the method has been already extensively employed for 2D materials, quantitative estimations of charge accumulation at defective sites have not been reported yet.

In this thesis it has been demonstrated for the first time that a quantitative analysis can be effectively obtained via a meticulous comparison of experiments, multislice 4D-STEM simulations, and all-electron full-potential DFT calculations. For this purpose, 4D-STEM experiments have been conducted on self-suspended monolayer *h*–BN. Our analysis has demonstrated that a direct measure of the charge transfer from boron to nitrogen is hindered by probe size broadening effects, given that the interatomic distance is comparable to the electron probe size. Following the results on pristine *h*–BN, the case of a zig-zag edge has been taken into account, where, in accordance with previous studies, an apparent strong enhancement of the electric field has been observed. However, by a comparison with DFT calculations, we demonstrated that this enhancement is not

due to a very strong local field, but rather to the probe-material interaction effects, and it is proportional to the electron probe size. While the probe finite size hinders a direct measurement of the surface field, charge accumulation can be precisely estimated when considering appropriate integration regions. This procedure has permitted to measure a charge depletion of ca. 0.37 e^- at the outer BN formula unit, which is in excellent agreement with the theoretical estimate of 0.4 e^-.

4D-STEM has also been used to identify the precise structure of point defects in monolayer *h*–BN, such as adatoms and boron monovacancy. We have shown that for this class of defects, 4D-STEM derived CoM maps overcome conventional imaging techniques, such as HAADF. Furthermore, a qualitative analysis of charge density redistribution at boron monovacancies in an *h*–BN monolayer was obtained by filtering the high-frequency components corresponding to the hexagonal lattice. This post-processing has permitted to demonstrate an accumulation of negative charges on boron vacancy site coupled with an accumulation of positive charges on neighboring nitrogen atoms.

The overall methodology developed opens wide perspectives for both quantitative and qualitative studies on charge redistribution in low-dimensional materials. In previous works these effects were only qualitatively estimated on monolayer 2D materials by comparing CoM maps obtained at defective and pristine area. In this thesis I have demonstrated that the definition of appropriate integration regions permits a quantitative estimation of charge transfer effects at the *h*–BN edge with a sensibility of a fraction of the electron charge at a few angstrom scale. This procedure can be extended for assessing charge redistribution in point defects, including adatoms, vacancies, or dopants. For these systems qualitative information has already been obtained using appropriate filters on charge density maps but quantitative evaluations can be in principle achieved by identifying relevant integration regions such as multiples unit cells centered at the point defects. However, particular care should be taken due to the high sensitivity of the method to integration limits and scan distortions. The methodology developed and applied to the *h*–BN case can be easily extended to other 2D systems. Edge effects in TMDs previously investigated only at a qualitative level by 4D-STEM can now be revisited in a more quantitative way. A successful application of the method can also be expected for point defects such as nitrogen dopants in graphene and single vanadium dopants in monolayer WSe_2, for which previous studies by HRTEM or 4D-STEM have reported a local negative charge accumulation at the defective site[8, 121].

Besides the simple monolayer case, further experiments may also be performed on more complex systems leading to the formation of moiré patterns such as twisted 2D bilayers and heterostructures. Preliminary experiments performed on a twisted *h*–BN bilayer are here reported in Fig. 5.1. 4D-STEM provides an image contrast enhancement in respect to more ordinary HAADF imaging. The long scale intensity fluctuations on field and charge density maps arise essentially from geometrical effects but the in-plane component of the long range moiré potential could be in principle extracted following the filtering principles illustrated in Sec. 2.5. However, to have an accurate representation of the low frequency moiré components, extended moiré regions are required. These structures can be hardly found in ordinary samples where well defined moiré patterns

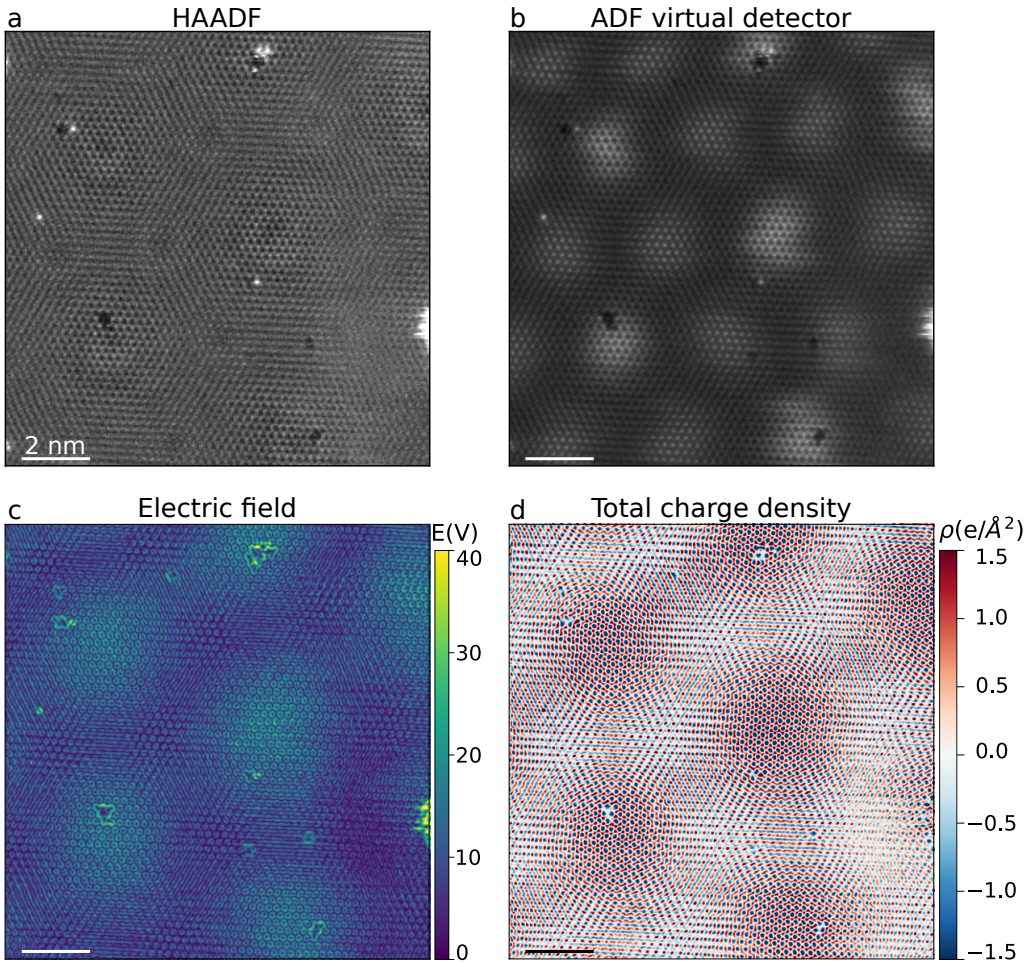

Figure 5.1: *(a) HAADF image of an h–BN moiré pattern. (b) 4D-STEM reconstructed ADF virtual detector of the same area as (a), showing a distinguished contrast. 4D-STEM derived (c) electric field modulus and (d) total charge density maps of the moiré pattern.*

occur only at regions were monolayers have been folded on themselves. A further complication arise from the amplitude of the moiré potential much smaller than the atomic potential.

A general limit to improve the CoM maps resolution and to achieve an effective atomic resolution is to have a good knowledge of the electron probe shape and size; a possible way to overcome this problem might be given by ptychography. Once the experimental electron probe is determined, it is in principle possible to directly reconstruct the phase map of the studied materials with an improved resolution removing aberrations related effect, which as demonstrated may affect the relative intensities in charge density maps. Another route could be the direct deconvolution of the experimental measurements with the reconstructed probe even if deconvolution usually enhance the noise of the

image. However, the very rigorous experimental requirements of ptychography and the instabilities of reconstruction algorithms make quantitative assessments of charge at the atomic scale still beyond the state of the art of the technique.

Finally 4D-STEM could be also used for the chemical identification of dopants in a 2D materials. For instance, it might be hard to perform EELS at ad-atoms due to the high mobility of this class of defects, but a chemical information can be retrieved via imaging. Contrast in CoM derived total charge density maps is directly proportional to the nuclear number Z, while in HAADF higher order polynomial makes more difficult to discriminate between different atomic species.

The second part of this thesis has regarded the testing of the ultimate performance of the XEOL setup installed at the RIXS branch of the SEXTANTS beamline, at the synchrotron SOLEIL. In this ambit I have established an operational protocol for XEOL measurements, allowing for an automatic record of XEOL spectra as a function of the incident X-ray energy scanned across the absorption edge of interesting elements. Benchmarks performed on different BN structures have shown an optical detection that spans from the far UV to the near IR, with a spectral resolution of few meV, bringing this setup close to the optical performances obtained by PL in the last years. The acquisition of excitation energy vs. emission energy maps has proven to be useful allowing to correlate luminescence and structure. In particular, by selecting a specific luminescence component and integrating the signal across the excitation energy, it is possible to extract the near edge fine structure responsible for the excitation. This procedure has been applied for the localization of Eu^{3+} dopants in the cubic phase of a mixed *h*–BN/*c*–BN crystal demonstrating that they lie solely on *c*–BN, and to identify the contribution of boron oxydes to the complex emission of usual *h*–BN samples.

Very bright emissions in *h*–BN, with a zero phonon line at 4.1 eV, are believed to be linked with the presence of carbon. Nevertheless a direct experimental proof has not been provided yet. XEOL could in principle answer to this open question: performing measurements on heavily carbon doped *h*–BN crystals, the XEOL signal should rise in resonance with the carbon K-edge. However, these measurements might be hard since the beamline presents a strong absorption peak at these energies due to the deposition of carbon on the beamline's optics.

XEOL measurements have also been performed to investigate the excitation transfer between *h*–BN and WS_2 in vertical heterostructures. Previous CL experiments showed that the encapsulation of different TMDs in between thick *h*–BN flakes gives rise to an enhancement of the luminescence together with sharper emission peaks, a behavior which has been tentatively attributed to the protective effect of *h*–BN and to an excitation transfer of the hole-electron pair from the wide band gap *h*–BN to the TMD layer. To study this effect, XEOL maps across the B K-edge and at 18 K have been performed on a vertical stack composed by a thick *h*–BN flake on which a WS_2 monolayer had been deposited. The PLY signal derived for the WS_2 exciton was strongly enhanced at the B K-edge, suggesting a direct electron-hole transfer between the *h*–BN surface layers and the WS_2 monolayer. The B K-edge absorption edge derived from the TMD PLY signals presented a distinct fine structure at energies higher than the π^* peak, suggesting

a possible re-hybridization between the boron orbitals and the WS_2 ones.

The XEOL setup is now operational and open to user projects. The idea of coupling RIXS with XEOL and therefore of integrating a XEOL setup at the inelastic branch of the SEXTANTS beamline is fruit of a tight collaboration between the STEM group of LPS and A. Nicolaou. In this ambit such a spectroscopy was integrated to a novel sample environment (MAGELEC) for performing operando RIXS experiments under electric and magnetic fields. This capability has already been employed in an ongoing study on the spectroscopic response of the 2D magnetic material CrSBr, which is part of the post-doctoral project of Victor Porée. The study involves the correlation between RIXS and XEOL: while the optical onset as a function of the magnetic field can be studied by XEOL, RIXS investigates the d-Cr orbitals on which magnetism takes place.

Further improvements for the XEOL setup are planned. A reflective optics will be used to avoid the strong chromatic aberration discussed in Sec. 4.3; due to the long work distances employed, defined by the physical constrains of the electromagnet, tailored optics might be necessary. Currently the XEOL spectrometer and CCD camera are not fully integrated in the control and acquisition system of SOLEIL, and complex scripts are required to synchronized the setup. The development of a dedicated device for TANGO (the device-oriented controls toolkit on which the SOLEIL acquisition system is based) will permit a full integration of the XEOL on the beamline control infrastructure.

Finally, the developed XEOL setup can be easily reproduced on other beamlines. The optical bench on which the spectrometer and CCD camera are placed is mounted on wheels to move it inside the SOLEIL synchrotron. It is currently under study to reproduce the setup for the GALAXIES beamline. The beamline can perform RIXS experiments in the hard X-ray domain complementing the capabilities of the SEXTANTS beamline. The beamline works in air, which simplifies the design of the XEOL optics but the motorization of the XEOL three axes micrometric translator will be necessary for remote control.

Within this PhD thesis I have demonstrated the successful implementation of two novel advanced characterization techniques, 4D-STEM and XEOL. The results obtained go beyond the state of the art of techniques and sketch the great potential of the methods. The maturity of these developments, both from an instrumental and methodological point of view, permits now to open my realizations also to other users. I am pleased to note that novel studies on which I am only marginally implicated are already on-going. While my works have been mostly focused on *h*–BN, I am hopeful that the arguments provided in this manuscript will contribute to define the domain of applicability of the techniques and ultimately to design novel successful experiments.

CHAPTER 6

Résumé en français

Les propriétés des matériaux peuvent changer à l'échelle nanométrique par rapport à leur équivalent en vrac en raison des hétérogénéités et des effets quantiques. Ces deux dernières décennies ont vu un intérêt croissant pour la nanoscience en raison de la diversité des disciplines scientifiques qu'elle englobe, allant de la physique à la chimie, en passant par les sciences des matériaux et la biologie. Cet intérêt est motivé par le désir de comprendre des propriétés uniques et de les utiliser pour des développements technologiques innovants. Cependant, afin d'étudier expérimentalement de telles propriétés, il existe une quête persistante de nouvelles techniques instrumentales et de méthodologies. Cette nécessité découle de la difficulté d'imager des structures et de mesurer des propriétés physiques à l'échelle nanométrique.

Une technique classique pour accéder à des informations structurales à l'échelle sub-nanométrique est la microscopie électronique en transmission (MET), qui, avec l'avènement de correcteurs d'aberration, a permis l'examen d'une large gamme de matériaux à l'échelle atomique. Une autre approche pour étudier des phénomènes localisés consiste à utiliser des techniques résonantes, où la localisation est obtenue par l'énergie sélective de l'excitation primaire, en accord avec des transitions spécifiques du matériau étudié. Les spectroscopies des rayons X réalisées auprès de sources de rayonnement synchrotron sont bien adaptées à cet objectif. Ce manuscrit s'inscrit dans ce contexte, présentant le développement et l'utilisation de techniques expérimentales innovantes et complémentaires liées à la microscopie électronique en transmission et aux rayonnements synchrotron pour l'étude des propriétés nanométriques.

4D-STEM Une sous-catégorie de la MET est la microscopie électronique en transmission à balayage (STEM), où une sonde fortement focalisée est balayée à travers la zone d'intérêt de l'échantillon. Le STEM offre généralement la possibilité de produire une variété de contrastes d'imagerie révélant des détails structuraux spécifiques, cela étant rendu possible en incorporant plusieurs détecteurs qui capturent les signaux d'électrons dispersés à différents angles. Les récents progrès dans les détecteurs rapides et haute-

ment sensibles ont considérablement amélioré les capacités des microscopes STEM. En particulier, la mise en œuvre de détecteurs pixellisés au plan de diffraction a permis la collecte de motifs complets de diffraction électronique en faisceau convergent (CBED) pour chaque position de la sonde, conduisant à la création d'un ensemble de données quadridimensionnel (4D-STEM). Cette avancée a élargi les capacités de la microscopie électronique, ouvrant la voie à de nouveaux observables, tels que les champs électriques et les densités de charge, avec des détails sans précédent.

Cette application spécifique du 4D-STEM a suscité un intérêt significatif au cours des cinq dernières années, se présentant comme un outil précieux pour l'étude des effets de charge à travers une gamme diversifiée de matériaux, allant des oxydes ferroélectriques aux matériaux défectueux de basse dimension. Cependant, dans cette dernière catégorie, la plupart des travaux publiés ont principalement présenté des résultats qualitatifs. Ces résultats mettent généralement en avant des cartes hypothétiques de champs électriques à l'échelle atomique et de densités de charge, soulevant ainsi des questions sur la nécessité d'une analyse quantitative plus convaincante.

De plus, dans la majorité de ces travaux, l'influence des interactions sonde-matériau n'a pas été explicitement abordée. Cela devient particulièrement crucial lors de l'exploration de systèmes défectueux, où les effets de la sonde peuvent affecter considérablement les mesures. Sans une étude approfondie de cette contribution, il existe un risque de tirer des conclusions trompeuses, pouvant potentiellement conduire à des inexactitudes dans l'interprétation physique des résultats.

Dans cette thèse, une étude exhaustive en 4D-STEM a été menée pour examiner les capacités ultimes de cette technique dans l'analyse quantitative du champ électrique et de la densité de charge dans les matériaux de basse dimension. Un interest particulier a été mis sur la compréhension de l'influence des effets liés à la sonde électronique sur la mesure de ces propriétés à l'échelle atomique. Cette étude a été réalisée sur le matériau 2D archétypal, le nitrure de bore hexagonal (*h*–BN). Composé d'atomes légers, le *h*–BN représente le candidat idéal pour explorer les capacités ultimes de la 4D-STEM pour des études de quantification du champ électrique et de la densité de charge. Plus important encore, le *h*–BN se caractérise par un certain nombre d'électrons de valence et de cœur comparables, ce qui permet de distinguer les deux contributions, et présente un transfert de charge significatif entre le bore et l'azote.

En effectuant une comparaison précise avec des simulations en 4D-STEM par la méthode des tranches multiples et des calculs DFT à potentiel complet tous électrons, cette thèse a démontré que l'analyse quantitative peut être effectuée de manière efficace, avec un accord exceptionnel entre les trois cas. Une attention particulière a été accordée à la compréhension de toutes les différentes composantes qui contribuent au déplacement des électrons, à savoir les noyaux et les électrons. Néanmoins, pour étudier les phénomènes de transfert de charge, il est nécessaire d'isoler les seules composantes électroniques. Cela a été rendu possible en soustrayant les contributions nucléaires, construites en plaçant une fonction delta normalisée par le numéro atomique aux sites atomiques et convoluée par la function de la sonde électronique. La comparaison entre la densité de charge électronique expérimentale et théorique a une fois de plus montré

un bon accord, mettant en évidence la grande sensibilité de cette technique. Cependant, au niveau atomique, il n'a pas été possible d'extraire une valeur numérique du transfert de charge du bore vers l'azote, qui est prédit être d'environ $2e^-$, en raison de l'effet d'élargissement dû à la taille de la sonde.

Suite à l'étude du *h*–BN non défectueux, les densités de champ électrique et de charge ont été évaluées pour le cas d'une extrémité en zigzag terminée par de l'azote. Comme déjà rapporté dans des études antérieures, une forte augmentation du champ électrique à la position de l'extrémité a été observée. Cependant, dans ce travail, j'ai démontré comment cette amélioration n'est pas purement due à un potentiel plus fort, mais plutôt aux effets d'interaction sonde-électronique, et semble être proportionnelle à la taille de la sonde. Cependant, cet effet important est probablement dû au fait que le champ électrique est une quantité vectorielle. La densité de charge, en revanche, est une quantité scalaire. Bien que l'intégration au niveau atomique ne soit pas possible en raison de dimensions similaires de la sonde électronique incidente et de la distance interatomique, l'intégration sur des zones plus grandes devrait donner un résultat précis. Cela a été appliqué au cas de l'extrémité en zigzag, où les fenêtres d'intégration correspondant à a se sont avérées donner des estimations correctes de la charge totale pour les états en vrac et en bordure, révélant une accumulation nette de charge positive d'environ 0,4 électrons.

La technique 4D-STEM a ensuite été utilisée pour la détermination structurale dans le cas de défauts ponctuels tels que les lacunes de bore et les adatomes de silicium et de calcium sur des feuilles peu épaisses de *h*–BN. Dans ce cas, les images à contraste amélioré produites par les champs électriques et les densités de charge se sont avérées permettre l'accès à des informations structurales difficiles à obtenir avec des techniques d'imagerie standard, telles que la HAADF. En particulier, dans le cas des lacunes de bore sur une feuille multicouche de *h*–BN, les effets indésirables des cartes de champ électrique liés à l'interaction sonde-échantillon sont utiles pour les localiser immédiatement. En ce qui concerne les adatomes, leur détermination structurale peut être facilement établie par la symétrie de la forme du champ électrique généré.

XEOL L'imagerie STEM est essentiellement basée sur les informations provenant de la diffusion élastique des électrons, mais les processus inélastiques peuvent également être étudiés avec la même résolution spatiale élevée, jusqu'au niveau atomique. La spectroscopie de perte d'énergie des électrons (EELS) est une technique bien établie qui, ces dernières années, a bénéficié de la disponibilité d'équipements monochromes performants qui ont permis d'étendre son domaine d'applicabilité énergétique. Il est désormais possible d'étudier une large gamme d'énergie, allant de quelques dixièmes de meV à quelques keV, donnant accès à diverses excitations telles que les phonons, les excitons, les plasmons et les excitations de cœur. Au cours des quinze dernières années, mon groupe d'accueil au LPS a également développé un équipement de catholuminescence spécifique pour la microscopie STEM. Cette installation combinant EELS et nano-CL a ouvert la voie à des études corrélatives des processus d'excitation et de désexcitation avec une résolution spatiale nanométrique.

Alors que les spectroscopies électroniques STEM offrent une grande sélectivité

spatiale, les sources synchrotron permettent une polarisation bien définie du rayonnement d'excitation et une sélectivité des éléments lorsque l'énergie est choisie en résonance avec des bords spécifiques du noyau. La spectroscopie EELS est traditionnellement associée à la spectroscopie d'absorption des rayons X près des bords (XANES) pour l'étude des structures fines sur les bords d'absorption du noyau. Les progrès récents de la spectroscopie EELS à basse énergie ont facilité les études dans le domaine IR-optique, un domaine énergétique accessible également par la spectroscopie inélastique de rayons X (résonante), (R)IXS. La RIXS se concentre sur les phénomènes d'excitation neutre avec des états d'énergie initiaux et finaux identiques à ceux de l'EELS, mais sa particularité réside dans le fait qu'il s'agit d'une technique résonante. Les deux techniques sont donc très complémentaires et les études corrélatives sont particulièrement adaptées.

En ce qui concerne l'étude des phénomènes de recombinaison dans le domaine optique, la cathodoluminescence peut être liée à la spectroscopie de luminescence optique excitée par les rayons X (XEOL). La XEOL est une technique d'entrée de photons de rayons X et de sortie de photons optiques qui implique la conversion de l'énergie des rayons X absorbée par les matériaux en photons optiques, ce qui implique des processus de transfert d'énergie en plusieurs étapes. Cette technique remonte aux premiers jours des rayons X et, au cours des dernières décennies, des dispositifs XEOL ont été installés dans diverses installations synchrotron et couplés à plusieurs techniques de rayons X. Cependant, son intégration avec les spectroscopies synchrotron qui étudient le domaine optique n'a pas encore été pleinement explorée. Dans ce contexte, il est tout à fait approprié de combiner RIXS et XEOL sur une seule ligne de faisceau. Cette approche serait similaire au couplage EELS-CL dans un STEM, permettant des études corrélées des phénomènes d'excitation et de recombinaison.

Ces quatre techniques spectroscopiques ont accès au domaine spectral UV-C, généralement difficile à atteindre par les techniques optiques, mais essentiel pour comprendre les matériaux à large bande interdite.

Une partie importante de ma thèse a été consacrée à l'implémentation et à la mise en service d'un nouveau dispositif XEOL UV-VIS sur la branche dédiée à RIXS de la ligne de faisceau de rayons X mous SEXTANTS, située au synchrotron SOLEIL. Une attention particulière a été portée à l'exploration de la corrélation entre la structure et la luminescence grâce à XEOL. En effet, XEOL permet de mesurer la luminescence en fonction de l'énergie du faisceau incident, en balayant les bords d'absorption du noyau des éléments de l'échantillon. À partir de l'intégration de l'intensité XEOL, il est possible de reconstruire ce que l'on appelle le Near-Edge XEOL, à partir duquel des structures fines d'absorption spécifiques peuvent être associées à des caractéristiques de luminescence bien définies.

Grâce à la synchronisation entre le spectromètre XEOL et le monochromateur de la ligne de faisceau, des cartes d'énergie d'excitation par rapport à la luminescence optique peuvent être collectées. Cette application particulière permet la séparation de différentes caractéristiques spectroscopiques de la luminescence et la dérivation de la structure responsable de ces caractéristiques.

Des benchmarks réalisés sur différentes structures BN ont montré une détection

optique qui s'étend de l'UV lointain au proche IR, avec une résolution spectrale de quelques meV, rapprochant ce dispositif des performances optiques obtenues par PL ces dernières années. L'acquisition de cartes d'énergie d'excitation par rapport à l'énergie d'émission s'est avérée utile pour corréler la luminescence et la structure. En particulier, en sélectionnant une composante spécifique de la luminescence et en intégrant le signal à travers l'énergie d'excitation, il est possible d'extraire la structure fine du bord proche responsable de l'excitation. Cette procédure a été appliquée à la localisation des dopants Eu^{3+} dans la phase cubique d'un cristal mixte *h*–BN/*c*–BN, démontrant qu'ils se trouvent uniquement sur *c*–BN, et pour identifier la contribution des oxydes de bore à l'émission complexe des échantillons *h*–BN habituels.

Des mesures XEOL ont également été réalisées pour étudier le transfert d'excitation entre *h*–BN et WS_2 dans les hétérostructures verticales. Des expériences CL antérieures ont montré que l'encapsulation de différents TMD entre des flocons épais de *h*–BN donne lieu à une augmentation de la luminescence ainsi qu'à des pics d'émission plus nets, un comportement qui a été provisoirement attribué à l'effet protecteur de *h*–BN et à un transfert d'excitation de la paire trou-électron de la large bande interdite de *h*–BN à la couche TMD. Pour étudier cet effet, des cartes XEOL à travers le bord B K et à 18 K ont été réalisées sur une pile verticale composée d'une épaisse couche d'*h*–BN sur laquelle une monocouche d'WS_2 avait été déposée. Le signal dérivé pour l'exciton WS_2 était fortement renforcé à l'arête B K, ce qui suggère un transfert direct électron-trou entre les couches de surface *h*–BN et la monocouche WS_2. Le bord d'absorption de l'arc B K dérivé des signaux du TMD présentait une structure fine distincte à des énergies plus élevées que le pic π^*, suggérant une réhybridation possible entre les orbitales du bore et celles de WS_2.

Bibliography

[1] J.-Y. Mao, S. Wu, G. Ding, Z.-P. Wang, F.-S. Qian, J.-Q. Yang, Y. Zhou, and S.-T. Han, *A van der Waals Integrated Damage-Free Memristor Based on Layered 2D Hexagonal Boron Nitride*, Small **18**, 2106253 (2022).

[2] J. I.-J. Wang et al., *Hexagonal boron nitride as a low-loss dielectric for superconducting quantum circuits and qubits*, Nat. Mat. **21**, 398 (2022).

[3] R. Bourrellier, S. Meuret, A. Tararan, O. Stéphan, M. Kociak, L. H. G. Tizei, and A. Zobelli, *Bright UV Single Photon Emission at Point Defects in h-BN*, Nano Lett. **16**, 4317 (2016).

[4] L. Pauling, *The structure and properties of graphite and boron nitride*, Proc. Natl. Acad. Sci. **56**, 1646 (1966).

[5] S. Yamamura, M. Takata, and M. Sakata, *Charge density of hexagonal boron nitride using synchrotron radiation powder data by maximum entropy method*, J. Phys. Chem. Solids **58**, 177 (1997).

[6] C. Rohmann, V. I. Yamakov, C. Park, C. Fay, M. Hankel, and D. J. Searles, *Interaction of Boron Nitride Nanotubes with Aluminum: A Computational Study*, The Journal of Physical Chemistry C **122**, 15226 (2018).

[7] L.-C. Yin, H.-M. Cheng, and R. Saito, *Triangle defect states of hexagonal boron nitride atomic layer: Density functional theory calculations*, Phys. Rev. B **81**, 153407 (2010).

[8] J. C. Meyer, S. Kurasch, H. J. Park, V. Skakalova, D. Künzel, A. Groß, A. Chuvilin, G. Algara-Siller, S. Roth, T. Iwasaki, U. Starke, J. H. Smet, and U. Kaiser, *Experimental analysis of charge redistribution due to chemical bonding by high-resolution transmission electron microscopy*, Nat. Mater. **10**, 209 (2011).

[9] K. Watanabe, T. Taniguchi, and H. Kanda, *Direct-band gap properties and evidence for ultraviolet lasing of hexagonal boron nitride single crystal*, Nat. Mater. **3**, 404 (2004).

[10] W.-Q. Han, L. Wu, Y. Zhu, K. Watanabe, and T. Taniguchi, *Structure of chemically derived mono- and few-atomic-layer boron nitride sheets*, Appl. Phys. Lett. **93**, 223103 (2008).

[11] B. Arnaud, S. Lebègue, P. Rabiller, and M. Alouani, *Huge Excitonic Effects in Layered Hexagonal Boron Nitride*, Phys. Rev. Lett. **96**, 026402 (2006).

[12] L. Wirtz, A. Marini, M. Gruning, and A. Rubio, *Excitonic effects in optical absorption and electron-energy loss spectra of hexagonal boron nitride*, (2005).

[13] L. Wirtz, A. Marini, M. Grüning, C. Attaccalite, G. Kresse, and A. Rubio, *Comment on "Huge Excitonic Effects in Layered Hexagonal Boron Nitride"*, Phys. Rev. Lett. **100**, 189701 (2008).

[14] G. Cassabois, P. Valvin, and B. Gil, *Hexagonal boron nitride is an indirect bandgap semiconductor*, Nat. Photonics **10**, 262–266 (2016).

[15] T. Q. P. Vuong, S. Liu, A. Van der Lee, R. Cuscó, L. Artús, T. Michel, P. Valvin, J. H. Edgar, G. Cassabois, and B. Gil, *Isotope engineering of van der Waals interactions in hexagonal boron nitride*, Nat. Mater. **17**, 152 (2018).

[16] E. Cannuccia, B. Monserrat, and C. Attaccalite, *Theory of phonon-assisted luminescence in solids: Application to hexagonal boron nitride*, Phys. Rev. B **99**, 081109 (2019).

[17] F. Paleari, H. P. C. Miranda, A. Molina-Sánchez, and L. Wirtz, *Exciton-Phonon Coupling in the Ultraviolet Absorption and Emission Spectra of Bulk Hexagonal Boron Nitride*, Phys. Rev. Lett. **122**, 187401 (2019).

[18] T. Q. P. Vuong, G. Cassabois, P. Valvin, A. Ouerghi, Y. Chassagneux, C. Voisin, and B. Gil, *Phonon-Photon Mapping in a Color Center in Hexagonal Boron Nitride*, Phys. Rev. Lett. **117**, 097402 (2016).

[19] T. T. Tran, K. Bray, M. J. Ford, M. Toth, and I. Aharonovich, *Quantum emission from hexagonal boron nitride monolayers*, Nat. Nanotechnol. **11**, 37 (2016).

[20] R. Egerton, *Electron Energy-Loss Spectroscopy in the Electron Microscope*, Springer, 2011.

[21] D. B. Williams and C. B. Carter, *Transmission electron microscopy: A textbook for materials science*, Springer, 2009.

[22] E. Ruska, *The development of the electron microscope and of electron microscopy*, Rev. Mod. Phys. **59**, 627 (1987).

[23] L. E. P. R. Buseck, J. M. Cowley, *High-Resolution Transmission Electron Microscopy and Associated Techniques.*, Oxfrod University Press, 1993.

[24] M. De Graef, *Introduction to Conventional Transmission Electron Microscopy*, Cambridge University Press, 2003.

[25] E. J. Kirkland, *Advanced computing in electron microscopy*, Springer, 2010.

[26] O. Krivanek, G. Corbin, N. Dellby, B. Elston, R. Keyse, M. Murfitt, C. Own, Z. Szilagyi, and J. Woodruff, *An electron microscope for the aberration-corrected era*, Ultramicroscopy **108**, 179 (2008).

[27] L. M. Brown, *Aberration-Corrected Analytical Transmission Electron Microscopy*, John Wiley & Sons, 2011.

[28] A. Zobelli, A. Gloter, C. P. Ewels, G. Seifert, and C. Colliex, *Electron knock-on cross section of carbon and boron nitride nanotubes*, Phys. Rev. B **75**, 245402 (2007).

[29] O. Krivanek, T. Lovejoy, and N. Dellby, *Aberration-corrected STEM for atomic-resolution imaging and analysis*, J. Microsc. **259**, 165 (2015).

[30] J. Pizarro, P. L. Galindo, E. Guerrero, A. Yáñez, M. P. Guerrero, A. Rosenauer, D. L. Sales, and S. I. Molina, *Simulation of high angle annular dark field scanning transmission electron microscopy images of large nanostructures*, Appl. Phys. Lett. **93**, 153107 (2008).

[31] P. D. Nellist, *The Principles of STEM Imaging*, Springer, 2011.

[32] C. Colliex, *From early to present and future achievements of EELS in the TEM*, Eur. Phys. J. Appl. Phys. **97**, 38 (2022).

[33] H. Tan, J. Verbeeck, A. Abakumov, and G. Van Tendeloo, *Oxidation state and chemical shift investigation in transition metal oxides by EELS*, Ultramicroscopy **116**, 24 (2012).

[34] W. Zhou, M. D. Kapetanakis, M. P. Prange, S. T. Pantelides, S. J. Pennycook, and J.-C. Idrobo, *Direct Determination of the Chemical Bonding of Individual Impurities in Graphene*, Phys. Rev. Lett. **109**, 206803 (2012).

[35] M. Tencé, J.-D. Blazit, X. Li, M. Krajnak, E. N. del Busto, R. Skogeby, L. Cambou, M. Kociak, O. Stephan, A. Gloter, and et al., *Electron Energy-loss Spectroscopy Using MerlinEM - Medipix3 Detector*, Microsc. Microanal. **26**, 1940–1942 (2020).

[36] Y. Auad, M. Walls, J.-D. Blazit, O. Stéphan, L. H. Tizei, M. Kociak, F. De la Peña, and M. Tencé, *Event-based hyperspectral EELS: towards nanosecond temporal resolution*, Ultramicroscopy **239**, 113539 (2022).

[37] C. Addiego, W. Gao, H. Huyan, and X. Pan, *Probing charge density in materials with atomic resolution in real space*, Nat. Rev. Phys. **5**, 117 (2023).

[38] W. Kohn and L. J. Sham, *Self-Consistent Equations Including Exchange and Correlation Effects*, Phys. Rev. **140**, A1133 (1965).

[39] P. Hohenberg and W. Kohn, *Inhomogeneous Electron Gas*, Phys. Rev. **136**, B864 (1964).

[40] P. Coppens and E. D. Stevens, *Accurate X-Ray Diffraction and Quantum Chemistry: The Study of Charge Density Distributions*, volume 10 of *Advances in Quantum Chemistry*, Academic Press, 1977.

[41] T. S. Koritsanszky and P. Coppens, *Chemical Applications of X-ray Charge-Density Analysis*, Chem. Rev. **101**, 1583 (2001).

[42] A. M. Makal, D. Plażuk, J. Zakrzewski, B. Misterkiewicz, and K. Woźniak, *Experimental Charge Density Analysis of Symmetrically Substituted Ferrocene Derivatives*, Inorg. Chem. **49**, 4046 (2010).

[43] A. Fischer, D. Tiana, W. Scherer, K. Batke, G. Eickerling, H. Svendsen, N. Bindzus, and B. B. Iversen, *Experimental and Theoretical Charge Density Studies at Subatomic Resolution*, J. Phys. Chem. A **115**, 13061 (2011).

[44] J. M. Zuo, *Measurements of electron densities in solids: a real-space view of electronic structure and bonding in inorganic crystals*, Rep. Prog. Phys. **67**, 2053 (2004).

[45] S. Shibata, F. Hirota, and T. Shioda, *Molecular electron density from electron scattering*, J. Mol. Struct. **485**, 1 (1999).

[46] J. M. Zuo, M. Kim, M. O'Keeffe, and J. C. H. Spence, *Direct observation of d-orbital holes and Cu–Cu bonding in Cu2O*, Nature **401**, 49 (1999).

[47] E. L. Wolf, *Principles of Electron Tunneling Spectroscopy*, Oxford University Press, 2011.

[48] G. Cox, D. Szynka, U. Poppe, K. H. Graf, K. Urban, C. Kisielowski-Kemmerich, J. Krüger, and H. Alexander, *Scanning tunneling microscopy of crystal dislocations in gallium arsenide*, Phys. Rev. Lett. **64**, 2402 (1990).

[49] S. M. Hus, R. Ge, P.-A. Chen, L. Liang, G. E. Donnelly, W. Ko, F. Huang, M.-H. Chiang, A.-P. Li, and D. Akinwande, *Observation of single-defect memristor in an MoS2 atomic sheet*, Nat. Nanotechnol. **16**, 58 (2021).

[50] D. Wong, J. Velasco, L. Ju, J. Lee, S. Kahn, H.-Z. Tsai, C. Germany, T. Taniguchi, K. Watanabe, A. Zettl, F. Wang, and M. F. Crommie, *Characterization and manipulation of individual defects in insulating hexagonal boron nitride using scanning tunnelling microscopy*, Nat. Nanotechnol. **10**, 949 (2015).

[51] C. R. Woods, P. Ares, H. Nevison-Andrews, M. J. Holwill, R. Fabregas, F. Guinea, A. K. Geim, K. S. Novoselov, N. R. Walet, and L. Fumagalli, *Charge-polarized interfacial superlattices in marginally twisted hexagonal boron nitride*, Nat. Commun. **12**, 347 (2021).

[52] S. L. Moore, C. J. Ciccarino, D. Halbertal, L. J. McGilly, N. R. Finney, K. Yao, Y. Shao, G. Ni, A. Sternbach, E. J. Telford, B. S. Kim, S. E. Rossi, K. Watanabe, T. Taniguchi, A. N. Pasupathy, C. R. Dean, J. Hone, P. J. Schuck, P. Narang, and D. N. Basov, *Nanoscale lattice dynamics in hexagonal boron nitride moiré superlattices*, Nat. Commun. **12**, 5741 (2021).

[53] S. Chiodini, J. Kerfoot, G. Venturi, S. Mignuzzi, E. M. Alexeev, B. Teixeira Rosa, S. Tongay, T. Taniguchi, K. Watanabe, A. C. Ferrari, and A. Ambrosio, *Moiré Modulation of Van Der Waals Potential in Twisted Hexagonal Boron Nitride*, ACS Nano **16**, 7589 (2022).

[54] T. Gemming, G. Möbus, M. Exner, F. Ernst, and M. Rühle, *Ab-initio HRTEM simulations of ionic crystals: a case study of sapphire*, J. Microsc. **190**, 89 (1998).

[55] S. Mogck, B. J. Kooi, J. T. M. De Hosson, and M. W. Finnis, *Ab initio transmission electron microscopy image simulations of coherent* Ag – MgO *interfaces*, Phys. Rev. B **70**, 245427 (2004).

[56] P. A. Doyle and P. S. Turner, *Relativistic Hartree–Fock X-ray and electron scattering factors*, Acta Crystallogr. A **24**, 390 (1968).

[57] T. Susi, J. Madsen, U. Ludacka, J. J. Mortensen, T. J. Pennycook, Z. Lee, J. Kotakoski, U. Kaiser, and J. C. Meyer, *Efficient first principles simulation of electron scattering factors for transmission electron microscopy*, Ultramicroscopy **197**, 16 (2019).

[58] D. GABOR, *A New Microscopic Principle*, Nature **161**, 777 (1948).

[59] D. Gabor and W. L. Bragg, *Microscopy by reconstructed wave-fronts*, Proceedings of the Royal Society of London. Series A. Mathematical and Physical Sciences **197**, 454 (1949).

[60] H. Lichte and M. Lehmann, *Electron holography—basics and applications*, Rep. Prog. Phys. **71**, 016102 (2007).

[61] *An improved mode of operation of a transmission electron microscope for wide field off-axis holography*, Ultramicroscopy **63**, 15 (1996).

[62] F. A. Ponce and D. P. Bour, *Nitride-based semiconductors for blue and green light-emitting devices*, Nature **386**, 351 (1997).

[63] C. Addiego, W. Gao, and X. Pan, *Thickness and defocus dependence of inter-atomic electric fields measured by scanning diffraction*, Ultramicroscopy **208**, 112850 (2020).

[64] S. Subakti, M. Daqiqshirazi, D. Wolf, M. Linck, F. L. Kern, M. Jain, S. Kretschmer, A. V. Krasheninnikov, T. Brumme, and A. Lubk, *Electron holographic mapping of structural reconstruction at mono- and bilayer steps of* $h-$BN, Phys. Rev. Res. **5**, 033137 (2023).

[65] L. Ortolani, F. Houdellier, M. Monthioux, E. Snoeck, and V. Morandi, *Surface electrostatic potentials in carbon nanotubes and graphene membranes investigated with electron holography*, Carbon **49**, 1423 (2011).

[66] D. Cooper, C.-T. Pan, and S. Haigh, *Atomic resolution electrostatic potential mapping of graphene sheets by off-axis electron holography*, J. Appl. Phys. **115**, 233709 (2014).

[67] F. Winkler, J. Barthel, A. H. Tavabi, S. Borghardt, B. E. Kardynal, and R. E. Dunin-Borkowski, *Absolute Scale Quantitative Off-Axis Electron Holography at Atomic Resolution*, Phys. Rev. Lett. **120**, 156101 (2018).

[68] S. Borghardt, F. Winkler, Z. Zanolli, M. J. Verstraete, J. Barthel, A. H. Tavabi, R. E. Dunin-Borkowski, and B. E. Kardynal, *Quantitative Agreement between Electron-Optical Phase Images of* WSe_2 *and Simulations Based on Electrostatic Potentials that Include Bonding Effects*, Phys. Rev. Lett. **118**, 086101 (2017).

[69] A. Harscher and H. Lichte, *Experimental study of amplitude and phase detection limits in electron holography*, Ultramicroscopy **64**, 57 (1996).

[70] E. Voelkl, *Noise in off-axis type holograms including reconstruction and CCD camera parameters*, Ultramicroscopy **110**, 199 (2010).

[71] V. Boureau, B. Sklenard, R. McLeod, D. Ovchinnikov, D. Dumcenco, A. Kis, and D. Cooper, *Quantitative Mapping of the Charge Density in a Monolayer of MoS2 at Atomic Resolution by Off-Axis Electron Holography*, ACS Nano **14**, 524 (2020).

[72] F. Kern, M. Linck, D. Wolf, N. Alem, H. Arora, S. Gemming, A. Erbe, A. Zettl, B. Büchner, and A. Lubk, *Autocorrected off-axis holography of two-dimensional materials*, Phys. Rev. Res. **2**, 043360 (2020).

[73] T. J. Pennycook, A. R. Lupini, H. Yang, M. F. Murfitt, L. Jones, and P. D. Nellist, *Efficient phase contrast imaging in STEM using a pixelated detector. Part 1: Experimental demonstration at atomic resolution*, Ultramicroscopy **151**, 160 (2015).

[74] M. C. Cao, Y. Han, Z. Chen, Y. Jiang, K. X. Nguyen, E. Turgut, G. D. Fuchs, and D. A. Muller, *Theory and practice of electron diffraction from single atoms and extended objects using an EMPAD*, Microscopy **67**, i150 (2017).

[75] C. Ophus, *Four-Dimensional Scanning Transmission Electron Microscopy (4D-STEM): From Scanning Nanodiffraction to Ptychography and Beyond*, Microsc. Microanal. **25**, 563–582 (2019).

[76] J. A. Hachtel, J. C. Idrobo, and M. Chi, *Sub-Ångstrom electric field measurements on a universal detector in a scanning transmission electron microscope*, Advanced Structural and Chemical Imaging **4**, 1 (2018).

[77] G. Brunetti, D. Robert, P. Bayle-Guillemaud, J. L. Rouvière, E. F. Rauch, J. F. Martin, J. F. Colin, F. Bertin, and C. Cayron, *Confirmation of the Domino-Cascade Model by LiFePO4/FePO4 Precession Electron Diffraction*, Chem. Mater. **23**, 4515 (2011).

[78] M. Gallagher-Jones, C. Ophus, K. C. Bustillo, D. R. Boyer, O. Panova, C. Glynn, C.-T. Zee, J. Ciston, K. C. Mancia, A. M. Minor, and J. A. Rodriguez, *Nanoscale mosaicity revealed in peptide microcrystals by scanning electron nanodiffraction.*, Communications biology **2**, 26 (2019).

[79] O. Panova, X. C. Chen, K. C. Bustillo, C. Ophus, M. P. Bhatt, N. Balsara, and A. M. Minor, *Orientation mapping of semicrystalline polymers using scanning electron nanobeam diffraction.*, Micron **88**, 30 (2016).

[80] V. B. Ozdol, C. Gammer, X. G. Jin, P. Ercius, C. Ophus, J. Ciston, and A. M. Minor, *Strain mapping at nanometer resolution using advanced nanobeam electron diffraction*, Appl. Phys. Lett. **106**, 253107 (2015).

[81] Y. Han, K. Nguyen, M. Cao, P. Cueva, S. Xie, M. W. Tate, P. Purohit, S. M. Gruner, J. Park, and D. A. Muller, *Strain Mapping of Two-Dimensional Heterostructures with Subpicometer Precision*, Nano Lett. **18**, 3746.

[82] C. Gammer, C. Ophus, T. C. Pekin, J. Eckert, and A. M. Minor, *Local nanoscale strain mapping of a metallic glass during in situ testing*, Appl. Phys. Lett. **112**, 171905 (2018).

[83] Y. Jiang, Z. Chen, Y. Han, P. Deb, H. Gao, S. Xie, P. Purohit, M. W. Tate, J. Park, S. M. Gruner, V. Elser, and D. A. Muller, *Electron ptychography of 2D materials to deep sub-ångström resolution*, Nature **559**, 343 (2018).

[84] H. Yang, R. N. Rutte, L. Jones, M. Simson, R. Sagawa, H. Ryll, M. Huth, T. J. Pennycook, M. L. Green, H. Soltau, Y. Kondo, B. G. Davis, and P. D. Nellist, *Simultaneous atomic-resolution electron ptychography and Z-contrast imaging of light and heavy elements in complex nanostructures*, Nat. Commun. **7**, 1 (2016).

[85] T. J. Pennycook, G. T. Martinez, P. D. Nellist, and J. C. Meyer, *High dose efficiency atomic resolution imaging via electron ptychography*, Ultramicroscopy **196**, 131 (2019).

[86] A. J. D'Alfonso, A. J. Morgan, A. W. Yan, P. Wang, H. Sawada, A. I. Kirkland, and L. J. Allen, *Deterministic electron ptychography at atomic resoluti*, Phys. Rev. B **89**, 064101 (2014).

[87] J. Madsen, T. J. Pennycook, and T. Susi, *ab initio description of bonding for transmission electron microscopy*, Ultramicroscopy **231**, 113253 (2021).

[88] C. Hofer, J. Madsen, T. Susi, and T. J. Pennycook, *Detecting charge transfer at defects in 2D materials with electron ptychography*, (2023).

[89] J. N. Chapman, P. E. Batson, E. M. Waddell, and R. P. Ferrier, *The direct determination of magnetic domain wall profiles by differential phase contrast electron microscopy.*, Ultramicroscopy **3**, 203 (1978).

[90] N. H. Dekkers and H. De Lang, *Differential Phase Contrast in a STEM*, Optik **41**, 452 (1974).

[91] N. Shibata, T. Seki, G. Sánchez-Santolino, S. D. Findlay, Y. Kohno, T. Matsumoto, R. Ishikawa, and Y. Ikuhara, *Electric field imaging of single atoms*, Nat. Commun. **8**, 1 (2017).

[92] F. M., *Le microscope à contraste de phase et le microscope interférentiel*, Editions du centre national de la recherche scientifique, 1953.

[93] I. Lazić, E. G. Bosch, and S. Lazar, *Phase contrast STEM for thin samples: Integrated differential phase contrast*, Ultramicroscopy **160**, 265 (2016).

[94] N. Shibata, S. D. Findlay, H. Sasaki, T. Matsumoto, H. Sawada, Y. Kohno, S. Otomo, R. Minato, and Y. Ikuhara, *Imaging of built-in electric field at a p-n junction by scanning transmission electron microscopy*, Sci. Rep. **5**, 10040 (2015).

[95] M. Lohr, R. Schregle, M. Jetter, C. Wächter, K. Müller-Caspary, T. Mehrtens, A. Rosenauer, I. Pietzonka, M. Strassburg, and J. Zweck, *Quantitative measurements of internal electric fields with differential phase contrast microscopy on InGaN/GaN quantum well structures*, Phys. Status Solidi B **253**, 140 (2016).

[96] T. P. Almeida, R. Temple, J. Massey, K. Fallon, D. McGrouther, T. Moore, C. H. Marrows, and S. McVitie, *Quantitative TEM imaging of the magnetostructural and phase transitions in FeRh thin film systems*, Sci. Rep. **7**, 17835 (2017).

[97] C. Chen, H. Li, T. Seki, D. Yin, G. Sanchez-Santolino, K. Inoue, N. Shibata, and Y. Ikuhara, *Direct Determination of Atomic Structure and Magnetic Coupling of Magnetite Twin Boundaries*, ACS Nano **12**, 2662 (2018).

[98] N. Shibata, S. D. Findlay, Y. Kohno, H. Sawada, Y. Kondo, and Y. Ikuhara, *Differential phase-contrast microscopy at atomic resolution*, Nat. Phys. **8**, 611 (2012).

[99] H. Yang, T. J. Pennycook, and P. D. Nellist, *Efficient phase contrast imaging in STEM using a pixelated detector. Part II: optimisation of imaging conditions.*, Ultramicroscopy **151**, 232 (2015).

[100] K. Müller-Caspary, F. F. Krause, T. Grieb, S. Löffler, M. Schowalter, A. Béché, V. Galioit, D. Marquardt, J. Zweck, P. Schattschneider, J. Verbeeck, and A. Rosenauer, *Measurement of atomic electric fields and charge densities from average momentum transfers using scanning transmission electron microscopy*, Ultramicroscopy **178**, 62 (2017).

[101] E. Waddell and J. Chapman, *Linear imaging of strong phase objects using asymmetrical detectors in STEM*, Optik **54**, 83 (1979).

[102] K. Müller, F. F. Krause, A. Béché, M. Schowalter, V. Galioit, S. Löffler, J. Verbeeck, J. Zweck, P. Schattschneider, and A. Rosenauer, *Atomic electric fields revealed by a quantum mechanical approach to electron picodiffraction*, Nat. Commun. **5**, 1 (2014).

[103] R. Close, Z. Chen, N. Shibata, and S. Findlay, *Towards quantitative, atomic-resolution reconstruction of the electrostatic potential via differential phase contrast using electrons*, Ultramicroscopy **159**, 124 (2015).

[104] Y. Cao, V. Fatemi, S. Fang, K. Watanabe, T. Taniguchi, E. Kaxiras, and P. Jarillo-Herrero, *Unconventional superconductivity in magic-angle graphene superlattices*, Nature **556**, 43 (2018).

[105] A. Lubk and J. Zweck, *Differential phase contrast: An integral perspective*, Phys. Rev. A **91**, 023805 (2015).

[106] M. P. Oxley and O. E. Dyck, *The importance of temporal and spatial incoherence in quantitative interpretation of 4D-STEM*, Ultramicroscopy **215**, 113015 (2020).

[107] G. Sánchez-Santolino, N. R. Lugg, T. Seki, R. Ishikawa, S. D. Findlay, Y. Kohno, Y. Kanitani, S. Tanaka, S. Tomiya, Y. Ikuhara, and N. Shibata, *Probing the Internal Atomic Charge Density Distributions in Real Space*, ACS Nano **12**, 8875 (2018).

[108] I. MacLaren, L. Wang, D. McGrouther, A. J. Craven, S. McVitie, R. Schierholz, A. Kovács, J. Barthel, and R. E. Dunin-Borkowski, *On the origin of differential phase contrast at a locally charged and globally charge-compensated domain boundary in a polar-ordered material*, Ultramicroscopy **154**, 57 (2015).

[109] T. Grieb, F. F. Krause, K. Müller-Caspary, R. Ritz, M. Simson, J. Schörmann, C. Mahr, J. Müßener, M. Schowalter, H. Soltau, M. Eickhoff, and A. Rosenauer, *4D-STEM at interfaces to GaN: Centre-of-mass approach & NBED-disc detection*, Ultramicroscopy **228**, 113321 (2021).

[110] K. Müller-Caspary, T. Grieb, J. Müßener, N. Gauquelin, P. Hille, J. Schörmann, J. Verbeeck, S. Van Aert, M. Eickhoff, and A. Rosenauer, *Electrical Polarization in AlN/GaN Nanodisks Measured by Momentum-Resolved 4D Scanning Transmission Electron Microscopy*, Phys. Rev. Lett. **122**, 106102 (2019).

[111] B. C. da Silva, Z. S. Momtaz, L. Bruas, J.-L. Rouviére, H. Okuno, D. Cooper, and M. I. den Hertog, *The influence of illumination conditions in the measurement of built-in electric field at p–n junctions by 4D-STEM*, Appl. Phys. Lett. **121**, 123503 (2022).

[112] B. C. da Silva, Z. Sadre Momtaz, E. Monroy, H. Okuno, J.-L. Rouviere, D. Cooper, and M. I. Den Hertog, *Assessment of Active Dopants and p–n Junction Abruptness Using In Situ Biased 4D-STEM*, Nano Lett. **22**, 9544 (2022).

[113] C. Yang, Y. Wang, W. Sigle, and P. A. van Aken, *Determination of Grain-Boundary Structure and Electrostatic Characteristics in a SrTiO3 Bicrystal by Four-Dimensional Electron Microscopy*, Nano Lett. **21**, 9138 (2021).

[114] Q. Jia and A. Gloter, *Real-Space Observation of Potential Reconstruction at Metallic/Insulating Oxide Interface*, Adv. Mater. Interfaces **10**, 2202165 (2023).

[115] K. Müller-Caspary, M. Duchamp, M. Rösner, V. Migunov, F. Winkler, H. Yang, M. Huth, R. Ritz, M. Simson, S. Ihle, H. Soltau, T. Wehling, R. E. Dunin-Borkowski, S. Van Aert, and A. Rosenauer, *Atomic-scale quantification of charge densities in two-dimensional materials*, Phys. Rev. B **98**, 121408 (2018).

[116] R. Ishikawa, S. D. Findlay, T. Seki, G. Sánchez-Santolino, Y. Kohno, Y. Ikuhara, and N. Shibata, *Direct electric field imaging of graphene defects*, Nat. Commun. **9**, 1 (2018).

[117] S. Fang, Y. Wen, C. S. Allen, C. Ophus, G. G. Han, A. I. Kirkland, E. Kaxiras, and J. H. Warner, *Atomic electrostatic maps of 1D channels in 2D semiconductors using 4D scanning transmission electron microscopy*, Nat. Commun. **10** (2019).

[118] Y. Wen, C. Ophus, C. S. Allen, S. Fang, J. Chen, E. Kaxiras, A. I. Kirkland, and J. H. Warner, *Simultaneous Identification of Low and High Atomic Number Atoms in Monolayer 2D Materials Using 4D Scanning Transmission Electron Microscopy*, Nano Lett. **19**, 6482 (2019).

[119] S. Calderon V, R. V. Ferreira, D. Taneja, R. Jayanth, L. Zhou, R. M. Ribeiro, D. Akinwande, and P. J. Ferreira, *Atomic Electrostatic Maps of Point Defects in MoS2*, Nano Lett. **21**, 10157 (2021).

[120] S. de Graaf, M. Ahmadi, I. Lazić, E. G. T. Bosch, and B. J. Kooi, *Imaging atomic motion of light elements in 2D materials with 30 kV electron microscopy*, Nanoscale **13**, 20683 (2021).

[121] D. Dosenovic, K. Sharma, S. Dechamps, J. L. Rouviere, Y. Lu, A. Mordant, M. den Hertog, L. Genovese, S. M. M. Dubois, J. C. Charlier, M. Jamet, A. Marty, and H. Okuno, *Atomic scale imaging of the negative charge induced by a single vanadium dopant atom in monolayer WSe_2 using 4D-STEM*, arXiv:2310.09246 (2023).

[122] J. Martis, S. Susarla, A. Rayabharam, C. Su, T. Paule, P. Pelz, C. Huff, X. Xu, H.-K. Li, M. Jaikissoon, V. Chen, E. Pop, K. Saraswat, A. Zettl, N. R. Aluru, R. Ramesh, P. Ercius, and A. Majumdar, *Imaging the electron charge density in monolayer MoS2 at the Ångstrom scale*, Nat. Commun. **14**, 4363 (2023).

[123] K. G. Scheuer, G. J. Hornig, and R. G. DeCorby, *Polymer transfer technique for strain-activated emission in hexagonal boron nitride*, Opt. Express **29**, 26103 (2021).

[124] O. Cretu, A. Ishizuka, K. Yanagisawa, K. Ishizuka, and K. Kimoto, *Atomic-Scale Electrical Field Mapping of Hexagonal Boron Nitride Defects*, ACS Nano **15**, 5316 (2021).

[125] W. S. J. Hummers and R. E. Offeman, *Preparation of Graphitic Oxide*, J. Am. Chem. Soc. **80**, 1339 (1958).

[126] J. N. Coleman et al., *Two-Dimensional Nanosheets Produced by Liquid Exfoliation of Layered Materials*, Science **331**, 568 (2011).

[127] S. J. Cartamil-Bueno, M. Cavalieri, R. Wang, S. Houri, S. Hofmann, and H. S. J. van der Zant, *Mechanical characterization and cleaning of CVD single-layer h-BN resonators*, npj 2D Materials and Applications **1**, 16 (2017).

[128] K. Suenaga, H. Kobayashi, and M. Koshino, *Core-Level Spectroscopy of Point Defects in Single Layer h-BN*, Phys. Rev. Lett. **108**, 075501 (2012).

[129] C. Gao, L. Tao, Y.-Y. Zhang, S. Du, S. T. Pantelides, J. C. Idrobo, W. Zhou, and H.-J. Gao, *Spectroscopic signatures of edge states in hexagonal boron nitride*, Nano Res. **12**, 1663 (2019).

[130] H. Park, Y. Wen, S. X. Li, W. Choi, G.-D. Lee, M. Strano, and J. H. Warner, *Atomically Precise Control of Carbon Insertion into hBN Monolayer Point Vacancies using a Focused Electron Beam Guide*, Small **17**, 2100693 (2021).

[131] R. Tay, J. Lin, S. H. Tsang, D. G. McCulloch, and E. H. T. Teo, *Probing the Atomic Structures of Synthetic Monolayer and Bilayer Hexagonal Boron Nitride Using Electron Microscopy*, Applied Microscopy **46**, 217 (2016).

[132] K. K. Kim, A. Hsu, X. Jia, S. M. Kim, Y. Shi, M. Hofmann, D. Nezich, J. F. Rodriguez-Nieva, M. Dresselhaus, T. Palacios, and J. Kong, *Synthesis of Monolayer Hexagonal Boron Nitride on Cu Foil Using Chemical Vapor Deposition*, Nano Lett. **12**, 161 (2012).

[133] G. H. Ryu, H. J. Park, J. Ryou, J. Park, J. Lee, G. Kim, H. S. Shin, C. W. Bielawski, R. S. Ruoff, S. Hong, and Z. Lee, *Atomic-scale dynamics of triangular hole growth in monolayer hexagonal boron nitride under electron irradiation*, Nanoscale **7**, 10600 (2015).

[134] T. A. Bui, G. T. Leuthner, J. Madsen, M. R. A. Monazam, A. I. Chirita, A. Postl, C. Mangler, J. Kotakoski, and T. Susi, *Creation of Single Vacancies in hBN with Electron Irradiation*, Small **19**, 2301926 (2023).

[135] Y. Wen, S. Fang, M. Coupin, Y. Lu, C. Ophus, E. Kaxiras, and J. H. Warner, *Mapping 1D Confined Electromagnetic Edge States in 2D Monolayer Semiconducting MoS2Using 4D-STEM*, ACS Nano **16**, 6657 (2022).

[136] J. Madsen and T. Susi, *The abTEM code: transmission electron microscopy from first principles*, Open Research Europe **1** (2021).

[137] R. Bader, *Atoms in Molecules: A Quantum Theory*, Oxford University Press, 1990.

[138] J. C. Meyer, A. Chuvilin, G. Algara-Siller, J. Biskupek, and U. Kaiser, *Selective sputtering and atomic resolution imaging of atomically thin boron nitride membranes*, Nano Lett. **9**, 2683 (2009).

[139] J. Kotakoski, C. H. Jin, O. Lehtinen, K. Suenaga, and A. V. Krasheninnikov, *Electron knock-on damage in hexagonal boron nitride monolayers*, Phys. Rev. B **82**, 113404 (2010).

[140] C. Jin, F. Lin, K. Suenaga, and S. Iijima, *Fabrication of a Freestanding Boron Nitride Single Layer and Its Defect Assignments*, Phys. Rev. Lett. **102**, 195505 (2009).

[141] S. Huotari, M. Cazzaniga, H.-C. Weissker, T. Pylkkänen, H. Müller, L. Reining, G. Onida, and G. Monaco, *Dynamical response function in sodium studied by inelastic x-ray scattering spectroscopy*, Phys. Rev. B **84**, 075108 (2011).

[142] W. Schülke, *Electron Dynamics by Inelastic X-Ray Scattering*, Oxford Series on Synchrotron Radiation, OUP Oxford, 2007.

[143] J.-P. Rueff and A. Shukla, *Inelastic x-ray scattering by electronic excitations under high pressure*, Rev. Mod. Phys. **82**, 847 (2010).

[144] J. Fink, M. Knupfer, S. Atzkern, and M. Golden, *Electronic correlations in solids, studied using electron energy-loss spectroscopy*, J. Electron Spectrosc. **117-118**, 287 (2001).

[145] R. Egerton, *Electron energy-loss spectroscopy in the electron microscope*, Springer, New York, 3rd edition, 2011.

[146] J.-P. Rueff and A. Shukla, *Inelastic x-ray scattering by electronic excitations under high pressure*, Rev. Mod. Phys. **82**, 847 (2010).

[147] L. J. P. Ament, M. van Veenendaal, T. P. Devereaux, J. P. Hill, and J. van den Brink, *Resonant inelastic x-ray scattering studies of elementary excitations*, Rev. Mod. Phys. **83**, 705 (2011).

[148] L. J. P. Ament, M. van Veenendaal, T. P. Devereaux, J. P. Hill, and J. van den Brink, *Resonant inelastic x-ray scattering studies of elementary excitations*, Rev. Mod. Phys. **83**, 705 (2011).

[149] A. Kotani and S. Shin, *Resonant inelastic x-ray scattering spectra for electrons in solids*, Rev. Mod. Phys. **73**, 203 (2001).

[150] S. Huotari, *Spectroscopy in the Frequency Domain*, Springer, 2012.

[151] M. Sacchi, N. Jaouen, H. Popescu, R. Gaudemer, J. M. Tonnerre, S. G. Chiuzbaian, C. F. Hague, A. Delmotte, J. M. Dubuisson, G. Cauchon, B. Lagarde, and F. Polack, *The SEXTANTS beamline at SOLEIL: a new facility for elastic, inelastic and coherent scattering of soft X-rays*, J. Phys. Conf. Ser. **425**, 072018 (2013).

[152] S. G. Chiuzbăian et al., *Design and performance of AERHA, a high acceptance high resolution soft x-ray spectrometer*, Rev, of Sci. Instrum. **85**, 043108 (2014).

[153] F. Briquez, O. Chubar, M.-E. Couprie, T. Ajjouri, F. Marteau, A. Mary, K. Tavakoli, and S. SOLEIL, *Construction of short period apple II type undulators at SOLEIL*, 30th International Free Electron Laser Conference (2008).

[154] S. G. Chiuzbăian, C. F. Hague, A. Avila, R. Delaunay, N. Jaouen, M. Sacchi, F. Polack, M. Thomasset, B. Lagarde, A. Nicolaou, S. Brignolo, C. Baumier, J. Lüning, and J.-M. Mariot, *Design and performance of AERHA, a high acceptance high resolution soft x-ray spectrometer*, Review of Scientific Instruments **85**, 043108 (2014).

[155] T. Taniguchi and K. Watanabe, *Synthesis of high-purity boron nitride single crystals under high pressure by using Ba–BN solvent*, J. Cryst. Growth **303**, 525 (2007).

[156] J. Koskelo, G. Fugallo, M. Hakala, M. Gatti, F. Sottile, and P. Cudazzo, *Excitons in van der Waals materials: From monolayer to bulk hexagonal boron nitride*, Phys. Rev. B **95**, 035125 (2017).

[157] R. Schuster, C. Habenicht, M. Ahmad, M. Knupfer, and B. Büchner, *Direct observation of the lowest indirect exciton state in the bulk of hexagonal boron nitride*, Phys. Rev. B **97**, 041201 (2018).

[158] M. Kociak and L. Zagonel, *Cathodoluminescence in the scanning transmission electron microscope*, Ultramicroscopy **176**, 112 (2017).

[159] N. Bonnet, H. Y. Lee, F. Shao, S. Y. Woo, J.-D. Blazit, K. Watanabe, T. Taniguchi, A. Zobelli, O. Stéphan, M. Kociak, S. Gradečak, and L. H. G. Tizei, *Nanoscale Modification of WS2 Trion Emission by Its Local Electromagnetic Environment*, Nano Lett. **21**, 10178 (2021).

[160] N. Bonnet, *Electron and optical spectroscopy of 2D semiconductors and defects in the electron microscope*, PhD thesis, Université Paris Slaclay, 2022.

[161] S. Fuhui, *Investigation of Exciton Linewidth and Lineshapes in Transition Metal Dichalocogenide van der Waals Heterostructures by Electron Microscopy and Spectroscopies*, PhD thesis, Université Paris Slaclay, 2022.

[162] T. K. Sham, D. T. Jiang, I. Coulthard, J. W. Lorimer, X. H. Feng, K. H. Tan, S. P. Frigo, R. A. Rosenberg, D. C. Houghton, and B. Bryskiewicz, *Origin of luminescence from porous silicon deduced by synchrotron-light-induced optical luminescence*, Nature **363**, 331 (1993).

[163] A. Rogalev and J. Goulon, X-ray excited optical luminescence spectroscopies, in *Chemical Applications Of Synchrotron Radiation: Part I: Dynamics and VUV SpectroscopyPart II: X-Ray Applications*, pages 707–760, World Scientific, 2002.

[164] P. Tola, A. Retournard, J. Dexpert-Ghys, M. Lemonnier, M. Pagel, and J. Goulon, *On the use of x-ray-excited optical luminescence (XEOL) for the analysis of multisite rare-earth systems*, Chem. Phys. **78**, 339 (1983).

[165] Goulon, J., Goulon-Ginet, C., Cortes, R., and Dubois, J.M., *On experimental attenuation factors of the amplitude of the EXAFS oscillations in absorption, reflectivity and luminescence measurements*, J. Phys. France **43**, 539 (1982).

[166] T. K. Sham, *International Tables for Crystallography. Vol. I: X-ray excited optical luminescence*, 2022.

[167] L. Liu, T.-K. Sham, W. Han, C. Zhi, and Y. Bando, *X-ray Excited Optical Luminescence from Hexagonal Boron Nitride Nanotubes: Electronic Structures and the Role of Oxygen Impurities*, ACS Nano **5**, 631 (2011).

[168] T. K. Sham, S. J. Naftel, P.-S. G. Kim, R. Sammynaiken, Y. H. Tang, I. Coulthard, A. Moewes, J. W. Freeland, Y.-F. Hu, and S. T. Lee, *Electronic structure and optical properties of silicon nanowires: A study using x-ray excited optical luminescence and x-ray emission spectroscopy*, Phys. Rev. B **70**, 045313 (2004).

[169] D. A. Evans, A. R. Vearey-Roberts, and N. Poolton, *Locating hexagonal and cubic phases in boron nitride using wavelength-selective optically detected x-ray absorption spectroscopy*, Appl. Phys. Lett. **89**, 161107 (2006).

[170] G. Martínez-Criado, A. Homs, B. Alén, J. A. Sans, J. Segura-Ruiz, A. Molina-Sánchez, J. Susini, J. Yoo, and G.-C. Yi, *Probing Quantum Confinement within Single Core–Multishell Nanowires*, Nano Lett. **12**, 5829 (2012).

[171] J. Segura-Ruiz, D. Salomon, A. Rogalev, J. Eymery, B. Alén, and G. Martínez-Criado, *Spatially and Time-Resolved Carrier Dynamics in Core–Shell InGaN/GaN Multiple-Quantum Wells on GaN Wire*, Nano Lett. **21**, 9494 (2021).

[172] S. Hageraats, K. Keune, S. Stanescu, J.-M. Laurent, W. Fresquet, and M. Thoury, *Combining X-ray excited optical luminescence and X-ray absorption spectroscopy for correlative imaging on the nanoscale*, J. Synchrotron Radiat. **28**, 1858 (2021).

[173] https://www.ceramoptec.com/products/fiber-bundles.html.

[174] T. Taniguchi and K. Watanabe, *Synthesis of high-purity boron nitride single crystals under high pressure by using Ba–BN solvent*, J. Cryst. Growth **303**, 525 (2007).

[175] T. Pelini, C. Elias, R. Page, L. Xue, S. Liu, J. Li, J. H. Edgar, A. Dréau, V. Jacques, P. Valvin, B. Gil, and G. Cassabois, *Shallow and deep levels in carbon-doped hexagonal boron nitride crystals*, Phys. Rev. Mater. **3**, 094001 (2019).

[176] E. Tsushima, T. Tsujimura, and T. Uchino, *Enhancement of the deep-level emission and its chemical origin in hexagonal boron nitride*, Appl. Phys. Lett. **113**, 031903 (2018).

[177] S. F. Chichibu, Y. Ishikawa, H. Kominami, and K. Hara, *Nearly temperature-independent ultraviolet light emission intensity of indirect excitons in hexagonal BN microcrystals*, J. Appl. Phys. **123**, 065104 (2018).

[178] A. Vokhmintsev, I. Weinstein, and D. Zamyatin, *Electron-phonon interactions in subband excited photoluminescence of hexagonal boron nitride*, J. Lumin. **208**, 363 (2019).

[179] L. Weston, D. Wickramaratne, M. Mackoit, A. Alkauskas, and C. G. Van de Walle, *Native point defects and impurities in hexagonal boron nitride*, Phys. Rev. B **97**, 214104 (2018).

[180] G. Cassabois, P. Valvin, and B. Gil, *Hexagonal boron nitride is an indirect bandgap semiconductor*, Nat. Photonics **10**, 262 (2016).

[181] A. Rousseau, M. Moret, P. Valvin, W. Desrat, J. Li, E. Janzen, L. Xue, J. H. Edgar, G. Cassabois, and B. Gil, *Determination of the optical bandgap of the Bernal and rhombohedral boron nitride polymorphs*, Phys. Rev. Mater. **5**, 064602 (2021).

[182] T.-K. Sham, *Photon-In/Photon-Out Spectroscopic Techniques for Materials Analysis: Some Recent Developments*, Adv. Mater. **26**, 7896 (2014).

[183] M. Ward, J. Smith, T. Regier, and T. Sham, 2d xafs-xeol spectroscopy–some recent developments, in *J. Phys. Conf. Ser.*, volume 425, page 132009, IOP Publishing, 2013.

[184] M. Udayakantha, J. V. Handy, R. D. Davidson, J. Kaur, G. Villalpando, L. Zuin, S. Chakraborty, and S. Banerjee, *Halide Replacement with Complete Preservation of Crystal Lattice in Mixed-Anion Lanthanide Oxyhalides*, Angew. Chem. **60**, 15582 (2021).

[185] A. Tararan, S. di Sabatino, M. Gatti, T. Taniguchi, K. Watanabe, L. Reining, L. H. G. Tizei, M. Kociak, and A. Zobelli, *Optical gap and optically active intragap defects in cubic BN*, Phys. Rev. B **98**, 094106 (2018).

[186] U. Vetter, T. Taniguchi, U. Wahl, J. Correia, A. Müller, C. Ronning, H. Hofsäss, M. Dietrich, and I. Collaboration, *Lanthanide Doped Cubic Boron Nitride*, MRS Online Proc. Libr. **744**, 838 (2003).

[187] U. Vetter, P. Reinke, C. Ronning, H. Hofsäss, P. Schaaf, K. Bharuth-Ram, and T. Taniguchi, *Europium doping of c-BN and ta-C thin films*, Diam. Relat. Mater. **12**, 1182 (2003).

[188] T. Taniguchi and S. Yamaoka, *Spontaneous nucleation of cubic boron nitride single crystal by temperature gradient method under high pressure*, J. Cryst. Growth **222**, 549 (2001).

[189] T. Taniguchi, K. Watanabe, and S. Koizumi, *Defect characterization of cBN single crystals grown under HP/HT*, Phys. Status Solidi A **201**, 2573 (2004).

[190] A. Nakayama, T. Taniguchi, Y. Kubota, K. Watanabe, S. Hishita, and H. Kanda, *Characterization of luminous-cubic boron-nitride single-crystals doped with Eu3+ and Tb3+ ions*, Appl. Phys. Lett. **87**, 211913 (2005).

[191] E. M. Shishonok, S. V. Leonchik, A. Braud, J. W. Steeds, O. R. Abdullaev, A. S. Yakunin, and D. M. Zhigunov, *Photoluminescence of micropowders of europium-doped cubic boron nitride*, J. Opt. Technol. **77**, 788 (2010).

[192] L. J. Terminello, A. Chaiken, D. A. Lapiano-Smith, G. L. Doll, and T. Sato, *Morphology and bonding measured from boron-nitride powders and films using near-edge x-ray absorption fine structure*, J. Vac. Sci. Technol. A **12**, 2462 (1994).

[193] I. Jiménez, A. Jankowski, L. J. Terminello, J. A. Carlisle, D. G. J. Sutherland, G. L. Doll, J. V. Mantese, W. M. Tong, D. K. Shuh, and F. J. Himpsel, *Near-edge x-ray absorption fine structure study of bonding modifications in BN thin films by ion implantation*, Appl. Phys. Lett. **68**, 2816 (1996).

[194] D. Berns, M. Cappelli, and D. Shuh, *Near-edge X-ray absorption fine structure spectroscopy of arcjet-deposited cubic boron nitride*, Diam. Relat. Mater. **6**, 1883 (1997).

[195] L. Liu, T.-K. Sham, and W. Han, *Investigation on the electronic structure of BN nanosheets synthesized via carbon-substitution reaction: the arrangement of B, N, C and O atoms*, Phys. Chem. Chem. Phys. **15**, 6929 (2013).

[196] S. J. Grenadier, A. Maity, J. Li, J. Y. Lin, and H. X. Jiang, *Origin and roles of oxygen impurities in hexagonal boron nitride epilayers*, Appl. Phys. Lett. **112**, 162103 (2018).

[197] T. Mueller and E. Malic, *Exciton physics and device application of two-dimensional transition metal dichalcogenide semiconductors*, npj 2D Materials and Applications **2**, 29 (2018).

[198] G. Wang, A. Chernikov, M. M. Glazov, T. F. Heinz, X. Marie, T. Amand, and B. Urbaszek, *Colloquium: Excitons in atomically thin transition metal dichalcogenides*, Rev. Mod. Phys. **90**, 021001 (2018).

[199] A. Raja, L. Waldecker, J. Zipfel, Y. Cho, S. Brem, J. D. Ziegler, M. Kulig, T. Taniguchi, K. Watanabe, E. Malic, T. F. Heinz, T. C. Berkelbach, and A. Chernikov, *Dielectric disorder in two-dimensional materials*, Nat. Nanotechnol. **14**, 832 (2019).

[200] P. Zhao, J. Yu, H. Zhong, M. Rösner, M. I. Katsnelson, and S. Yuan, *Electronic and optical properties of transition metal dichalcogenides under symmetric and asymmetric field-effect doping*, New J. Phys. **22**, 083072 (2020).

[201] D. Rhodes, S. H. Chae, R. Ribeiro-Palau, and J. Hone, *Disorder in van der Waals heterostructures of 2D materials*, Nat. Mater. **18**, 541 (2019).

[202] A. Arora, N. K. Wessling, T. Deilmann, T. Reichenauer, P. Steeger, P. Kossacki, M. Potemski, S. Michaelis de Vasconcellos, M. Rohlfing, and R. Bratschitsch, *Dark trions govern the temperature-dependent optical absorption and emission of doped atomically thin semiconductors*, Phys. Rev. B **101**, 241413 (2020).

[203] F. Shao, S. Y. Woo, N. Wu, R. Schneider, A. J. Mayne, S. M. de Vasconcellos, A. Arora, B. J. Carey, J. A. Preuß, N. Bonnet, M. Och, C. Mattevi, K. Watanabe, T. Taniguchi, Z. Niu, R. Bratschitsch, and L. H. G. Tizei, *Substrate influence on transition metal dichalcogenide monolayer exciton absorption linewidth broadening*, Phys. Rev. Mater. **6**, 074005 (2022).

[204] F. Cadiz, E. Courtade, C. Robert, G. Wang, Y. Shen, H. Cai, T. Taniguchi, K. Watanabe, H. Carrere, D. Lagarde, M. Manca, T. Amand, P. Renucci, S. Tongay, X. Marie, and B. Urbaszek, *Excitonic Linewidth Approaching the Homogeneous Limit in MoS_2-Based van der Waals Heterostructures*, Phys. Rev. X **7**, 021026 (2017).

[205] S. Zheng, J.-K. So, F. Liu, Z. Liu, N. Zheludev, and H. J. Fan, *Giant enhancement of cathodoluminescence of monolayer transitional metal dichalcogenides semiconductors*, Nano Lett. **17**, 6475 (2017).

[206] H. Zeng, G.-B. Liu, J. Dai, Y. Yan, B. Zhu, R. He, L. Xie, S. Xu, X. Chen, W. Yao, and X. Cui, *Optical signature of symmetry variations and spin-valley coupling in atomically thin tungsten dichalcogenides*, Sci. Rep. **3**, 1608 (2013).

[207] K. H. Shin, M.-K. Seo, S. Pak, A.-R. Jang, and J. I. Sohn, *Observation of Strong Interlayer Couplings in WS2/MoS2 Heterostructures via Low-Frequency Raman Spectroscopy*, Nanomaterials **12** (2022).

[208] W. Zhao, Z. Ghorannevis, K. K. Amara, J. R. Pang, M. Toh, X. Zhang, C. Kloc, P. H. Tan, and G. Eda, *Lattice dynamics in mono- and few-layer sheets of WS2 and WSe2*, Nanoscale **5**, 9677 (2013).

[209] F. Pizzocchero, L. Gammelgaard, B. S. Jessen, J. M. Caridad, L. Wang, J. Hone, P. Bøggild, and T. J. Booth, *The hot pick-up technique for batch assembly of van der Waals heterostructures*, Nat. Commun. **7**, 11894 (2016).

[210] L. Wang, I. Meric, P. Y. Huang, Q. Gao, Y. Gao, H. Tran, T. Taniguchi, K. Watanabe, L. M. Campos, D. A. Muller, J. Guo, P. Kim, J. Hone, K. L. Shepard, and C. R. Dean, *One-Dimensional Electrical Contact to a Two-Dimensional Material*, Science **342**, 614 (2013).

[211] P. K. Chow, R. B. Jacobs-Gedrim, J. Gao, T.-M. Lu, B. Yu, H. Terrones, and N. Koratkar, *Defect-Induced Photoluminescence in Monolayer Semiconducting Transition Metal Dichalcogenides*, ACS Nano **9**, 1520 (2015).

[212] J. Shang, X. Shen, C. Cong, N. Peimyoo, B. Cao, M. Eginligil, and T. Yu, *Observation of Excitonic Fine Structure in a 2D Transition-Metal Dichalcogenide Semiconductor*, ACS Nano **9**, 647 (2015).

[213] Z. He, X. Wang, W. Xu, Y. Zhou, Y. Sheng, Y. Rong, J. M. Smith, and J. H. Warner, *Revealing Defect-State Photoluminescence in Monolayer WS2 by Cryogenic Laser Processing*, ACS Nano **10**, 5847 (2016).

[214] G. Plechinger, F.-X. Schrettenbrunner, J. Eroms, D. Weiss, C. Schüller, and T. Korn, *Low-temperature photoluminescence of oxide-covered single-layer MoS2*, Physica Status Solidi - Rapid Research Letters **6**, 126 (2012).

[215] S. Tongay, J. Suh, C. Ataca, W. Fan, A. Luce, J. S. Kang, J. Liu, C. Ko, R. Raghunathanan, J. Zhou, F. Ogletree, J. Li, J. C. Grossman, and J. Wu, *Defects activated photoluminescence in two-dimensional semiconductors: interplay between bound, charged and free excitons*, Sci. Rep. **3**, 2657 (2013).

[216] T. Kato and T. Kaneko, *Optical Detection of a Highly Localized Impurity State in Monolayer Tungsten Disulfide*, ACS Nano **8**, 12777 (2014).

[217] D. Sercombe, S. Schwarz, O. D. Pozo-Zamudio, F. Liu, B. J. Robinson, E. A. Chekhovich, I. I. Tartakovskii, O. Kolosov, and A. I. Tartakovskii, *Optical investigation of the natural electron doping in thin MoS2 films deposited on dielectric substrates*, Sci. Rep. **3**, 3489 (2013).

[218] T. Korn, S. Heydrich, M. Hirmer, J. Schmutzler, and C. Schüller, *Low-temperature photocarrier dynamics in monolayer MoS2*, Appl. Phys. Lett. **99**, 102109 (2011).